ON TEMPORAL FEATURES OF AIRBORNE ODOUR PLUMES

SUBMITTED TO THE UNIVERSITY OF HERTFORDSHIRE IN PARTIALFULFILMENT OF THE REQUIREMENTS OF THE DEGREE OF

DOCTOR OF PHILOSOPHY

SAMUEL SUTTON
SCHOOL OF COMPUTER SCIENCE
CENTRE FOR COMPUTER SCIENCE AND INFORMATICS RESEARCH
UNIVERSITY OF HERTFORDSHIRE
HATFIELD

SUPERVISORS:

PROF. MICHAEL SCHMUKER
PROF. VOLKER STEUBER

SEPTEMBER 2024

ABSTRACT

Animals navigate towards food, mates, and away from predators by exploiting transient fluctuations in odour concentration carried in turbulent plumes. Understanding how these fluctuations encode information about source proximity, and which strategies animals use to act on them, is essential for developing robust robotic odour source localization. This thesis presents two studies using high-resolution planar laser-induced fluorescence (PLIF) recordings of acetone vapour plumes in a benchtop wind tunnel (Connor, McHugh and J. P. Crimaldi, 2018), spanning four release configurations: near-bed release at 10 cm/s, and freestream release at 5 cm/s, 10 cm/s, and 20 cm/s.

The first study extends the bout analysis pipeline of Schmuker, Bahr and Huerta (2016), originally developed for metal oxide (MOX) gas sensors, to optically recorded PLIF plume data. Bout count, duration, amplitude, and inter-bout interval (IBI) each exhibit systematic spatial structure: bout counts follow a non-linear sigmoidal decline with downwind distance along the plume centre line, crosswind profiles are approximately Gaussian, and IBI increases with source distance as an inverted Gaussian. Principal component analysis confirms that these statistics together encode odour source proximity.

The second study applies three biologically inspired in-silico navigation strategies to the same PLIF data: a direction-sensing (DS+) and non-direction-sensing (DS−) strategy modelled on walking *Drosophila*, and a cast-and-surge (CS) strategy modelled on flying insects. The CS strategy outperformed both walking strategies across the majority of release configurations. The dominant factor was the behaviour adopted in the absence of odour: crosswind casting was consistently more effective than random walking at relocating the plume.

Together, these findings establish a quantitative link between turbulent plume structure and the transient odour statistics available to navigating animals and robots.

ACKNOWLEDGMENTS

I would like to take this opportunity to thank all the people who have made this journey an enjoyable and one-of-a-kind learning experience. Firstly, I would like to thank my principal supervisor, Michael Schmuker, for imparting his passion for the challenges of olfaction and robotic navigation, for offering guidance at every turn, and for the myriad opportunities he has provided over the years. I would also like to express my gratitude to my secondary supervisor, Volker Steuber, for his continued support, discussions and encouragement, particularly over the last year. Your patience and advice has been invaluable. A very special thanks goes to Justus Verhagen for your support, encouragement and many fruitful discussions. From my office in Peterborough to the lab in New Haven, you have been a true friend and mentor.

I would like to thank all of those I have had the pleasure of interacting with during my time at the University of Hertfordshire. I would specifically like to thank those in the BioML lab, the Biocomputation group and those in NeuroNex Odor2Action network for making me feel very welcome. There are many who have come and gone in the time it has taken me to finish my thesis - not to mention the changes brought about by the pandemic and moving house multiple times - but I value all of the friendships I have formed over the years, and cherished the lively journal club discussions (and occasional follow-ups at the pub afterwards). There are too many people to name individually, but you have all kept me going and I thank you.

A very special thank you to my fiancée, Ellie. You have been endlessly patient and supportive from start to finish; I could not have dreamt of doing this without you. Thank you for your inspiring speeches when I faltered, for pretending to understand my latest new figures and for stepping up again and again when I needed you. To my newborn daughter, Darcy: you have made the last few months especially challenging and exciting, but I wouldn't change a thing. Dad, I am incredibly grateful for your continued encouragement and unconditional support, which has never faltered. It didn't go unnoticed when you let me talk through my latest obscure branch of research late into the night over a glass of whiskey. Thank you to my siblings, Chel, Ginny and Adam, for supporting me and not begrudging my absence at games nights; to my in-laws, Sue, Trev and Mike, for encouraging me and believing in me (even as we entered year seven!); and to my friends who showed up without fail whenever I called upon them. Thank you to Lexi and Kira for forcing me out of the house every single day, whatever the weather.

Lastly, I would like to thank the hard-working NHS staff at Watford General and Luton and Dunstable hospitals for saving my life on multiple occasions these past seven years - I wouldn't be here without your intervention.

CONTENTS

1 Introduction 1

1.1 Aims of the Thesis 1

1.2 Contribution to Knowledge 3

1.3 Dissemination from the Thesis 3

2 Literature Review 5

2.1 Odour Landscapes 5

2.2 Active Sensing of Odours 7

2.3 Animal Olfactory Systems 8

2.4 Understanding Odour Motion 16

2.5 Measuring Airborne Plumes 20

2.6 Sensed Odour Statistics 27

2.7 Navigation Strategies 29

2.8 Conclusions 35

3 Bout Analysis in Realistic Turbulent Plumes 36

3.5 Introduction 38

3.6 Materials and Methods 40

3.6.1 Input Data 40

3.6.2 Finding the turbulent plume Boundaries 41

3.6.3 Bout Detection Algorithm 45

3.6.4 Scaling the Amplitude Threshold 49

3.7 Results 51

3.7.1 Downwind Distance 51

3.7.2 Crosswind Distance 67

3.7.3 Whole Plume 76

3.7.4 Compensating for Wind Speed 85

3.8 Discussion 90

3.9 Conclusion 96

4 In-silico Insect-Like Navigation Strategies in Airborne Turbulent Plumes 97

4.5 Introduction 99

4.6 Materials and Methods 101

4.6.1 Plume Recordings 101

4.6.2 In-silico Agents 102

4.7 Results 108

4.7.1 Scenario A: Agents Position initialised at Downwind Extent 108

4.7.2 Scenario B: Agents Position Randomly initialised 116

4.8 Discussion 127

4.9 Conclusion 130
5.1 General Discussion 131
5 Conclusions 131
6 Bibliography 135
A Appendix 1 163
A.1 Preliminary Data Analysis 163
A.1.1 Spectral Analysis Along the Plume Centre Line 163
A.1.2 Kernel Shapes 170
A.1.3 Influence of Kernel Parameters on Bout Counts 170
A.2 Impact of Crosswind Distance on Normalized Bout Statistics 174
A.3 Bout Intermittency 177
A.4 Impact of Sample Duration on Bout Count 180
A.5 Downwind PCA Tables 185
A.6 Crosswind PCA Tables 186
A.7 Full Plume PCA Tables 188
A.8 Wind speed PCA Tables 189
A.9 Sample Duration Regression Table 190
B Appendix 2 193
B.1 Scenario A: Agents Position Initialized at Downwind Extent 193
B.2 Scenario B: Agents Position Randomly Initialized 197
B.3 Validation of Parameter Selection 200
C Appendix 3 207
C.1 Addendum 207
C.1.1 Gaussian Model 207
C.1.2 Odour Source 207
C.1.3 Mixture Density 208
C.1.4 Mass Emission Rate and Flux 209
C.1.5 Results 209
C.1.6 Discussion 210

LIST OF FIGURES

Figure 2.1 Schematic representations of vertebrate and insect olfactory receptors 9
Figure 2.2 Common neural circuit motif in rodents and insects. 10
Figure 2.3 The Drosophila olfactory pathway. 11
Figure 2.4 Diagram of circuit organization of the olfactory bulb 13
Figure 2.5 Normalized concentration distributions of three flow cases 26
Figure 2.6 Definition of the four most popular features in transient signals 27
Figure 2.7 A typical time series of the odour concentration at a given point in space, from Celani, Villermaux and Vergassola (2014) 28
Figure 2.8 Orientation in turbulent odour field. 31
Figure 2.9 Casting frequently follows plume truncation. 33
Figure 3.1 Schematic of experimental layout (Connor, McHugh and J. P. Crimaldi, 2018) 40
Figure 3.2 Instantaneous concentration plots 42
Figure 3.3 Tracking the average plume using laterally fitted Gaussian kernels 44
Figure 3.4 Signal processing pipeline from Schmuker, Bahr and Huerta (2016) 45
Figure 3.5 Our Signal processing pipeline 45
Figure 3.6 Bout analysis pipeline 45
Figure 3.7 Our filtering pipeline with demonstrative signals. 47
Figure 3.8 The bout detection analysis pipeline with demonstrative signals. 48
Figure 3.9 Bout statistics diagram demonstrating bout count, duration, amplitude and IBI 49
Figure 3.10 Amplitude Threshold Scaling using filtered impulse response 50
Figure 3.11 Statistics of bouts against downwind distance. 52
Figure 3.12 Bout count based distance prediction. 56
Figure 3.12 Bout count based distance prediction (cont.). 57
Figure 3.13 PCA of trial mean bout statistics on centre line of the plume. 61
Figure 3.13 PCA of trial mean bout statistics on centre line of the plume (cont.). 62
Figure 3.14 Statistics of bouts against crosswind distance. 68
Figure 3.15 PCA of trial mean bout statistics of five crosswind profiles. 71
Figure 3.15 PCA of trial mean bout statistics of five crosswind profiles (cont.). 72
Figure 3.16 Overview of trial mean bout statistics within $\mu \pm 2\sigma$ crosswind. 77
Figure 3.16 Overview of trial mean bout statistics within $\mu \pm 2\sigma$ crosswind (cont.). 78

Figure 3.17 PCA of trial mean bout statistics in plume within $\mu \pm 2\sigma$ crosswind. 81
Figure 3.17 PCA of trial mean bout statistics in plume within $\mu \pm 2\sigma$ crosswind (cont.). 82
Figure 3.18 Bout statistics of the freestream release configuration plotted against downwind distance divided by wind speed. 86
Figure 3.19 PCA Bout statistics of the free-stream release configuration plotted against downwind distance divided by wind speed. 88
Figure 3.20 Schematic of downwind and crosswind trends in the freestream datasets 91
Figure 3.21 Average trends of bout statistics over plume 93
Figure 4.1 Instantaneous concentration plots 102
Figure 4.2 Agent Schematic Overview 103
Figure 4.3 Agent Strategy Flow Charts 103
Figure 4.4 Initial Position Schematics 105
Figure 4.5 Simulation Pipeline Flow Chart 106
Figure 4.6 Scenario A: DS- Trajectories 109
Figure 4.7 Scenario A: DS+ Trajectories 111
Figure 4.8 Scenario A: Cast Surge Trajectories 113
Figure 4.9 Scenario A: Performance Metric Analysis 115
Figure 4.10 Scenario B: DS- Trajectories 117
Figure 4.11 Scenario B: DS+ Trajectories 120
Figure 4.12 Scenario B: Cast Surge Trajectories 122
Figure 4.13 Scenario B: Performance Metric Analysis 125
Figure A.1 Impact of downwind distance on odour concentration 164
Figure A.2 Impulse response of Butterworth filters 164
Figure A.3 Splitting Signal split into frequency components 165
Figure A.4 Spectral Analysis 167
Figure A.5 Spectral Analysis full downwind extent. 168
Figure A.6 Impulse response of Gaussian, Derivative, EWMA and the combined filters at 15Hz for our selected filter values 169
Figure A.7 Kernel Shapes for Bout Analysis Filter Cascade. 170
Figure A.8 Crosswind Plume Tracking 171
Figure A.9 Effect of filter kernel parameters on bout count curves. 173
Figure A.10 Min-max normalized statistics of bouts against crosswind distance. 175
Figure A.11 Bout Intermittency 179

Figure A.12 Schematic illustrating the sampling duration procedure. The total trial length is divided into equal sub-windows of decreasing duration, and bout statistics are computed for each window independently. This allows the dependence of bout count and bout frequency estimates on sample duration to be characterised. 180
Figure A.13 Centre line: impact of sampling duration on bout count and frequency 182
Figure A.14 Full plume: regression coefficients for sampling duration vs. bout frequency 184
Figure B.1 Scenario A: Navigation Strategy Performance Analysis 194
Figure B.2 Scenario A: DS+ Parameter Search. 196
Figure B.3 Scenario B: Navigation Strategy Performance Analysis 198
Figure B.4 Scenario B: DS+ Parameter Search. 199
Figure B.5 Validation Parameter Search for DS- 202
Figure B.6 Validation Parameter Search for DS+ 204
Figure B.7 Validation Parameter Search for CS 205
Figure C.1 Modelled diffusion of acetone (dashed) with measured average PLIF normalized concentration. 211

LIST OF TABLES

Table 3.1 Calculated Amplitude Threshold. 50
Table 3.2 Sigmoid Function Values 59
Table A.1 Downwind Explained Variance 185
Table A.2 Downwind Feature Covariance Table 185
Table A.3 Downwind Feature Loading Table 186
Table A.4 Crosswind Explained Variance 186
Table A.5 Crosswind Feature Covariance Table 187
Table A.6 Crosswind Feature Loading Table 187
Table A.7 Full Plume Explained Variance 188
Table A.8 Full Plume Feature Covariance Table 188
Table A.9 Full Plume Feature Loading Table 189
Table A.10 Wind Speed Explained Variance 189
Table A.11 Wind speed Feature Covariance Table 189
Table A.12 Wind speed Feature Loading Table 190
Table A.13 Sample Duration Regression Table 191
Table A.14 Sample Duration Regression Table Continued 192
Table B.1 Scenario A: Best performing agent parameters 197
Table B.2 Scenario B: Best performing agent parameters 200
Table C.1 Acetone Coefficients for Antoine Equation taken from https://www.chesolver.com/antoine. 208
Table C.2 Mass flux Q in m/s m^3/s and the mass emission rate $\dot{M}$ in ml/m of acetone at the source for three wind speeds. 209

ABBREVIATIONS

AL	Antennal Lobe; first olfactory processing region in the insect brain
CS	Cast-and-Surge; flying insect navigation strategy combining cross-wind casting with upwind surging on odour contact
DS−	Non-Direction-Sensing; walking insect navigation strategy using odour-gated anemotaxis without stereo sensor comparison
DS+	Direction-Sensing; walking insect navigation strategy using stereo sensor correlation to infer odour direction
EAG	Electroantennography; technique measuring the summed electrical potential across an insect antenna in response to odour stimuli
EWMA	Exponentially Weighted Moving Average; recursive filter used in bout analysis to remove slow sensor drift
FTP	Flow Transition Point; boundary in the test section separating the near-bed viscous sublayer from the freestream flow
GPCR	G-protein-Coupled Receptor; class of odorant receptors that transduce chemical signals via intracellular G-proteins
HRC	Hassenstein–Reichardt Correlator; elementary motion detector model underlying insect optomotor responses
IBI	Inter-Bout Interval; time elapsed between the end of one odour bout and the start of the next
MOX	Metal Oxide sensor; gas sensor that detects volatile compounds via changes in semiconductor resistance
OB	Olfactory Bulb; first olfactory processing region in the vertebrate brain
OR	Odorant Receptor; receptor protein expressed on olfactory neurons that binds specific odorant molecules
ORN	Olfactory Receptor Neuron; sensory neuron bearing odorant receptors that transmits signals to the AL or OB
OSN	Olfactory Sensory Neuron; used interchangeably with ORN, particularly in the vertebrate literature
PCA	Principal Component Analysis; dimensionality reduction technique that identifies axes of maximum variance

PC1 First Principal Component; axis of greatest variance identified by PCA

PC2 Second Principal Component; axis of second greatest variance identified by PCA

PDF Probability Density Function; statistical function describing the relative likelihood of a continuous random variable taking a given value

PID Photoionization Detector; gas sensor that ionises volatile compounds with UV light to measure concentration

PIV Particle Image Velocimetry; optical technique for measuring instantaneous velocity fields in fluid flows

PLIF Planar Laser-Induced Fluorescence; optical technique for imaging scalar concentration fields in a two-dimensional plane of a fluid

PN Projection Neuron; second-order olfactory neuron relaying processed signals from the AL or OB to higher brain regions

RMS Root Mean Square; measure of the magnitude of a varying quantity

RMSE Root Mean Square Error; measure of the average deviation between predicted and observed values

ROI Region of Interest; defined spatial sub-region selected for analysis

SIF Spatial Integration Factor; ratio of sensor separation distance to the characteristic turbulence length scale of the local plume

1

INTRODUCTION

1.1 AIMS OF THE THESIS

The primary aim of this thesis is to uncover the odour cues used by organisms to navigate towards or away from turbulent odour sources, and to evaluate biologically inspired strategies for exploiting those cues. In turbulent flows, instantaneous odour concentration is highly variable, yet animals reliably locate sources over meaningful distances; understanding how transient concentration statistics encode proximity is therefore central to developing robust plume-based navigation.

This thesis comprises a literature review and two manuscripts. Both manuscripts use recordings of turbulent plumes (Connor, McHugh and J. P. Crimaldi, 2018) captured optically using the planar laser-induced fluorescence (PLIF) technique. The published wind tunnel recordings (Connor, McHugh and J. P. Crimaldi, 2018) span three release configurations: freestream plumes at 10 cm/s and 20 cm/s, and a near-bed plume at 10 cm/s. A fourth configuration — a freestream plume at 5 cm/s — was not included in the original publication but was kindly provided to us by the original authors; this unpublished dataset is used alongside the three published configurations throughout both manuscripts. Together, the four configurations explore the impact of both wind speed and boundary layer proximity on the resultant turbulent plume structure. We use these plumes to quantify the relationship between the statistics of odour concentration fluctuations and odour source distance, and to test navigation strategies against realistic plume data.

Schmuker, Bahr and Huerta (2016) introduced the concept of *bouts* — the portion of an odour signal in which a sharp rise in concentration occurs — and showed that bout count increases with proximity to an odour source in turbulent plumes. However, the bout paradigm was previously applied only to gas recordings from metal oxide (MOX) sensors; whether the same statistical relationships hold in optically recorded plume data, and whether statistics beyond bout count carry additional information, remained open questions. In our first manuscript, we extend the bout pipeline to PLIF-recorded plumes and characterise the full suite of bout statistics — count, duration, amplitude, and inter-bout interval (IBI) — as a function of downwind distance and crosswind position. Whereas turbulent plume recordings are typically analysed in terms of mean concentration and intermittency (Celani, Villermaux and Vergassola, 2014), we aim to establish whether bout statistics can provide a richer and more robust basis for source proximity estimation and navigation.

In order to accomplish this goal we must achieve the following objectives:

1. Establish adequate parameters for the filter pipeline and an adaptive amplitude threshold, adapting filters originally selected for noise removal in MOX sensor recordings to the PLIF signal.

2. Develop a method to locate the average plume boundaries and centre line, enabling bout statistical trends to be extracted as functions of both downwind and crosswind position.

3. Determine whether the bout count relationships established by Schmuker, Bahr and Huerta (2016) for MOX sensors also hold in PLIF recordings.

4. Characterise the spatial structure of bout count, duration, amplitude, and IBI along the plume centre line and across the crosswind plume profile.

5. Extract the combined relationship between all four bout statistics and odour source distance across the full plume extent.

6. Demonstrate how release height and wind speed alter the plume structure and the resulting bout statistical trends.

7. Establish whether bout statistics can be used to estimate odour source distance.

In the second manuscript, we apply biologically inspired in-silico navigation strategies to the same PLIF datasets. Two strategies are modelled on the behaviour of walking *Drosophila* (Kadakia et al., 2022) — one using stereo odour sensing to infer direction (DS+), one relying on odour-gated anemotaxis alone (DS−) — and a third models the cast-and-surge strategy of flying insects (K. L. Baker et al., 2018; Budick and Dickinson, 2006). Our aim is to identify which strategy most robustly locates the odour source across different turbulent plume configurations, without prior knowledge of the source location.

We set out the following objectives to achieve this goal:

1. Demonstrate the application of simple in-silico biologically inspired navigation strategies in realistic PLIF plume data.

2. Determine whether stereo direction sensing confers a meaningful advantage over odour-gated anemotaxis alone.

3. Contrast the performance of walking *Drosophila*-inspired strategies with a flying insect cast-and-surge strategy.

4. Establish how odour release configuration affects the relative performance of the three navigation strategies.

1.2 CONTRIBUTION TO KNOWLEDGE

- The bout analysis pipeline of Schmuker, Bahr and Huerta (2016), originally developed for MOX sensor recordings, is adapted and validated for optically captured PLIF plume data, including re-optimisation of cascade filter parameters for this new data modality.
- Spatial maps of all four bout statistics (count, duration, amplitude, and IBI) are produced for multiple wind tunnel release configurations, including wind-speed-compensated maps for the freestream cases.
- The relationship between bout count and odour source proximity is characterised both along the plume centre line and across the crosswind profile, revealing a non-linear sigmoidal decline with downwind distance.
- The combined relationship between bout count, duration, amplitude, and IBI and odour source distance is quantified for the full plume extent.
- Principal component analysis is used to demonstrate that bout statistics together encode odour source proximity.
- Three biologically inspired in-silico navigation strategies are applied to and evaluated in realistic PLIF-recorded turbulent plume data, providing a direct comparison of strategy performance across multiple release configurations.
- The relative performance of direction-sensing, non-direction-sensing, and cast-and-surge strategies is characterised, identifying the dominant behavioural factor — casting versus random walking in the absence of odour — that determines success rate.

1.3 DISSEMINATION FROM THE THESIS

1. Psarrou, M., Sutton, S., True, A., Crimaldi, J., Schmuker, M. 'Decoding odour source location in realistic plumes from spatiotemporal concentration dynamics'. ECRO XXXII 2022, Berlin, Germany: Poster Presentation
2. Sutton, S., True, A., Crimaldi, J., and Schmuker, M. 'Odor direction sensing with stereo antennae improves simulated odor source localization in realistic turbulent plumes'. ECRO XXXII 2022, Berlin, Germany: Poster Presentation
3. Psarrou, M., Sutton, S., True, A., Crimaldi, J., Schmuker, M. 'aBout plume dynamics: extracting meaningful odor features for active sensing'. SfN 2022, San Diego, USA: Poster Presentation
4. Psarrou, M., Sutton, S., True, A., Crimaldi, J., Schmuker, M. 'aBOUT plume dynamics: extracting meaningful odour features for active sensing'. NeuroNex Investigators Meeting 2022, San Diego, USA: Poster Presentation

5. Sutton, S., True, A., Crimaldi, J., and Schmuker, M. 'Navigation Strategies of Drosophila-like Agents in a Turbulent Odour Plume'. SPECS 2023, Hatfield, UK: Oral Presentation

6. Sutton, S., Psarrou, M., True, A., Crimaldi, J., Schmuker, M. 'Bout Analysis in Turbulent Plumes'. Unpublished

7. Sutton, S., True, A., Crimaldi, J., Schmuker, M. 'In-silico Insect-like Navigation Strategies in Airborne Turbulent Plumes'. Unpublished

2

LITERATURE REVIEW

Recent advancements in minification and temporal resolution improvements of MOX type electronic noses (e-nose) technology (Dennler, Drix, Rastogi et al., 2022; Dennler, Drix, Warner et al., 2024; Drix, Dennler and Schmuker, 2022), capable of millisecond resolution multiple sensor recording, make biologically inspired robotic olfactory navigation more feasible. This multifaceted area of study combines topics from organic chemistry to fluid mechanics and robotics. Before embarking on robotic trials, in-silico simulation of bio-inspired olfactory navigation strategies (Kadakia et al., 2022) allows for exploration into the odour cues available to organisms at a fine spatial separation of sensors and highlights the complexities of navigating a dynamic and complex odour landscape. High spatial resolution recordings of plumes (Connor, McHugh and J. P. Crimaldi, 2018) provide a crucial insight and a backbone for further analysis of the spatial and temporal statistical properties of odour plumes.

The content of the main body of the thesis determined the scope of this literature review. We focus on airborne odour plumes and the statistics of the odour fluctuations. We explore how odour plumes are recorded and statistically analysed, how flying and walking insects navigate odour plumes and computer models (in-silico) of bio-inspired navigating agents. Future robotic experiments are anticipated to be conducted under controlled laboratory conditions in a wind tunnel, focusing on the statistics of odour concentration fluctuations exploited by navigating organisms rather than on odour discrimination.

2.1 ODOUR LANDSCAPES

Chemosensation is one of the oldest senses to have evolved (Wyatt, 2014) and provides information critical to the survival of organisms, from bacteria to animals alike. Bacteria and Archaea follow chemical gradients to a source of nutrients (Szurmant and Ordal, 2004) or more favourable growth conditions (Quax, Albers and Pfeiffer, 2018). Animals have evolved to successfully and reliably navigate great distances to locate food sources (Crenshaw, 1996; Finelli et al., 2000; McLeese, 1973; Tamburri et al., 1996; Thar and Fenchel, 2001; Zjacic and Scholz, 2022), mates (Atema and Engstrom, 1971; Gleeson, Adams and A. B. Smith, 1987; N. Vickers, 2000; Yen and Strickler, 1996) or to avoid predation (De Meester and Cousyn, 1997; Mathis and R. F. Smith, 1993; Tomba, Keller and P. A. Moore, 2001). Odour provides critical navigation cues to terrestrial animals when carried in airborne plumes (Gire, Kapoor et al., 2016; N. Vickers, 2000) or as surface trails (Khan, Sarangi and Bhalla, 2012; Means, Alexander and O'Neal, 1992; Porter, Craven et al., 2007; Thesen, Steen and Døving, 1993;

Wallace, Gorny and Whishaw, 2002), and aquatic animals in water as odour flumes (M. A. Koehl et al., 2001; M. J. Weissburg, 1997; M. Weissburg, 2000; Zimmer and Butman, 2000; Zimmer-Faust et al., 1995).

The concept of the 'odour-landscape' was introduced by Atema (1996) and Nevitt, Veit and Kareiva (1995). It describes the dynamic three-dimensional distribution of odorant concentrations spread by turbulent dispersion and molecular diffusion (explored here further in section 2.4), that can be visualized as evolving peaks and valleys representing a characteristic of a particular odorant. These characteristics include: the odour concentration, with the highest peak being the odour source; fluctuations in the concentration (odour-peak landscape), with peaks getting steeper and taller near the source; and additional features such as odour composition. With prior knowledge of the features of an odour landscape, an organism can theoretically enter the landscape and navigate to or from an odour source.

The odour landscape as perceived by organisms that are large relative to the Kolmogorov length scale (i.e. the smallest size of eddies, see section 2.4) is highly complex relative to that experienced by microscopic organisms (J. P. Crimaldi, Wiley and Koseff, 2002; P. A. Moore, M. J. Weissburg et al., 1994; Webster and M. J. Weissburg, 2001; Zimmer and Butman, 2000). The odour field fluctuates unpredictably in space and time at these scales — not in the deterministic sense of chaos theory, but in the sense that instantaneous concentration cannot be predicted from position alone (Kikas et al., 2001; P. Moore and Atema, 1988; P. A. Moore and Grills, 1999; P. A. Moore, M. J. Weissburg et al., 1994). Even the smallest flying or walking insects are orders of magnitude larger than the Kolmogorov scale (typically on the order of 1 mm), so all such animals effectively sample odour at a macroscopic spatial scale and must contend with turbulent flows (J. P. Crimaldi, M. A. Koehl and Koseff, 2002; J. P. Crimaldi and Koseff, 2001; Murlis, Elkinton and Carde, 1992). The turbulent nature of airflow disturbs any gradients that might form through diffusion and structures the plume in isolated patches of varying concentrations, creating an odour signal that is dynamic in both space and time (Celani, Villermaux and Vergassola, 2014; J. P. Crimaldi and Browning, 2004; Murlis, Elkinton and Carde, 1992; Murlis and Jones, 1981; Mylne and Mason, 1991; Shraiman and Siggia, 2000). Importantly, individual odour filaments may be transported relatively undiluted for many metres before being torn apart and mixed with clean air by small-scale turbulence (Murlis and Jones, 1981).

Spatial scale impacts how an organism perceives the odour landscape. The spacing between their olfactory sensors impacts the sensory information they receive. To this end, M. Weissburg (2000) defined a spatial integration factor (SIF), which quantifies the ratio of the separation between an animal's olfactory sensors to the characteristic turbulence length scale of the local plume. A larger SIF indicates that the sensors are widely spaced relative to the turbulent microstructure, enabling simultaneous sampling of more distinct concentration regions and potentially richer spatial information. We describe the limits that impact turbulent flow further in section 2.4. Movement also impacts odour sensation. In section 2.2 we further explore some of the mechanisms of active sensing.

2.2 ACTIVE SENSING OF ODOURS

Active sensing is a crucial mechanism by which movement influences how an animal perceives odour plumes. This process involves the deliberate or adaptive movement of animals to enhance their ability to detect and interpret chemical signals in their environment (J. Crimaldi et al., 2022; Huston et al., 2015; Wachowiak, 2011). Animals employ various active sensing strategies to optimize their perception of odours. Sniffing behaviours and head movements help animals adjust their sensory input and improve their ability to localize and identify odours, sampling a broader area or refining the detection of specific chemical cues.

Sniffing plays a crucial role in how organisms perceive and interpret their olfactory environment. It significantly influences an organism's perception of the odour landscape (Wachowiak, 2011). In mice, for example, sniffing is a key mechanism for exploring and identifying odours. Research highlights the importance of sniffing patterns in their sensory processing, with mice synchronizing rapid three-dimensional head movements with fast sniffing at a millisecond timescale (Findley et al., 2021). This rapid sniffing acts as an adaptive filter for detecting changes in the odour landscape: high-frequency sniffing attenuates the neural signals encoding odorant identity in olfactory receptor neurons, reducing sensitivity to sustained stimuli, while lower sniffing frequencies cause minimal such attenuation (Verhagen, Wesson et al., 2007). Similarly, rats use sniffing to gather olfactory information (Kepecs, Uchida and Mainen, 2007; Wachowiak, 2011), and their sniffing behaviour has been extensively studied to understand how they navigate their environment. Sniffing behaviour is essential for odour identification, imposing a temporal structure on olfactory receptor neuron (ORN) input that shapes the responses of postsynaptic neurons and may optimize the central processing of odour information (Kepecs, Uchida and Mainen, 2006, 2007). In marine environments, lobsters employ an adjacent-sniffing strategy by flicking their antennae or antennules to allow water to penetrate their chemosensory hair arrays. This helps them detect and localize chemical cues in their surroundings (J. P. Crimaldi, M. A. Koehl and Koseff, 2002; M. A. Koehl et al., 2001; M. Koehl, 2006; Schmitt and Ache, 1979).

Locusts move their antennae towards higher odour concentrations and actively impose intermittency — the fraction of time during which detectable odour is present — in sensed odour through antennal movements (Huston et al., 2015) Flies employ wing flapping to enhance olfactory stimuli by drawing odorants to their antennae (C. Li, Dong and K. Zhao, 2018; J. Li and Shew, 2020). Bumblebees exhibit a stereotypical motion of their antennae when smelling odours, regardless of the odours' diffusivity (Claverie, Buvat and Casas, 2023; Mertes, Carcaud and Sandoz, 2021). The antennal movement, however, is influenced by the odour characteristics (Cholé et al., 2022; Lei et al., 2022). These movements and orientations may also be related to strategies for obtaining additional information about the odour source (Gascue et al., 2022).

Rearing or alternation behaviour in foraging mammals is an important adaptive strategy that enables them to effectively sample both airborne and ground-based odour sources. It entails the animal rearing on its hind legs or raising its head, followed by a pause to sniff the air. Different animals sniff at different heights, which alters details of the plumes but does not affect the general conclusions (Rigolli, Reddy et al., 2022). Dogs modify their speed and head position according to their search location distance. When close to a trail, dogs search with their head up and run quickly, but when their search takes them farther from the odour source, they are more likely to search with their nose to the ground, moving more slowly (Jinn, Connor and Jacobs, 2020).

2.3 ANIMAL OLFACTORY SYSTEMS

Here we address how odour information is processed by animals and what differences exist in the olfactory systems of insects and vertebrates. Where studies involve rodents specifically (rats or mice), we use the more specific term; where findings apply across mammals or the broader vertebrate class, we use the broader term.

Animals with bilaterally symmetric body plans (Bilateria) generally have pairs of olfactory organs. Mammals have a pair of nostrils (nares) connected to a nasal cavity. A mucosal layer covers the olfactory epithelium, upon which sit the olfactory sensory neurons (OSNs), also termed olfactory receptor neurons (ORNs) (Shorey, 1976). Insects have ORNs housed in the antennae and maxillary palps. The sensing structures of insects and vertebrates differ but share common features (fig. 2.1).

For both insects and vertebrates, odorants that are dissolved in the mucus or sensory lymph reach the OSNs and bind to odorant receptors (ORs). This binding triggers a transduction pathway that controls the opening of plasma membrane ion channels and subsequent voltage changes in the OSN (Reddy, Murthy and Vergassola, 2022).

ORs comprise a family with dozens to over a thousand members (Buck and Axel, 1991; Kurian et al., 2021; Su, Menuz and Carlson, 2009; Vosshall et al., 1999). The biology of ORs vary widely and includes both ligand-gated ion channels and G-protein coupled receptors (GPCRs — receptors that transduce binding events into intracellular signals via G-proteins rather than by directly gating an ion channel). ORs also exhibit many complex properties such as agonism (ligand binding that activates the receptor) and antagonism (ligand binding that inhibits it) for different ligands, as well as adaptation — the progressive reduction in response magnitude with sustained stimulation (Inagaki et al., 2020; Pfister et al., 2020; Reddy, Zak et al., 2018; Reisert and H. Zhao, 2011; Singh et al., 2019; Xu et al., 2020; Zak et al., 2020). Odorant identity is coded by a combinatorial activation of multiple receptors (Malnic et al., 1999; Su, Menuz and Carlson, 2009), with the timing or latency of activation potentially playing a privileged role (C. D. Wilson et al., 2017).

The OSN responses in different insects to fluctuating stimuli suggest they can respond rapidly (Lemon and Getz, 1997; Mafra-Neto and Cardé, 1994; Riffell, Shlizerman et al., 2014;

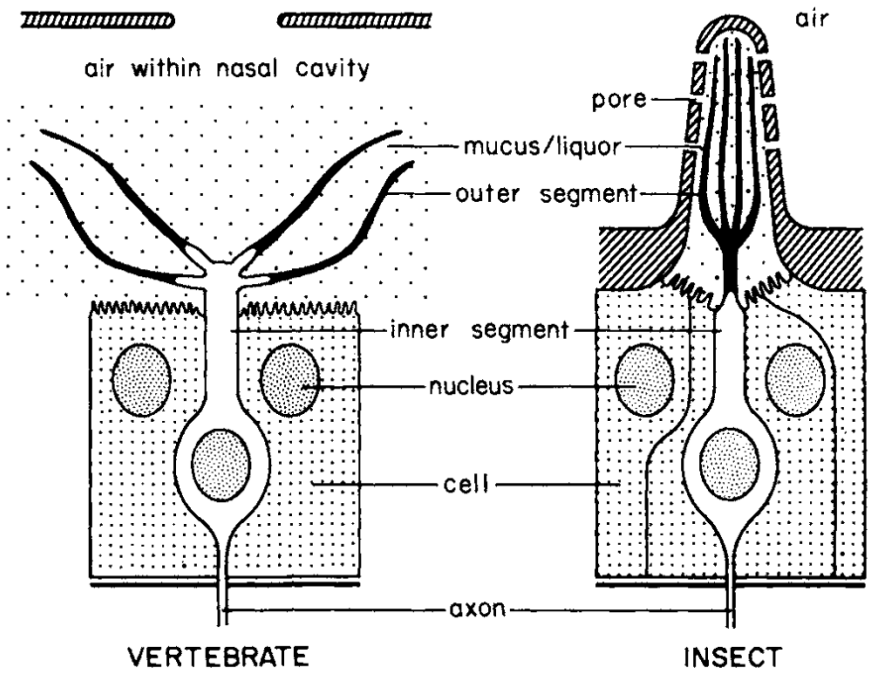

Figure 2.1: Schematic representations of vertebrate and insect olfactory receptors, with possibly analogous structures drawn similarly. From Shorey (1976).

Szyszka et al., 2014), a single neuron transmits several bits ($\approx$ 4bits/s) of information per second (Geffen et al., 2009). Drosophila ORN responses can peak in 30ms and terminate in 200ms (Nagel and R. I. Wilson, 2011; Schuckel, Torkkeli and French, 2009). Careful estimation of impulse response filters of OSNs in Drosophila points toward integration times of $\approx$ 100ms (Martelli, Carlson and Emonet, 2013). Speed may be important for insects because they experience rapidly fluctuating, wind-borne odour filaments, and they can potentially use the information contained in these fluctuations to locate an odour source (Murlis, Elkinton and Carde, 1992; Silbering and Benton, 2010). Experiments in vertebrates show similar or slightly slower ORN response to odorant encounters. For frog ORN, the response to a brief pulse (25ms) of odorants, cineole or acetophenone, requires 400ms to peak and 1,000ms to terminate (Bhandawat, Reisert and Yau, 2005). Calcium imaging experiments in mice reveals diverse ORN temporal response patterns with respiration modulation and glomerular activity occurring $200 - 500ms$ after the response onset (Spors, Wachowiak et al., 2006; Wachowiak and Cohen, 2001). Wesson et al. (2008) demonstrates the ability of rats to discriminate between odours and respond to novel ones in as little as 140ms, suggesting receptor input arrives at the Olfactory Bulb (OB) $100 - 150ms$ after inhalation begins, with central processing and response initiating within $50 - 100ms$.

Vertebrate receptors can be narrowly tuned, broadly tuned, or anything in between (Saito et al., 2009). Vertebrate ORNs are noisy and spontaneously active, partly owing to transduction noise in ORs — stochastic spontaneous activations of the receptor signalling cascade (Reisert, 2010) — and preferentially signal the onset of odour responses, owing to adaptation in

transduction and spike generation (the desensitisation of both the receptor cascade and action potential firing under sustained stimulation) (Reisert, 2000). They resemble Drosophila ORNs in that both have broadly overlapping odour selectivity, with similar receptor types responding to similar sets of odorants (Haddad et al., 2010).

Vertebrate ORNs are reportedly sensitive to air speed (Mozell, Kent and Murphy, 1991; Scott, 2006; E. C. Sobel and Tank, 1993). Terrestrial vertebrates actively control air flow through their noses and thereby use air speed to modulate olfactory transduction (Johnson, Mainland and N. Sobel, 2003; Schoenfeld and Cleland, 2005). Drosophila have comparatively little control over air flow across their olfactory organs, so it may be advantageous that Drosophila ORNs are insensitive to air speed (Zhou and R. I. Wilson, 2012).

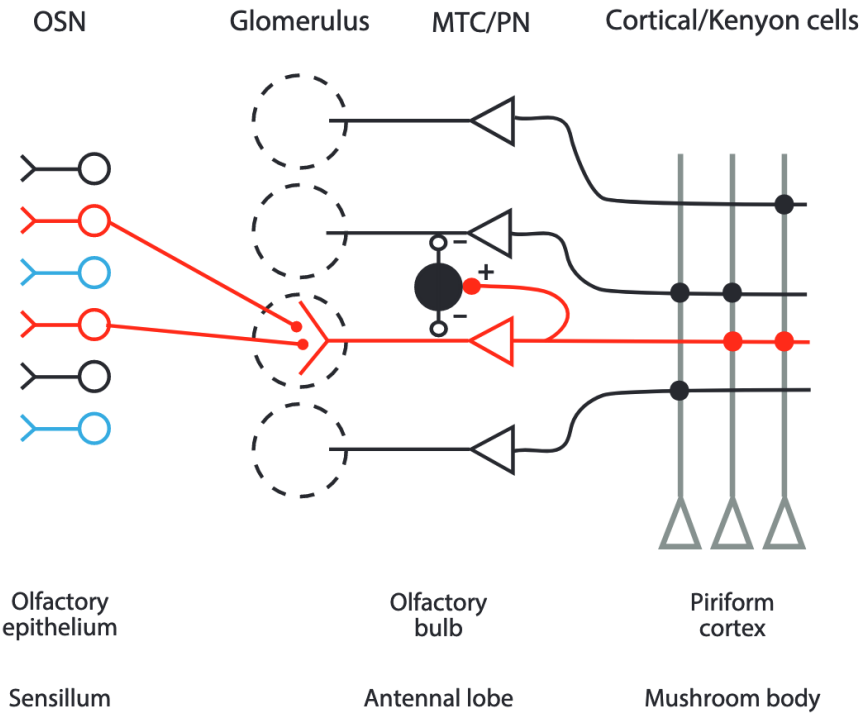

Figure 2.2: Common neural circuit motif in rodents and insects. OSNs expressing a particular receptor type out of a large repertoire (indicated by like colours) converge selectively in individual glomeruli in the OB, making connections with MTCs or PNs. Local circuit elements in the OB or AL include inhibitory neurons (shown as a black circle) that receive excitation from MTCs/PNs and reciprocally inhibit them. MTCs/PNs project to multiple brain regions, including the piriform cortex/mushroom body, where they are thought to make dispersed, random, and sparse connections (shown as intersecting wires, with connections denoted by small circles). From Reddy, Murthy and Vergassola (2022).

The circuit motif of insects and vertebrates more broadly also shows analogous features (fig. 2.2). In most animals, individual OSNs express a single OR, and all OSNs expressing a particular OR connect to spatially local units called glomeruli. This convergence principle is highly conserved and likely serves to reduce noise by signal averaging as well as to keep channels of information in the early stages separate (Reddy, Murthy and Vergassola, 2022). The antennal lobe is the first brain region of the fly olfactory system. It is therefore analogous

to the vertebrate OB, and like the bulb, it is organized into discrete neuropil compartments, also called glomeruli (R. I. Wilson, 2013).

Individual glomeruli serve as relatively isolated units of sampling by second-order neurons. In structures that house glomeruli and downstream neural circuits (OB in mammals and AL in insects), there is a rich network of neurons that are thought to process information with a goal of normalization, redundancy reduction, and decorrelation (R. I. Wilson, 2013; Zhang and Firestein, 2002). Information from the first stage (OB or AL) is passed on to multiple higher brain regions (Brann and Datta, 2020). Projections from the insect AL target the mushroom body, a key centre for multimodal information integration and memory formation (Modi, Shuai and Turner, 2020), and the lateral horn, which is associated with innate behaviours (Das Chakraborty and Sachse, 2021). In mammals, the output of the OB reaches multiple areas including olfactory cortex, amygdala, and ventral striatum (Brann and Datta, 2020).

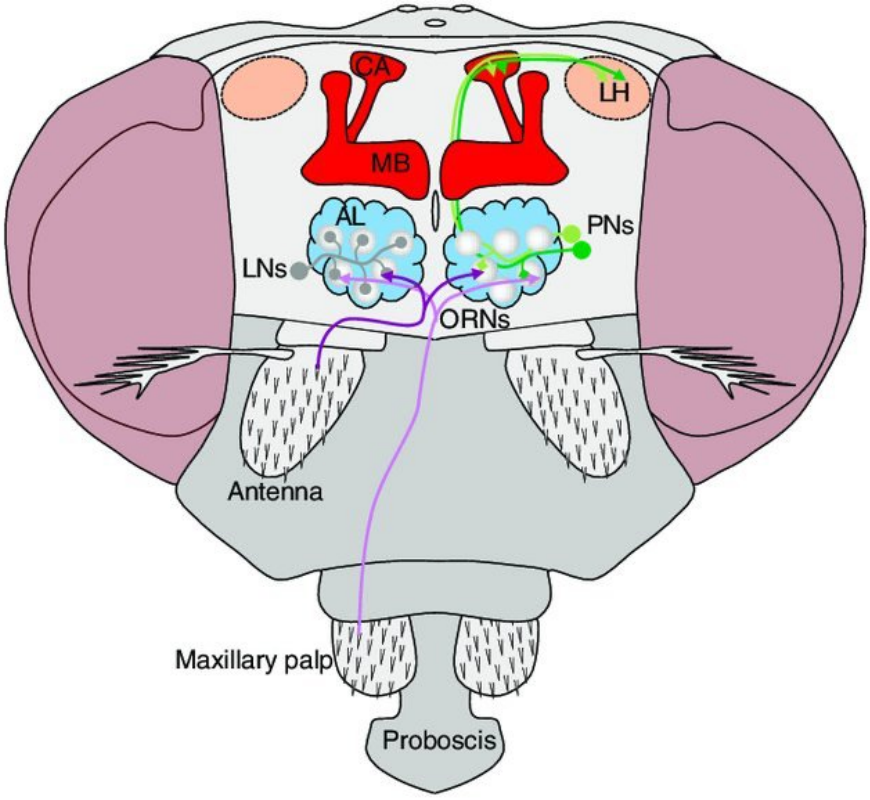

Figure 2.3: The Drosophila olfactory pathway. Olfactory receptor neurons (ORNs) in sensillae on the 3rd antennal segments and the maxillary palps project their axons bilaterally into individual glomeruli in the antennal lobe (AL). In these glomeruli, ORN input is integrated and processed by the action of mostly multiglomerular excitatory and inhibitory local interneurons (LNs). Processed odour information is then relayed to the calyx (CA) of the mushroom body (MB) and the lateral horn (LH) by uniglomerular projection neurons (PNs). From Perisse et al. (2013).

In *Drosophila*, these olfactory structures — the antennae and maxillary palps — are covered by finger-like protrusions called sensilla (fig. 2.3). These sensilla contain the dendrites of

ORNs, and each sensillum typically houses exactly two ORNs (although some types of sensilla house three or four ORNs) (R. I. Wilson, 2013).

Drosophila ORNs can be segregated into discrete types on the basis of their odour responses (De Bruyne, Clyne and Carlson, 1999; De Bruyne, Foster and Carlson, 2001; Van Der Goes Van Naters and Carlson, 2007; Yao, Ignell and Carlson, 2005). These types turn out to map rather neatly onto patterns of odorant receptor expression (Benton et al., 2009; Hallem, Ho and Carlson, 2004). In total, there are ≈ 50 ORN types, corresponding roughly to the $50-60$ odorant receptors expressed in the adult antennae and maxillary palps (Benton et al., 2009; Couto, Alenius and Dickson, 2005; De Bruyne, Clyne and Carlson, 1999; De Bruyne, Foster and Carlson, 2001; Elmore et al., 2003; Fishilevich et al., 2005; Van Der Goes Van Naters and Carlson, 2007; Yao, Ignell and Carlson, 2005).

For neural coding, temporal information carried by neuron firing spikes in the invertebrate olfactory system is critical for encoding the odorant (Laurent, 2002; Perez-Orive et al., 2002; Stopfer et al., 1997). Research in invertebrates indicates that stimulus duration for puffs of odour perceived from odour plumes is a key temporal parameter that needs to be decoded by higher brain centres (Cardé and Willis, 2008; Christensen and Hildebrand, 1997; Heinbockel, Christensen and Hildebrand, 1999; Park et al., 2014). Stimulus duration is processed in the antennal lobe in invertebrates (Christensen and Hildebrand, 1997; Heinbockel, Christensen and Hildebrand, 1999). In moths information on odour duration is encoded by macroglomerular complex (MGC) antennal lobe projection neurons; the MGC is a set of enlarged glomeruli specialised for processing the species-specific sex pheromone blend (Christensen and Hildebrand, 1997).

Terrestrial vertebrates draw air into their noses before it encounters ORNs, a process that likely disperses odour filaments and smooths fluctuations in concentration (Schoenfeld and Cleland, 2005). Odour molecules pass through a rather complex environment (or filter) of mucosae, which contain various odour-binding proteins and enzymes that modify odour molecules (Uchida, Poo and Haddad, 2014). There are also complex interactions introduced by the structure of the epithelium that impact the sorption of odorants (Schoenfeld and Cleland, 2005, 2006; Scott et al., 2014).

The first processing stage in the olfactory system and a crucial hub, the olfactory bulb (OB) (fig. 2.4) plays a key role in the neural representation of odours, encoding odour identity, intensity and timing (A. Li, Rao et al., 2020). Olfactory information encoded by OSNs is processed by the OB before transmission to upstream brain areas (Cleland, 2014; Gire, Restrepo et al., 2013). Odour stimulation evokes odour and cell-specific temporal patterns of activity in the OB. These include modulation of firing rates across various timescales and synchronous oscillations at different frequencies (Bathellier, Gschwend and Carleton, 2010; R. I. Wilson and Mainen, 2006). Odour molecules bind to ORs with different affinities, resulting in various latencies and temporal dynamics of OSN firing and glomerular activations (Spors and Grinvald, 2002; Spors, Wachowiak et al., 2006). OB circuits that are

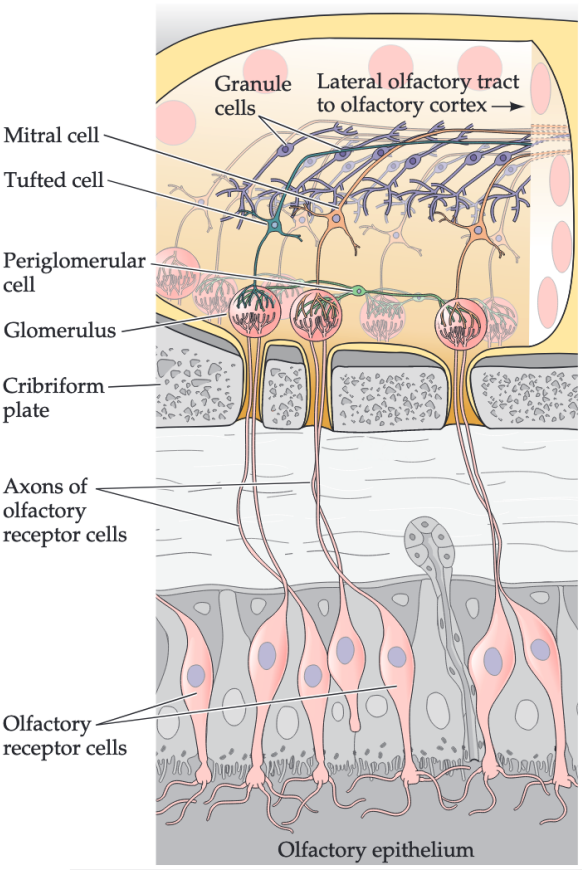

Figure 2.4: Diagram of the circuit organization of the olfactory bulb, shown as a cutaway view from its medial surface. Olfactory receptor cell axons synapse with mitral cell apical dendritic tufts and periglomerular cell processes within glomeruli. From Purves (2017).

engaged with increased OSN input also add more complex temporal dynamics (Uchida, Poo and Haddad, 2014).

There are $\approx 1,000$ types of glomeruli in the rodent OB, each receiving input from thousands of olfactory receptor neurons (ORNs) expressing only 1 of the > 1000 gene-specified olfactory receptors (Mombaerts, 2006; Mori, Nagao and Yoshihara, 1999; Zapiec and Mombaerts, 2015). Each glomerulus receives input from one type of ORN and the output of each glomerulus is likely to reflect its inputs. However, lateral inhibition between glomeruli might decorrelate the glomerular outputs. With this in mind, the tuning of the glomeruli to a set of odours is remarkably broad (Verhagen, K. L. Baker et al., 2023).

Odour information is encoded in the firing of the post-synaptic 2^{nd} order mitral and tufted cells (M/Ts) after complex processing by the neural circuits within the OB (A. Li, Rao et al., 2020). The main output neurons, the M/Ts, receive direct excitatory input from the OSNs at the glomeruli (Vaaga and Westbrook, 2016). There are large numbers of GABAergic interneurons (neurons that release γ-aminobutyric acid, the principal inhibitory neurotransmitter, thereby suppressing target cell activity) in almost all the layers, as well as dopaminergic interneurons (neurons releasing dopamine, a neuromodulator that regulates signal gain and contrast) in the glomerular layer, and both are involved in the neural circuits that mediate transmission from the OSNs to the M/Ts and shape the firing properties of M/Ts in response to odours (Burton, 2017; Vaaga, Yorgason et al., 2017).

Odour information encoded in the OB is subsequently transformed and read out (decoded) by neurons in the piriform cortex (PC). The PC is the most important cortical region for olfaction and projects directly back to the OB. It plays a major role in odour preference learning, odour pattern separation, olfactory learning, odour fear memory and the processing of odour objects (Meissner-Bernard et al., 2019; Schaffer et al., 2018; D. A. Wilson and Sullivan, 2011). Odour-evoked activation has been observed directly in pyramidal axons projecting from PC to the OB (Boyd et al., 2015; Otazu et al., 2015). Neurons within the PC that respond to an odour are broadly distributed in space without apparent spatial organization (Illig and Haberly, 2003; Miura, Mainen and Uchida, 2012; Poo and Isaacson, 2009; Rennaker et al., 2007; Stettler and Axel, 2009). A single odour activates about $10 - 30\%$ of its neurons (Miura, Mainen and Uchida, 2012; Poo and Isaacson, 2009; Stettler and Axel, 2009). The breadth of odour tuning varies among neurons; although most neurons are select to a few odours, some neurons are broadly activated by many (Miura, Mainen and Uchida, 2012; Poo and Isaacson, 2009; Zhan and Luo, 2010). A limiting factor of current results is that most of the studies using behaviour have focused on the relatively simple task of odour discrimination (Uchida, Poo and Haddad, 2014).

Recording in awake rats showed that temporal responses of anterior PC neurons are simple, consisting mainly of transient burst spiking that is tightly locked to sniff onset (Miura, Mainen and Uchida, 2012), and the spike counts in this sniff-locked neural activity convey reliable odour information (Gire, Whitesell et al., 2013; Miura, Mainen and Uchida, 2012). In contrast, spike timing conveyed little additional information about odour identity

compared with information provided by total spike counts over the entire sniff cycle (Miura, Mainen and Uchida, 2012). Furthermore, the overall firing rates of ensemble neurons correlated with the trial-by-trial accuracy of perceptual decisions in a psychophysical odour-discrimination task. These results suggested that there is a profound transformation in the way odours are represented in the OB and the anterior PC: In the PC, odour representations are distributed and do not show odour-specific spatial patterns as seen in the vertebrate OB (Friedrich and Korsching, 1997; Meister and Bonhoeffer, 2001; Rubin and Katz, 1999; Uchida, Takahashi et al., 2000). Furthermore, the importance of spike timing–based coding is much reduced in the anterior PC compared with the OB.

OSNs respond to mechanical stimulation suggesting that sniffing can activate the OSNs (Connelly et al., 2015; Wu et al., 2017). Respiration and sniffing control the access of odours to the OSNs and play an important role in olfactory discrimination and perception (Wachowiak, 2011). In the OB, activity of different types of neurons, as well as the neural circuits, are modulated dramatically by sniffing (A. Li, Rao et al., 2020; Verhagen, Wesson et al., 2007). When sniffing frequency exceeds 4 Hz, sniff-locked response patterns shift to sustained response patterns, which may be an important mechanism for selectively suppressing OSN activation by background odours during exploratory high-frequency sniffing (Wachowiak, 2011). Respiration gates the sensory input response of the M/Ts, (Iwata, Kiyonari and Imai, 2017; Short et al., 2016) and sustained odorant sampling at higher frequencies leads to increasing decorrelation of the M/T cell population response pattern over time (Díaz-Quesada et al., 2018).

In mammals, the flow of information is clearly lateralized as both hemispheres do not have any cross-connection until the anterior olfactory nucleus (Bennett, 1968; Brunjes, Illig and Meyer, 2005). This connection enables vertebrates to compare inter-naris odour information (stereo olfaction; (Esquivelzeta Rabell et al., 2017; Rajan, Clement and Bhalla, 2006)), and temporal information from internasal timing differences can be used for directional cues (Arzi and N. Sobel, 2010; Gardiner et al., 2014; Gottfried, 2005; Porter, Anand et al., 2005; Rajan, Clement and Bhalla, 2006).

Detection of the specific phase of the stimulus within the sniff has been found to be an important stimulus timing parameter that mice can use to make behavioural decisions with 10 ms precision (Smear et al., 2011). In the OB of mammals, the firing pattern of M/T cells, such as sniff-locked spikes and theta- ($4-10\,Hz$) and gamma- ($10-100\,Hz$, with $40\,Hz$ of most interest) correlated spikes — rhythmic oscillatory activity that synchronises neural populations and is thought to gate information transfer between brain regions — are considered as an important cue for olfactory encoding (Cury and Uchida, 2010; F. O. David et al., 2009; Gire, Restrepo et al., 2013; Gschwend, Beroud and Carleton, 2012; Narikiyo, Manabe and Mori, 2014; Shusterman et al., 2011). Both input and output neurons in the olfactory bulb encode information that allows for the detection of differences in odour intermittency and intermittency encoding in M/T cells are affected by sniff frequency (Gumaste et al., 2024). Mice can behaviourally discriminate between odour plume samples of high and low

intermittency and active sampling behaviour can predict discrimination success (Gumaste et al., 2024).

Mice are capable of detecting temporal properties that may indicate distance from and composition of an odour source, these include intermittency, odour duration, odour whiff frequency and the temporal correlation of fluctuating odours (Ackels et al., 2021; Dasgupta et al., 2022; Hopfield, 1991; A. Li, Gire et al., 2014; Rebello et al., 2014). We explore these further in section 2.6. Before an odorant can be detected and acted upon by an organism, it has to travel from an odour source. In the next section (section 2.4), we explore the physical laws that dictate how odours move in fluids.

2.4 UNDERSTANDING ODOUR MOTION

In the case of airborne odour plumes, odour molecules are released into the atmosphere from an odour source and are subsequently carried by wind. As an odour is carried away from its source, the plume expands and the plume's mean concentration of odour molecules falls (Murlis, Elkinton and Carde, 1992). The structure of an odour plume and how it evolves is defined by the physical and chemical properties of the odorant and by the physical properties of the carrier fluid (air) and its flow (wind) (J. P. Crimaldi and Browning, 2004; P. Moore and J. Crimaldi, 2004).

Fluid motion occurs in one of two states, laminar and turbulent. Turbulence is the usual state of fluid motion. In laminar flow, fluids follow smooth paths in parallel layers with little or no mixing, eddies or swirls, and occurs where the Reynolds number (eq. (2.1)) is low. The laminar flow regime occurs in fluids with low velocity, low density or high viscosity or some combination of each. The Reynolds number (Re) is a dimensionless quantity that characterizes the magnitude of inertial effects compared to the magnitude of viscous effects of a flow:

$$Re = \frac{uL}{\nu} = \frac{\rho u L}{\mu} = \frac{\text{inertia}}{\text{kinematic viscosity}}, \tag{2.1}$$

where u denotes a typical flow speed, L denotes a characteristic length scale of the flow (body length for external flows/duct diameter for internal flows), ν is the kinematic viscosity of the fluid, ρ is the density of the fluid and μ is the dynamic viscosity of the fluid. The kinematic viscosity ν is the ratio of dynamic viscosity μ to the density of the fluid ρ, therefore $\nu = \mu/\rho$. Its typical values are $1.500 \times 10^{-5} m^2/s$ for air and $1.000 \times 10^{-6} m^2/s$ for water. Dusenbery (1992) states that typically for $Re > 1.000 \times 10^4$ momentum in the flow overpowers viscous damping and turbulent flow develops, for $Re < 2.000 \times 10^3$ the flow is considered laminar and for intermediate values turbulence may or may not develop.

Turbulent flow transports heat, matter, and momentum far better than laminar flow (Tennekes and Lumley, 1972). Turbulent flow has a spatial structure described by White (1974) as having five key characteristics: Fluctuations in pressure and velocity (and temperature

where there is heat transfer) in all three directions, superimposed upon a mean value of each property; Eddies or fluid packets of many sizes that intermingle and fill the shear layer, down to the Kolmogorov length scale; Random variations in the fluid properties that have a particular form; Self sustaining motion, which once triggered can maintain itself through new eddies replacing those lost by viscous dissipation, especially in wall-bounded flows; Mixing, where turbulent eddies move in three dimensions causing rapid diffusion of mass, momentum and energy, entraining fluid from non-turbulent zones, producing a gradient in the time-mean flow. These characteristics enhance transport because turbulent eddies and fluctuations introduce a level of mixing and spreading that molecular diffusion alone cannot achieve in laminar flow.

The Navier-Stokes equations (eq. (2.2)) govern the motion of fluid flow. The incompressible Navier–Stokes equations are generally defined as:

$$\frac{\partial \mathbf{u}}{\partial t} + (\mathbf{u} \cdot \nabla)\,\mathbf{u} = -\frac{\nabla p}{\rho} + \nu \nabla^2 \mathbf{u} + \mathbf{f}, \tag{2.2}$$

where $\mathbf{u}$ is the flow velocity field, p is the pressure, ρ is the (mass) density of the fluid, ν is kinematic viscosity, $\nabla\cdot$ is the divergence, $\mathbf{f}$ represents body accelerations acting on the continuum, for example gravity, inertial accelerations, electrostatic accelerations, and so on.

The continuity equation:

$$\nabla \cdot \mathbf{u} = 0, \tag{2.3}$$

ensures that the fluid is incompressible, meaning that the divergence of the velocity field is zero.

The incompressible Navier–Stokes equations can be broken down to the following:

- $\frac{\partial \mathbf{u}}{\partial t}$: The local rate of change of velocity with time.
- $(\mathbf{u} \cdot \nabla)\,\mathbf{u}$: The convective term, representing the change in velocity due to the movement of the fluid.
- $-\frac{\nabla p}{\rho}$: The pressure gradient term, representing the force exerted by pressure differences.
- $\nu \nabla^2 \mathbf{u}$: The viscous term, representing the effects of viscosity (internal friction) in the fluid.
- $\mathbf{f}$: External forces acting on the fluid.

The incompressible flow assumption holds well with all fluids at low Mach numbers (M). The Mach number is a dimensionless quantity that represents the ratio of flow velocity past a boundary to the local speed of sound. $M = \frac{u}{c}$, where u is local flow velocity with respect to boundaries and c is the speed of sound in a medium such as air that varies with temperature. Typically, animals exist in a subsonic regime $M < 0.8$.

The advection-diffusion equation dictates the transport and dispersion of the odorant within the flow (P. Moore and J. Crimaldi, 2004). Advection is the motion of particles along with the bulk flow, whereas diffusion is the net movement of particles from areas of high concentration to areas of low concentration, and acts to erase spatial gradients. Convection is the collective motion of particles in a fluid and encompasses both diffusion and advection. The advection-diffusion equation is given by:

$$\frac{\partial \phi}{\partial t} + \mathbf{u} \cdot \nabla \phi = \nabla \cdot (D \nabla \phi), \tag{2.4}$$

where ϕ is the scalar quantity (e.g., concentration, temperature), $\mathbf{u}$ is the velocity vector of the fluid, D is the diffusion coefficient, ∇ represents the gradient operator, $\nabla\cdot$ represents divergence and $\nabla\phi$ represents the gradient of the scalar quantity.

In turbulent flow, energy cascades from large eddies (large-scale turbulent structures) down to smaller and smaller eddies until it reaches the Kolmogorov length scale. At this scale, the turbulent kinetic energy is dissipated into heat due to viscosity. The Kolmogorov length scale defines the smallest size of eddies in a turbulent flow, which directly impacts how odour molecules are mixed and dispersed in the atmosphere. It is defined as:

$$\eta = \left(\frac{\nu^3}{\epsilon} \right)^{1/4}, \tag{2.5}$$

where ν is the kinematic viscosity of the fluid and ϵ is the average rate of dissipation of turbulence kinetic energy per unit mass and $\epsilon \propto \frac{\tilde{u}^3}{l}$. The Kolmogorov length scale can be obtained as the scale at which the Reynolds number (Re) is equal to 1.

When animals or sensors detect odours, the fine-scale structure of the plume, influenced by the Kolmogorov length scale, can determine how the odour is perceived—whether it's a constant presence or experienced as intermittent whiffs. As the Kolmogorov length scale is typically very small (on the order of millimetres or less in atmospheric conditions), it highlights the high resolution required for detecting and interpreting odour cues present within plumes in turbulent environments.

Reddy, Murthy and Vergassola (2022) state that the Péclet number ($Pé$) is equivalent to Re for the transport of particles, low $Pé$ flows are dominated by molecular effects, whereas high $Pé$ corresponds to turbulent transport. The Péclet number is a dimensionless number that characterizes the relative importance of advection to diffusion in a fluid flow and is defined as:

$$Pé = \frac{UL}{D} = \frac{\text{advective transport rate}}{\text{diffusive transport rate}}, \tag{2.6}$$

where U is a characteristic velocity of a fluid, L is characteristic length scale and D denotes mass diffusivity or diffusion coefficient of the scalar quantity. For flows where $Pé_L \to 0$ advection is negligible, diffusion dominates, for $Pé_L = 1$ diffusion and advection occur over

equal times, for $Pé_L \gg 1$ diffusion happens in much longer time compared to advection, and for $Pé_L \to \infty$ diffusion is negligible, advection dominates.

The Schmidt number characterizes the relative rates of momentum diffusion (viscous diffusion) and mass diffusion:

$$Sc = \frac{Pé}{Re} = \frac{\nu}{D} = \frac{\text{viscous diffusion rate}}{\text{molecular (mass) diffusion rate}}, \tag{2.7}$$

where ν is the kinematic viscosity and D is the mass diffusivity.

While both numbers involve the mass diffusivity D, they provide different insights. The Schmidt number provides information about the relative importance of diffusion and viscosity, whereas the Péclet number provides information about the relative importance of advection and diffusion.

The Batchelor scale (η_B) defines the size of a fluid droplet that will diffuse in the same amount of time it takes for the energy in an eddy of size η to dissipate (Batchelor, 1959) and is usually defined as:

$$\eta_B = \frac{\eta}{\sqrt{Sc}} = \left(\frac{\nu D^2}{\epsilon}\right)^{1/4}. \tag{2.8}$$

It is most relevant to mixing scalar quantities (i.e. temperature, chemical concentrations, or odour molecules) in a turbulent flow. The Kolmogorov scale defines the smallest eddy size in the velocity field, where viscous dissipation happens. In contrast, the Batchelor scale represents the smallest scale at which fluctuations in scalar fields — such as temperature or chemical concentration — persist before being smoothed out by molecular diffusion. This scale is typically smaller than the Kolmogorov scale when $Sc > 1$ (as is the case for odour molecules in air), because molecular diffusion of the scalar is slower than the viscous dissipation of kinetic energy in the smallest eddies; scalar gradients therefore persist at spatial scales smaller than the Kolmogorov scale. The Batchelor scale is generally smaller than the Kolmogorov scale when the Schmidt number (Sc) is greater than 1. This means that scalar transport takes place at scales smaller than the smallest eddies in a turbulent flow.

At the molecular scale, diffusion acts to smooth out chemical gradients by Brownian motion. Turbulent mixing stirs and elongates features in the odour field, creating chemical filaments with sharp concentration gradients at their edges. This turbulent stirring is distinct from molecular diffusion: it operates through the advective action of eddies rather than Brownian motion, and in most turbulent flows it is the dominant mechanism dispersing odour away from the source. Dispersion combines both advection and diffusion. It encompasses the effects of turbulent intermingling of fluid particles (stirring), molecular diffusion due to Brownian motion (mixing) and at larger scales spreading due to effectors of shear in mean velocity field (shear dispersion).

As fluid approaches boundaries, its velocity decreases. The viscosity of the fluid affects the magnitude and extent of shear stress near these boundaries, creating what is known as

the boundary layer. In this layer, viscous interactions become pronounced, leading to the suppression of turbulent motions and mixing. Within the boundary layer, the mean velocity gradient is highest near the bed, resulting in considerable dispersion of chemicals due to this mean shear. Chemicals in this near-wall region tend to exhibit a streaky, persistent characteristic (P. Moore and J. Crimaldi, 2004). In high Reynolds number flows, where fluid viscosity is lower, the impact of shear stresses is reduced. However, the effects of the boundary layer can still be significant, particularly when analysing flows with large length scales or plumes near boundaries.

To fully grasp the complexities of turbulence on plume structures, measurements of plumes must be taken either in the field or in artificially produced plumes in controlled laboratory wind tunnels. In the next section we summarize the methods of measuring and recording plumes.

2.5 MEASURING AIRBORNE PLUMES

Taking measurements of odour plumes that can be used to further understand the factors that animals naturally account for and that impact the odour landscape, is not as straightforward as one might assume. Towards this goal, many methods have been used to extract odour information from airborne odour plumes. Here we highlight frequently used past studies, techniques and technologies that are used to explore the odour dynamics and complex structure of odour plumes. We briefly summarize their findings and highlight the limitations.

Early outdoor plume experiments used a flame-photometric apparatus (Barynin and M. Wilson, 1972) to record fluctuations in the chemical tracers sulphur dioxide and phosphorus pentafluoride up to $5km$ from their source (Hadjitofi and M. Wilson, 1979). They demonstrated that odour plumes carry information from which the source distances can be estimated from samples recorded between $5 - 50Hz$, but found distance estimates suffered when concentration was highest in stable condition. Fackrell (1978) used a flame ionization detector to sample dilute propane tracer gas. They demonstrated a concentration sensitivity sufficient to detect $1ppm$ of propane in air and extrapolated downwind concentration correlation and variance measurements from seven positions that matched well with theoretical results.

Atmospheric diffusion experiments using ion generators and detectors produce negatively charged ionized air as a tracer and electrically detect ions hundreds of metres from the source at temporal resolutions of a few milliseconds (Jones, 1977, 1983; Jones and Guilliford, 1979; Jones and Hutchinson, 1976). B. W. Boreham, Jones and Griffiths (1985) demonstrated passive ion collectors (Langmuir probes) as an improvement over active ion collectors in outdoor plume measurements. The caveat of this probe is that it measures ion flux as opposed to aspirated ion collectors that measure ion concentration, and therefore its output is proportional to ion concentration and windspeed. This means to determine ion concentration, instantaneous windspeed must also be measured. The field trials demonstrated use of

Langmuir probes measuring unipolar ions up to 15m downwind from point source and saw significant signal amplitude over this range of distances. However, unipolar ions exaggerate plume expansion due to repulsion between ions and image forces (i.e. forces that act on charged particles due to the presence of conducting or grounded surfaces) in the ground deflect the plume as a whole (Murlis and Jones, 1981). The generation of bipolar ions was employed to address the excessive plume expansion observed in unipolar ion experiments. The mutual electrostatic attraction between positive and negative ions resulted in a more controlled and potentially narrower plume (B. W. Boreham and Harvey, 1984a,b). B. W. Boreham (1986) captured vertical and horizontal profiles of mean flux of the bipolar ionized air to the wind direction within a wind tunnel . They expand their experiments to simulate dispersion of pollutant particle around buildings, using model building and trees in a wind tunnel to demonstrate the impact of increased surface roughness. They state that the cross-sectional profiles of mean ion concentration was shown to remain Gaussian, with the vertical concentration profile extending a distance above the model buildings.

Electroantennography (EAG) is used to directly measure a response to a given odour from the antenna of a moth. It has been extensively used to determine the extent of and uncover the odour cues used by moths from pheromone plumes. Miller and Roelofs (1978) used an electroantennogram from antennae of male gypsy moths *Lymantria dispa (L.)* to characterize a plume of disparlure (sex pheromone). They documented EAG tracing of antenna drawn horizontally through a wind tunnel plume and found that the EAG response/voltage drops at plume centre line showed sharp plume boundaries. T. C. Baker and Haynes (1989) recorded oriental fruit moth *Grapholita molesta* EAG responses in stationary and pushed mobile EAG (at various speeds and various source concentrations) in a wind tunnel and at various distances from source (3, 10 and 30m) in the field. They describe source peak-to-trough EAG amplitudes as bursts. In the wind tunnel they observed that the amplitude and frequency of bursts increased with source emission rate. High burst frequencies diminished burst amplitude. A high wind speed did not reduce burst amplitude and resulted in a higher frequency burst, suggesting amplitude attenuation. The slope of EAG onsets increased significantly across the range of airspeeds, with a proportionally greater increase in the onset slope than in the recovery slope. In the field burst amplitudes diminished at 30m downwind but burst frequency did not. Murlis, Willis and Carde (2000) compared ionized air collected with Langmuir probes to electroantennography recording in an open field and forest plumes at distances of up to 20m. With passive collector improvements, they were able to detect a trend in burst lengths and return periods that increased as source-to-receptor distance increased. Burst lengths recorded in the forest were longer than those in open field trials, this was explained by the lower average wind speeds in the forest, but changes in turbulence structure also contributed. They demonstrated significant relationships between signal strength and distance from the source for both field and forest data and showed that there was a close relationship between the time-dependent structure of an EAG response and the fine-scale structure of an odour plume as revealed by an ion tracer. The temporal

and spatial structure of odour plumes shows that several features of odour systematically vary with distance from the odour source.

N. J. Vickers, Christensen et al. (2001) made paired EAG and intracellular recordings in male moths (*Heliothis virescens*) to explore how odour plume dynamics influence how odour information is encoded by the brain. Initially EAG recording were made of a wind-bourne odour plume at nine sequential sampling points. At low wind speeds ($35cm/s$), both the largest EAG bursts and the most frequent fluctuations in EAG activity occurred in the central zone of the plume with virtually no activity at the peripheral sampling sites. As wind speed increased, however, the plume became more dispersed and larger-amplitude EAG bursts occurred more frequently at the peripheral sites. The amplitude of the bursts generally decreased as wind speed increased, and the location of the largest-amplitude responses shifted from the plume centre to its periphery. At the highest wind speed ($120cm/s$), the centre of the plume was characterized by higher-frequency, lower amplitude bursts. To simulate a natural airborne plume at the same sampling locations, odour contacts with a single antennae were made brief and frequent (up to $5s^{-1}$) with a wind speed of $60cm/s$. The antennal responses then showed significant variation in amplitude over the course of stimulation. In-flight recordings were then made and the amplitude distribution of plume contacts were considerably more uniform across the plume. The results indicated that an animal's own in-flight movements influence the detection of odour pulses striking the antenna, and that the initial sensory representations of the odour stimulus in the brain may vary considerably depending on the animal's level of activity. The intracellular recordings revealed that the onset of spike trains in the projection neurons (PNs) closely matched the onset of the EAG, occurring with a nearly constant latency of $44.3 \pm 1.7ms$, irrespective of the EAG amplitude. The mean firing rate and the peak instantaneous firing rate of PN spiking were both proportional to the amplitude of the EAG burst. However, they did not show significant variation with the rate of change of the EAG. Consequently, in the moth's olfactory system, the timing of PN spike patterns was strongly influenced by both the intensity of the stimulus and the dynamics of the odour plume.

A photoionization detector (PID) measures gas concentrations by ionizing molecules with UV light and detecting the resulting ions. It is used to detect volatile organic compounds (VOCs) and other gases. Mylne and Mason (1991) conducted experiments using photoionization detectors (PIDs) with propylene as a tracer gas to study concentration fluctuations within a dispersing plume of pollutants in the atmosphere, over distances ranging from 50 to 1000 meters. The tracer was released at a constant rate for a measurement period between 15 and 30 minutes. These experiments were carried out across three different field sites under near-neutral or slightly convective meteorological conditions. Due to issues such as detector contamination or temperature changes, the PID offset drifted slowly over time. To address this, they subtracted an offset from their time series data. Despite this, their findings were generally consistent with other studies on concentration fluctuations, but they extended the range of measurements considerably. The time series data revealed intermittent periods of

fluctuating non-zero concentrations, interspersed with periods of essentially zero concentration. They observed a rapid initial decrease in *fluctuation intensity* — defined as the ratio of the RMS concentration to the time-mean concentration, $\sigma_c / \langle C \rangle$, a dimensionless measure of how variable the concentration is relative to its mean — with distance from the source. At greater distances, the intensity approached a relatively constant non-zero value. In the along wind direction, fluctuation intensity decreased quickly close to the source but then stabilized to a nearly constant value at greater distances. *Conditional intensity*, computed from time periods when concentration was significantly non-zero (above a noise threshold), displayed a similar pattern; computing this statistic only during plume-present periods removes the diluting effect of the zero-concentration periods. The *intermittency factor* — the proportion of time during which the measured concentration exceeded a noise threshold (formally defined and discussed in section 2.6) — increased gradually with distance, although this increase might have been influenced by the relatively smooth terrain of the longer-range experimental sites, which resulted in less plume meandering. In their analysis of cross-sections of the plume, the variation in fluctuation statistics was primarily influenced by the proportion of time during which the concentration was effectively zero. They found that the intensity of concentration fluctuations, $\sigma_c / \langle C \rangle$, was minimized on the plume centre line and increased toward the edges. This variation was attributed to the changing intermittency factor, with only minor variations in conditional intensity. The maximum value of fluctuation intensity on the plume centre line was affected by the prevailing turbulence structure and intensity, which were determined by the meteorological conditions and terrain characteristics. Finally, they developed a conceptual model describing plume dispersion influenced by turbulent eddies of various scales. Up to 1000 meters, eddies in the atmospheric surface layer with scales larger than the transverse dimension of the instantaneous plume caused it to meander. Similarly, scaled eddies acted to break up the plume and mix it with clean air, while smaller-scale eddies facilitated mixing within the plume itself. The conditional statistics, based on significantly non-zero concentrations, showed only slight variations across the plume.

Justus et al. (2002) conducted experiments using miniature photoionization detectors (miniPIDs) with propene and air in a wind tunnel. These experiments featured fast-response detectors positioned at four locations to study pulsed horizontal and vertical plumes. They also included a continuous point source and a continuous point source with an oscillatory wake. Wind speed was simultaneously measured using a 3D sonic anemometer. In each flow regime tested, the signal from the miniPID was intermittent and fluctuated in strength. When the tracer source was pulsed, artificially introduced intermittency dominated along the length of the plume. For continuous plumes, a fixed sensor registered greater intermittency than for an oscillatory plume; in the oscillatory case, the plume swept back and forth across the sensor, producing shorter individual burst durations but also shorter inter-burst intervals as the plume returned regularly, and therefore lower overall intermittency. Separately, the intermittency recorded by a stationary sensor within the plume tended to underestimate the intermittency that a moving insect would experience navigating upwind: locomotion

carries the insect in and out of plume filaments more actively than a fixed sensor positioned at a single cross-section. The oscillatory plume was approximately twice the diameter of the continuous plume and expanded more rapidly as it travelled downstream. The well-mixed internal structure of the oscillatory plume exhibited slightly shorter burst lengths and lower intermittency compared to the continuous plume, though there were significant differences in concentration. This indicated that an oscillatory plume was likely to provide a more constant stimulus and a lower mean concentration compared to a continuous plume.

A MOX (Metal-Oxide) sensor detects gases by measuring changes in electrical resistance in a metal-oxide semiconductor material. When the target gas interacts with the sensor, it alters the resistance, which is then used to determine the gas concentration. MOX sensors are commonly used for detecting gases like carbon monoxide, methane, and various volatile organic compounds. Historically metal oxide semiconductor (MOX) gas sensors have been plagued with a slow recovery after gas encounters and baseline drift (J. Burgués and S. Marco, 2019; Dennler, Rastogi et al., 2022; Monroy, González-Jiménez and Blanco, 2012). Various approaches have been suggested to mitigate these issues (Drix and Schmuker, 2021; Monroy, González-Jiménez and Blanco, 2012; Pashami, Lilienthal and Trincavelli, 2012). MOX sensors are sensitive to humidity, temperature and pressure fluctuations. Huerta et al. (2016) saw an improvement in online discrimination performance by accounting for external humidity and temperature variations. Arrays of MOX sensors are generally referred to as electronic noses (e-noses) and are used to record odours in wind tunnels (Vergara et al., 2013), outdoors (Dennler, Drix, Rastogi et al., 2022), in robotic navigation (Vuka et al., 2017) and for environmental monitoring (Khorramifar et al., 2023). Vergara et al. (2013) used nine custom eight-sensor boards lined perpendicular to the wind direction within a wind tunnel to iteratively capture odour plumes over six positions downwind of the odour release. They captured odour plumes of ten analytes at varying concentrations at three different wind speeds of $0.1 m/s$, $0.21 m/s$ and $0.34 m/s$ and used a linear support vector machine (SVM) to discriminate between the analytes. The dataset published by Vergara and colleagues has become a standard benchmark in the field. However, Dennler, Rastogi et al. (2022) uncovered significant drift of the MOX sensors of this dataset allowing them to correlate the recording batch to the sensor baseline before the gas exposure. Recently, efforts have also been made to accelerate the response time and sensitivity of gas sensors. Martinez, Burgués and Marco (2019) accounted for slow sensor response times through blind deconvolution. The use of a digital band-pass filter to boost bandwidth saw improvements in MOX response time by at least a factor of four (Burgues, Valdez and S. Marco, 2019) . Drix, Dennler and Schmuker (2022) used rapid hotplate temperature modulation with MEMS-MOX sensors to achieve improved natural olfactory scene recognition over extended timespans. Although MOX sensor recordings require a degree of post-processing, they are a promising technology for effectively measuring odour plumes due to their minimal impact on plume flow and their affordability. Recent advancements in MOX sensors make them fast (response times improved by at least a factor of four through digital band-pass filtering (Burgues, Valdez and

S. Marco, 2019)), small and light enough for precision robotic navigation of odour plumes (J. Burgués, Hernández et al., 2019; Vuka et al., 2017).

A non-invasive method of capturing both the structure and concentration of turbulent scalars in wind tunnels is through planar-laser induced fluorescence (PLIF). PLIF requires pairing of a fluorescent dye with a pulsed laser to illuminate a flow with a laser sheet and capture images of the light scattered by the molecules of the flow using a high speed camera (J. P. Crimaldi, 2008; Van Cruyningen, Lozano and Hanson, 1990). It enables detailed reconstructions of flows in two-dimensional planes (Dahm and Dimotakis, 1987; Koochesfahani and Dimotakis, 1985). The LIF technique expands to capture three-dimensional volumes (Tian and Roberts, 2003; Van Vliet et al., 2004; Yoda, Hesselink and Mungal, 1994), Arroyo and Hinsch (2008) provides a detailed review of 3D extensions. The goal of these experiments is to capture the advection of a passive scalar by the turbulent flow. A passive scalar is a diffusive contaminant in a fluid flow introduced at such a low concentration that it has no effect on the fluid motion itself (Shraiman and Siggia, 2000; Warhaft, 2000). The term "scalar" indicates that the quantity has magnitude only (unlike a vector quantity such as velocity), and "passive" indicates that the contaminant does not alter the flow that carries it — the dye or odour is simply advected and diffused by the pre-existing velocity field. Different experimental cases (e.g. odour release height, wind speed, carrier fluid) results in significant changes in the resulting spatial and temporal structure of the passive scalar.

Recent experiments have improved the spatial and temporal resolution capabilities of the PLIF technique for recording plumes (J. P. Crimaldi and Koseff, 2001) and airborne odour plumes (Connor, McHugh and J. P. Crimaldi, 2018). Post processing schemes were applied that increased accuracy and lowered noise, by mitigating common sources of error. Connor, McHugh and J. P. Crimaldi (2018) generated acetone vapour as a fluorescent odour surrogate (Lozano, Yip and Hanson, 1992) mixed with helium to achieve neutral buoyancy, passively releasing it into a low-speed benchtop wind tunnel. They demonstrate three test cases with different release heights and wind speeds: near-bed release $10cm/s$; freestream release at $10cm/s$; freestream release at $20cm/s$. From the recordings they produce cross-stream profiles of mean concentrations that exhibit symmetry and self-similarity but differ significantly in spatial distributions of mean and RMS concentrations among the three test cases. Concluding that the proximity to the viscous sub-layer of the near-bed case causes the scalar to spread rapidly but maintain a high concentration and small relative fluctuations throughout the test section. This contrasts with the freestream case with a limited spatial plume extent as mean concentrations were rapidly diluted away from the source.

From recorded odour plumes, we can extract the overall structure of the odour plume, but the odour cues that are used by animals to determine their location in proximity to an odour source still need to be extracted. In the next section we explore the statistics that have previously been studied that offer clues to organisms about odour source proximity.

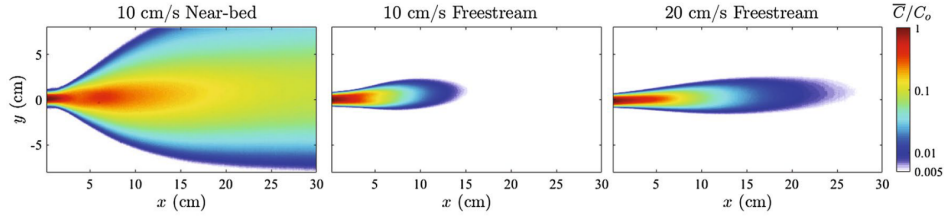

(a) Normalized mean concentration distributions for each of the three flow cases

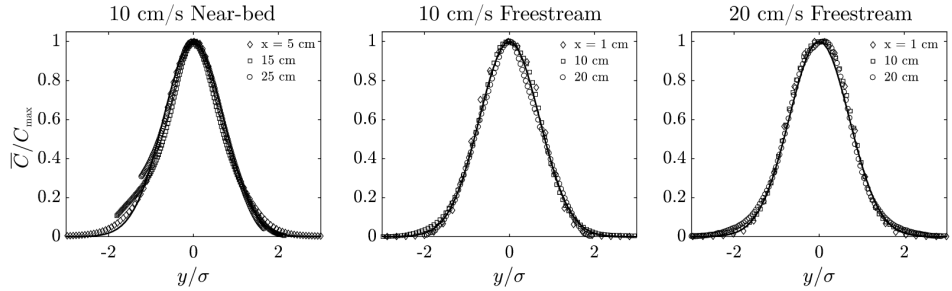

(b) Lateral profiles of normalized mean concentration at x = 5, 15, and 25 cm for the near-bed case (left), and at x = 1, 10, and 20 cm for each of the freestream cases (middle and right). Data are normalized via a fit to a Gaussian curve (solid line)

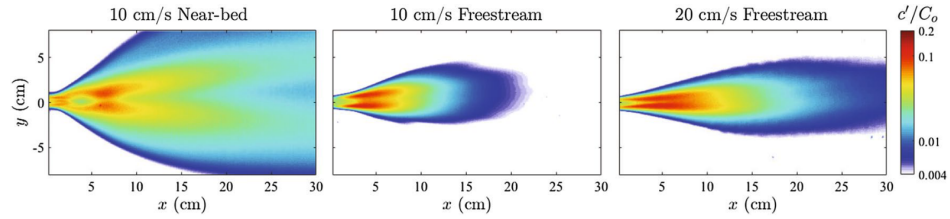

(c) Normalized root-mean-square concentration distributions ($C_{rms}/C_0 = \sigma_c/C_0$, where σ_c is the standard deviation of instantaneous concentration and C_0 is the source concentration) for each of the three flow cases

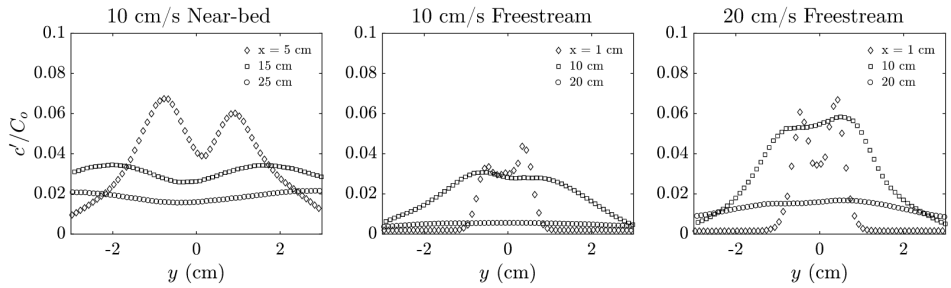

(d) Lateral profiles of normalized root-mean-square concentration (C_{rms}/C_0) for each of the flow cases.

Figure 2.5: From Connor, McHugh and J. P. Crimaldi (2018).

2.6 SENSED ODOUR STATISTICS

Carmel et al. (2003) states that in the case of $\Psi_i(t)$ as a measured signal of the ith sensor, the four most popular features of transient signals are (see fig. 2.6): the difference between the peak and the baseline Ψ_i^{max}, where the baseline is the background signal level in the absence of odour and the beginning of the response is the point at which the signal first rises above this baseline; the area under the curve A_i; the area under the curve left of the peak A^{max}; the time from the beginning of the signal to the peak T_i^{max}; Often more than one feature per signal is used, working with a subset of the aforementioned features.

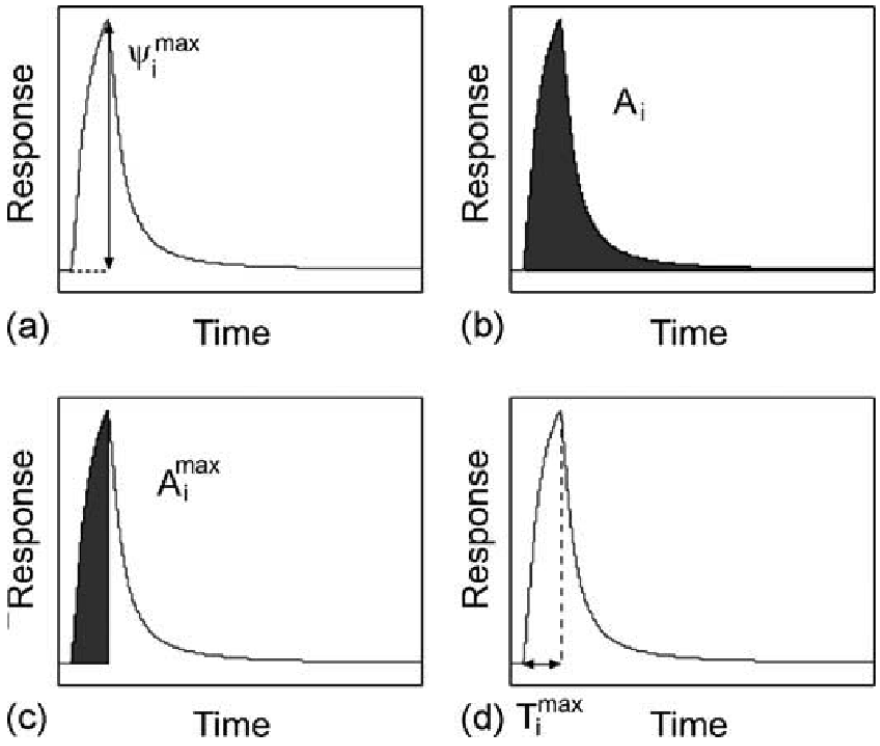

Figure 2.6: Definition of the four most popular features in transient signals: (a) the difference between the peak and the baseline, Ψ_i^{max}; (b) the area under the curve, A_i; (c) the area under the curve left of the peak, A^{max}; (d) the time from the beginning of the signal to the peak, T_i^{max}. From Carmel et al. (2003).

In section 2.5, we described plume recording techniques, but depending on the technique used to record an odour signal, other features that expand on the typical time series features have been derived and used to extract useful information from odour signals.

Various methods have been used to produce feature maps of odour plumes. The mean length of bursts, where bursts are defined as periods of active signal above threshold, as in Justus et al. (2002) and Murlis and Jones (1981) have been used in experiments recorded with Unipolar ionized air and PID. Mylne and Mason (1991) explored peak-to-mean ratio, peak-to-conditional-mean ratio, fluctuation intensity and conditional intensity. P. A. Moore and Atema (1991) demonstrated features such as: odour pulse height - the highest concentration

measured against background; pulse length - the duration of a pulse; pulse onset slope - the maximum value of rising slope of pulse. Concentration change spectrums were also produced for electrochemical electrodes (P. A. Moore and Atema, 1991) and for PID (Mylne and Mason, 1991) experiments.

PLIF recordings instantaneously capture the entire test section as opposed to a point in space, and therefore produce very detailed feature maps. J. P. Crimaldi, Wiley and Koseff (2002) and Connor, McHugh and J. P. Crimaldi (2018) (fig. 2.5) demonstrate two-dimensional maps of instantaneous and mean concentration, and concentration variance or root-mean-square concentration from PLIF recordings.

Justus et al. (2002) followed the convention of Jones (1983) and Murlis and Jones (1981) when defining intermittency as the probability of zero signal, $1-\gamma$, or the proportion of time in which concentration was below a noise threshold. With this definition, zero intermittency is associated with a continuous signal, increasing intermittency is linked to less overall signal activity which is intuitive. Note that many authors use a different convention, defining intermittency as, γ, the probability of non-zero signal. Intermittency factor has been explored in ionized air (Jones, 1983; Murlis and Jones, 1981), PID recordings (Justus et al., 2002; Mylne and Mason, 1991) and PLIF recording (Connor, McHugh and J. P. Crimaldi, 2018; J. P. Crimaldi, Wiley and Koseff, 2002; Gumaste et al., 2024).

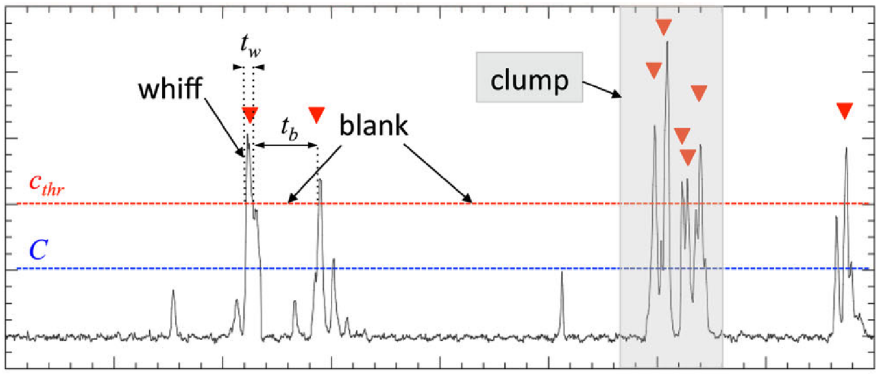

Figure 2.7: A typical time series of the odour concentration at a given point in space. Red triangles indicate the occurrence of whiffs, i.e., intervals when the local concentration is above the threshold c_{thr} indicated by the red line. For olfactory searches, the threshold is comparable to the sensitivity of the pheromone receptors of the insects. The blue line indicates the average concentration C in the regions where the signal is above the noise level. From Celani, Villermaux and Vergassola (2014).

Other features have been used to estimate the distance between a sensor and a gas source. 'Whiff and blank' features are commonly extracted from turbulent plume recordings (Celani, Villermaux and Vergassola, 2014; Mylne and Mason, 1991; Rigolli, Magnoli et al., 2022; Yee, Chan et al., 1995; Yee, Kosteniuk et al., 1993). These features are demonstrated in fig. 2.7. It has previously been shown that the whiff duration and up crossing time can be used to estimate gas source distance, but these features are odour concentration dependent.

Bouts (Schmuker, Bahr and Huerta, 2016) are a transient feature that offer a rapid and largely gas concentration independent method of estimating source distance primarily

extracted from bout counts. Bout analysis was specifically designed for use on gas recordings from MOX sensors. It extracts short timescale features from the first derivative of the response of MOX sensors. Bouts are essentially the rising edge of the derivative of the MOX sensor response that occurs after an odour is encountered. The bout method was designed with an initial band-pass filter cascade to mitigate baseline drift, slow recovery and high frequency electrical noise. A low pass Gaussian filter is used for the high frequency electrical noise. An exponentially-weighted moving average attempts to mitigate the slow sensor recovery (Muezzinoglu et al., 2009). The derivative combined with low-pass filtering can increase MOX sensor bandwidth by a factor of four (Burgues, Valdez and S. Marco, 2019). In Schmuker, Bahr and Huerta (2016) bouts were used to predict the source-receptor distance using MOX sensors in wind tunnel experiments (Vergara et al., 2013). Whiff up crossing time and the Bout feature both suggest that crucial information about source proximity occur within the initial increase of odour concentration.

In order to navigate to an odour source, these odour cues must be used in conjunction with navigation strategies to be of use to an organism. In the next section we explore navigation strategies that have been well observed in insects.

2.7 NAVIGATION STRATEGIES

The task of navigating to an odour source has been broken into three critical steps (Kowadlo and Russell, 2008): search for the presence of a target chemical; search for the source guided by chemical and other sensing; verification of the identified source. The most focus in navigation research has been on the second step.

Knowledge of odour source distance is relevant to odour source search, as it provides information about how far an organism must travel and may inform when to switch between search strategies. Estimating this distance reliably from concentration statistics requires either averaging over long sampling periods (to obtain stable statistics) or exploiting the fast fluctuations in concentration directly, since instantaneous concentration is highly variable in turbulent flow. A gradient ascent towards greater time-average gas concentration may be sufficient to locate an odour source in a purely diffusive flow, but in nature odorants are often carried in turbulent flows (Hengenius et al., 2021). What strategies do animals employ to navigate turbulent flows without sampling for long periods of time?

When describing the movement of animals, the morpheme 'taxis' is often used. It refers to the movement of an organism in response to a specific stimulus. Chemotaxis involves directional movement towards or away from chemical signals, allowing organisms to navigate in response to the presence of chemicals in their environment. Anemotaxis is the movement in response to wind direction, helping organisms orient themselves based on air currents. Tropotaxis involves the use of stereo or bilateral sense organs to compare sensory inputs from different sides of the body, enabling organisms to move towards a more favourable condition by evaluating differences in stimuli. Klinotaxis is a strategy where an organism

turns towards the strongest signal by continuously adjusting its direction in relation to the intensity of the stimulus, often observed as a casting behaviour in various insects. Each of these taxis types represents a unique mechanism by which organisms adapt their movement to optimize their response to environmental cues.

Invertebrates navigate odour plumes in both the freestream and boundary layer (near-bed) conditions, in air and water. Early studies of male moths suggest that they detect and navigate pheromone plumes over kilometres (Bossert and E. O. Wilson, 1963; Collins and Potts, 1932). Elkinton et al. (1987) deemed kilometre-scale navigation unlikely, arguing that the synthetic lures used in such studies — including those of Charlton and Cardé (1982) — released odour at rates substantially greater than the natural pheromone release rate of female gypsy moths. Regardless of this, moth navigation strategies have been very well studied. Recently though, focus has turned to navigation strategies of flies. Flies have been suggested as a model organism for genetic modification and for ease of rearing. Moths and flies reliably navigate airborne odour plumes to seek out food and mates.

Moths use various mechanisms to navigate toward pheromone sources. Kennedy and Marsh (1974) observed that male moths flying upwind towards a scent-producing female use optomotor reactions to ground patterns for anemotactic guidance. When the odour stimulus is lost, their flight path shifts from upwind to crosswind with intermittent left-right reversals. Similar behaviours are noted in other insects, such as *Drosophila* and *A. kiihniella*, where they also exhibit crosswind tracks or overshoot the source when the odour is lost. Kennedy (1978) distinguished two forms of chemo-klinotaxis: longitudinal chemo-klinotaxis, in which the animal modulates its upwind speed in response to concentration changes along its direction of travel, and transverse chemo-klinotaxis, in which the animal steers laterally to maintain itself within the odour plume. Kennedy found no evidence for the longitudinal form in field studies, suggesting that insects rely more on transverse chemo-klinotaxis. The guidance mechanism most consistently supported for moths is optomotor anemotaxis — upwind steering driven by the perception of ground-pattern movement, triggered by odour contact — rather than by direct gradient-following, which is difficult to achieve given that sustained concentration gradients rarely persist in natural turbulent conditions. In wind tunnel experiments, Marsh, Kennedy and Ludlow (1978, 1981) showed that male *Plodia interpunctella* moths use zigzag patterns to home in on pheromone sources, adjusting their airspeed and turning based on the pheromone input. Similar results were found by Kennedy, Ludlow and Sanders (1980), who identified two contrasting anemotactic behaviours: upwind flight in response to pheromone increases and crosswind flight with track reversals in response to decreases.

C. T. David, Kennedy and Ludlow (1983) demonstrated tracks of male gypsy moths approaching a source of sex pheromone (and bubbles to visualize local wind direction), they concluded that moth use odour-modulated anemotaxis to steer by the wind (fig. 2.8). T. C. Baker (1990) proposed a model where a phasically modulated response to pheromone pulses generates upwind surges, while a tonic response maintains counter turning. N. J. Vickers

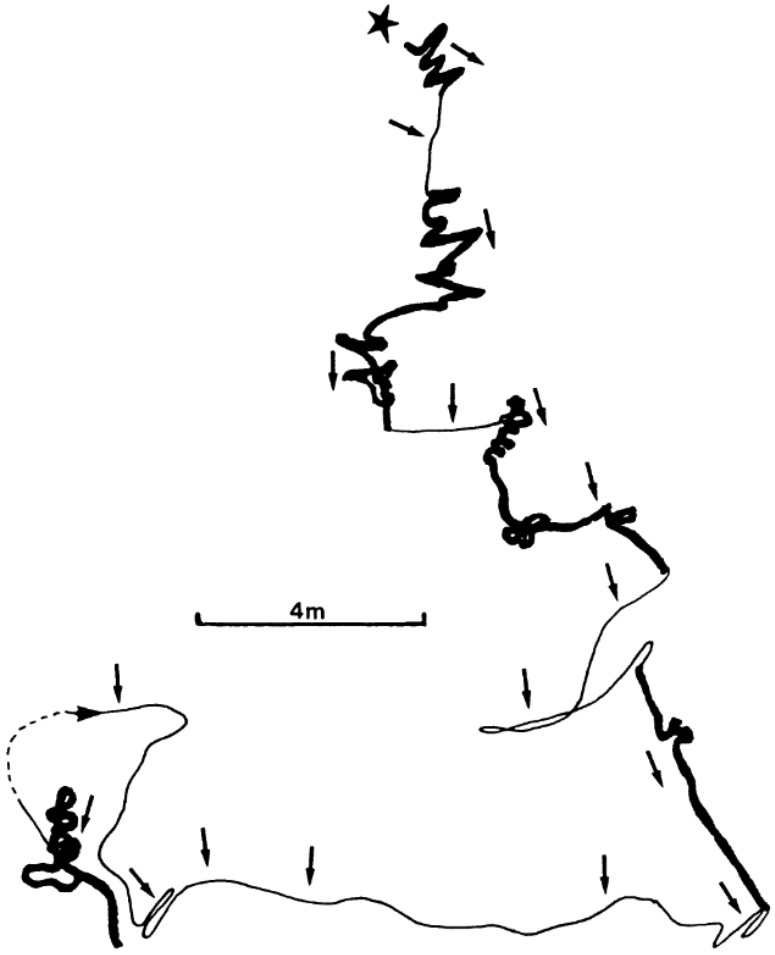

Figure 2.8: Orientation in turbulent odour field. Flight path of male gypsy moth toward a source of female attractant pheromone continuously released at the star. Average wind direction is from top to bottom of the figure, but the turbulence causes local wind direction to vary from place to place and from time to time. Arrows indicate local wind direction at the time of moth passage, measured by releasing soap bubbles and photographing their displacement to visualize the instantaneous flow field. The track is drawn thick when the moth is in a patch of odour. From Atema, Fay et al. (1988), originally from C. T. David, Kennedy and Ludlow (1983).

and T. C. Baker (1994) and Willis and Arbas (1991) further refined this model, showing that insects' flight behaviour is influenced by rapid, phasic responses to pheromone fluctuations, which guide their trajectory and maintain consistent turning patterns. It has also been shown that moths fly straighter upwind and faster within odour plumes where the intermittency is lower (Mafra-Neto and Cardé, 1994; N. J. Vickers and T. C. Baker, 1994). These studies collectively illustrate that while optomotor anemotaxis and pheromone-guided zigzagging are well-established, the mechanisms of odour-regulated flight remain complex and involve interactions between pheromone concentrations and wind conditions.

Flies and moths display distinct behaviours when navigating odour plumes. In homogeneous plume conditions, moths often deviate from the plume, while flies typically maintain a straight upwind trajectory (Budick and Dickinson, 2006; Kellogg, Frizel and Wright, 1962; Wright, 1964). In *Drosophila melanogaster*, strong osmotropotaxis, or the tendency to turn towards higher odour concentrations, has been observed; however, its effectiveness is constrained by the proximity of olfactory sensors (Borst and Heisenberg, 1982). Anemotaxis, or wind-based navigation triggered by olfactory signals, is well-documented across various insect species (Kellogg, Frizel and Wright, 1962; Kramer, 1976; Traynier, 1968). Budick and Dickinson (2006) explored the short-term response of *Drosophila melanogaster* to plume encounter and loss, and the long-term response to constant odour stimulation (fig. 2.9). Cast identification was algorithmically identified from a change from upwind flight, and plume contact and loss was extrapolated from flight trajectories.

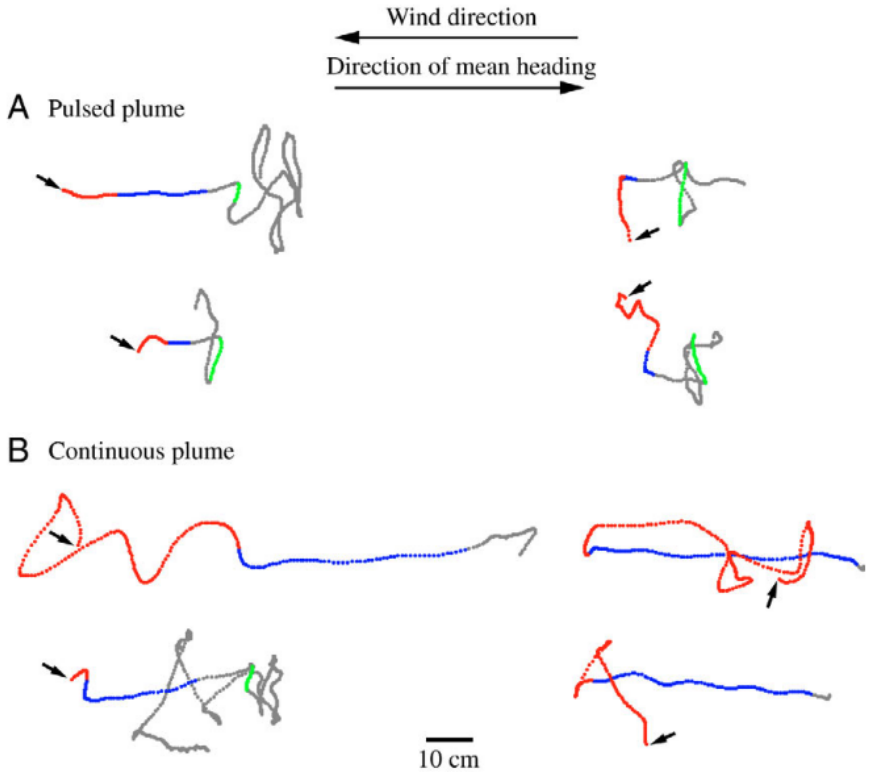

Figure 2.9: Casting frequently follows plume truncation. (A) Four representative trajectories from the large diameter pulsed banana odour plume illustrate flight prior to plume contact (red), within the plume (blue), and following plume loss due to truncation (grey). The first cast, as defined by their cast identification algorithm, is plotted in green. (B) In the continuous large diameter plume, casting rarely initiated within the plume. Colour designations are the same as in panel (A) — flight prior to plume contact (red), within the plume (blue), and first cast in green — except that grey here indicates plume loss due to the fly exiting the plume laterally rather than plume truncation. Arrows indicate the initiation of fly tracking, but in some cases several points were excised from the beginning of the track in order to enhance the clarity of the trajectory. From Budick and Dickinson (2006)

.

Studies by Zanen et al. (1994) and Budick and Dickinson (2006) reveal that *Drosophila* exhibit varying flight patterns depending on the presence of odour. Without odour, they demonstrate stereotypical crosswind casting, whereas in a homogeneous odour cloud, they maintain a rapid upwind heading. Furthermore, *Drosophila* adjust their behaviour during short-term encounters with odour plumes, engaging in surging when odour is present and casting when it is lost (Bhandawat, Maimon et al., 2010; Budick and Dickinson, 2006). The role of mechanosensors in guiding these upwind turns has been emphasized (Bhandawat, Maimon et al., 2010). *Drosophila melanogaster*'s response to odour plumes encompasses both upwind surging and crosswind casting, influenced by the structure of the plume and odour concentration (Gaudry, Nagel and R. I. Wilson, 2012; van Breugel and Dickinson, 2014). Research by Álvarez-Salvado et al. (2018) using high-throughput assays demonstrated that walking *Drosophila* respond to the presence of odour by running upwind and engaging in local searching upon odour offset. While wind orientation relies

on antennal mechanoreceptors, the search behaviour is driven primarily by the detection of odour during encounters. Walking *Drosophila* use stochastic navigation strategies, adjusting their movement based on recent odour encounters (Demir et al., 2020). Additionally, long-distance flight behaviour in *Drosophila* shows how wind influences dispersal and trajectory, with flies capable of covering significant distances under still or moderate winds (Leitch et al., 2021). Recent studies highlight that the frequency and duration of odour encounters significantly impact walking *Drosophila* navigation, affecting their turning behaviour (Jayaram et al., 2023). The frequency and duration of time between odour whiffs have also been shown to impact the pausing and orienting behaviour of *Drosophila* (Álvarez-Salvado et al., 2018; Demir et al., 2020).

It is clear from this work that, when flying, both moths and flies will use a cast-surge model, with minor differences occurring in the homogeneous plume case. However, Borst and Heisenberg (1982) did cast doubt on the ability for *Drosophila* to effectively determine whether the encountered plume is homogeneous. It is also clear that the strategies of walking and flying *Drosophila* also vary considerably.

Vergassola, Villermaux and Shraiman (2007) proposed the search algorithm called 'Infotaxis'. Its aim was to navigate dilute and turbulent environments in which traditional chemotaxis, that relies on a local concentration gradient, becomes ineffective due to sporadic odour detection and rapid signal decay. Instead of sensing gradients, infotaxis viewed odour source navigation as an information acquisition about the source location, and its strategy was to locally maximize the expected rate of information gain. It achieved this by continuously updating a posterior probability distribution for the source location using Bayes' formula — which prescribes how a prior belief should be revised in light of new evidence — based on the intermittent "hits" (odour detections) received. Information gain was quantified by the reduction of Shannon's entropy of this probability distribution — a measure of the uncertainty, or spread, of the distribution, which decreases as the estimated source location becomes more certain. The infotaxis strategy balanced an "exploration versus exploitation trade-off" by selecting movements that maximized this expected entropy reduction, combining the goal of finding the source with the need to gather more information. Interestingly, this approach leads to "zigzagging" and "casting" trajectories similar to those observed in moths and flies (Budick and Dickinson, 2006; Kellogg, Frizel and Wright, 1962; Wright, 1964). It also proved more efficient than chemotaxis in dilute conditions, with a linear scaling of average search time with initial distance compared to the exponential time required of the latter. Infotaxis was found to be robust to fluctuations and inhomogeneities of the plume making it ideal for use in olfactory robots that navigate challenging dilute environments.

2.8 CONCLUSIONS

The literature reviewed here establishes three interlocking themes that motivate the experimental and simulation work of this thesis.

Animals exploit transient odour statistics, not mean concentration. The olfactory systems of insects and vertebrates are adapted to detect rapid fluctuations in odour concentration rather than slow changes in the mean. Sniffing, antennal flicking, and bilateral sensing are all strategies for sampling the intermittent, filamentous structure of turbulent plumes. The key temporal features that carry information about source distance and location — bout count, duration, amplitude, and inter-bout interval — are reviewed in section 2.6 and form the basis of the bout analysis presented in chapter 3.

Turbulent plume structure encodes distance and direction. The statistics of odour fluctuations change systematically with distance from the source: bout count decreases non-linearly, intermittency increases, and filament structure becomes coarser. These trends are not easily accessible to a time-averaged sensor but are recoverable through transient feature extraction. Crucially, the degree to which these trends are accessible depends on the flow regime and release configuration — boundary-layer (near-bed) plumes differ fundamentally from freestream plumes, with implications for both animals and robots navigating them. Chapter 3 tests whether these trends are present in high-resolution PLIF recordings and quantifies how they vary with wind speed and release height.

Simple biologically inspired strategies can navigate turbulent plumes. Animals do not require detailed concentration maps to find odour sources; surge-and-cast strategies triggered by intermittent odour contact are sufficient in many conditions. The benefit of stereo sensing — comparing signals from spatially separated receptors — depends on plume structure. Chapter 4 tests three such strategies in the PLIF plume data to determine when direction sensing confers an advantage and how the cast-and-surge strategy compares to purely reactive approaches.

Together, these themes motivate a unified approach: characterise the plume, extract bout statistics, and test navigation strategies in the same high-resolution dataset. Future work aims to transfer these findings to physical robots equipped with miniaturised MOX sensors (Dennler, Drix, Warner et al., 2024), closing the loop between biological olfaction, plume physics, and robotic implementation.

3

BOUT ANALYSIS IN REALISTIC TURBULENT PLUMES

Samuel Sutton [a], Maria Psarrou [a], Aaron True [b], John Crimaldi [b], and Michael Schmuker [a]

[a] Centre of Data Innovation Research, School of Physics, Engineering & Computer Science, Department of Computer Science, Biocomputation Research Group, University of Hertfordshire, UK

[b] Civil, Environmental, and Architectural Engineering, University of Colorado Boulder, CO, USA

3.1 KEYWORDS

Turbulent odour plumes; planar laser-induced fluorescence; bout analysis; concentration fluctuations; inter-bout interval; odour source proximity; wind tunnel; olfactory navigation

3.2 PREFACE

This chapter contains a preliminary manuscript in the form of a systematic application of bout analysis (Schmuker, Bahr and Huerta, 2016) on an optical planar laser-induced fluorescence (PLIF) dataset. Bout analysis was originally designed for and applied to time series captured using metal oxide (MOX) type gas sensors. Our analysis is carried out on four different release configurations of an acetone vapour plume in a wind tunnel (Connor, McHugh and J. P. Crimaldi, 2018). We highlight the impact of the gas release conditions on the bout statistical features calculated from the turbulent plume and how they change with proximity to the gas source.

3.3 CREDIT CONTRIBUTION STATEMENT

Samuel Sutton: Conceptualization, Investigation, Formal analysis, Software, Visualization, Writing - Original Draft, Writing - Review & Editing **Maria Psarrou**: Conceptualization, Investigation, Writing - Original Draft (Introduction) **Aaron True**: Data Curation, Conceptualization **John Crimaldi**: Data Curation, Conceptualization **Michael Schmuker**: Conceptualization, Writing - Review & Editing, Supervision

3.4 ABSTRACT

The spatio-temporal features of concentration in turbulent odour plumes are used by organisms that track scents to their source. Statistics of the rising flanks of concentration fluctuations are sufficient to extract odour source distance. Here we introduce Bout statistics,

a biomimetic event-based approach to quantify such features. We analyse the relationship between odour source distance, in both the downwind and crosswind direction, and the extracted Bout statistics of turbulent plumes recorded in a wind tunnel. Bout features consistently encode relative source location across different wind speeds, but reflect the considerable differences between plumes depending on whether the odour was released near a boundary surface (near-bed) or in mid-air (free-stream).

3.5 INTRODUCTION

Essential to many organisms' survival is their ability to locate the release source of an odour and then adjust their behaviour accordingly based on the odour identity (foraging, mate-seeking, shelter-seeking, hazard-avoidance). This entails navigation through the realm of a turbulent odour plume and the perception of its dynamics (J. Crimaldi et al., 2022).

Each odour plume is characterized by a unique set of statistics that can be translated to sensory cues for successful odour navigation and source tracking (K. L. Baker et al., 2018; Marin, Schaefer and Ackels, 2021). As the odour plume travels and expands downstream from its release site, it breaks up into non-homogeneous concentration patches and forms eddies resulting in changes with distance in the concentration mean, variance and intermittency and its overall dynamic spatio-temporal structure (Celani, Villermaux and Vergassola, 2014; J. P. Crimaldi and Koseff, 2001; Pannunzi and Nowotny, 2019). The spatio-temporal distribution of the concentration fluctuations and its intermittency pattern depend on the physical distance from the odour source, as well as the wind direction and carrier speed of the odour (Celani, Villermaux and Vergassola, 2014; Connor, McHugh and J. P. Crimaldi, 2018; Justus et al., 2002; Murlis, Elkinton and Carde, 1992; Murlis, Willis and Carde, 2000; Mylne and Mason, 1991; Riffell, Shlizerman et al., 2014; Schmuker, Bahr and Huerta, 2016; N. J. Vickers, Christensen et al., 2001).

Dynamics of realistic plumes also differ based on the proximity of the release site to a boundary, such as the ground in natural settings, or a wall or the floor in a wind tunnel. For instance, odour plume recordings obtained by planar laser-induced fluorescence (PLIF) exhibit spatio-temporal mean concentration fluctuation profiles specific to the odour release location. Generally, odour plumes develop with a large-scale symmetry along their midline in a homogeneous advective carrier flow. However, the development of the plume is strongly affected by the release geometry. When released in mid-air, far away from the ground and other borders ("freestream"), the plumes exhibit a relatively narrow form, with marked inhomogeneity depending on the turbulence present in the transporting stream and its speed. Concentration patches develop that lead to intermittent odour encounters in downstream detectors. In contrast, "near-bed" (ground-based) release configurations exhibit more extended lateral spreading and less concentration variations, due to the boundary layer inhibiting the development of turbulent eddies (Connor, McHugh and J. P. Crimaldi, 2018). These differences in the odour plume structure offer a rich and diverse information space of available navigation cues and offer possible adaptations to the way that animals access and assess this information during olfactory tasks. It has been shown that animals do not rely on the mean concentration for navigation and source localization but rather on rapid sampling, which might involve sensing of intermittency or detection of the odour filamentous structures (J. Crimaldi et al., 2022).

A way to extract meaningful information for odour source localization from the plume is to decode its turbulence-induced intermittent and sparse fluctuations as events that represent

the inherent spatio-temporal plume dynamics, termed "bouts" (Najaran, 2021; Schmuker, Bahr and Huerta, 2016). Bout analysis is a bio-inspired event based algorithm that has been proposed for odour-source localization and mapping. It has been used for post-hoc data analysis, such as predicting source localization in the controlled environments of small wind-tunnels (Schmuker, Bahr and Huerta, 2016), and in real-time robot-based gas detection in larger enclosed spaces (J. Burgués, Hernández et al., 2019, 2020). The plume landscape recordings are translated to bouts, which roughly represent events of rapidly rising portions of a gas sensor's signal amplitude. The bout count is strongly correlated with the distance from the source under various wind conditions, inside a wind tunnel (J. Burgués, Hernández et al., 2019; Schmuker, Bahr and Huerta, 2016). However, recent research suggests that in open environments, where the wind conditions cannot be controlled, other bout-derived features, such as the average bout amplitude could be a better estimator for the distance from the source (Vuka et al., 2017).

In this work we investigate realistic plumes using bout analysis (Schmuker, Bahr and Huerta, 2016) and determine whether distributions of bout statistical features (count, amplitude, duration, inter-bout interval) map the plume landscapes and provide cues for odour source localization. We explore high spatio-temporal resolution PLIF recordings of near-bed and freestream odour release configurations (Connor, McHugh and J. P. Crimaldi, 2018), both downwind and crosswind from the plume's mid-line. Our results show that (a) the temporal features of the odour plume are encoded in the bout statistical features, (b) the odour plume condition, and in particular its release mode could be deciphered by its bout features profile, (c) the bout features provide comprehensive cues about the distance from the odour source, (d) bout analysis is an efficient bioinspired algorithm for the analysis of realistic plumes.

3.6 MATERIALS AND METHODS

3.6.1 *Input Data*

We analysed turbulent air plumes obtained from PLIF in a benchtop wind tunnel previously described in Connor, McHugh and J. P. Crimaldi (2018). This data provides a high-resolution view of the complex structure and the spatio-temporal dynamics of odour plumes in air under varying release conditions. We systematically conducted our analysis on four experimental cases in which the odour release was isokinetic (i.e. matching mean flow velocity in the wind tunnel). Three cases are freestream release, in which the odorant was released at the centre line of the tunnel at 14 cm above the floor of the test section, at mean flow velocities of 10 cm/s and 20 cm/s (published in Connor, McHugh and J. P. Crimaldi (2018)) and 5 cm/s (an unpublished configuration kindly provided to us by the original authors). One case we refer to as near-bed release, with a release height of 0.6 cm above a false floor that spans the width and length of the test section, tested at a mean flow velocity of 10 cm/s (Connor, McHugh and J. P. Crimaldi, 2018).

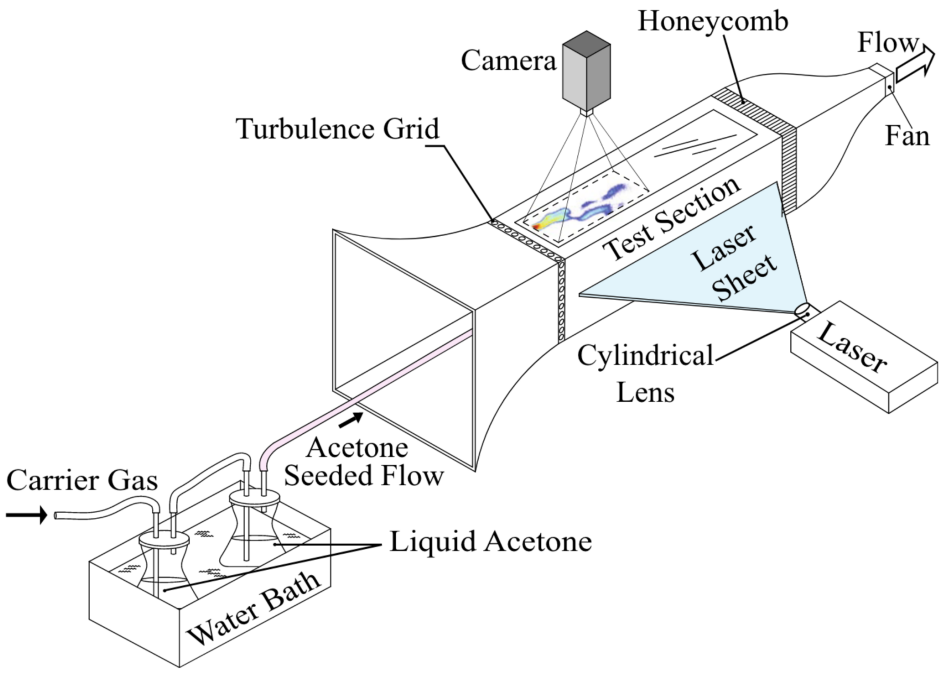

Figure 3.1: Schematic of experimental layout (Connor, McHugh and J. P. Crimaldi, 2018)

Figure 3.1 is a schematic of the flow facility in which the experiments were carried out. The test section was 1m long with a height and width of 0.3m. Turbulence was induced in the bulk flow at the upstream inlet after a contraction using a turbulence grid consisting of 6.4mm diameter rods with a 25.5mm mesh spacing. Acetone vapour was released in a carrier gas of helium (41%v/v) and air (59%v/v) to ensure neutral buoyancy. A honeycomb

conditioner was at the downstream end of the test section and mean air flow speed was varied by controlling a suction fan.

The acetone vapour was excited by a $15Hz$ pulsed laser shaped into a $1mm$ thick light sheet parallel to the floor of the test section. Images of the resulting fluorescing gas were captured with a synced high-quantum efficiency camera at a native resolution of 2048×2048 and 2×2 binned on-camera. The captured raw images I_N were processed to provide source-normalized concentration levels C/C_0 with the following equation adapted from J. P. Crimaldi (2008):

$$\frac{C}{C_0} = \frac{1}{a_c}\frac{I_N - b}{B - b}, \tag{3.1}$$

where B was the distribution of light in ROI captured by the camera with a constant uniform acetone concentration, b was the dark response obtained from 500 images of the test section when absent of any acetone signal, and a_c was a calibration coefficient for normalizing the concentration C based on the source concentration C_0 at the tube exit. Connor, McHugh and J. P. Crimaldi (2018) established an RMS noise of the PLIF system at $0.001C_0$ in the absence of acetone and report a detectability limit equal to five times the RMS noise floor ($0.005C_0$). Processed images were then additionally 2×2 binned to a final resolution of 512×512 or $0.74mm/pixel$. We post processed the data, by zeroing values ($C = 0.0$) below the noise floor ($\frac{C}{C_0} < 0.005$) to remove erroneous low amplitude fluctuations below this detectability limit.

Each release configuration had a number of repeated trials in which the gas was released and recorded for four minutes ($240s$). The freestream datasets have 10, 9 and 10 repeated trials for the $5cm/s$, $10cm/s$ and $20cm/s$ wind speeds, respectively. The near-bed $10cm/s$ dataset had five repeated trials. Figure 3.2 shows randomly selected but representative frames from the first trial of each release configuration. Significant structural differences of the turbulent plume of the four release conditions are evident. Each metric reported here is an average over all trials of each release configuration unless otherwise stated.

3.6.2 *Finding the turbulent plume Boundaries*

With repeated trials of each release configuration we asked: "How can we determine the average location of a temporally dynamic turbulent plume?" Here we establish a method that approximates the centre line of the plume and its edges for downstream and crosswind analysis, respectively. It has been previously observed that the average concentration over time of the plume should decrease downwind at the centre line and towards the plume edges. Therefore, we extended a method used by Connor, McHugh and J. P. Crimaldi (2018), in which a parametric Gaussian is fitted to binned cross-wind (lateral) profiles of the time-averaged concentration, taken perpendicular to the mean flow direction. Binning was necessary to spatially smooth the data and enable stable Gaussian approximations for each release configuration.

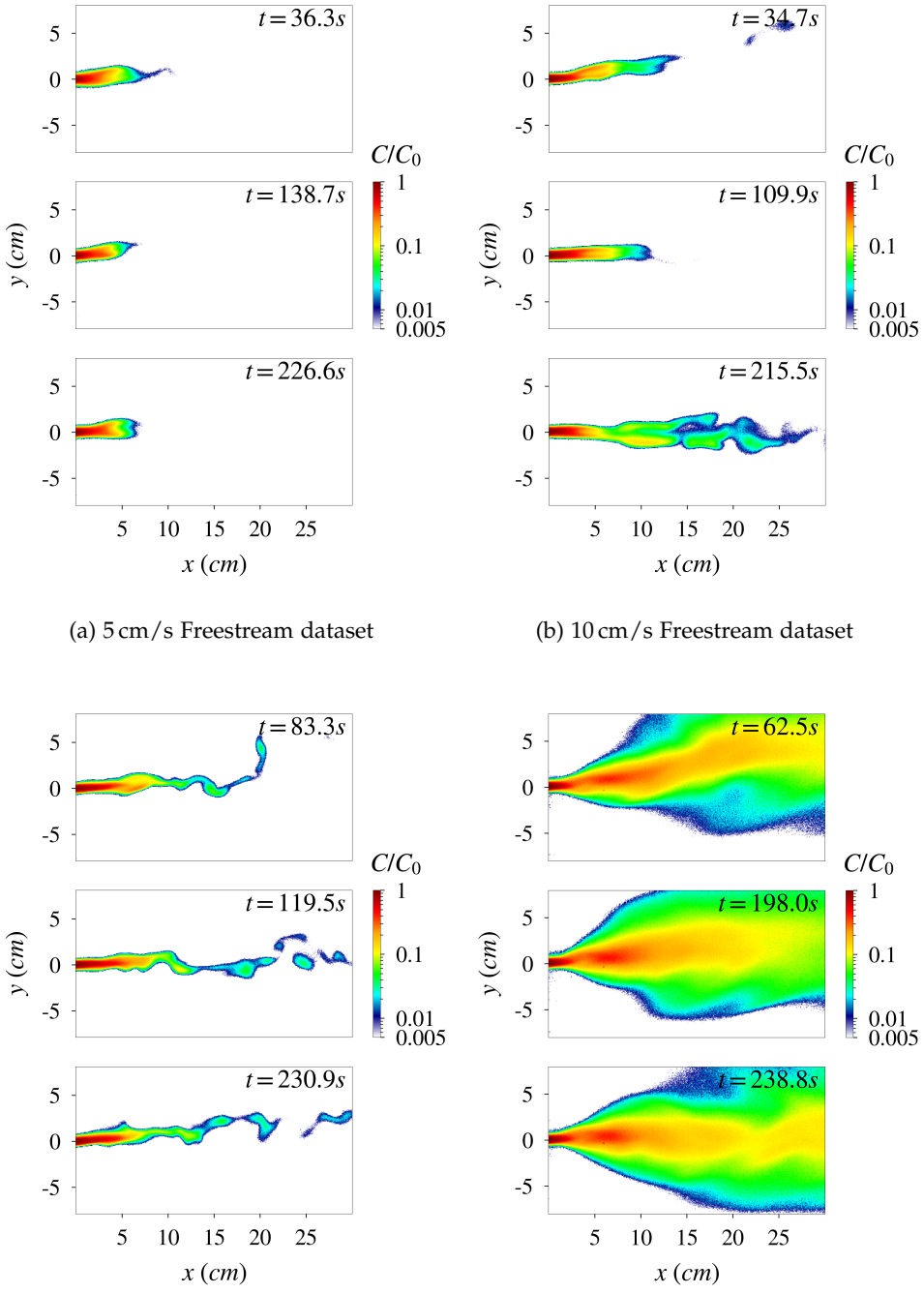

(a) 5 cm/s Freestream dataset

(b) 10 cm/s Freestream dataset

(c) 20 cm/s Freestream dataset

(d) 10 cm/s Near-bed dataset

Figure 3.2: Instantaneous concentration plots of three randomly selected, non-consecutive frames drawn from the first trial of each of the four odour release configurations. The frames were selected from early, mid, and late periods within the 240 s trial to illustrate the range of instantaneous plume structures; because the plume was continuously generated, the specific timestamps are not indicative of plume evolution. The odour source was located at the origin ($x = 0\,cm$, $y = 0\,cm$) and the overall flow direction was towards positive x. The log colour scale ranges from the observed mean source concentration at the source ($C/C_0 = 1$) to the detectability limit of the acetone PLIF system, i.e. the noise floor ($C/C_0 = 5 \times 10^{-3}$).

The fit Gaussian G_σ kernel is described by the following:

$$G_\sigma = a \cdot \exp\left(\frac{-(y-\mu)^2}{2 \cdot \sigma^2}\right), \tag{3.2}$$

with an arbitrary real constant a as a scaling variable for fitting the height of the curve to the maximum concentration at the centre point of the plume, μ as the lateral offset of the centre of the kernel and σ to fit the Gaussian RMS width of the curve to the horizontal extent of the plume.

For each release configuration, we averaged concentration over every trial by pixel ($\bar{C}/C_0$) and binned an additional two pixels ($1.5mm$) laterally, with respect to the test section dimensions, in the y direction and seven pixels longitudinally ($5.2mm$) in the x direction either side of every x and y pixel. We then fit the Gaussian curve to the lateral profiles of each of the 405 x pixel increments. These lateral profiles are considered crosswind profiles of the average wind direction. We used the best fitting Gaussian after a maximum of 1000 iterations of **scipy.curve_fit**.

To illustrate the result of the plume tracking, we plot the μ of each of the fit Gaussian kernels up to $\mu \pm 3\sigma$. We also plot the mean concentration of every pixel averaged over the trials for each dataset, coloured by a log colour map $\bar{C}/C_0$. The plotted concentration shown is the data before binning and is used to illustrate the average position of the plume for comparison with our Gaussian kernel approximated plume position.

For each x pixel kernel we scored the fit of the curve using the root-mean-square error (RMSE):

$$\text{RMSE} = \sqrt{\frac{1}{N}\sum_{j=1}^{N}\left(\hat{G}_\sigma(y_j) - \bar{C}(y_j)/C_0\right)^2}, \tag{3.3}$$

where N is the number of lateral bins, $\hat{G}_\sigma(y_j)$ is the fitted Gaussian value at lateral position y_j, and $\bar{C}(y_j)/C_0$ is the binned time-averaged concentration at that position. We plotted the RMSE (eq. (3.3)) as a function of downwind distance x. The RMSE in fig. 3.3 shows that the plume boundary approximation method was robust for all datasets. The $5cm/s$ freestream release configuration showed the greatest RMSE of 0.16 where $x > 10cm$, this was due to very low odour concentration in this area on average also shown in fig. 3.2a. One must remain cognisant of the fact that these are approximations of the overall plume location for each of the release configurations. The Gaussian curves were fit to a smoothed summation of all of the data of the $240s$ trials and therefore cannot represent the dynamic nature of the turbulent plume structure. These models provided a good approximation of the plume centre line with μ of the Gaussian for each of the y profile. We chose $\mu \pm 2\sigma$ as a good approximation of the plume bounds where the presence of odour was greater than the noise floor on average. This model of the plume location on average provided a foundation

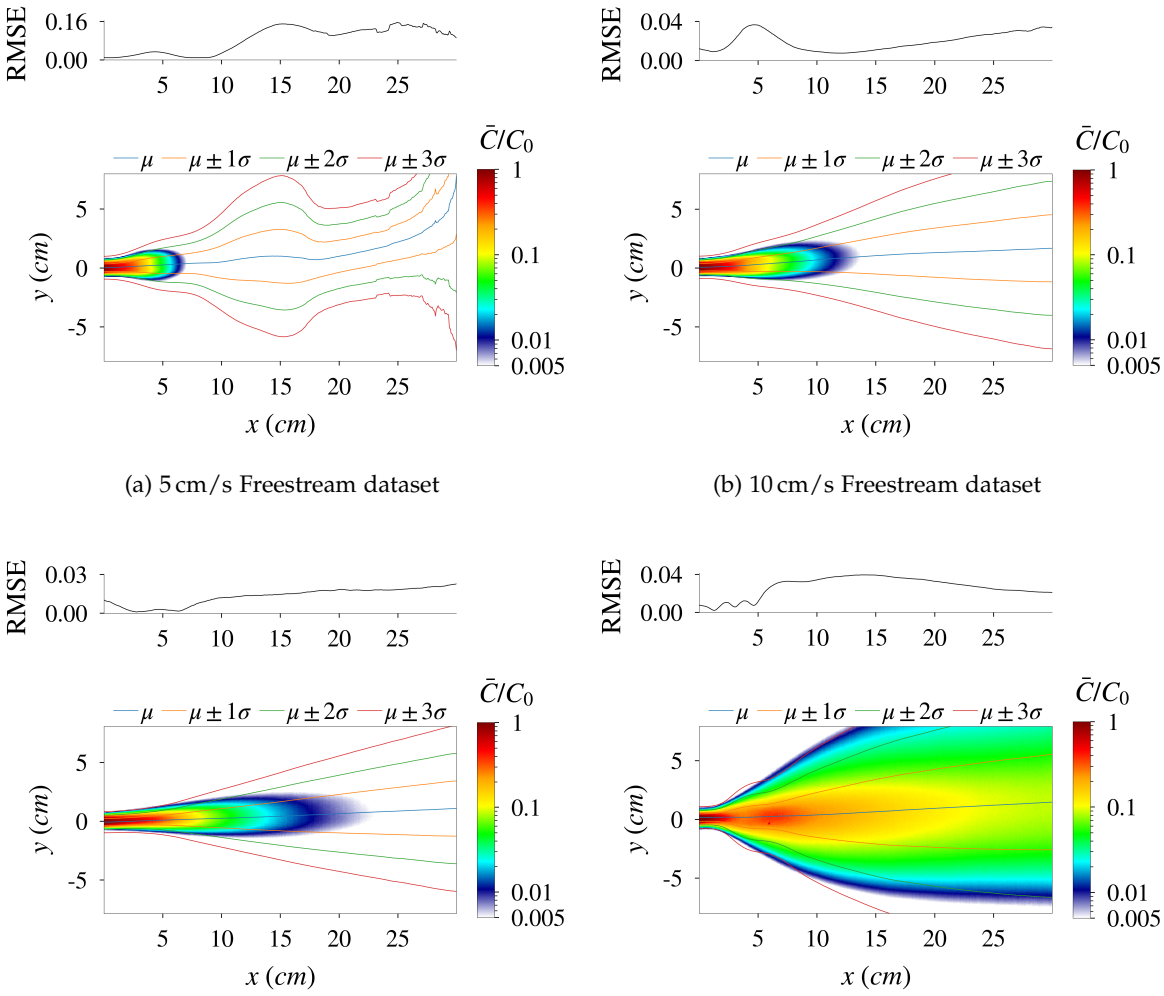

(a) 5 cm/s Freestream dataset

(b) 10 cm/s Freestream dataset

(c) 20 cm/s Freestream dataset

(d) 10 cm/s Near-bed dataset

Figure 3.3: Tracking the average plume using laterally fitted Gaussian kernels. For each of the four release configurations we plot the following; a top panel showing RMSE of the fitted Gaussian to the binned concentration, a bottom panel showing the average plume concentration over each trial and dataset with the mean and the mean with up to plus and minus three standard deviations of the Gaussian kernels.

for further exploration into the impact of downwind and crosswind distance on the plume statistics across the repeated trials.

3.6.3 *Bout Detection Algorithm*

The Bout detection algorithm (Schmuker, Bahr and Huerta, 2016) was originally designed to be a concentration invariant method of extracting information that enabled gas source distance prediction in turbulent plumes. This method could extract fast fluctuations in odour concentration that were considered difficult to capture using MOX-type sensors due to their slow recovery. A cascading filter approach enhanced fast transients before bout detection was applied. An initial bandpass filter cascade removed low and high frequency noise from the input signal. Trends from analysis of the Vergara et al. (2013) dataset showed that downwind distance was linearly encoded by average bout count, while a lateral displacement is encoded by the variance of the bout counts. Our aim was to determine whether these trends that were originally observed in a comparatively low spatial resolution and large wind tunnel dataset are also present in the PLIF recordings. We therefore applied the same bout detection method but modified the filter pipeline to be used with the PLIF data.

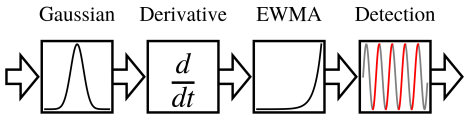

Figure 3.4: Signal processing pipeline from Schmuker, Bahr and Huerta (2016)

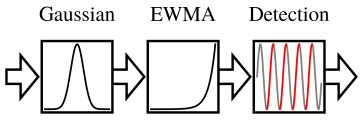

Figure 3.5: Our Signal processing pipeline

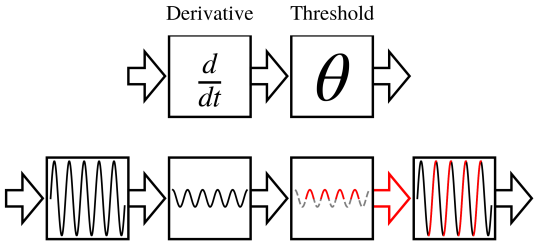

Figure 3.6: Bout analysis pipeline

Here, we use a method adapted from Schmuker, Bahr and Huerta (2016) that was previously applied to MOX-type sensor recordings and apply it to the PLIF data. Although the bout filtering pipeline shown in fig. 3.4 was originally conceived for removal of high frequency electrical noise and compensating for the slow recovery of the MOX sensors, not applicable for this PLIF data, it still serves as a tool for targeting a frequency band and removing noise. We expand on the analysis by exploring not only bout counts but other bout statistics. Figure 3.5 shows a schematic overview of our filter cascade. The data was first smoothed S_{smooth} by convolving it S with a Gaussian filter G with a selected standard deviation (σ_{smooth}) and rolling window of $M = 10 \cdot \sigma_{smooth}$, to remove high frequency noise.

$$S_{smooth} = S * G, \tag{3.4}$$

where the asterisk $*$ denotes a convolution and G was defined as

$$G(n) = \exp^{\left[-\frac{1}{2}(n/\sigma_{smooth})^2\right]}, \tag{3.5}$$

in which n is the sample index within the window, ranging from 0 to $M-1$, $M = 10 \cdot \sigma_{smooth}$ is the total window length in samples, and σ_{smooth} is the standard deviation of the Gaussian kernel in seconds.

For each time point x_t in the input signal S, the smoothed value y_t is calculated as a weighted average of the data points within the current rolling window. The weights Wk generated by **scipy.signal.windows.gaussian** and defined by eq. (3.5) are applied to the data points such that the peak of the Gaussian aligns with the approximate centre of the backward-looking window slice. Specifically, for a window ending at time t and covering data points $x_{t-M+1}, \ldots, x_t$, the weight Wk is applied to the data point $x_{t-M+1+k}$.

Therefore, the smoothed value y_t at time t is defined as:

$$y_t = \frac{\sum_{k=0}^{M-1} W_k \cdot x_{t-M+1+k}}{\sum_{k=0}^{M-1} W_k} \tag{3.6}$$

where:

- $\mathbf{y}_t$ is the smoothed output value at time t.
- $x_{t-M+1+k}$ is the data point from the original signal at index $t - M + 1 + k$.
- The denominator $\sum_{k=0}^{M-1} W_k$ is the sum of the Gaussian weights, which ensures that the output is a true weighted average.

Our method shown in fig. 3.5 diverges from Schmuker, Bahr and Huerta (2016) who then formed the derivative of the filtered signal using the **numpy.diff** function,

$$x_t = S_t - S_{t-1}, \tag{3.7}$$

and applied a leaky integration of the derivative using an exponentially weighted moving average (EWMA) using **pandas.Series.ewm** with a selected halflife (τ_{half}).

$$\begin{aligned} y_0 &= x_0 \\ y_t &= (1-\alpha) \cdot y_{t-1} + \alpha x_t, \end{aligned} \tag{3.8}$$

$$\alpha = 1 - exp^{(-ln(2)/\tau_{half})}, \text{ for } \tau_{half} > 0, \tag{3.9}$$

Their filter cascade that produced the filtered signal S'_{filt} that can be expressed as

$$S'_{filt} = S * G * D * E. \tag{3.10}$$

in which the signal S is convolved $*$ by three kernels: A Gaussian kernel G of width σ_{smooth}, a differentiating kernel D of the form $[1, -1]$ and an exponential kernel E with a halflife τ_{half}.

We forgo the derivative and our filtered signal can be expressed as

$$S_{filt} = S * G * E. \tag{3.11}$$

This means our filtered and normalized concentration remains as units of C/C_0 as opposed to C'/C_0.

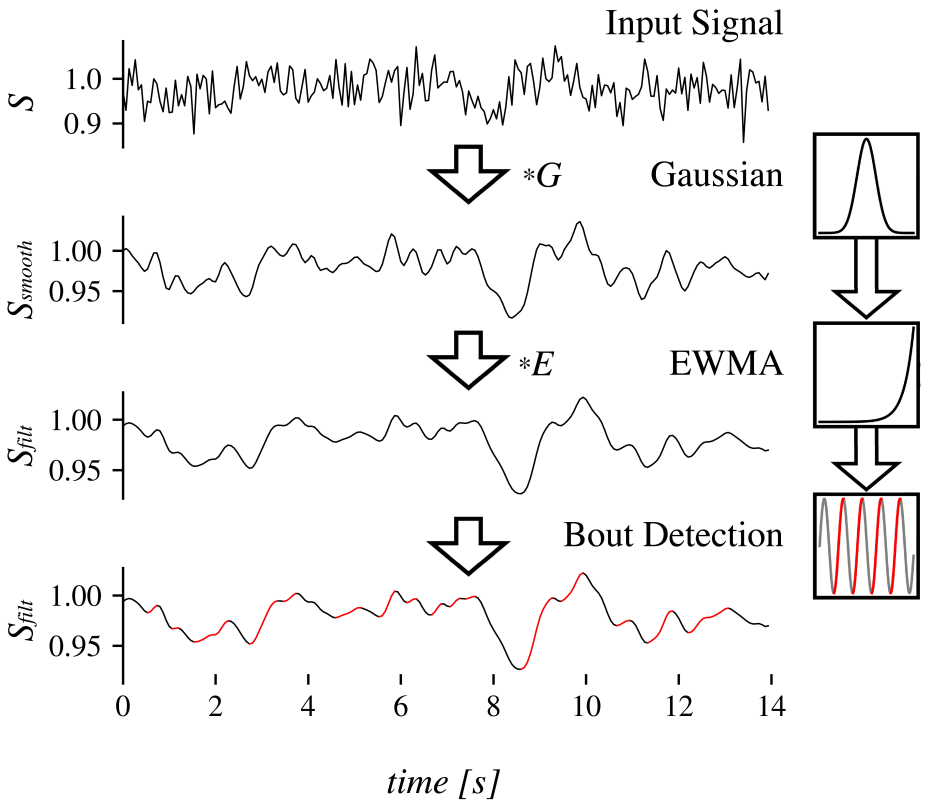

Figure 3.7: Our filtering pipeline with demonstrative signals.

Figure 3.7 demonstrates our filtering pipeline with a demonstrative signal. We show the input signal S that first undergoes Gaussian smoothing to become S_{smooth}, then an EWMA to become S_{filt} and finally bout detection to extract the amplitude gated rising portions of the signal.

For bout detection, we applied the same analysis pipeline as Schmuker, Bahr and Huerta (2016) to the filtered signal shown in fig. 3.6. As shown, we apply a derivative of the filtered signal with **numpy.diff**,

$$y'_t = y_t - y_{t-1}, \tag{3.12}$$

and then extract the times of the portion of signal above a selected amplitude threshold (θ).

$$\begin{aligned} b_t &= 1 \quad \text{if } y'_t > \theta \\ b_t &= 0 \quad \text{otherwise.} \end{aligned} \tag{3.13}$$

This period above the amplitude threshold represents the rising flank of the filtered signal. Schmuker, Bahr and Huerta (2016) defined this area as a *Bout*.

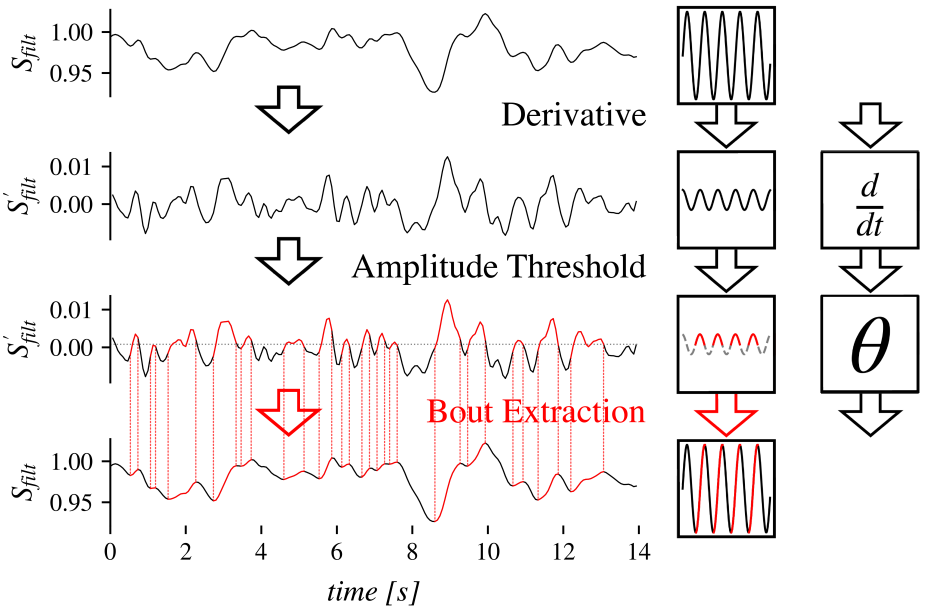

Figure 3.8: The bout detection analysis pipeline with demonstrative signals.

Figure 3.8 demonstrates the bout detection analysis pipeline using a demonstrative signal. The top panel shows the filtered input signal S_{filt}, the derivative of this signal is extracted S'_{filt}, and from this the timing of the portions that exceed a selected amplitude threshold θ is extracted and applied back to the input signal.

Figure 3.9 shows the key statistics that we calculated from the extracted bouts. Firstly, we analysed the count or number of bouts during a sampling period. Each trial consisted of a single 240*s* recording in which the plume was fully established before the recording began; the plume had reached a steady-state structure across the full test section prior to capture. For all but appendix A.4, we used the full trial duration of 240*s* as the sampling period. The plume recording began when the plume had already been established and odour had already reached the end of the test section and so the time of a sample does not impact downwind concentration.

The bout amplitude (a_{bout}) is the difference between the maximum and minimum value of the filtered signal derivative within a bout:

$$a_{bout} = y_{t_2} - y_{t_1}, \tag{3.14}$$

Bout duration (T_{bout}) is the difference between the end and start times of a bout in seconds:

$$T_{bout} = t_2 - t_1, \tag{3.15}$$

The inter-bout interval (*ibi*) is the time between consecutive bouts, defined as the difference between the start time of a bout and the end time of the previous bout:

$$ibi = post_{t_1} - pre_{t_2} \tag{3.16}$$

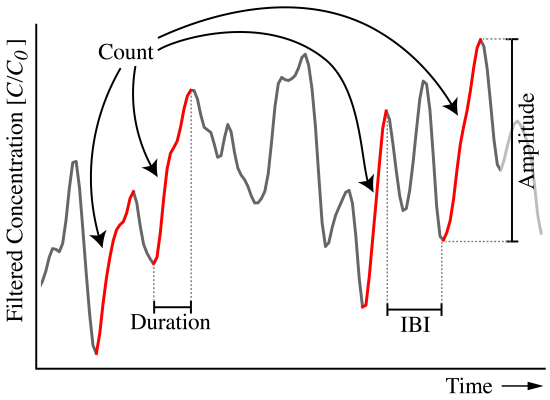

Figure 3.9: Bout statistics diagram demonstrating bout count, duration, amplitude and IBI on an demonstrative signal (grey). The example signal shows four extracted bouts (red) that are the rising portions that exceed an amplitude threshold. The second bout has the bout duration (time between the start and end of a bout) highlighted. The IBI (time between bouts) is demonstrated between the third and fourth bout, and the bout amplitude (difference between the maximum and minimum value of the bout) is highlighted on the fourth bout.

Figure 3.9 demonstrates each of these bout statistics on an example signal. We used each of the bout statistics to determine whether they provide information about a sampling position in relation to the odour source, either downwind or crosswind distance within the plume.

3.6.4 *Scaling the Amplitude Threshold*

To establish an amplitude threshold for the bout detection algorithm that remains comparable across varying filter parameters, we established a method of scaling the threshold. We used the noise floor value ($0.005C_0$) the smallest detectable unit of concentration by the camera previously calculated as five times the RMS noise floor of the PLIF system in the absence of acetone (Connor, McHugh and J. P. Crimaldi, 2018). In order to establish the new value of the amplitude threshold after the filter cascade, we create an instantaneous pulse of the noise floor value and apply the signal processing pipeline. The resulting maximum value provides our scaled filtered amplitude threshold. This value is dependent upon the filter values and is therefore calculated for each filter value explored.

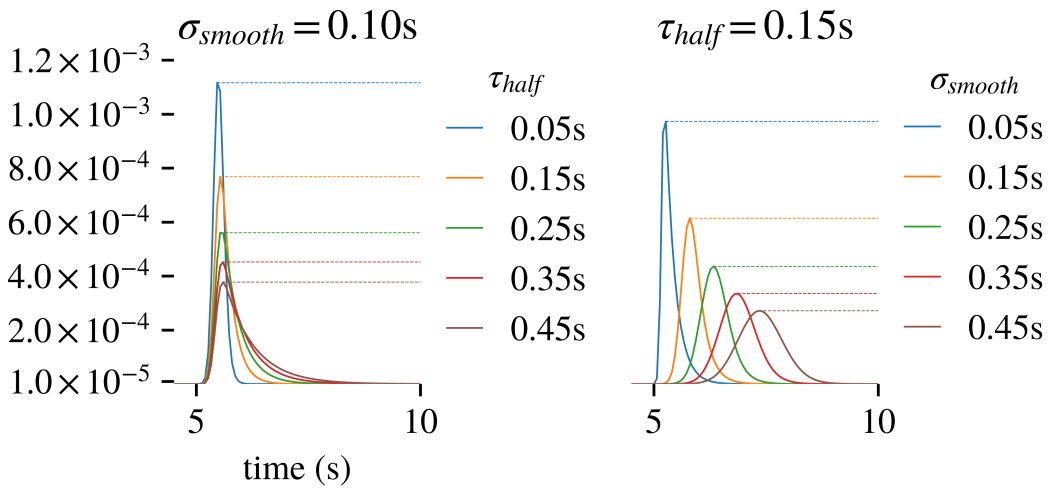

Figure 3.10: Amplitude Threshold Scaling using filtered impulse response. Left panel shows a filtered impulse with varying EWMA τ_{half} and fixed Gaussian filter σ_{smooth}, right panel with varying σ_{smooth} and fixed τ_{half}.

Figure 3.10 demonstrates the impulse response of selected filter parameters. The impulse occurred at 5s and the maximum value of the impulse response was taken as the amplitude threshold. The left panel shows a fixed σ_{smooth} of 0.10s and varying values of τ_{half}. We see that with increasing τ_{half} we decrease the magnitude of the impulse response. The right panel shows a τ_{half} of 0.15s and varying values of σ_{smooth}. Increasing σ_{smooth} not only reduces the magnitude but delays the impulse response. In appendix A.1.3 we explore the impact of the kernel parameters on the bout count curves along the centre line of the plume μ. We summarize the calculated amplitude thresholds values in table 3.1.

$\sigma_{smooth}(s)$	$\tau_{half}(s)$	calculated θ
0.10	0.05	0.001
	0.15	7.680×10^{-4}
	0.25	5.610×10^{-4}
	0.35	4.520×10^{-4}
	0.45	3.770×10^{-4}
0.05	0.15	9.730×10^{-4}
0.15		6.140×10^{-4}
0.25		4.350×10^{-4}
0.35		3.350×10^{-4}
0.45		2.710×10^{-4}

Table 3.1: Calculated Amplitude Threshold. Grey box shows used threshold unless stated otherwise.

3.7 RESULTS

3.7.1 *Downwind Distance*

3.7.1.1 *Impact of downwind distance on bout statistics*

With the plume centre line (μ) established for the four release configurations, we explored the impact that downwind distance from the odour source (x) has on bout statistics. The fluctuations in concentration in the transported odorant change in amplitude, duration and frequency as the plume travels further downwind. The statistics of the extracted bouts, periods of increasing concentration above a threshold (see section 3.6.3), also change with distance from the odour source. Here we highlight not only the differences in the bout statistical curves brought about by downwind distance from the odour source, but also compare the impact of the odour release configuration on the calculated statistic. The centre line is an approximation established from the spatially averaged concentration across trials, and so these figures should be considered alongside the plume tracking figures in section 3.6.2.

In fig. 3.11, we calculate the four bout statistics for each pixel along the approximated plume centre line (μ) over the entire length of the trial and for each of the odour release configurations. The plotted count represents the number of bouts encountered during the length of the trial. For each bout, we record: the duration (the time between the start and end of the bout); the amplitude of the bout (the difference between the end and the start of the bout in the derivative of the filtered concentration); and the inter-bout interval or IBI (the time between the end of one bout and the start of the next). Each trial has only one bout count value for its duration, but the duration, amplitude and IBI have different values for each bout, and we therefore plot the mean for each trial in grey and the average across trials in black. We expect the different statistics to express different relationships with downwind distance, that is, IBI decreasing with increasing duration. We also expect to see artefacts where statistics artificially increase cross-trial variance where bout counts are low. Where bouts occur, these statistics could potentially be used to improve the accuracy of odour source distance prediction.

In fig. 3.11, we see that for all odour release configurations, the mean bout amplitude initially increases and then decreases with downwind distance ($x(cm)$) along the plume centre line. Where these bout amplitudes peak, they highlight a transition from linear to turbulent flow of the odorant in the wind tunnel – the source effect. It should be noted that we see an increase in the downwind distance between the odour source and this flow transition point (FTP) with increasing wind speed in the freestream datasets, shown by the vertical dotted grey line: the FTP occurs at $x \approx 3.3\,cm$ for the $5\,cm/s$ dataset, $x \approx 4.3\,cm$ for the $10\,cm/s$ dataset, and $x \approx 7.0\,cm$ for the $20\,cm/s$ dataset. Before this FTP, all freestream datasets show a strong negative correlation of bout count and a positive correlation of mean duration with downwind distance. This means that in the linear flow area, bout counts

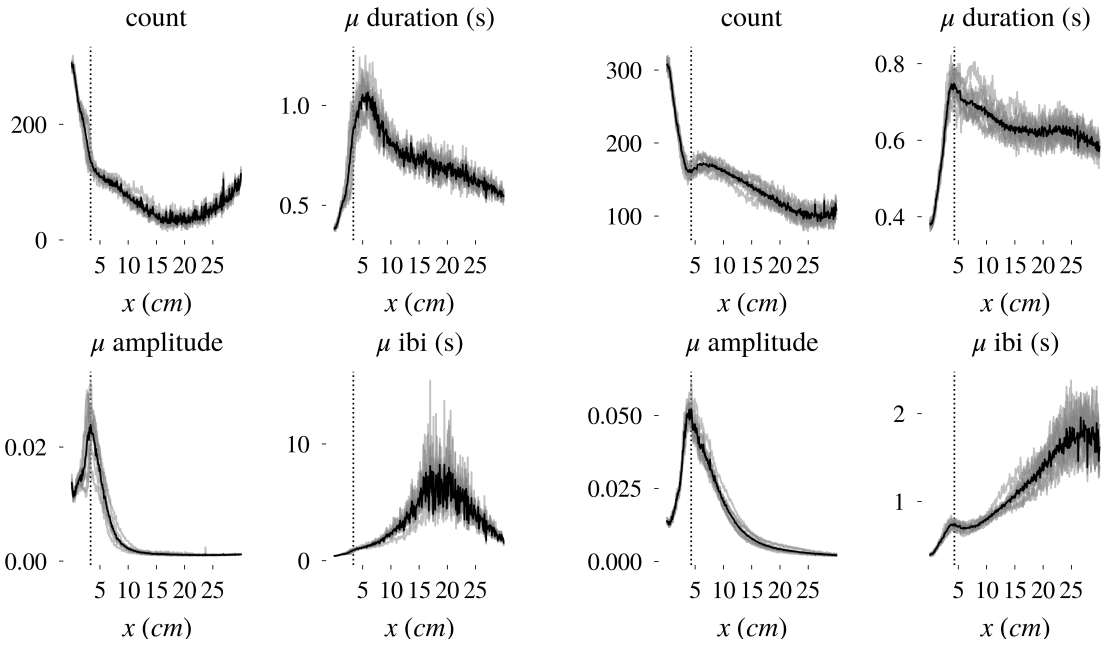

(a) 5 cm/s Freestream dataset

(b) 10 cm/s Freestream dataset

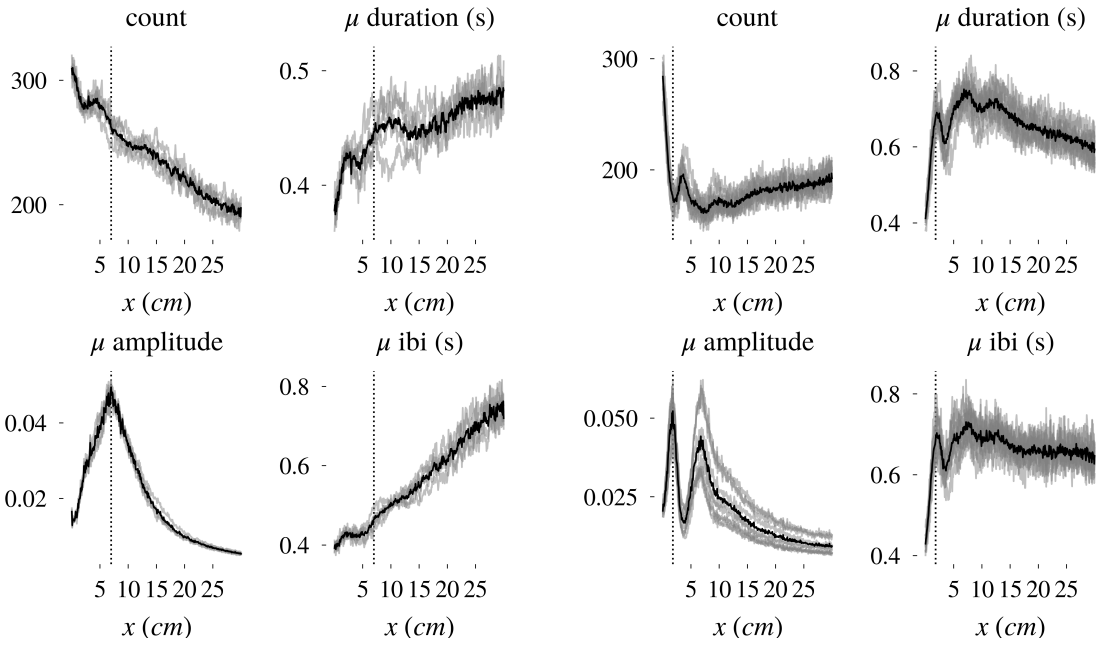

(c) 20 cm/s Freestream dataset

(d) 10 cm/s Near-bed dataset

Figure 3.11: Statistics of bouts against downwind distance (x, in cm) along the plume centre line (μ). Top left panel shows bout count per 240s trial; top right shows mean bout duration (s); bottom left shows mean bout amplitude (C/C_0); bottom right shows mean inter-bout interval (IBI, s). For each statistic, individual trials are shown in grey with the trial mean shown in black. The vertical dotted grey line marks the flow transition point (FTP), approximated as the downwind position of the maximum trial-mean bout amplitude.

decrease, but the duration increases as we move further from the source. The $10cm/s$ near-bed release dataset shows two initial peaks in amplitude, potentially caused by a standing wave due to proximity to the false floor and extending the source effect. This FTP can be considered an artefact of the experimental design and these peaks in bout amplitude can be used to highlight the distance at which this occurs. As bout analysis has primarily been used for odour source localization in odour plumes in turbulent flow regimes, we consider the linear flow area less important in our analysis and focus on the statistics after this FTP. After the FTP, where the plume is in a more turbulent regime, we see that all freestream release datasets show a non-linear decrease in bout count and an increase in inter-bout intervals where bouts occurred. Conversely, the near-bed dataset showed an increase in bout counts and a decrease in IBI, with increasing x after the flow transition.

In the $5cm/s$ freestream dataset, if we focus on the area where bouts occur in the fig. 3.11a and after the FTP i.e. $4cm < x < 17.5cm$, we see bout count decreased non-linearly from ≈ 120, initially slowly and then quickly after $7cm$ to zero bouts. We also see that bout counts increase after $17.5cm$ but these are low amplitude low duration bouts with high IBI. We see average durations increase up to $\approx 1s$ just beyond the FTP and then decrease, with trial variance the greatest at the peak. The amplitudes non-linearly decrease with x and IBIs increase to a peak at $17.5cm$ and then decrease beyond. This small area of the plume shows a diversity in the statistics of the bouts in which we have a transition between two areas: an area closer to the source in which we have a consistently larger number of longer bouts to an area that declines quickly in the number of bouts with shorter durations. Throughout this transition, we see bout amplitudes steadily decline. We see high IBIs with decreasing bout duration at downwind distances greater than $17.5cm$. This is potentially caused by infrequent transients evidenced by the medium duration, low amplitude bouts producing longer inter-bout intervals.

Looking to the $10cm/s$ freestream dataset, fig. 3.11b shows similar relationships of the statistics with downwind distance (x), but over a larger area i.e. between $\approx 5cm$ to $25cm$. Bout counts decrease non-linearly from ≈ 190 down to ≈ 100, with a slight increase just beyond the FTP and a levelling out beyond $20cm$. Average bout duration initially decreases from $0.75s$ to $0.65s$ at $15cm$ and slowly increases before decreasing again at $25cm$ – trial variance appears high throughout. The average amplitude appears to exponentially decrease from 0.05 to ≈ 0 throughout. The IBI non-linearly increases from $1s$ to $2s$ and appears to be inversely proportional to bout count, but with an increase in trial variance with downwind distance. Again, we see multiple areas in which the bout statistics highlight the same structures of fluctuations in the concentration along the centre line of the plume. We appear to be seeing a compressed version of the $5cm/s$ statistical relationships, caused by increasing wind speed. We move from an area in which bout counts and average bout duration slowly decrease, along with bout amplitude to an area in which the bout amplitudes are very low, the counts level off along with the durations and the IBI significantly increases. The

trial variance appears to remain low for all statistics where bouts occur and increase at the downwind extent of the wind tunnel and plume.

The $20cm/s$ freestream dataset in fig. 3.11c shows the same compression of these statistical relationships. We appear to capture only the initial decrease in bout count in which counts decrease linearly with increasing x throughout. We see only an initial increase of average bout durations before they level off. The average amplitude exponentially decreases after the initial peak and IBIs linearly increase with x. We can clearly see the increase in IBI with distance without the skewing introduced by low amplitude bout, as we do not see bout counts drop below ≈ 180 – therefore the trial variance remains low for all statistics.

The 10cm/s near-bed dataset in fig. 3.11d shows very different relationships between the bout statistics and downwind distance x. Most notably, the bout counts increase rather than decrease and remain high with ≈ 180 bouts at its lowest point. The counts still decrease after the transition point, but they then increase until the downwind extent of the wind tunnel. After the second peak in the bout amplitudes, we do still see an exponential decrease in the average amplitudes, with one trial showing a second peak in amplitude equivalent to the first. Another strange phenomenon is that the IBIs appear to match the duration, initially increasing up to $\approx 0.65s$ and $\approx 0.75s$, respectively. This means that the frequency of fluctuations in the concentration increase with distance from the source and therefore an increase in count. We can infer that the introduction of the false floor allows for fluctuations in the concentration to travel over a much greater distance with the same wind speed, without seeing as much of a decrease in the amplitudes.

Overall, fig. 3.11 provides useful insight into the impact of the release configurations and downwind distance on bout statistics along the average centre line of the plume. Each statistic is independently affected by the propagation of the odorant throughout the wind tunnel and the dynamic structure of the plume. This suggests that it might be possible to use a combination of the statistics to determine not only the distance from the odour source, but the release configuration of the odour.

3.7.1.2 *Predicting downwind distance from bout count*

In the previous section we explored the impact of the downwind distance and the odour release configuration on bout statistics along the average plume centre line (μ), and we established that the other bout statistics are correlated with bout count. Here we explore the feasibility of odour source proximity prediction from the statistics of the bouts that occurred along the approximated centre line of the plume (μ). In the freestream datasets, the bout count distance curves appear to follow the same non-linear decreasing relationship, with wind speed extending the bout count curve further downwind from the FTP.

For every release configuration and for every pixel along the approximated centre line of the plume (μ), we plot the bout count per trial and the average bout count over trials (right panel fig. 3.12). To determine whether odour source distance can be predicted from bout count alone, we fit inverse sigmoid curves to the trial average bout count along the centre

line of the plume. For the three freestream datasets, we fit an inverse sigmoid curve to the trial mean values of bout counts between the FTP and either the point at which trial average bout counts reached a minima before increasing ($5cm/s$ and $10cm/s$ freestream datasets) or to the extent of x, simply omitting the linear portion of the plume. To highlight the impact of distance on the fluctuations in odour concentration, we select five sample points within the fitting area and plot a $50s$ segment of the filtered signal from the first trial of each dataset (black line) and we highlight the extracted bouts (Figure 3.12 left panel red line).

The parametric inverse sigmoid function we used to fit the bout count distance curves can either be expressed as a function of the bout count (r), eq. (3.17), or as a function of downwind distance (x) in cm as in eq. (3.18).

$$r(x) = \frac{r_{max} - r_{min}}{1 + e^{k(x - x_0)}} + r_{min}. \tag{3.17}$$

$$x(r) = \frac{ln(\frac{r_{max} - r}{r - r_{min}})}{k} + x_0. \tag{3.18}$$

Where r_{max} defines the maximum bout count or extent of the curve on $y(cm)$, k is the slope of the curve. r_{min} is the minimum observed bout count. x_0 is the horizontal offset of the mid-point of the curve on x defined in cm. In table 3.2, we outline the values for each freestream configuration curve. We fit the inverse sigmoid function (eq. (3.17)) to the turbulent flow area of average bout count curves using **curve_fit** from the **scipy.optimize** package. An initial guess was used to aid the fitting of the curves. For r_{max} and r_{min}, we used the maximum and minimum observed bout counts, respectively. We used a value of 0.015 for an initial k and for x_0 we selected the pixel that had the bout count value closest to halfway point between the maximum and minimum values of the observed bout counts and used its x pixel value.

We plot the curves (Figure 3.12 right panel red dashed line) by regressing the curves for each pixel value downwind. To evaluate how well the fitted sigmoid could predict downwind distance from an observed bout count, we inverted the curve (eq. (3.18)) and computed the root-mean-square error (RMSE) of the predicted distance x_{pred} against the true pixel distances x_{ref}:

$$RMSE = \sqrt{\frac{1}{N}\sum_{i=1}^{N}\left(x_{pred,i} - x_{ref,i}\right)^2}. \tag{3.19}$$

This RMSE is therefore expressed in cm and quantifies the average error in predicting downwind position from bout count alone. The RMSE values of each fit are outlined in table 3.2.

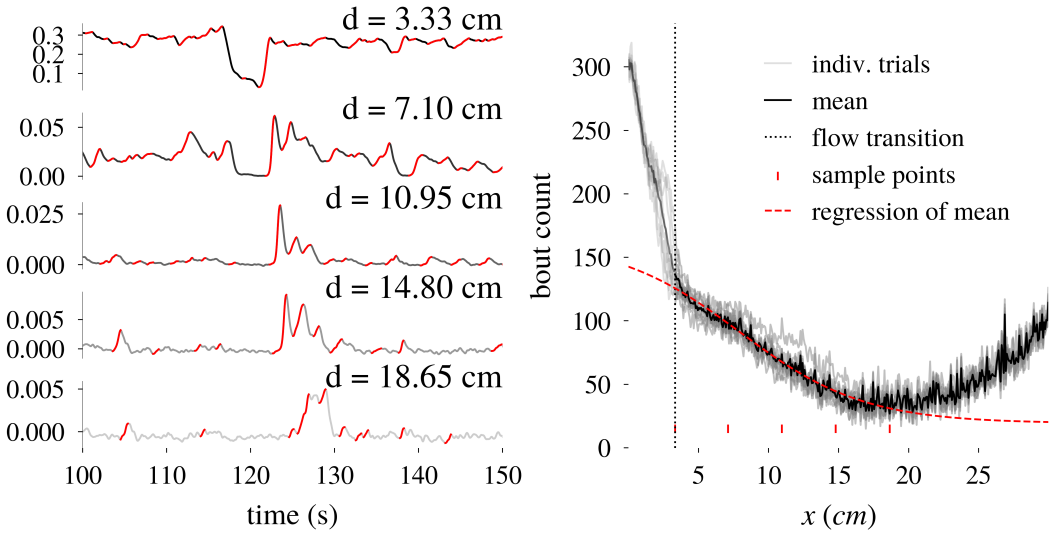

(a) 5 cm/s Freestream dataset

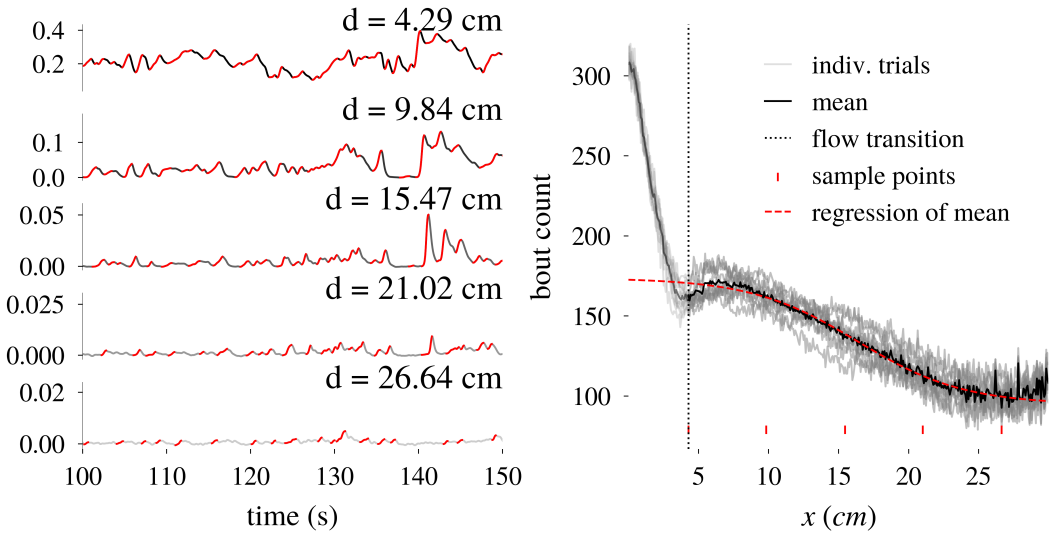

(b) 10 cm/s Freestream dataset

Figure 3.12: Bout count based distance prediction. **Left panel**: 50*s* segments of filtered odour concentration (C/C_0, y-axis) vs time (s, x-axis) at five sample distances from the first trial, with detected bouts highlighted in red; red points on right panel indicate the corresponding sample distances. **Right panel**: bout count per 240*s* trial (y-axis) vs downwind distance x (cm, x-axis) for individual trials (grey) and trial mean (black). Vertical dotted grey line marks the FTP. Red dashed line (freestream only) shows the fitted inverse sigmoid curve.

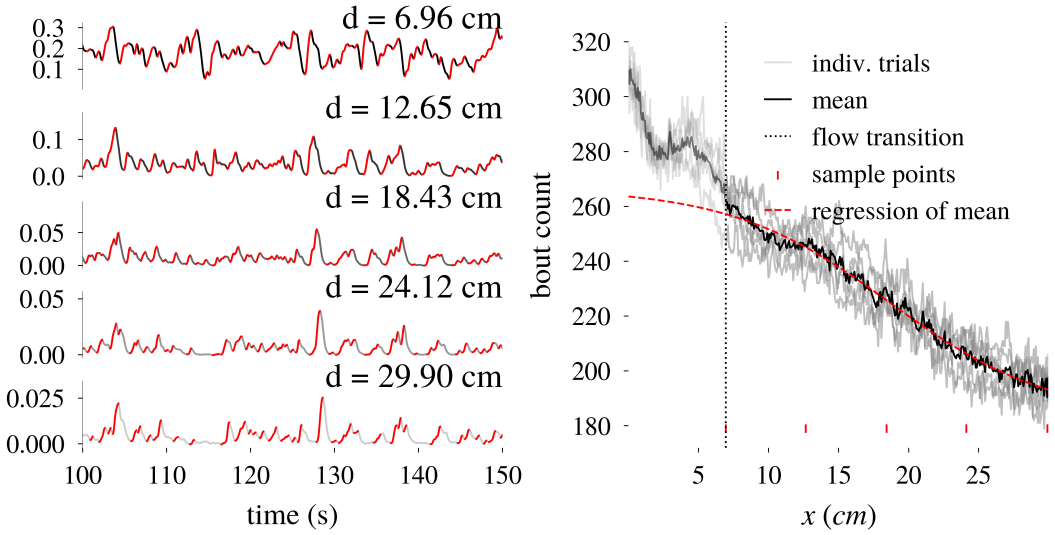

(c) 20 cm/s Freestream dataset

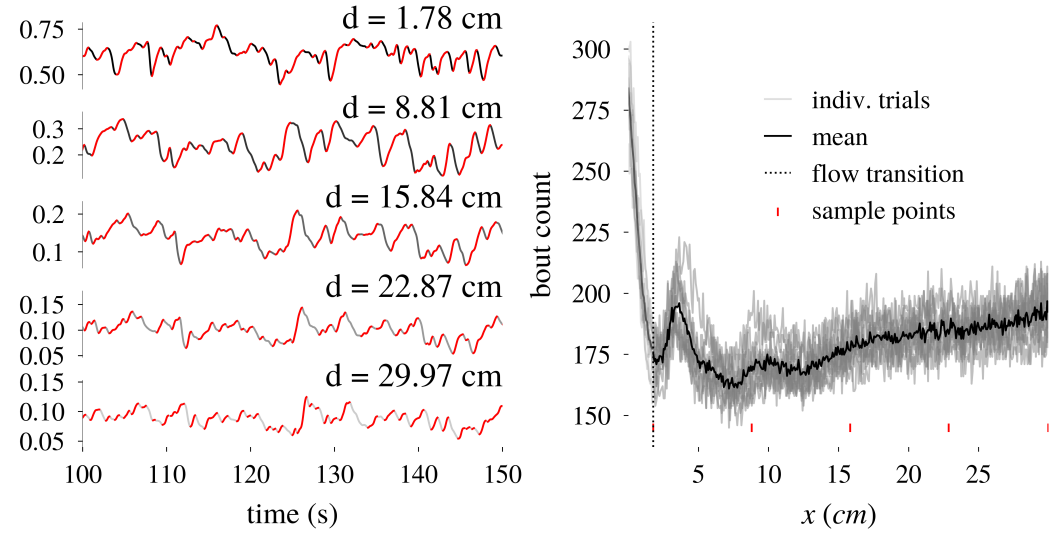

(d) 10 cm/s Near-bed dataset

Figure 3.12: Bout count based distance prediction (cont.). **Left panel**: 50*s* segments of filtered odour concentration (C/C_0, y-axis) vs time (s, x-axis) at five sample distances from the first trial, with detected bouts highlighted in red. **Right panel**: bout count per 240*s* trial (y-axis) vs downwind distance x (cm, x-axis); grey lines are individual trials, black line is the trial mean. Vertical dotted grey line marks the FTP. Red dashed line (freestream only) shows the fitted inverse sigmoid curve.

The sampled signal amplitude plots clearly show transients of the odorant concentration travelling downwind and decreasing in amplitude. In the 10 and 20cm/s datasets, where sample points are more closely aligned, we see a delay between transients decreasing with increasing wind speed. In the 5 and 10cm/s datasets, smaller fluctuations in concentration do not travel the full extent of the sampled area. However, the near-bed dataset shows that even small fluctuations in concentration travel the full extent of the sampled area – this is due to the plume's proximity with the floor.

Figure 3.12 shows that for freestream datasets bout count decreases non-linearly with distance from the odour source, whilst the near-bed dataset shows a small increase in bout count with distance after an initial decrease. For all datasets, we see bout amplitude (the peak concentration of each detected bout) decreasing with distance. Comparing across freestream datasets, we see that with increasing wind speed, the bout amplitude decreases less with distance from the odour source. The maximum trial mean bout count at the FTP is ≈ 130 in the 5cm/s dataset, ≈ 170 in the 10cm/s dataset and 260 in the 20cm/s dataset per 240s. We were able to successfully fit a sigmoid curve for all freestream datasets, and with increasing wind speeds, we see the horizontal extent of the sigmoid curve increases downwind, potentially due to increase trial variance but also because of a missing section of the curve beyond the captured test section for the 20cm/s freestream dataset.

Figure 3.12a of the 5cm/s freestream dataset data shows bout counts decrease to a minima at 18.65cm for all trials and has a maximum of ≈ 130 bout counts at the FTP. The relationship between bout counts and distance remains mostly constant across trials, with one outlier trial showing slightly higher bout counts in comparison. We sample five points between the FTP and the point at which bout counts were ≤ 18.65, which allows us to analyse the filtered signal where bouts with a significant amplitude were present. We see the maximum signal amplitude at the FTP drops from 0.3 down to $0.005\frac{C}{C_0}$ over this sampled region. This indicates that, at this wind speed, the plume is unable to carry the odorant over a long distance in any significant concentration, resulting in decreasing lower bout counts with distance. Beyond the minima the bout counts increase once more but as seen in fig. 3.12a become more intermittent and with very low amplitudes.

Figure 3.12b shows bouts of low amplitude even at the 26.64cm sample point, with the odorant concentration not falling below the calculated noise floor. The steepness of the sigmoid curve falls off at $\approx 20cm$ but the minima in bout counts is still ≈ 100.We see sampled odorant concentrations reach 0.4 at the FTP drop to a maximum of 0.05 at 15.47cm and then significantly drop further downwind. This is mirrored in the bout counts that follow the sigmoid curve with a relatively stable cross trial variance throughout the extent of the wind tunnel.

Figure 3.12c, the 20cm/s freestream dataset only appears to show the top of the fit sigmoid with the gradient not significantly decreasing before the downwind extent of the wind tunnel. This suggests that we can compensate for wind speed as we are looking at the same relationship with distance (we explore this further in section 3.7.4). We see similar

concentrations of odorant at the FTP as we did with both the 5 and 10cm/s datasets. However, the maximum odorant concentration at the extent of the wind tunnel 29.97cm still shows a maximum concentration of 0.025, equivalent to the 15.47cm sample point in the 10cm/s dataset and the 10.95cm sample point in the 5cm/s dataset. There is also a more linear decrease in the maximum odorant concentrations over the five sample points in this dataset.

Comparatively, fig. 3.12d the nearbed dataset shows higher filtered signal amplitudes throughout, with the maximum odorant concentrations of 0.75 and 0.1 at the FTP and extent of the wind tunnel, respectively. We also do not see the same sigmoidal non-linear decrease in bout count as shown within the freestream datasets within the extent of this plume. Taken together, this suggests that proximity to the viscous sublayer (VSL) reduces odorant diffusion. Our approximation of the FTP using the maximum bout amplitude peak may be erroneous due to the lack of turbulent flow within the extent of the plume. We see a consistent peak in bout count across trials at $\approx 4cm$ – this could align with the trough between the two amplitude peaks seen in fig. 3.11d and is an area of low amplitude, high bout frequency caused by a standing wave.

We chose a sigmoid curve because it provides a good approximation of the bout count over distance curve, but the ability to predict x position from the bout counts becomes impossible at the maxima and minima of the curve. The fit sigmoid curves and therefore the average bout count distance curves appear to mainly be influenced by the wind speed, with the slope of the curve shown in its entirety for 5cm/s and 10cm/s and only the initial portion of the curve for the 20cm/s dataset. We explore this further in section 3.8.

Release Config.	Wind Speed (cm/s)	r_{max}	r_{min}	slope k	x_0 (cm)	RMSE (cm)
Freestream	5	163.13	19.30	0.23	7.94	1.015
	10	173.68	94.76	0.26	16.35	1.670
	20	266.60	183.13	0.18	18.67	0.999

Table 3.2: Sigmoid Function Values

Table 3.2 shows the parameters of the sigmoid curves for each freestream release configuration. The maximum bouts (r_{max}) and minimum (r_{min}) bouts of the sigmoid curves increase with wind speed. With increasing wind speed, we see the slope of the curve (k) remain at ≈ 0.2 bouts per cm but the horizontal offset of the mid-point of the curve ($x0$) increase. This suggests that with increasing wind velocity, the odorant is carried further downwind and the frequency of concentration fluctuations decrease over a longer distance.

In section 3.7.1.3, we further explored how the bout statistics were not only impacted by downwind distance from the odour source, but also how all the statistics covary and whether the variance of the statistics measured along the centre line of the plume (μ) can purely be explained by the distance from the source.

3.7.1.3 *Visualising bout statistics along the mid-line of the plume with PCA*

In section 3.7.1.1, we demonstrated that the statistics of bouts that are measured along the approximated average plume mid-line (μ) show consistent change with their distance from the odour source in the freestream datasets. We previously explored the fitting of a sigmoid curve to the bout count downwind distance curves in section 3.7.1.2 and examined how the sigmoid curve could be used to predict the distance from the odour source. We also established in fitting the curves that there was a transition in the flow regime that varied in downwind distance with release configuration, and that a sigmoid curve could not be used in the near-bed release configuration to predict downwind distance.

In fig. 3.13, we visualize the trial average bout statistics along the centre line (μ) of the plume using principal component analysis (PCA). Before applying the PCA, we followed the same procedure conducted on the data before fitting in section 3.7.1.2. We removed all values upwind of the FTP (the initial peak in bout amplitude) and we retained all data beyond the FTP to either the bout count minima or the downwind extent. We plot the standardized data projected along PC1 and PC2 in a 2D plot colouring each pixel from each trial by its location along the mid-line of the plume between zero and 30cm downwind distance. The input data to the PCA did not include the pixel location and therefore any trends seen in the plotted data originated purely from the variance of the bout statistics. We also plot the covariance matrix to demonstrate how the bout statistics varied in relation to each other. The covariance matrix is recovered from the eigenvectors, the eigenvalues and the noise variances, and illustrates how pairs of each of the input features covary with one another on average. We plot the loading of the principal components in a contribution matrix to show the impact of the statistic on each of the four principal components. The loading highlights the explained variance that each statistical feature contributes to each of the eigenvectors or principal components. Finally, we plot a scree-plot that shows the sum of the explained variance or eigenvalue of each of the principal components. When looking at the two-dimensional dimensionally reduced and standardized statistics, it is important to consider the percentage of variance each principal component represents.

The covariance matrix in fig. 3.13 shows that for the most part in freestream datasets, the bout count, duration and amplitude all positively covary. This means that, where one statistic increases, there is an increase in the other on average. The magnitude of the bout duration covariance with bout counts lessens to zero with increasing wind speed, suggesting that this relationship is not robust to wind speed. IBI either has a negative or very low positive covariance with other statistics, most notably bout count, in which it is strongly negative regardless of wind speed. The near-bed dataset shows strongly negative covariance of bout counts with other statistics, with all other statistics strongly positively covarying. These relationships appear to be very dependent on the release configuration, however the near-bed dataset differs the most.

Figure 3.13a, shows the results of the PCA conducted on the bout statistics of each trial calculated along the centre line of the plume (μ) in the 5cm/s freestream dataset. The scree

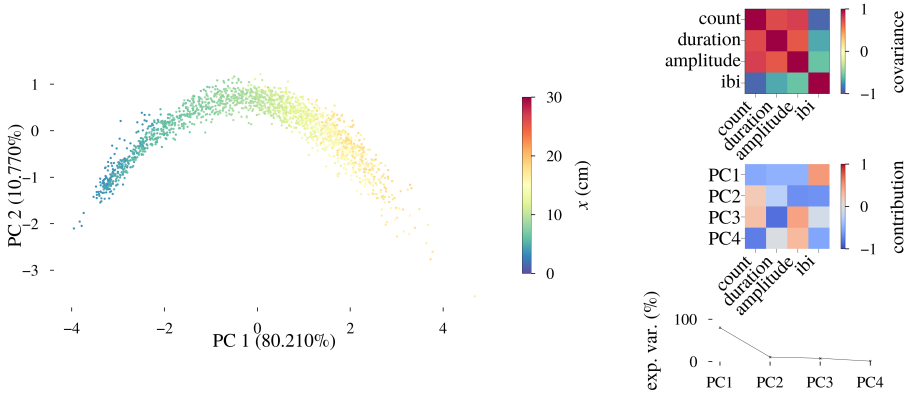

(a) 5 cm/s Freestream dataset

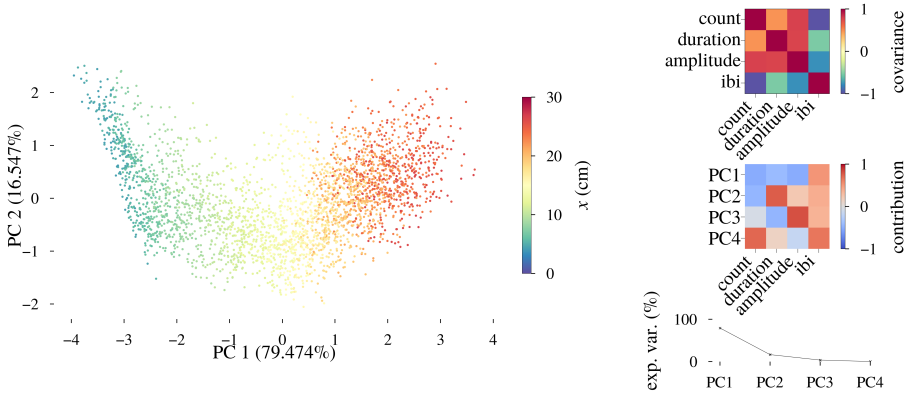

(b) 10 cm/s Freestream dataset

Figure 3.13: PCA of trial mean bout statistics on the average centre line of the plume. Left panel shows PC1 vs PC2 coloured by downwind distance. Right top shows covariance of input statistics, right middle shows explained variance contribution of each statistic to the principal components. Right bottom show a scree plot of explained variance percentage of each principal component.

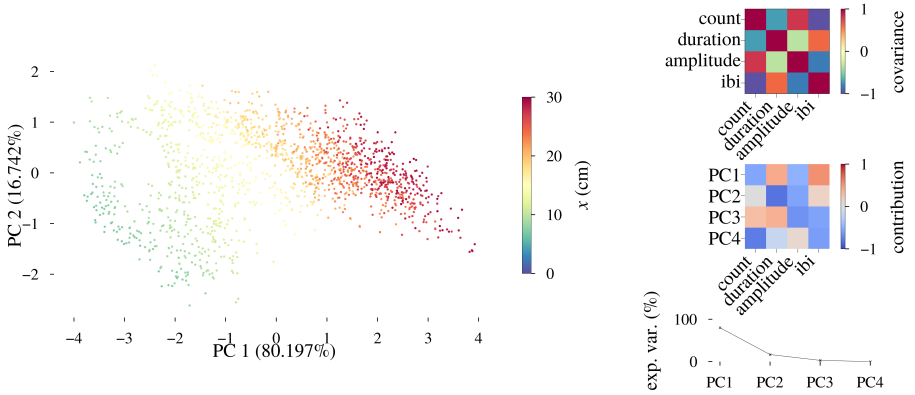

(c) 20 cm/s Freestream dataset

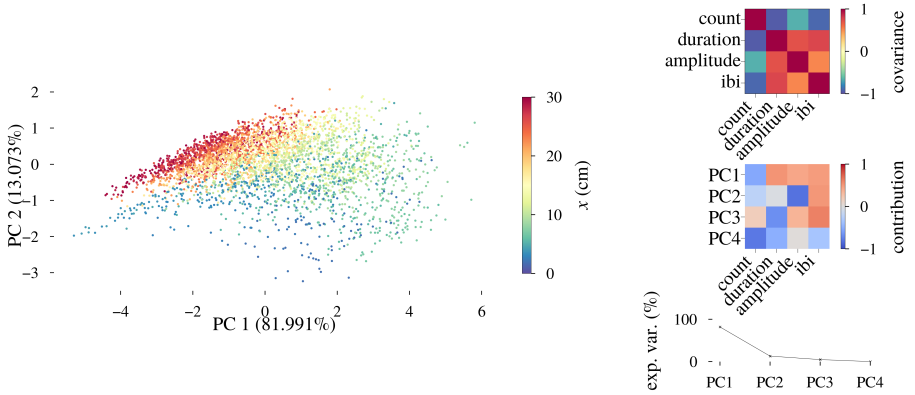

(d) 10 cm/s Near-bed dataset

Figure 3.13: PCA of trial mean bout statistics on the average centre line of the plume. Left panel shows PC1 vs PC2 coloured by downwind distance. Right top shows covariance of input statistics, right middle shows explained variance contribution of each statistic to the principal components. Right bottom show a scree plot of explained variance percentage of each principal component (cont.).

plot shows that the first two principal components represent 91% of the explained variance with the PC1 and PC2 representing 80.21% and 10.77%, respectively. One can see a relatively equal loading of each of the four bout statistics for the first principal component, with bout count showing the greatest absolute loading -0.54 and IBI having the second greatest loading of 0.50. The second principal component, equivalent to roughly an eighth of the explained variance of the first, shows amplitude having the greatest absolute contribution of -0.68 followed by IBI of -0.66 and duration of -0.24. It should be noted that the overall orientation of a principal component is sign-arbitrary: multiplying all loadings of a given PC by -1 yields an equally valid solution, so the absolute direction of a PC axis carries no intrinsic meaning. Therefore, the absolute value of each loading describes its contribution magnitude to the component. The signs of loadings are meaningful only relative to each other *within the same PC*: features with the same sign vary together along that axis, while features with opposite signs vary in opposite directions. In the $5cm/s$ freestream dataset, for example, count, duration and amplitude share the same sign in PC1 (all negative) whilst IBI has the opposite sign (positive), indicating that IBI varies in the opposite direction to the other three statistics along PC1. The second principal component shows amplitude and IBI both with the largest absolute contributions, opposite in sign to bout count, indicating these pairs vary in opposite directions along PC2. The covariances of the features describe the average relationships that exist within the bout statistics of this dataset. We see that IBIs negatively covary with all other statistics, most strongly with bout count and secondly with bout duration and finally with amplitude. This suggests that on average, where bout counts are high, we see longer and greater amplitude bouts and shorter IBIs. All other statistics positively covary with each other on average, the greatest being amplitude and count and secondly duration and count.

Plotting the standardized statistics principal component space, we see these four-dimensional data reduce to two-dimensions – along with being dimensionally reduced, the data is also aligned with its two-dimensions of greatest variance. In fig. 3.13 left panel, we plot the two-dimensional projection, colouring each projected bout statistic data point by its downwind distance from the odour source ($x(cm)$). With this colouring, we see data points that represent distance values between the FTP at $x = 3.3cm$ in blue, to the point at which bout counts fall below reach a minima at $x = 18.7cm$. Even within this small area of the overall wind tunnel, we see enough statistical variance along the plume centre line that we see an alignment of downwind distance with increasing PC1. With the significant loading of both amplitude and IBI in PC2, one can speculate that these two bout statistics are most likely encoded by PC2.

The results of a PCA conducted on the trial average bout statistics along the centre line of the plume for each trial in the $10cm/s$ freestream dataset are shown in fig. 3.13b. The first two principal components represent 79.47% and 16.55% of the explained variance, respectively, with a total of 96.02%. Bout count, amplitude and IBI share equal contribution to the loading of PC1 with both count and amplitude having a negative loading of -0.52

and IBI having the only positive loading of 0.52. This is also reflected in the covariance of the bout statistics, with the IBI showing a clear negative covariance with the bout count, amplitude and duration, with standardized covariance values of -0.98, -0.54 and -0.77, respectively. This covariance relationship is clearly aligned with the axes of greatest variance in this dataset. However, the bout duration shows the strongest contribution to the PC2 with a value of 0.76, suggesting a strong positive correlation to the axis with the second most variance in the dataset, orthogonal to the first principal component. Bout count shows a negative correlation with PC2, with a value of -0.46, whilst IBI shows a positive correlation with a value of 0.40, and bout amplitude shows a mild positive correlation, with a value of 0.23. This could be explained by the relatively low covariance of bout duration with bout count (0.48) and lower covariance with IBI (-0.54), along with a high positive covariance with bout amplitude at 0.77. This suggests that in the $10cm/s$ freestream dataset, bout durations tend to be longer, with higher amplitudes and only mildly impacted by bout counts and slightly impacting IBIs. We see that PC1 encodes downwind distance from the odour source well. The downwind distances increase from $4.3cm$ to $26.6cm$, parallel to the PC1 axis, showing clear alignment. PC2 most probably encodes variation in bout duration, with a decrease in the variance of the duration of bouts occurring between $10cm$ and $20cm$, shown here as a valley narrowing in relation to PC2.

For the $20cm/s$ freestream dataset shown in fig. 3.13c, the PCA results show slightly less variance explained by the first principal component and more by the second principal component than in either of the lower wind speed freestream datasets. We still see $\approx 97\%$ of the explained variance represented by the first two principal components, but PC1 explains 80.2% and PC2 explains 16.74%. The trend we see is that with increasing wind speed, explained variance remains at around 80% for PC1 but increases for PC2. The trend for bout duration being the main feature contributing to the loadings of PC2 continues with a magnitude of -0.82 and a value of only 0.41 in PC1. PC1 also sees bout count showing an inverse loading to IBI, with values of -0.55 and 0.54, respectively. Bout counts and IBI both have the greatest contribution to PC1, followed by bout amplitude with a value of -0.48. PC2 shows a greater absolute contribution of bout amplitude with -0.56 and a lesser contribution of the remaining features ordered by absolute contribution – with IBI and bout count having loadings of 0.13 and 0.01. These relationships can be somewhat explained by the covariance of the features. Again, we see a negative covariance of counts and IBI, with an almost perfect covariance of the standardized features of -0.99. This means that, in this dataset, observed IBIs almost always decreased with increasing bout counts. Here we see bout counts and durations negatively covary with a magnitude of -0.72, unlike in the $5cm/s$ and $10cm/s$ freestream datasets, with values of 0.74 and 0.48, respectively. This means that on average bout durations decreased where bout counts were higher. This could be due to the limited section of the sigmoidal curve of bout counts expressed in this dataset. Due to the higher wind speed, we never see the bout counts minima, seen in both the $5cm/s$ and $10cm/s$ freestream datasets, and therefore do not see the trends that exist in latter parts

of the odour plume. This suggests that closer to the odour source bout durations tend to increase with decreasing bout count – also illustrated in fig. 3.12c. Bout amplitude and bout duration also negatively covary. The bout statistics are clearly significantly impacted by the wind speed. What is important to consider though, is that with increasing wind speed the plume is carried further downwind, and so we are only seeing part of the downwind extent of the centre line of the plume compared to what we see in the two lower wind speed freestream datasets. However, we do still see a good encoding of downwind distance in the variance of these statistics, with a clear alignment and positive correlation between PC1 and $x(cm)$. Based on the shown feature loadings, one can assume that the variance seen in the axis of PC2 can be attributed to the bout duration, with a strong negative correlation and a narrowing or decrease in variance of bout durations between $10cm$ and $20cm$.

Each of the freestream datasets demonstrates a strong encoding of downwind distance by PC1, suggesting the downwind distance is the strongest source of bout statistical variance along the mid-line of these plumes. They each showed a strong negative covariance between bout counts and IBI, with a decreasing covariance between bout duration and bout count or amplitude with increasing wind speed. This could be purely attributed to the wind speed's impact on the odour concentration fluctuations present along the mid-line of the plume, or to the side effects of seeing a different part of the plume.

The PCA results shown in fig. 3.13d, shows strikingly different trends in the bout statistics of the near-bed than those present in the freestream datasets. PC1 represents 81.99% of the explained variance, whilst PC2 is only 13.07%, with a cumulative explained variance of 95.06% in the first two principal components. Similarly to the freestream datasets, we see relatively equal loading of the bout statistics in PC1, with bout counts as either equal to or the greatest absolute contribution. However, a key difference to the freestream datasets is that the sign of the bout count contribution to the loading of PC1 opposes all other statistics. This is reflected in and can be attributed to the strongly negative covariance of bout counts with bout duration, IBI and bout amplitude, with decreasing absolute standardized values of -0.95, -0.91 and -0.66, respectively. Another observation is that duration shows a loading of 0.53, whereas in the freestream dataset the bout duration was attributed the least contribution of all the bout statistics to PC1. Both bout amplitude and bout duration positively covary with IBI, with values of 0.52 and 0.76. In the near-bed dataset, the statistic with the greatest absolute contribution to PC2 is amplitude, with a value of -0.83. These differences to the freestream dataset PCA results also most likely explain why the near-bed dataset shows the worst alignment of PC1 with downwind distance from the odour source. However, we do see a consistent decrease in source distance when increasing PC1 and decreasing PC2, with bout statistics from $30cm$ occurring at low values of PC1 and high PC2. Statistics from very low values of $x(cm)$ appear to sparsely span both PC1 and PC2 space, whilst values $x > 10cm$ appear more compact where PC2 > -1 and negatively correlated with PC1. This could be an artefact of poor approximation of the FTP for this dataset. Proximity to the false floor caused greater lateral spread of the plume and carried it much farther than the plume in the

$10cm/s$ dataset – this also reduced the overall variance of each of the bout statistics present within this plume. This meant that the downwind distance from the odour source was likely not the greatest contributor of variance within this dataset, unlike in the freestream datasets.

PC1 is always the component with the greatest explained variance, and for all datasets the explained variance of PC1 is consistently $> 79\%$. For all freestream datasets, bout count and amplitude all show a negative correlation with PC1, and IBI has a positive correlation. However, the sign of the contribution only describes the feature's correlation with the PC and the magnitude of the contribution provides the most information. The bout count was always either tied with or was the greatest contributing feature to PC1 across the release configurations. Bout count and the IBI also always shared inverse loading and a consistently negative covariance. PC2 is the eigenvector with the second-most explained variance, and for the freestream datasets shows contribution of the bout statistics becoming less consistent. No two release configurations showed similar statistical contributions to PC2. However for the freestream datasets, durations showed the greatest absolute contribution to PC2. The magnitude of the contribution is the important takeaway, whilst the sign of the loading should only be considered relative to the contribution of the other features to the same principal component; the overall sign orientation is arbitrary and can flip depending on the orientation of the PC vector. The approximately equal absolute loading of the four statistical features for PC1 in all datasets suggests that they each have a large impact on the majority of the variance. We list all calculated values of each of the release configuration datasets for the explained variances, covariances and contributions in table A.1, table A.2, and table A.3, respectively.

Up until this point, we have focused on the statistics of bouts along the average centre line of the plume. We have shown how downwind distance impacts the bout count, amplitude and duration as well as the IBI, and that each of these statistics covary as a result of the plume structure in different release configurations. However, the structure of the plume also extends crosswind. In section 3.7.2.1, we analyse the impact of crosswind distance whilst also considering downwind distance from the odour source on the bout statistics.

3.7.2 *Crosswind Distance*

3.7.2.1 *Impact of crosswind distance on bout statistics*

Previously, we looked at the impact of downwind distance from the odour source on the bout statistics and explored how fluctuations in concentration of the transported odorant changed as the plume travels downwind. We see in all datasets that the odorant also disperses laterally as it travels away from the source and the amount it expands over the distances differs between odour release configurations. With increasing wind speed, the transported odorant not only travels further downwind but the lateral dispersion of the odorant increases as the plume travels downwind. Here we further analyse the impact of the crosswind distance by exploring bout statistics in lateral profiles at selected downwind distances, matching those sampled in section 3.7.1.1.

In fig. 3.14, we plot the mean across trials for bout count, mean bout duration, mean bout amplitude and mean IBIs at the same five equally spaced sample distances selected on the mid-point of the plume (μ), but we plot lateral profiles of y between $\mu \pm 2\sigma$ crosswind. As in section 3.7.1.1, the plotted bout counts are the counts averaged over each trial in a dataset, while the remaining statistics are calculated on a per-bout basis and are therefore the average statistic of each bout in a trial averaged over trials. The number of samples for each of the five distances differ due to the width of the plume at the distance. We therefore normalized between the extracted plume width from section 3.6.2 for each x distance plotted.

Across all three freestream datasets in fig. 3.14, we see the same crosswind relationships in the bout statistics because of the selected downwind sampling locations. The bout counts consistently show a bell-shaped distribution with decreasing counts at increasing downwind distance. We see two peaks in the crosswind amplitude either side of the centre line close to the source, flattening out as we move further downwind. IBIs show an inverted bell-shaped crosswind distribution, increasing both downwind and at the edges of the plume. The bout durations mirror the IBIs, however on average the durations decrease downwind apart from in the $20cm/s$ dataset. The near-bed dataset shows very similar shapes of statistics overall, but with bout counts increasing with downwind distance and a less clear bell-shaped distribution. The structure of the duration curves also have two peaks but skewed in the positive $\frac{y}{\sigma}$ direction. The counts, duration and IBIs are also skewed in the same direction.

In fig. 3.14a, we can see that, for the $5cm/s$ dataset, at the sample location closest to the source ($3.3cm$), bout counts decrease from 135 at the centre of the plume down to a minimum of 105 at the edge of the plume. At $18.6cm$, counts are ≈ 27 at the centre and are on average 34 at the plume edges. At the FTP, the duration increases from the centre of the plume at approx $0.8s$ to approx $1.2s$ at $\mu \pm 1.5\sigma$ and then back down to an average of 0.8 at the edge of the plume. However, at $18.6cm$, we see durations at the centre of the plume at around $.68s$ decrease slightly $\approx .67s$ at the edges. Average bout amplitudes close to the FTP have two peaks with a larger positive σ peak reaching $\frac{C}{C_0} \approx 0.06$ and troughs at the centre of the plume and edges of the plume at $\frac{C}{C_0} \approx 0.24$ and decrease close to the noise floor for downwind

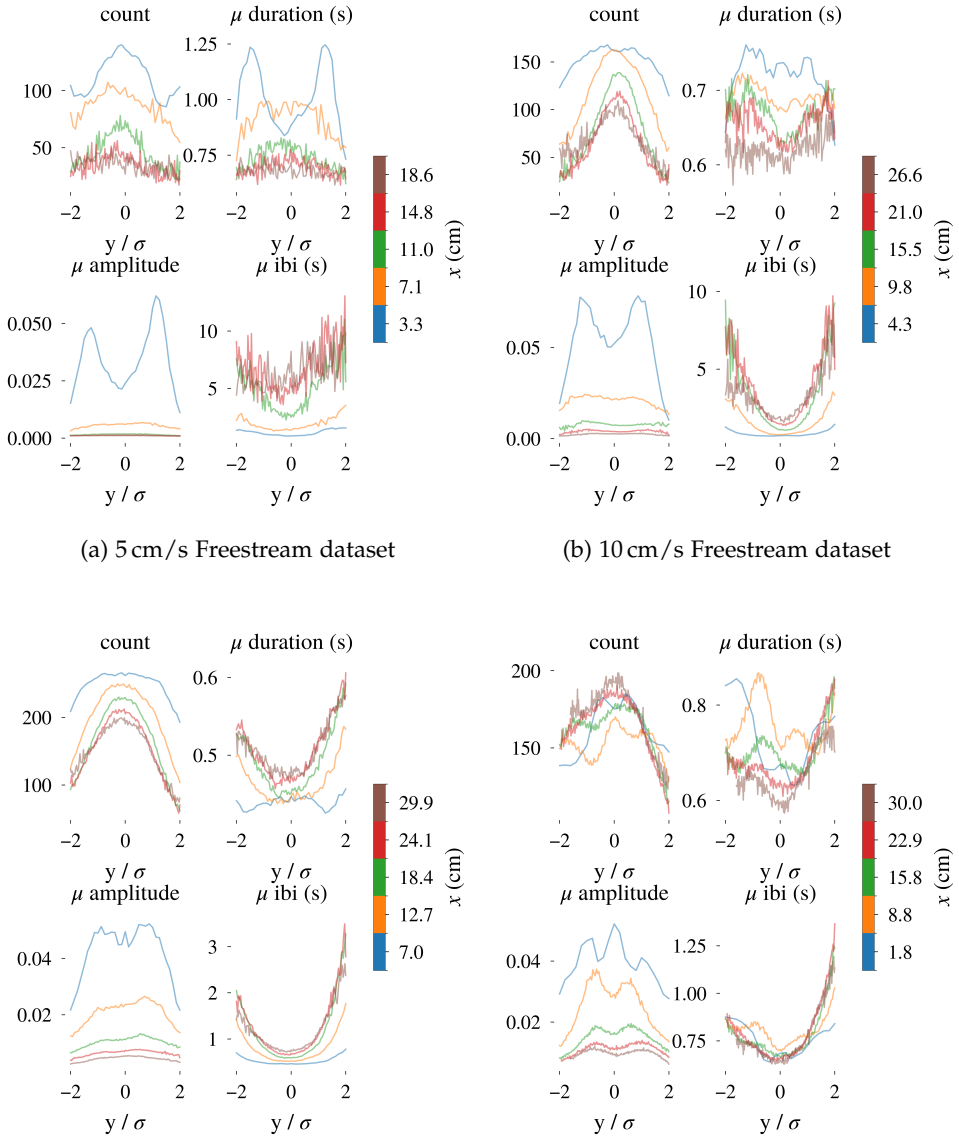

(a) 5 cm/s Freestream dataset

(b) 10 cm/s Freestream dataset

(c) 20 cm/s Freestream dataset

(d) 10 cm/s Near-bed dataset

Figure 3.14: Statistics of bouts against normalised crosswind distance (y/σ) at five selected downwind distances (coloured lines, from close to the FTP to the bout-count minima or plume extent). Top left panel shows bout count per 240*s* trial; top right shows mean bout duration (s); bottom left shows mean bout amplitude (C/C_0); bottom right shows mean inter-bout interval (IBI, s). Lines are coloured from dark to light with increasing downwind distance.

distances $\geq 11.0cm$. Average IBIs range from $< 1s$ up to $> 10s$ at the positive σ edge of the plume and $\approx 8s$ at the negative edge. The distinct inverted bell shape of the lateral profiles of IBIs becomes noisy at $11.0cm$, with a minimum value of $\approx 2.8s$ at the centre up to an average of $\approx 7.5s$ at the edges. Overall, we see much more noise at greater downwind distances for the $5cm/s$ dataset, potentially due to a great number of sample points but most likely due to more intermittent bouts at greater distances.

The same statistical trends continue in the freestream dataset with a $10cm/s$ wind speed, shown in fig. 3.14b. At the FTP, bout counts decrease from ≈ 160 down to ≈ 120, with counts only significantly decreasing closer to the edges of the plume and a more gradual drop off in bout count than in the $5cm/s$ dataset. This trend does not continue for downwind distances $\geq 9.8cm$. Further downwind, we see the non-linear decrease in counts more clearly at the centre line of the plume, accompanied by a flattening of the crosswind bell curve with the $21.0cm$ and $26.6cm$. The average bout duration curves become noisy for downwind distances $\geq 15.5cm$. The crosswind duration curve at the FTP remains flat between the two peaks at $\approx .73s$ or between $y = \mu \pm 1.75sigma$. Plotted downwind distances $\geq 9.8cm$ show an increase in bout duration from the centre line to the plume edges and for $\geq 15.5cm$ decrease again at one or both edges of the plume. This decrease in bout duration is either the result of poor plume edge approximation or more likely represents the real edge of the plume. We see the same double peak in bout amplitude at the FTP as is present in the $5cm/s$ dataset. The scale of the peaks, ≈ 0.09, make any equivalent structure in further downwind distances difficult to see, but a non-linear decrease in bout amplitude with increasing downwind distance is still present. For all sampled downwind distances, we see the IBIs form an inverted bell-shape crosswind distance curve that increases in minimum IBI with downwind distance. The IBIs range from $\approx 0.7s$ at the centre to $\approx 1.2s$ at the edges of the plume for the flow transition sample point. For the sample point at the downwind extent of the wind tunnel, $\approx 1.8s$ at the plume centre line up to $> 8s$ at the plume edges. The $10cm/s$ crosswind data shows less skew in either lateral direction than the $5cm/s$ dataset. This dataset shows either a better plume approximation, higher bout counts overall throughout the wind tunnel or less lateral drift of the plume in either direction than the $5cm/s$ dataset.

As previously explored in section 3.7.1.2, the freestream $20cm/s$ wind speed dataset (fig. 3.14c) displays a linear decrease in the bout counts with downwind distance at the centre line of the plume, because only the initial part of the sigmoid curve of bout counts is encapsulated within this dataset. For the FTP, bout counts decrease from ≈ 260 at the centre line to ≈ 200 at the plume edge. At the $29.9cm$ sample point, counts decrease from ≈ 190 down to between 80 and 120 at the edges of the plume. After the initial downwind sample point, the crosswind curves for the bout counts, durations and IBIs remain relatively constant but decrease or increase in magnitude. For all sample points $\geq 12.7cm$, average duration ranged from $\approx 0.4s$ up to $\approx 0.6s$ and $\approx 0.5s$ at the positive and negative σ plume edges, respectively. IBIs ranged from $0.45s$ at the centre line up to $3s$ at the positive and $2s$ at the negative σ plume edges. Again the scale of the average amplitude curve at the FTP

(maximum $\frac{C}{C_0} \approx 0.046$) makes it difficult to see the structure of the curves further downwind due to the exponential decrease in amplitude with increasing downwind distance. We only see a marginal increase in average duration and IBI at the centre line with increased magnitude of the IBI at the edges of the plume. Only seeing part of the overall structure of the plume illuminated more clearly the impact crosswind plume distance has on the bout statistics.

In fig. 3.14d, due to suboptimal prediction of the FTP in the $10cm/s$ near-bed dataset, for both the $1.8cm$ and $8.8cm$ sampled distance points, the bout statistics curves do not clearly follow the same trends as those sampled further downwind. The average bout amplitude is the only plotted statistic that shows a consistent trend between all downwind distances $\geq 8.8cm$, with a bimodal distribution non-linearly decreasing in magnitude with increasing x. If one ignores the two sampled distances close to the odour source, we see a lateral skew in the results towards positive σ in the average counts, bout durations and IBIs, but all the statistics follow the same relationship with crosswind plume distance that appear in the freestream datasets. The key difference is that bout counts increase in magnitude with downwind distance.

To summarize, regardless of downwind distance, we see bout counts decreasing towards the edge of the plume. Bout durations increase in length and in some cases further downwind we see durations decrease closer to the plume edge. IBIs mirror the trend of the bout durations but on average are an order of magnitude longer than the bouts, except in the near-bed dataset in which they are less than double the length. We also see the amplitude of the bouts initially increase and then decrease moving outwards from the centre line of plume.

3.7.2.2 *Visualizing Crosswind Distance with PCA*

In this subsection, we apply PCA to the trial average bout statistics of crosswind lateral profiles between $\mu \pm 2.0\sigma$ at five selected downwind distances between the FTP and the bout count minima or plume extent for the four release configurations. This is to further illustrate the impact of crosswind distance on the bout statistics, and to determine whether the impact of downwind and crosswind distance on the bout statistics can be linearly separated. The analysis will also determine whether distance, either crosswind or downwind, is the greatest source of variance within the bout statistics and show how each of the statistics covary within each dataset. We colour each standardized statistic vector oriented in PC space, firstly by downwind distance $x(cm)$ and secondly by crosswind distance between μ and $\mu \pm 2.0\sigma$. As noted in section 3.7.1.3, the absolute orientation of each PC axis is sign-arbitrary; only the relative signs of loadings within the same PC, and their magnitudes, are meaningful.

As seen in the scree plot in the bottom right panel of the $5cm/s$ freestream dataset figure (fig. 3.15a), the first two principal components represent 90.6% of the explained variance of the bout statistics. PC1 represents 74.4% of the explained variance (shown in the right centre loadings panel) of which the bout count, duration, IBI and then amplitude contribute

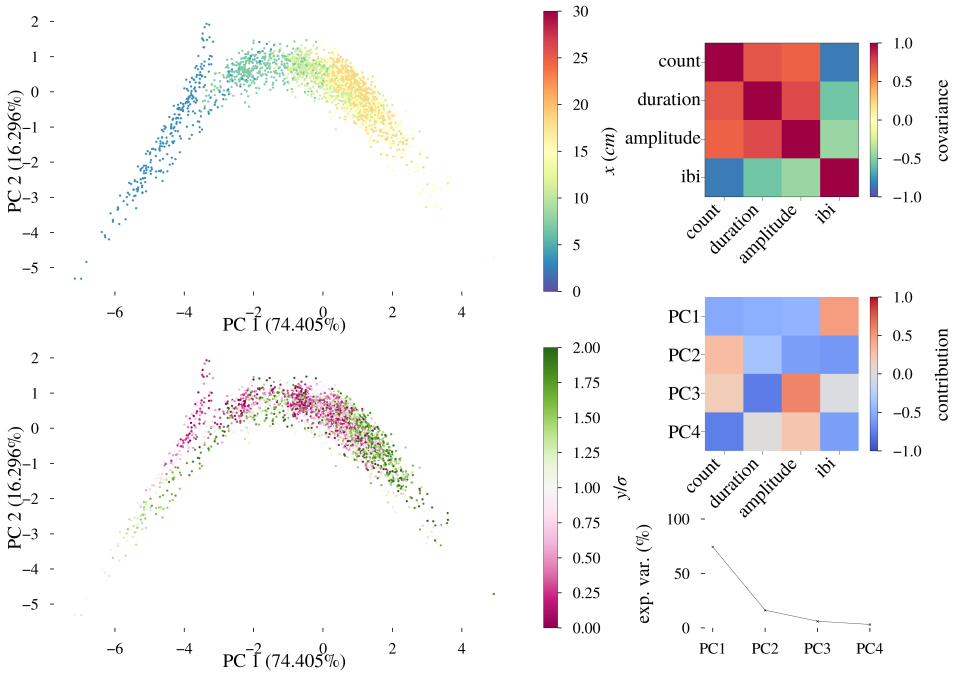

(a) 5 cm/s Freestream dataset

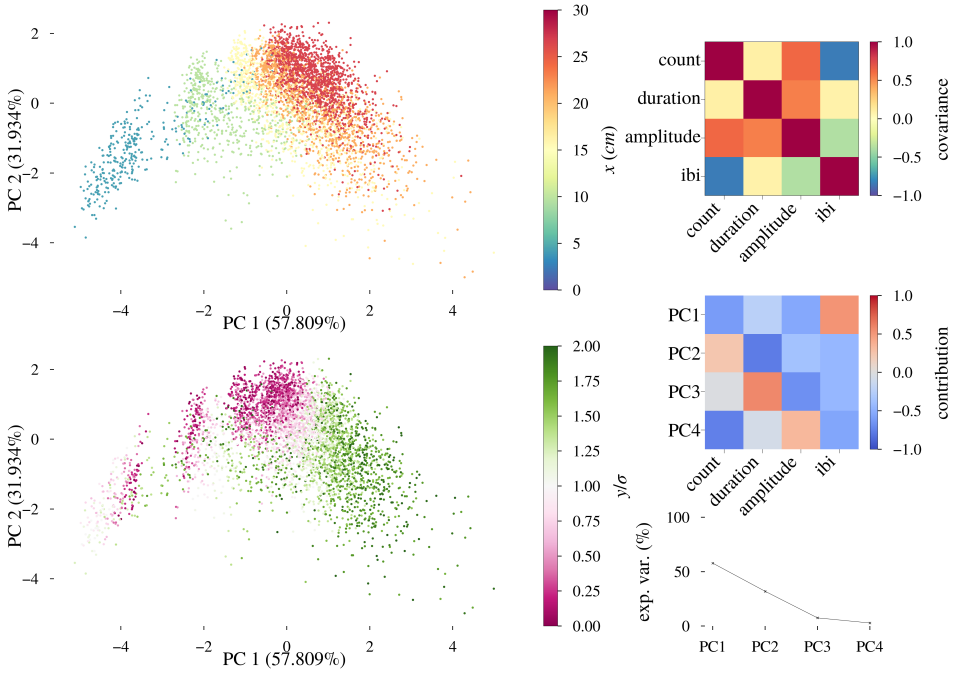

(b) 10 cm/s Freestream dataset

Figure 3.15: PCA of trial mean bout statistics of five crosswind profiles. Left top panel shows PC1 vs PC2 coloured by downwind distance. Left bottom panel shows PC1 vs PC2 coloured by normalized crosswind distance. Right top shows covariance of input statistics, right middle shows explained variance contribution of each statistic to the principal components. Right bottom show a scree plot of explained variance percentage of each principal component.

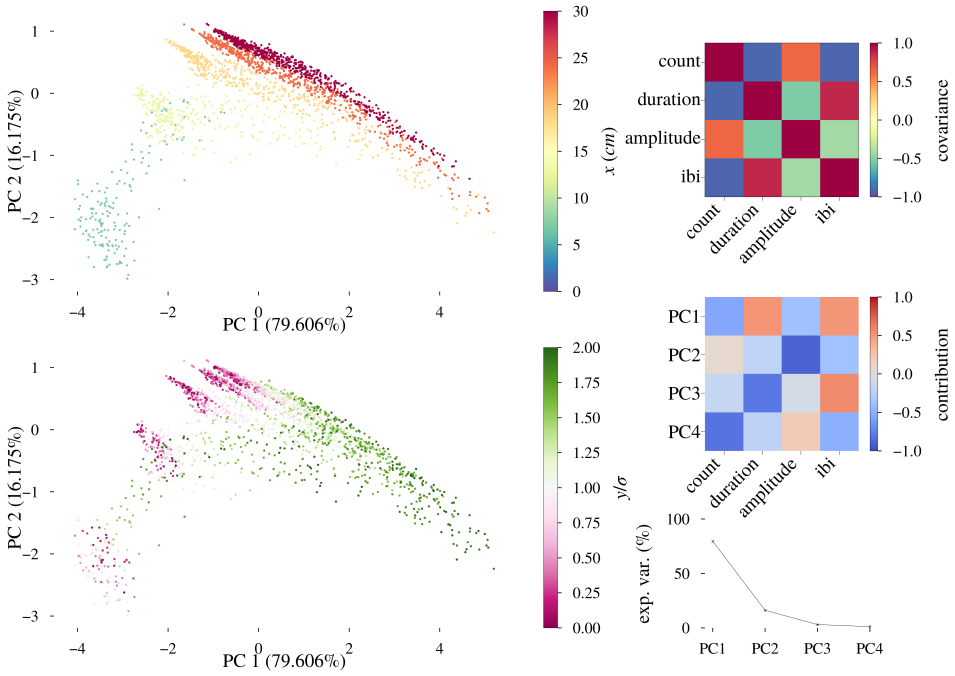

(c) 20 cm/s Freestream dataset

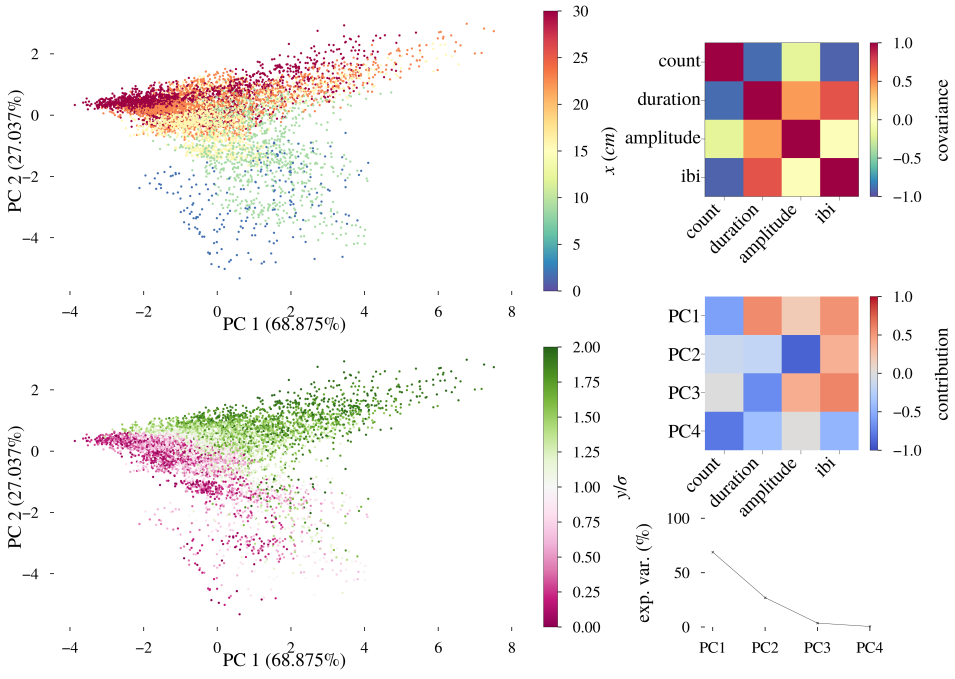

(d) 10 cm/s Near-bed dataset

Figure 3.15: PCA of trial mean bout statistics of five crosswind profiles. Left top panel shows PC1 vs PC2 coloured by downwind distance. Left bottom panel shows PC1 vs PC2 coloured by normalized crosswind distance. Right top shows covariance of input statistics, right middle shows explained variance contribution of each statistic to the principal components. Right bottom show a scree plot of explained variance percentage of each principal component (cont.).

with slightly decreasing absolute values (-0.54, -0.51, 0.48 and -0.47, respectively). This means that bout amplitude, count, and duration all decrease with increasing PC1 as IBI increases. The statistics that contribute the most to the explained variance of PC2 are IBI and the bout amplitude, with values of -0.64 and -0.60. Bout count, duration and amplitude all positively covary between values of 0.64 and 0.75 and all negatively covary with IBI with count having the greatest covariance of -0.81. The top left panel shows each of the bout statistic vectors coloured by downwind distance, of which we have five selected distances. We see a clear positive correlation between PC1 and downwind distance, although there is overlap between distances and no clear separation, potentially due to how close each of the selected distances are to one another. The bottom left panel shows the same bout statistics vectors, but coloured based on normalized crosswind distance between the approximated plume bounds. We see a weaker and less clear alignment of crosswind distance with PC2 than of downwind distance with PC1, showing a moderate negative correlation with centre line points appearing at higher PC2 values. This could be due lower variance of statistics vectors closer to the centre line of the plume and between then FTP and bout count minima patches of vectors, with further crosswind vectors having greater variance and therefore spreading out in the direction of negative PC2.

The PCA results from the $10cm/s$ freestream dataset in fig. 3.15b shows 58% of its explained variance, represented by the first two principal components. We see a smaller loading of bout duration in PC1 than in the $5cm/s$ wind speed dataset, with a value of -0.24, with the most contribution coming from the bout count, amplitude and finally the IBI, with values of -0.61, -0.54 and 0.53. The contribution of bout duration is significantly more in PC2, in having the greatest absolute value of -0.78 and the least contribution from bout count with a value of 0.24. This is somewhat explained in the covariance between bout count and duration, and between duration and IBI, with values of 0.10 and 0.08, suggesting that, when averaging over crosswind distance and downwind distance, bout durations appear fairly independent of bout count and IBI for this dataset. The largest positive covariance present in this dataset comes from the bout count and amplitude, with a value of 0.62, and the greatest negative covariance is between bout count and IBI, with a value of -0.84. All other covariance pairs are $\leq |0.54|$. The top left panel, with the bout statistics vectors plotted in PC space and coloured by downwind distance, show clear alignment of downwind distance PC1 and good separation of the first three sampled downwind distances, with the values $\approx\geq 20cm$ overlapping. The bottom left panel shows the same bout statistic vectors coloured by normalized crosswind distance. The crosswind values appear to increase in alignment with PC1, but separated into downwind distance groups, suggesting that the variance produced by crosswind distance is essentially equal to the variance produced by downwind distance. PC2 appears to mostly represent the variance at greater crosswind distances within the downwind distance seperated blobs, and caused by bout duration and increasing IBI at the plume edge.

For the 20cm/s freestream dataset shown in fig. 3.15c, the first two principal components represent 95.8% of the explained variance. We see essentially equal absolute loadings of bout count (-0.55), duration (0.53) and IBI (0.52), and a significantly lower contribution of amplitude (-0.39) for PC1. For PC2, the amplitude is the contributing statistical feature with the greatest magnitude, with a value of -0.90, and all other loadings $\leq |0.38|$. Here we see strong negative covariances of both duration and IBI with bout counts of values -0.91 and -0.92 and a positive covariance of 0.63 for amplitude with bout count. Duration also has a strong positive covariance with IBI, with a value of 0.87. In the 20cm/s downwind PCA (fig. 3.13c), we see a low covariance of durations and counts, and durations and IBIs, suggesting that these strong covariance relationships demonstrated in fig. 3.15c arise purely from the crosswind distance. We can see clear clustering of the downwind distance sample points in the top left panel, with downwind distance increasing with decreasing PC2 and increasing PC1. We see a clearer alignment in the bottom left panel between crosswind distance and PC1, still with separation of the downwind distance clusters.

For the near-bed 10cm/s dataset shown in fig. 3.15d, the explained variance of the first two principal components are 96.0%. As in the 20cm/s dataset, we see relatively equal loadings of count (-0.59), duration (0.57), IBI (0.53) and amplitude (0.20). We see much greater absolute loading of amplitude in the second principal component than in the first, with a value of -0.90. The loading of the bout count in PC1 is the only negative feature – this is reflected in the covariance of the counts in sign and magnitude of the covariance pairs, with the other three bout statistics having values of -0.92, -0.89 and -0.19 for IBI, duration and amplitude, respectively. The only other negative covariance pair is between amplitude and IBI with a very low value of -0.04. All other covariance pairs are positive, with the most significant being IBI and duration (0.70), and amplitude and duration (0.46). This means that, on average, with the influence of crosswind distance, duration, amplitude and IBI decrease with increasing bout count. The 10cm/s near-bed shows more overlapping of bout statistical vectors in the top left panel than the 10cm/s freestream dataset. However, there is clear alignment of crosswind and downwind distance with PC2, as both are positively correlated. This means that the greatest statistical variance in the bout statistics cannot be attributed to either downwind or crosswind distance, with the variance in the bout amplitude being the most robust statistic for determining distance from the odour source.

We see no statistical trends across each of the release configurations, potentially due to the nature of the sampling. Because we include data from both downwind and crosswind sample locations, we introduce non-linearity into the bout statistical variances, making it more difficult for the PCA to extract a singular cause of variance in the statistics. However, for the 5cm/s freestream dataset, we do see a clear encoding of downwind distance in PC1 and crosswind distance in PC2, but with overlap of downwind sample clusters. In the 10cm/s freestream dataset, we see clear encoding of downwind distance in PC1, but the crosswind distance is also encoded in PC1, potentially due to the spatial separation of the downwind sample points. For the 20cm/s freestream dataset, a combination of both PC1 and

PC2 encodes both downwind and crosswind distance in perpendicular directions, but the variances in the bout statistics do not cleanly align with the axes of greatest variance. Finally, for the $10cm/s$ near-bed dataset, PC2 encodes both downwind and crosswind distance, but the overall bout statistical similarity caused by the proximity to the false floor across the dataset means that the greatest variance is caused by a combination of all of the bout statistics. It is clear from these results that the complex plume structure introduces non-linearity into the bout statistics when combining crosswind profiles across downwind sample points. We list all calculated values of each of the release configuration datasets for the explained variances, covariances and contributions in table A.4, table A.5, and table A.6, respectively.

3.7.3 *Whole Plume*

3.7.3.1 *Bout statistics in whole plume*

Up to this point, we have explored the impact of downwind distance along the average centre line of the plume, as well as perpendicular lateral profiles crosswind at selected downwind distances. The complex plume structure cannot be fully explored by only comparing the bout statistics when isolating their relationships in a specific direction. Therefore, in fig. 3.16, we visualize the previously explored bout statistics in relation to their location within the wind tunnel regardless of direction. We calculate the trial mean bout statistic for every location within the plume bounds $\mu \pm 2\sigma$ and visualize the statistic in its location within the plume (x, y). We colour each calculated statistic based on a log colour map to demonstrate the impact of location on the bout statistic that, in most cases, spans orders of magnitude over the plume extent. This visualization will enable the analysis of these plume statistics without the abstract concept of relating bout statistic crosswind location to a position along a Gaussian distribution of average plume concentration or downwind location to a sigmoidal curve of bout counts, and instead places the statistic in relation to its actual location within the wind tunnel and downwind distance from the source.

Figure 3.16a $5cm/s$ dataset shows poor plume edge approximation for distances $x \geq 10cm$, with plume edge bounds increasing and then decreasing in lateral width. We see bout counts decrease from the source from a maximum of 300 down to < 20 on average for distances $x \approx 15cm$ and $y > 2cm$, with most bouts occurring in the area $x \leq 10cm$. There is an area of relatively higher bout counts with a positive σ lateral shift from the centre line between $x = 15cm$ and the downwind plume extent, suggesting that even at this low wind speed fluctuations in odour concentration occur throughout the wind tunnel but significantly decrease in amplitude past $x = 15cm$. Where bouts do occur at values > 100, the duration of the bouts remain on the order of seconds never more than $10s$, with small areas of low duration bouts ($< 0.1s$ on average) at the plume edges at downwind distances $x \geq 10cm$. Here bout amplitudes remain relatively constant throughout the plume extent, with the highest amplitudes occurring either side of the plume centre line at downwind distances $x \leq 5cm$ and very low bout amplitudes (down to 1.000×10^{-4}) occurring on the negative σ edge of the plume from $x = 10cm$ and, on the positive σ edge of the plume, from $x \approx 17cm$ onwards. IBIs remain low where bout counts are high (downwind distance $x \leq 10cm$) with a significant increase between $x = 10cm$ and $x = 25cm$, and areas of low and high IBIs further downwind. IBIs range from $1.000 \times 10^{-1}s$ up to on average $\approx 20s$ where there are low bout counts. Although we see bout counts occurring throughout the observed plume extent, the area with the highest bout counts spans the width of the approximated plume bounds at $\mu \pm 2.0\sigma$ and abruptly decreases at $x \approx 10cm$ downwind. There is also a narrow area of high average bout counts that skews the calculated statistics due to the low bout counts further downwind.

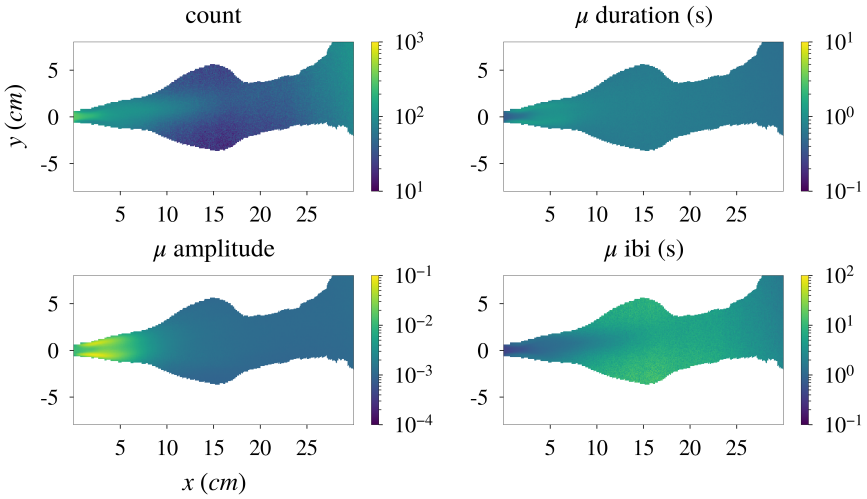

(a) 5 cm/s Freestream dataset

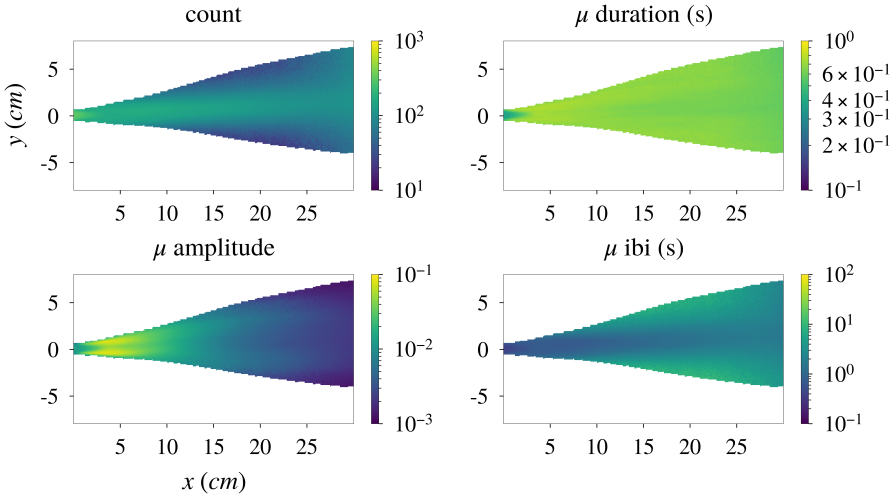

(b) 10 cm/s Freestream dataset

Figure 3.16: Overview of trial mean bout statistics within $\mu \pm 2\sigma$ crosswind. All panels use a logarithmic colour scale. Top left panel shows bout count, top right shows the trial means of the mean duration of bouts. Bottom left shows the trial mean of the average bout amplitude and bottom right shows the trial mean of the average inter-bout intervals. All mean statistics are first averaged over the duration of the trial and then by their pixel location across trial. Bout counts are total bouts over a trial averaged across trials by pixel location.

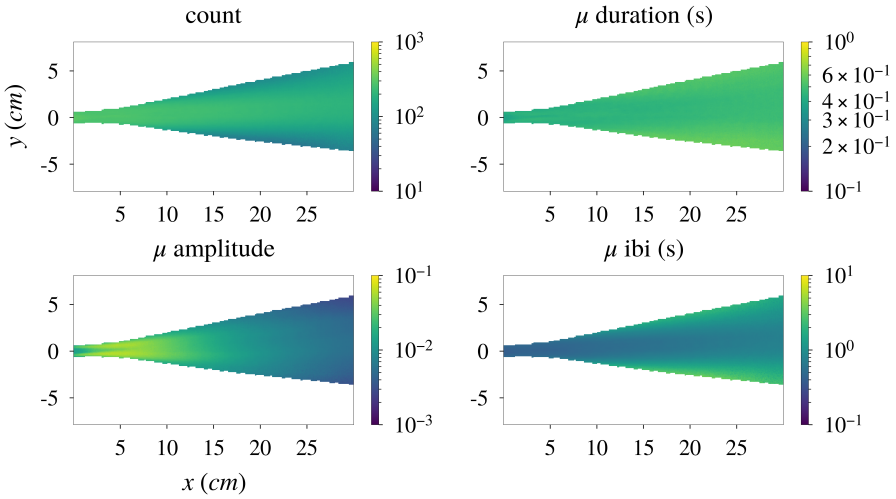

(c) 20 cm/s Freestream dataset

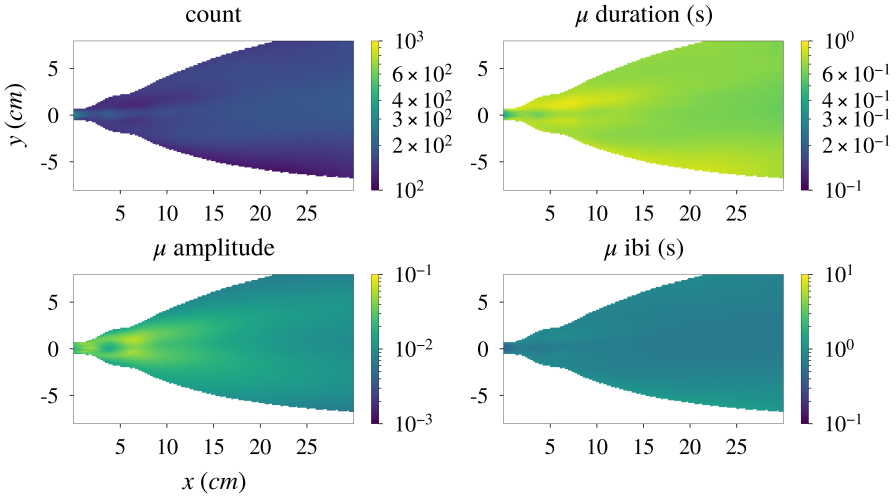

(d) 10 cm/s Near-bed dataset

Figure 3.16: Overview of trial mean bout statistics within $\mu \pm 2\sigma$ crosswind. All panels use a logarithmic colour scale. Top left panel shows bout count, top right shows the trial means of the mean duration of bouts. Bottom left shows the trial mean of the average bout amplitude and bottom right shows the trial mean of the average inter-bout intervals. All mean statistics are first averaged over the duration of the trial and then by their pixel location across trial. Bout counts are total bouts over a trial averaged across trials by pixel location (cont.).

Doubling the wind speed to $10cm/s$ produces a more consistent approximation of plume bounds and more consistent crosswind and downwind relationships with bout statistics, as shown in fig. 3.16b. One can see an area of bout counts ≥ 300 along the centre line of the plume, only decreasing below 100 for distances $x > 20cm$. We also see that average bout counts decrease crosswind perpendicular to the centre line of the plume to values at the edge of the plume that also decrease with downwind distance. Average bout durations do not exceed $0.8s$ and remain relatively constant throughout the plume, with areas of shorter bouts at the plume source and along the mid-line of the plume for $x \geq 5cm$, not falling below $0.38s$. The bout amplitudes show a similar relationship to the $5cm/s$ dataset, with the highest values occurring between $x \geq 2.0cm$ and $x < 7cm$ with high spots either side of the plume centre line. This bi-modal distribution of amplitudes perpendicular to the plume centre line occurs throughout the plume downwind extent, with the distribution widening with increasing downwind distance and plume width. The amplitudes also reduce overall with increasing downwind distance. Again, IBIs appear to be inversely related to bout counts, with low IBIs (down to $1.000 \times 10^{-1}s$) occurring in areas of high bout counts and increasing with downwind and crosswind distance up to $15.5s$.

Compared to the $10cm/s$ dataset, the $20cm/s$ dataset shown in fig. 3.16c sees a downwind extension of all the statistical relationships. Bout counts remain in the order of 1.000×10^2 throughout the entire downwind extent of the wind tunnel over a wider crosswind area between the plume edges, only showing a significant decrease at the plume edges for downwind distances $x \geq 10cm$. Bout durations remain high throughout the plume extent ($> 0.55s$ on average) with a slight increase up to no more than $0.62s$ at the plume edges where bout counts decrease. Amplitudes show the same bi-modal distribution from the source that lessens in magnitude with increasing downwind distance to the plume extent. Overall, amplitudes increase from the source to a maxima at $x = 5cm$ and then consistently decrease with downwind distance, and only at the edges of the plume where bout counts are low. IBIs continue to show an inverted mirroring of the bout counts from at lowest $1.000 \times 10^{-1}s$, with the largest IBIs (up to $10s$) occurring at the plume edges where bout counts are low. After $x = 10cm$, IBIs consistently increase crosswind and with downwind distance.

In the near-bed dataset shown in fig. 3.16d, we see bout counts range from 105 up to a maximum of 285 bouts. Average bout counts remain high throughout the extent of the plume, with the highest values only occurring along the plume centre line and close to the odour source $x \leq 5cm$. We also see comparatively low areas of bout counts (≈ 120) along the plume edges where $x \leq 10cm$ and only on the negative σ plume edge for distances $x \geq 10cm$. Average bout duration, amplitude and IBI inversely mirror the trends of the bout counts, showing comparatively high values where bout counts are low. Bout durations appear highest ($\approx 1s$) between $x = 2cm$ and $x = 15cm$ and increase from the plume mid-line before decreasing again at the plume edges, and are lowest at the odour source, slightly increasing with downwind distance. Amplitudes show the same areas of high and low

values with the bi-modal distribution perpendicular to the centre line of the plume, however the magnitude of the amplitudes appear to be more impacted by the lower bout counts with a more gradual decrease with downwind distance. IBIs show a direct correlation with the bout durations, but appear to be on average slightly longer than the bout durations, ranging from between 1.4s down to 0.4s on average. Compared to the 10cm/s freestream dataset, the near-bed dataset shows significantly higher bout counts throughout the plume and similar ranges of bout durations and amplitudes, but an order of magnitude shorter IBIs on average. This suggests that the presence of the false floor leads to much farther travelling odour concentration fluctuations that remain consistent throughout the extent of the wind tunnel, whilst the freestream dataset shows increasing durations of the pauses between fluctuations with downwind distance within the plume extent.

The bout statistics are impacted by their distance from the odour source differently depending on the release configuration. Plumes in the freestream configuration see a greater impact on the statistics based on downwind distance from the odour source – where wind speeds are lower, a more significant drop off in bout counts was seen, paired with an increase in IBIs. In comparison, the near-bed configuration saw more of an impact on crosswind distance due to the false floor over its plume extent. The practical implication is that a navigating organism could use a gradient ascent on bout count and descent on IBI to steer towards the source in freestream conditions; however, this strategy would be less reliable in the near-bed configuration, where the relative lack of downwind decay means the same cue gradients are weaker. These relationships to source distance manifest as variance in the plume statistics. We therefore further explore the variance present in this data in section 3.7.3.2.

3.7.3.2 *Visualising bout statistics against downwind and crosswind distance with PCA*

Here we apply PCA to demonstrate the extent of the impact of downwind and crosswind distance on the bout statistics across the entire plume extent for each release configuration. We select data points located in $\mu \pm 2\sigma$ of the plume, and only retain the vectors downwind of the FTP and upwind of either the bout count minima or downwind extent. As noted in section 3.7.1.3, the absolute orientation of each PC axis is sign-arbitrary; only the relative signs of loadings within the same PC, and their magnitudes, are meaningful.

The first two principal components in the 5cm/s freestream dataset represent 91.5% of the explained variance, as shown in the bottom right panel in fig. 3.17a. All of the bout statistical features show relatively equal contribution magnitude to PC1, the bout count (-0.54), duration (-0.51), amplitude (-0.47) and the IBI with a positive contribution (0.47). PC2 saw a different story, in which the contribution of IBI dominated with -0.67, followed by amplitude with -0.59, duration with -0.36 and finally bout count with 0.27. The most significant covariance occurred between bout count and IBI with a value of -0.84, followed by amplitude and duration, and duration and bout count both pairs with a value of 0.75 and amplitude and bout count with 0.65. Count, duration and amplitude all shared positive

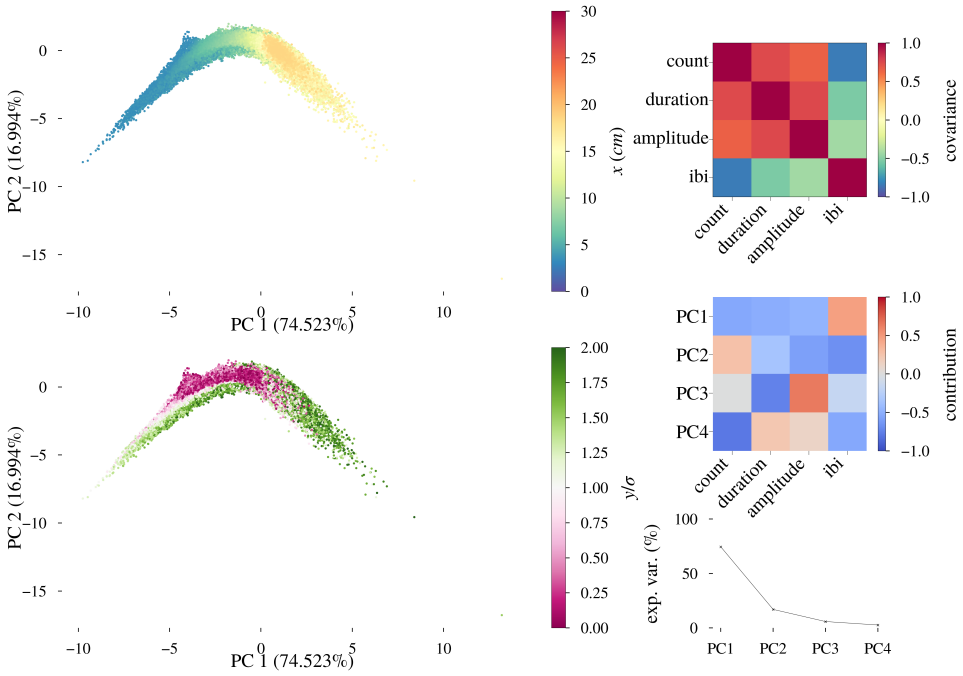

(a) 5 cm/s Freestream dataset

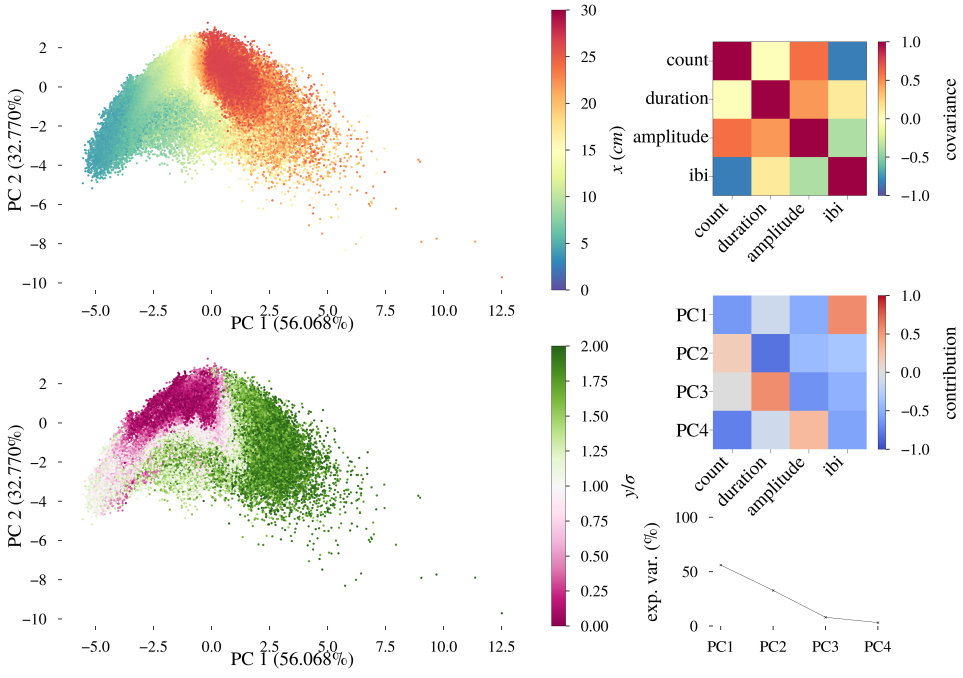

(b) 10 cm/s Freestream dataset

Figure 3.17: PCA of trial mean bout statistics in plume within $\mu \pm 2\sigma$ crosswind. Statistics are visualised on a log colour map. Top left panel shows PC1 vs PC2 coloured by downwind distance (x, cm). Bottom left panel shows PC1 vs PC2 coloured by normalised crosswind distance (y/σ). Right top shows covariance of input statistics, right middle shows explained variance contribution of each statistic to the principal components. Right bottom shows a scree plot of explained variance percentage of each principal component. Downwind distance begins from the maximum trial mean of the bout amplitudes.

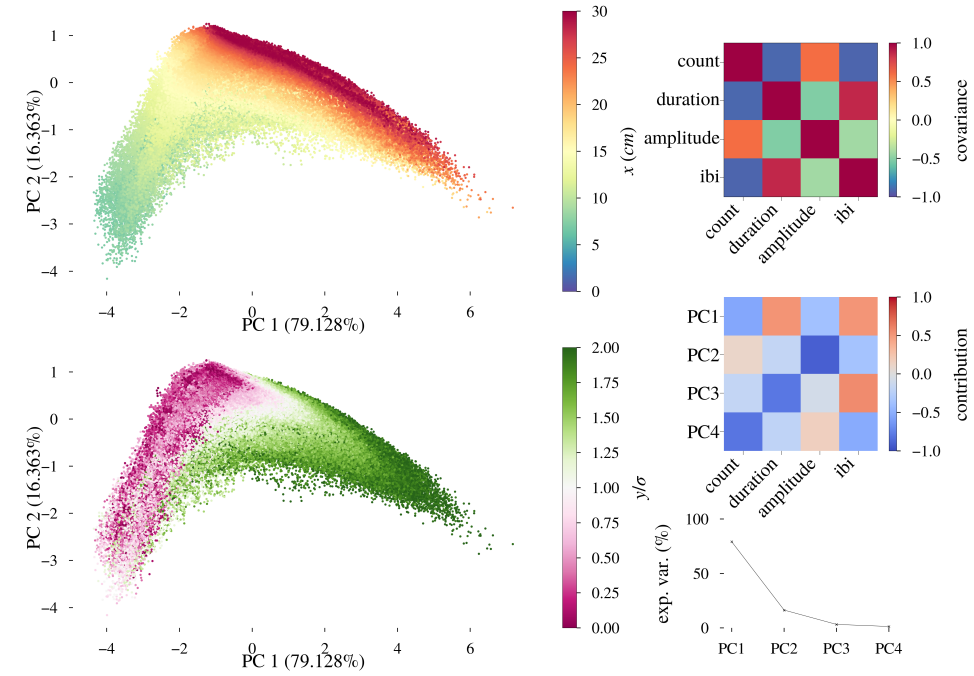

(c) 20 cm/s Freestream dataset

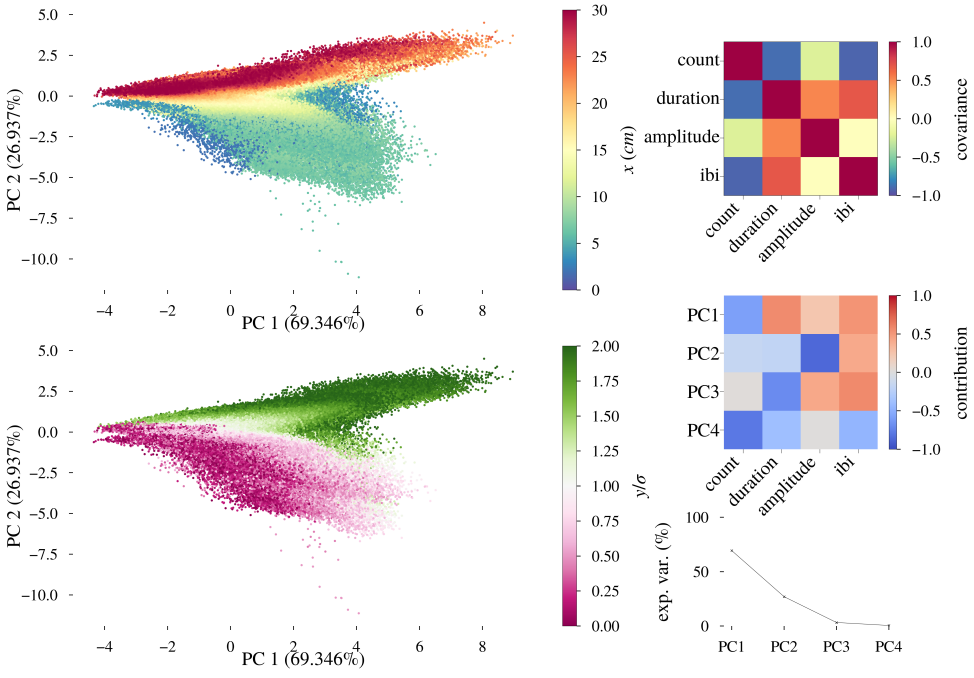

(d) 10 cm/s Near-bed dataset

Figure 3.17: PCA of trial mean bout statistics in plume within $\mu \pm 2\sigma$ crosswind. Statistics are visualised on a log colour map. Top left panel shows PC1 vs PC2 coloured by downwind distance (x, cm). Bottom left panel shows PC1 vs PC2 coloured by normalised crosswind distance (y/σ). Right top shows covariance of input statistics, right middle shows explained variance contribution of each statistic to the principal components. Right bottom shows a scree plot of explained variance percentage of each principal component. Downwind distance begins from the maximum trial mean of the bout amplitudes (cont.).

covariances and IBI shared only negative covariances with the other statistics. On average, an increase in bout count meant an increase in amplitude and duration and a decrease in IBIs throughout the plume in the $5cm/s$ freestream dataset. We see a strong encoding of downwind distance with PC1 and crosswind distance PC2, with a clear positive correlation between PC1 and x and negative correlation between PC2 and y/σ. With the complexity introduced by sampling bout statistics across the plume, PCA is surprisingly successful at showing the downwind distance as the source of greatest variance within the dataset and crosswind distance as the second-most.

In the $10cm/s$ freestream dataset shown in the bottom right panel of fig. 3.17b, the first two principal components represent 88.8% and of the explained variance. The absolute loadings of PC1 in order of decreasing magnitude are the bout count (-0.63), IBI (0.57), amplitude (-0.52) and a significantly lower value for the bout duration of -0.12. We see the bout duration absolute contribution significantly increase in PC2 to -0.81, with all other bout statistical contributions $\leq |0.43|$. The greatest absolute covariance pair are the bout count and IBI (-0.83), followed by bout count and amplitude (0.59), and then between amplitude and duration (0.47). The low covariance between duration and bout count of -0.03 could explain its low contribution to PC1 and high contribution to PC2, as these bout statistical variance sources do not appear to align. There is a clear positive correlation between PC1 and downwind distance, and a negative correlation between crosswind distance and PC2. The strong contribution of duration to PC2 suggests that bouts become longer with increasing distance from the centre line of the plume on average. However, because the features are standardized, the strength of the contribution does not reflect the real scale of the change compared to other bout statistics. We see good encoding of downwind and crosswind distance overall, with the exception of crosswind distance encoding of an area of downwind distance sample points $\geq 20cm$.

The first two principal components of the $20cm/s$ freestream dataset shown in fig. 3.17c explain 95.5% of the bout statistical variance. We see relatively equal loadings of three of the four bout statistics and a much lower contribution of the bout amplitude (-0.38), with the bout count, duration and IBI contributing -0.55, 0.53 and 0.52, respectively. We also see a much higher contribution in PC2 from the bout amplitude -0.91, with a conversely insignificant contribution of bout count 0.10 and other bout statistics contributing $\leq |0.36|$. It would appear as if the covariance of bout count and the other bout statistical features inversely mirror their contributions to PC1, with strong negative covariances of bout duration (-0.91) and IBI (-0.92) and a not insignificant positive covariance of amplitude (0.59). The third greatest absolute covariance calculated is between bout duration and IBI, with a value of 0.87, suggesting that these bout statistics are likely dependent on each other, which is expected as we have previously seen IBIs mirror bout durations closely in crosswind profiles and, in some cases, downwind along the centre line of the plume. We see a switching of the source of greatest variance compared to lower wind speeds, in which PC1 now encodes crosswind distance and PC2, for the most part, encodes downwind distance. This could be a

result of the plume in this dataset only capturing the initial section of the sigmoidal curve of bout counts that represents the overall downwind plume structure. Therefore, there is comparatively more variety in the bout statistics captured crosswind due to the majority of the downwind structure of the plume being cut off.

The $10cm/s$ near-bed dataset in fig. 3.17d shows that the first two principal components represent 96.2% of the explained variance. The PC1 bout statistical feature loadings in decreasing order of absolute contribution are the bout count (-0.59), bout duration (0.57), IBI (0.52) and, finally, the bout amplitude (0.24). As we have seen previously, the bout statistical feature with the lowest contribution to PC1 has the highest absolute contribution to PC2, with the amplitude being -0.87, followed by the IBI at 0.42, the bout duration at -0.19 and, finally, the bout count at -0.17. Interestingly, the bout statistical covariances with bout count are all negative, meaning that in the $10cm/s$ near-bed dataset, we see on average a decrease of IBI (-0.92), bout duration (-0.89) and amplitude (-0.23) with increasing bout counts. The lowest absolute covariance in this dataset is between the bout amplitude and the IBI (0.01), suggesting that these statistics are essentially independent of one another. The bout duration shows a positive covariance between the bout amplitude and the IBI, with values of 0.52 and 0.69, respectively. Due to the plume's proximity to the false floor (the key difference between the freestream and near-bed datasets), we see low overall alignment of the majority of the bout statistics with downwind and crosswind distance. We therefore see that the crosswind and downwind distance are encoded by the second-greatest source of variance (PC2). This can be attributed mainly to the bout amplitude, which decreases with downwind distance and with crosswind distance on average.

The PCA results from the $5cm/s$ and $10cm/s$ datasets both show the most similarity in the statistical trends, the covariances and the encoding of downwind and crosswind distance. The $20cm/s$ dataset differs in that the greatest source of variance becomes crosswind distance and, secondarily, the downwind distance, most likely due to the cutting off of the downwind extent of the plume. The introduction of a false floor in the near-bed dataset reduces the overall variance of the bout statistics, meaning that the secondary source of variance encodes downwind and crosswind distance, and the greatest source of variance becomes the bout amplitude. In this analysis, we have demonstrated how the bout statistics vary in the entire plume on average, and explored how the variances within the bout statistics can be used to identify the different release configurations and which of the bout statistics can reliably infer crosswind and downwind distance in the plume.

3.7.4 *Compensating for Wind Speed*

In section 3.7.1.1, we show the impact of downwind distance of bout statistics along the centre line of the plume and compare bout statistical curves across the freestream datasets at wind speeds of $5cm/s$, $10cm/s$ and $20cm/s$. In section 3.7.1.2, we demonstrate a clear fitting of sigmoidal curves to the bout count downwind distance curves and saw that increasing wind speed extended the reach of the fitted curves. We hypothesized that for the $20cm/s$ dataset, we only saw part of the bout count sigmoidal curve due to this downwind extension, but saw the full sigmoidal curve for the lower wind speed freestream datasets. If this is true for the bout counts, we hypothesize that the other bout statistics could share the same downwind relationships at different scales due to differing wind speeds. Here we show that, by compensating for wind speed, each of the bout statistics show similar downwind distance relationships along the centre line of the plume. In fig. 3.18, we plot the average bout statistics across trials of each of the freestream datasets along the centre line of the plume μ against the downwind distance $x/windspeed$, starting from the FTP.

For the $5cm/s$ dataset, the bout statistics shown are between the FTP at $3.3cm$ and the bout count minima at $18.6cm$. When we divide by the wind speed of $5cm/s$, the data is plotted between 0.67 $1/s$ and 3.73 $1/s$ $x/windspeed$. The FTP for the $10cm/s$ and $20cm/s$ freestream datasets occur at $4.3cm$ and $7.0cm$. For $10cm/s$ the bout count minima occurred at $26.6cm$ and for $20cm/s$ at the $29.9cm$. These values are scaled with the wind speed, making the flow transition 0.43 $1/s$ and 0.35 $1/s$, and the extent 2.66 $1/s$ and 1.50 $1/s$ $x/windspeed$ for the $10cm/s$ and $20cm/s$ datasets, respectively.

The top left panel of fig. 3.18 shows the bout counts of the $5cm/s$, $10cm/s$ and $20cm/s$ freestream datasets plotted against $x/windspeed$. We see that the bout counts for each dataset non-linearly decrease with increasing $x/windspeed$, and the maximum observed bout counts increase with increasing wind speed. For the $5cm/s$ dataset, the point at which the gradient of the bout counts is greatest occurs between $\approx$ 1.5 $1/s$ and $\approx$ 3.0 $1/s$ $x/windspeed$. The $10cm/s$ dataset provides a clear picture of the sigmoid curve, with the greatest slope occurring between $\approx$ 1 $1/s$ and $\approx$ 2 $1/s$ $x/windspeed$. We only see the upper portion of the sigmoid curve in the $20cm/s$ dataset, with the minimum bout count not falling below the maximum value of bout counts of the $10cm/s$ dataset. However, we do see an increase in the gradient of the bout count curve, an increase from $\approx$ 0.5 $1/s$ $x/windspeed$. In scaling the downwind distance, we see a clear alignment of the sigmoid bout count distance curves even with only a portion of the curve captured in the wind tunnel along the centre line of the plume. On visual inspection, we see an increase by a factor of 0.5 in bout counts between the scaled bout distance curves between the $5cm/s$ to the $10cm/s$ dataset, and the $10cm/s$ to the $20cm/s$ dataset. We do not have enough data for the $20cm/s$ dataset to determine whether this trend continues further downwind.

In the top right panel of fig. 3.18, we show the average bout durations of the three freestream datasets. We see that the bout duration decreases with increasing wind speed,

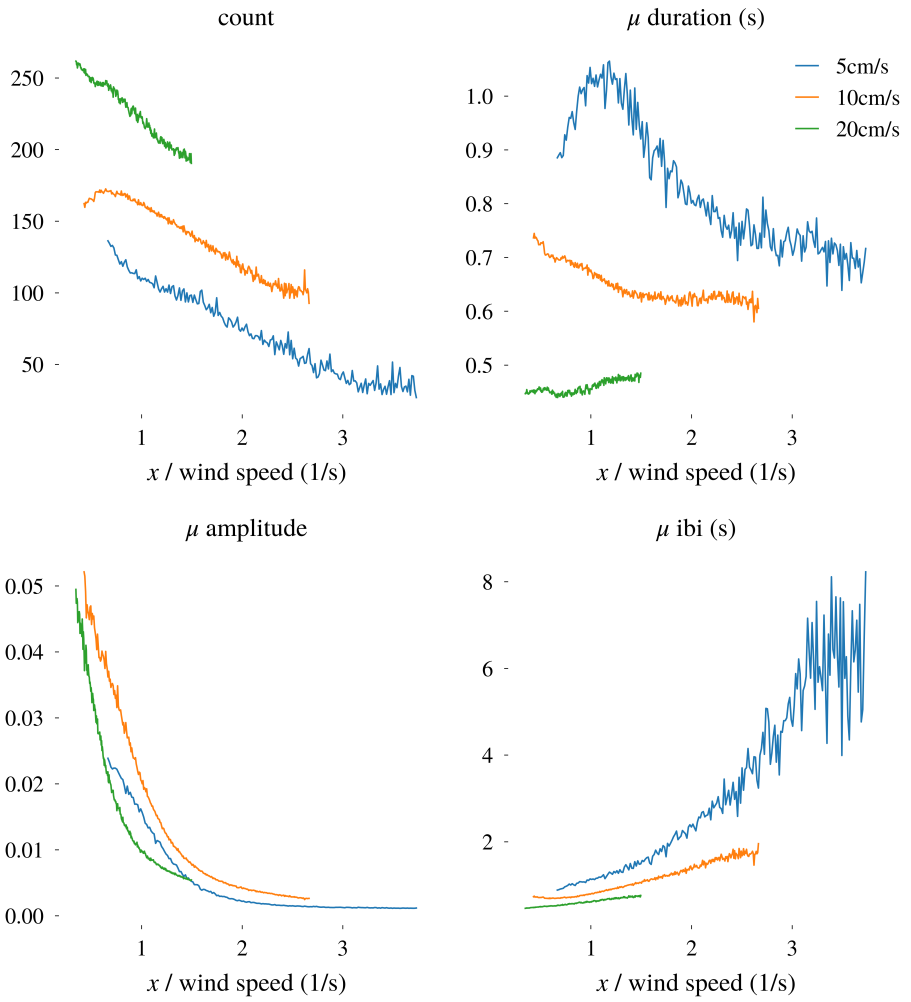

Figure 3.18: Bout statistics of the freestream release configuration plotted against downwind distance divided by wind speed (x/U, s). Top left panel shows bout count per 240s trial; top right shows average bout duration (s); bottom left shows average bout amplitude (C/C_0); bottom right shows average IBI (s). The $5cm/s$ dataset is plotted in blue, $10cm/s$ in orange and the $20cm/s$ in green. Data points with fewer than 15 bouts per trial are excluded to suppress noisy statistics at the plume edges.

with no overlap of values between wind speeds. The upper and lower bounds of the bout durations are 1.07s and 0.64s for the 5cm/s dataset, 0.74s and 0.58s for the 10cm/s dataset, and 0.48s and 0.44s for the 20cm/s dataset. There is an initial increase in duration in the 5cm/s wind speed up to the maxima of 1.07s at $\approx$ 1.2 $1/s$ and then a non-linear decrease down to $\approx$ 0.7s. This dataset appears the most noisy of the three wind speeds, potentially due to a lower bout counts overall, with the noise most prominently occurring where bout counts are less than 50. However, the noise is more likely caused by the low wind speed producing more trial-by-trial variance due to poor plume centre line approximation. In the 10cm/s dataset, we did not see an initial increase in bout duration and instead see a steady decrease in bout duration down to $\approx$ 1.5, with duration remaining steady downwind. The scales of the ranges of the 5cm/s and 10cm/s bout durations make the 20cm/s difficult to interpret because they are significantly larger, though we do see a decrease in durations at $\approx$ 0.4, followed by a shallow incline. The sharp decrease in bout durations appears to occur upwind of the sharp decrease in bout counts. We see a shallow increase in bout duration where bout counts decrease more significantly beyond 1.0 $1/s$. The occurrence of these features in the bout duration distance curves are clearly connected to other features in the bout count curves. This suggests complex plume features exist at distances consistently scaled by the wind speed.

The bottom left panel of fig. 3.18 shows average bout amplitudes for the three freestream datasets. Bout amplitudes appear to exponentially decay with distance at least until 2.0 $1/s$. The maximum average bout amplitude more than doubles between the 5cm/s and the 10cm/s dataset but actually decreases with the 20cm/s. This suggests that average bout amplitude increases with increasing wind speed, and then significantly decreases between 10cm/s and 20cm/s. These results could mean that bout amplitude does not linearly scale with wind speed, and therefore we should not linearly scale downwind distance. However, this may be an artefact of the averaging of significantly more bouts in the 20cm/s versus the 10cm/s wind speed dataset.

In the bottom right panel of fig. 3.18, we plot the average IBI of the three freestream datasets. The 5cm/s IBI appears to exponentially grow with increasing downwind distance, with noisy values from $\approx$ 2.5 $1/s$. The 10cm/s appears to inversely mirror the equivalent bout count curve, with low values to $\approx$ 1.5, a significant increase up to $\approx$ 2.5. The small scale of change in values makes it difficult to interpret the 20cm/s wind speed IBIs in comparison to the lower wind speeds, although we do see an increase in average IBI from the FTP to the downwind extent at 1.5 $1/s$. The IBIs appear to negatively correlate with wind speed, with larger values of IBI occurring at lower wind speeds. This could be explained by higher bout counts and longer bout durations regardless of downwind distance scaling.

Overall, the 5cm/s and 10cm/s freestream datasets provides the clearest and most extensive picture of each of the average bout statistics along the plume centre line (μ). We do see the same bout statistical trends occurring across datasets. The bout statistics that appear to be the most robust to downwind distance and wind speed are the bout count and average

bout amplitude. We see clear alignment of bout statistical curves with each of the release configurations. However, the bout amplitudes do not appear to scale linearly with wind speed.

Although the bout statistical relationships do not appear to be consistently linear, the average variances present in the bout statistics with increasing wind speed and along the centre line of the plume may be great enough to linearly decompose the high dimensional data points in order to distinguish the distance from the source, and also extrapolate the wind speed. To this end, we conduct a PCA on each of the bout statistical vectors calculated for each x pixel along the centre line of the plume in each of the trials where the pixel is beyond the FTP and down to the bout count minima. This will allow us to not only determine whether downwind distance from the source or wind speed are the greatest source of variance within the bout statistics, but also provide more clarity on the covariances of the bout statistics on average.

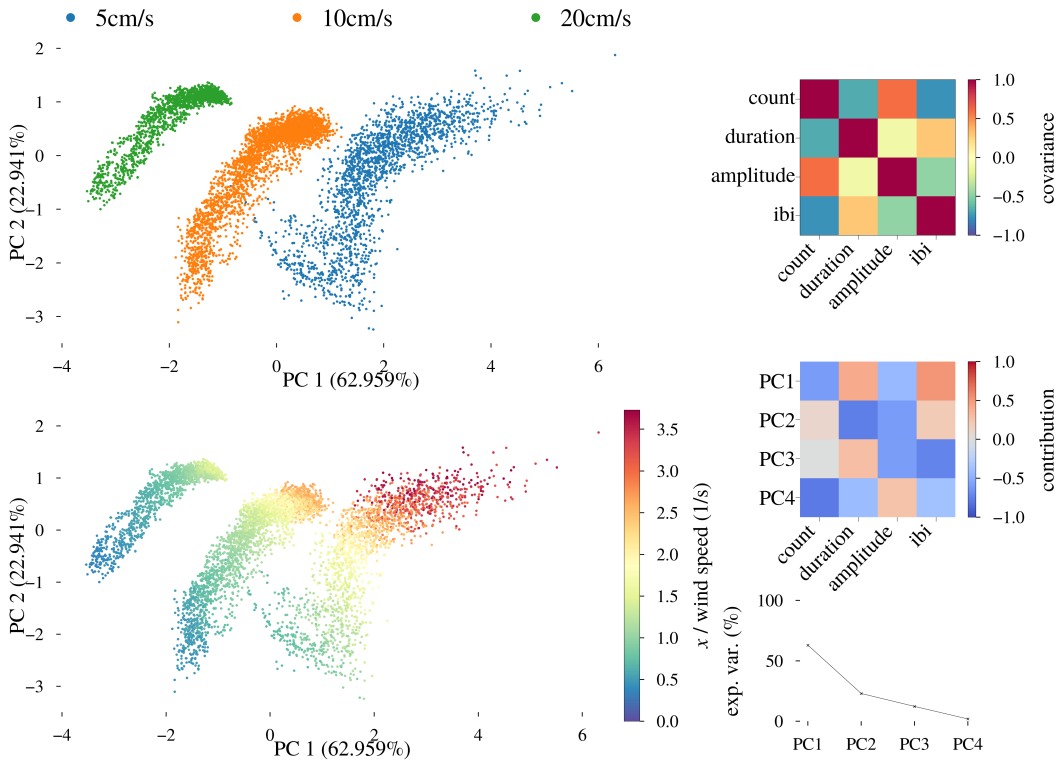

Figure 3.19: PCA Bout statistics of the free-stream release configuration plotted against downwind distance divided by wind speed.

Looking at the scree plot in the bottom right panel of fig. 3.19, we see that the first two PCs represent 85.9% of the explained variance. The middle plot on the right shows the loadings that illustrate the contribution of the following bout statistics to PC1: bout count, IBI, bout amplitude and bout duration, in order of absolute contribution, with values -0.61,

0.52, −0.43 and 0.40, respectively. The statistics showing the greatest individual loading to PC2 is bout duration, with a value of −0.76. The covariance (top right panel) pair with the greatest magnitude is with bout count and IBI value of −0.76 followed closesly by duration with −0.67. These strong covariance values suggest that the bout counts impact these two other bout statistics the most on average i.e. with increasing bout counts, we are likely to see decreasing IBI and bout duration. The weakest covariances of bout statistics are between the duration and amplitude (−0.11), suggesting that these statistics are essentially independent when viewed across wind speed datasets.

The top left panel shows the bout statistics plotted in two-dimensional PC space and coloured by the wind speed of the datasets. We see a clear separation in both PC1 and PC2, as wind speed decreases most with increasing PC1 and slightly increases with PC2. The bottom left panel shows the same statistics plotted in the same two-dimensional PC space, but coloured by $x/windspeed$. There is a clear positive correlation between scaled downwind distance and both PC1 and PC2, with greater values of $x/windspeed$ occurring consistently regardless of the wind speed of the dataset. The variance seen in the PC2 axis can be attributed to increased bout duration variance closer to the odour source at ≤ 1.5 $x/windspeed$, whilst PC1 can be attributed mostly to bout count but also the other three statistics to a lesser degree.

It is clear that the bout statistics calculated along the centre line of the plume are dependent on bout count, either positively or negatively covarying with bout counts regardless of wind speed. The PCA plots provide insight into the scale and origin of this covariance, be it downwind distance from the odour source or the wind speed. We list all calculated values of each of the release configuration datasets for the explained variances, covariances and contributions in Table table A.10, table A.11, and table A.12, respectively.

3.8 DISCUSSION

The PLIF wind tunnel datasets provide a new insight into the complexity of structures that exist within odour plumes that organisms use to find mates, food, or avoid predation. We comprehensively analysed the odour concentration fluctuations of turbulent scalars in three different wind speeds and two odour release heights. Bout counts were previously shown to reasonably estimate odour source distance in a wind tunnel using few sampling locations (Schmuker, Bahr and Huerta, 2016). The filter cascade that preceded the bout analysis, necessitated by noise from the MOX sensor recording modality, provided a method to tailor the targeted fluctuation frequencies, but required modification and tuning for use in this optically captured dataset. We hope that this application of bout analysis to PLIF captured turbulent scalars shed more light on the ever-evolving spatial temporal dynamics of odour plumes in which change occurs even at a millimetre scale.

Initially, to explore the impact of downwind and crosswind distance from the plume source, we determined the average location of the plume within the test section (section 3.6.2). We fitted Gaussian curves to y profiles of spatially binned average concentration $\frac{\bar{C}}{C_0}$ for the entire downwind extent of the wind tunnel, as was previously done to a lesser extent in Connor, McHugh and J. P. Crimaldi (2018) . This provided a good estimation of the location of the plume within the wind tunnel and provided an approximate centre line as $\mu = y/\sigma = 0$ and the plume edge boundaries using $\mu \pm 2\sigma$. We could then place the calculated bout statistics in a normalized model of the average plume location, allowing us to compare and contrast the impact of downwind and crosswind distance not only within repeated trials of the same release configuration, but also across the three wind speeds of the freestream plume configuration and the two $10cm/s$ odour release height configurations. Atema (1988) states that when flow becomes turbulent odour distribution patterns are no longer predictable except when averaged over time. While this method allowed analysis of the impact of the location within the plume structure across trials, we must acknowledge that the established plume boundaries and centre line were only Gaussian approximations of the time-averaged concentration profile; the instantaneous plume meanders substantially around this mean, so a location labelled as "centre line" or "plume edge" is a statistical average, not a fixed physical boundary. However, in establishing average plume bounds, we aimed to map clear and general impacts of odour source distance regardless of the evolving spatial temporal plume structure. Even with this approximation of the plume bounds, we see clear impacts of the different release configurations: an increase in wind speed extended the average concentration farther downwind; a low wind speed led to a comparatively poor plume boundary fit due to a lack of clear plume structure and a veering off farther downwind; the near-bed configuration showed the greatest lateral dispersion.

With the mapped plume bounds, we explored the impact of the release configuration on average bout count and bout count dependent statistics whilst isolating the downwind and crosswind directions. In fig. 3.20, we illustrate the overall trends observed in the

bout statistical relationships with downwind and crosswind distance seen in the freestream datasets. The schematic shows labelled curves for each of the four bout statistics as a function of downwind distance (horizontal axis) and crosswind distance from the plume centre line (shown as a separate lateral profile inset). Dashed vertical lines mark the FTP and the bout-count minima; arrows indicate the direction of each statistic's change from the FTP to the plume extent, and for the crosswind profiles from the centre line to the plume edge. We propose that each wind speed dataset's bout statistical distance curve represents a section of the same overall curve. With increasing wind speed the curve extends further downwind, and we therefore see less of the overall plume structure within the same 30*cm*.

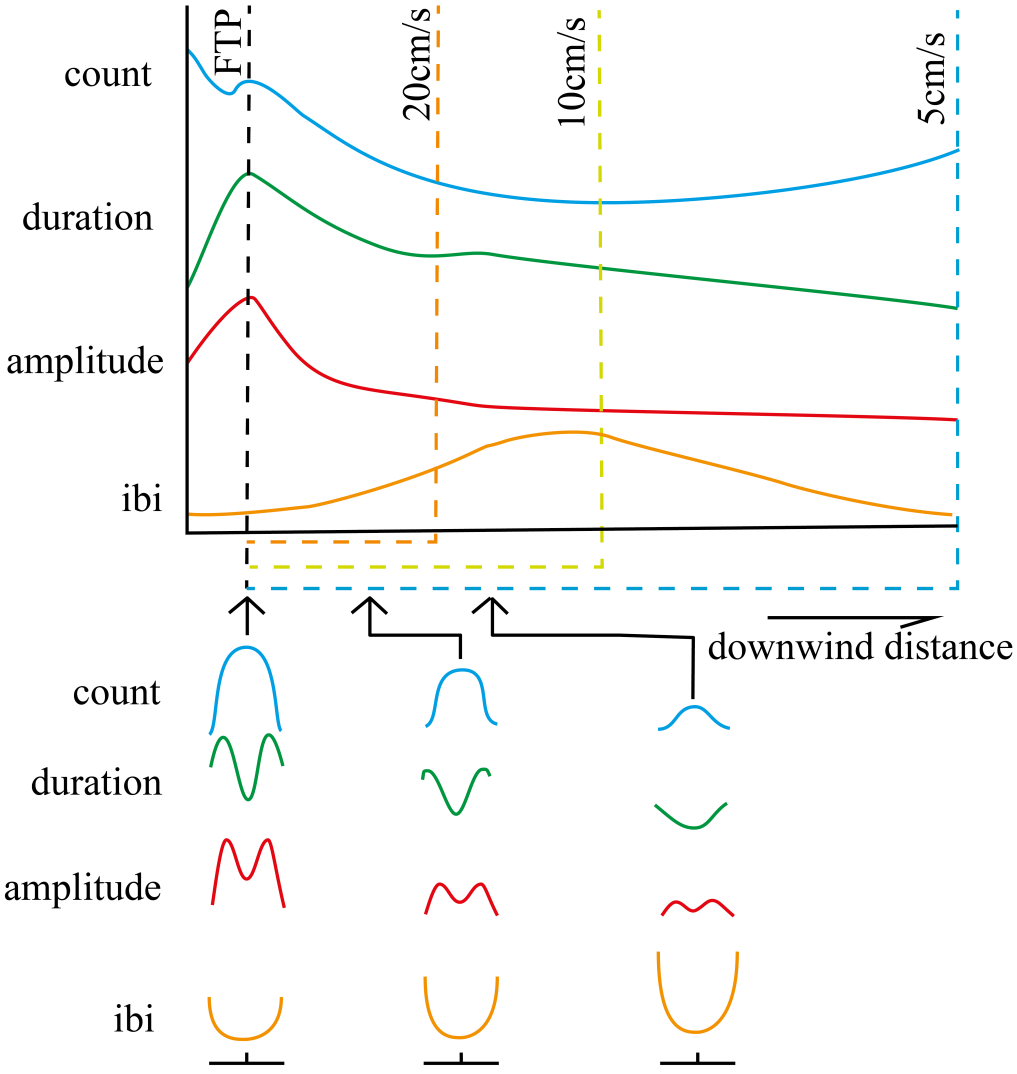

Figure 3.20: Schematic of downwind and crosswind trends in the freestream datasets. Dashed lines represent the downwind extent of the trends that we see due to wind speed extending the plume further downwind.

We identified a flow transition point (FTP) based on the initial amplitude peaks as the scalar travelled downwind. Before this FTP, bout counts decreased with bout duration and amplitude increased significantly from the source. Fast low amplitude bouts in a laminar flow at the odour source transitioned to a slower high amplitude turbulent regime at the FTP. From the FTP, we saw that overall bout counts decreased with downwind and crosswind distance in all freestream configurations, before increasing slightly where amplitudes became low. Amplitudes and durations decreased downwind initially exponentially and then more slowly. IBI, which varied inversely with bout count, increased with downwind distance on average; at the distal plume extent, where bout counts were very low and amplitudes and durations had fallen, IBIs decreased again. This overall increase in IBI with source distance mirrors the well-documented trend of increasing odour intermittency with downwind distance, reported across measurement modalities including ionized air (Murlis and Jones, 1981), photoionization detectors (Mylne and Mason, 1991), and PLIF (Connor, McHugh and J. P. Crimaldi, 2018; J. P. Crimaldi, Wiley and Koseff, 2002); the growing intervals between bouts reflect the increasingly sparse and fragmented nature of odour contact as plume filaments thin and disperse. In the crosswind profiles we saw counts decrease outwards with curves becoming more shallow with increasing downwind distance. Bout durations and amplitudes increased and then decreased with crosswind distance, with amplitudes showing narrower peaks compared to bout durations. In profiles lateral to the downwind direction, both duration and amplitude decreased overall with downwind distance and the bout duration curve widened. IBI sharply increased toward the plume edges with downwind distance. Crosswind duration and amplitude can be approximated with a bimodal distribution that decreases in amplitude and widens with downwind distance. The elevated duration and amplitude at the plume edges rather than the centre line is consistent with the observation by Mylne and Mason (1991) that the intensity of concentration fluctuations is minimised on the plume centre line and increases towards the edges; boundary-crossing contacts between odour-bearing filaments and clean ambient air produce sharp, isolated encounters rather than the sustained signal present near the centre line, and these are reflected in the higher bout statistics at the plume periphery.

The same overall bout statistic curves were seen in the three freestream datasets at different wind speed, but differ in downwind extent and magnitude. All bout statistics are averages and do not represent the variance present within the data.

To further demonstrate overall trends in bout statistics for the freestream plumes we combined the full plume bout statistics between the FTP and either the bout count minima or the downwind extent. We normalized the statistics and the crosswind distance, then spatially averaged based on downwind distance over wind speed. Finally, we applied a Gaussian filter to smooth statistics and remove noise to show general trends across the freestream datasets. We applied a $1:4$ aspect ratio between the crosswind and downwind axes (i.e. 1 unit crosswind per 4 units downwind) to aid visualisation of the plume's lateral dispersion

relative to its downwind extent, and to visually distinguish the two directions from one another, as the observed lateral dispersion differed based on wind speed.

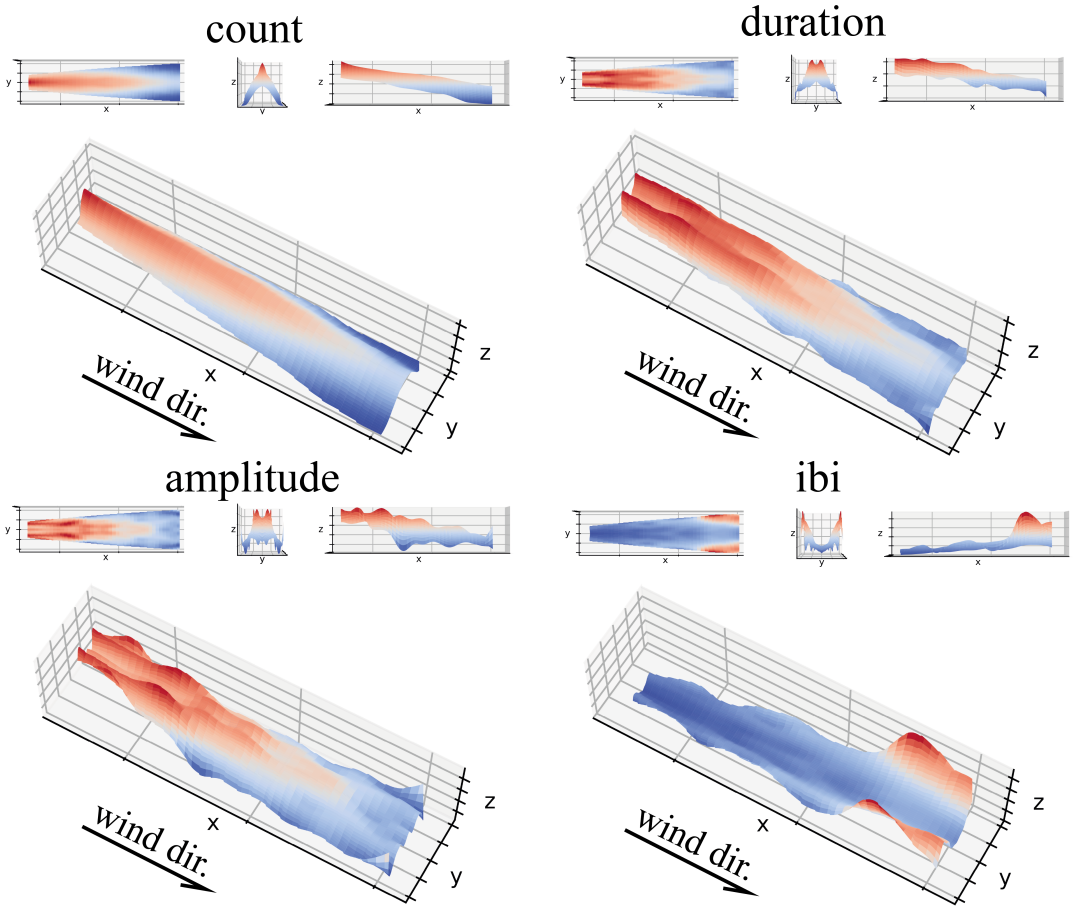

Figure 3.21: Average trends of bout statistics over plume from combined normalized statistics of extracted portions of the freestream datasets. Each of the four statistics show three orthogonal view and one isometric view of the average statistic plume.

From fig. 3.21, it is evident that bout counts are highest at the centre and close to FTP, and decrease with crosswind and downwind distance (visible in all three orthogonal views and most clearly in the isometric view). Counts, duration and amplitude all decreased with downwind distance, with the most pronounced decrease occurring close to the source (as shown in the downwind profile view of each statistic). Duration and amplitude remained low along the centre line and at the crosswind edges of the plume with peaks either side of the centre line, visible in the crosswind profile views. This suggests that a gradient descent on these statistics will not allow navigation to the source — the plume is more complex. Highest IBIs occur with downwind distance and at the crosswind plume edges; lowest occur at the centre line, as shown in the crosswind profile view of the IBI panel. A gradient ascent on bout counts and descent on IBI may allow successful navigation to the odour source. The clear trends shown here indicate that the bout statistical relationships are consistent across the three wind speeds. The key original contributions of this work, relative to Schmuker,

Bahr and Huerta (2016), are threefold. First, Schmuker, Bahr and Huerta (2016) applied bout analysis to a single MOX sensor recording at a handful of spatial locations; here we apply it to the full two-dimensional spatial extent of PLIF recordings, allowing characterisation of bout statistics across both downwind and crosswind axes simultaneously. Second, Schmuker, Bahr and Huerta (2016) reported a linear relationship between bout count and downwind distance; with increased spatial resolution we find a sigmoidal relationship (see the fitted curves and parameters in fig. 3.12 and table 3.2), revealing structure that could not be resolved from the sparser dataset. Third, we characterise how bout duration, amplitude, and IBI covary with position within the plume, going beyond the bout count metric alone. Even with an increased spatial resolution compared to the Vergara et al. (2013) dataset analysed by J. Burgués and S. Marco (2020) and Schmuker, Bahr and Huerta (2016), we uncover similar trends of downwind distance encoded by bout count and lateral displacements encoded by bout count variance.

When fitting the sigmoid curves to trial average bout counts along the plume centre line of freestream datasets for varying wind speeds, omitting source effects, we saw that with increasing wind speed the fit sigmoid move toward downwind extent to the point of the $20cm/s$ dataset not showing the full sigmoid curve. Increasing wind speed increased the bout count peak of the sigmoid curve, consistent with the higher number of shorter-duration fluctuations near the FTP observed in the $20cm/s$ freestream dataset (see fig. 3.11). Relying on sigmoid fitting for source distance approximation on bout count alone, although visually accurate, makes approximation at distance or close to the source impossible due to flattening areas of the sigmoid curve. As described in section 3.6, statistics were calculated from the full $240s$ duration of each trial (each trial being a single recording in which the plume was fully established prior to capture), but we do further explore the impact of sample duration in the supplementary section appendix A.4. Successful navigation of turbulent scalars to their source could be achieved using bout statistics alone, but would likely not be robust. A strategy to mitigate areas in which bout count is low or bout count reaches a maxima close to the odour source would be essential.

We omit the near-bed release configuration from our overall trend comparison. Along the plume centre line, the bout amplitudes remained greater than the amplitude threshold on average. With increasing downwind distance from the FTP to the downwind extent the bout count consistently increased, bout duration and IBI decreased. These trends in the near-bed bout statistic curves suggested that its proximity to the floor reduced the turbulent diffusion of the odorant concentration. Scalars released within or near the boundary layer tend to exhibit streaky, persistent concentration fields rather than the intermittent filamentous structure characteristic of freestream plumes: the strong mean velocity gradient near the bed drives lateral shear dispersion, while the viscous sublayer suppresses the turbulent mixing that generates intermittency in freestream conditions (P. Moore and J. Crimaldi, 2004). The scalar release within the boundary layer increased odour dispersion and meant that concentration remained high throughout the test section with small relative fluctuations and

relatively laminar flow (Connor, McHugh and J. P. Crimaldi, 2018) as seen in fig. 3.2d. These factors and the choice of constant filter parameters for all release configurations meant that bout analysis failed to extract the same trends within the near-bed dataset as observed in the freestream. We therefore conclude that the bout statistical trends seen in the near-bed datasets were not directly comparable to those of the freestream dataset, likely due to the less turbulent nature of the near-bed plume.

The rapid apparent dissipation of plume concentration with downwind distance observed in the PLIF recordings was investigated further in the addendum (appendix C.1). A Gaussian plume model fitted to the measured concentration along the plume centre line suggests the measured downwind extent is broadly consistent with model predictions, and in some configurations exceeds them. However, the differential diffusivity of helium (the carrier gas) and acetone raises a potential concern: helium diffuses approximately 6.6× faster than acetone, meaning the acetone may separate from its helium carrier and exit the laser sheet plane, causing the plume to appear to dissipate more rapidly than it truly does. A direct fluorescence-to-concentration calibration would be required to resolve this ambiguity.

3.9 CONCLUSION

We demonstrate the application of a processing technique of bout analysis, typically reserved for MOX recordings, on PLIF wind tunnel recordings of turbulent scalars. PLIF data provides a unique opportunity to explore statistics of bouts simultaneously in time over the entire experimental area in high spatial resolution. These datasets provided a clear demonstration of the impact of wind speed and release height on the bout statistics and their spatial relationship to the odour source distance. Insights from this analysis allowed us to expand our understanding of the core aspects of the turbulent plumes that enable organisms to locate the source of an odour.

Turbulent scalars in the freestream showed a decrease in average bout count with downwind distance, however with increased spatial resolution this relationship was not linear. We fit three sigmoid curves to the three wind speeds and showed an increase in the downwind extent of these curves with increasing wind speed. On average variance of bout counts did increase with crosswind distance, but this relationship was gated by the bout counts. At the lateral edges and downwind plume extent, the bout counts decreased resulting in an overall decrease in bout count variance making variance an unreliable method of approximating lateral displacement.

Extracting overall trends of bout statistics and sampling location within the plume under the assumption of linear correlation with PCA showed clear encoding of downwind distance by PC1 along the plume midline and wind speed, for the downwind and crosswind distance by PC1 and PC2, respectively, in crosswind profiles and interchangeably in full plume analysis of all freestream datasets.

The near-bed release configuration did not show the same trends as the freestream, with consistently increasing bout count with downwind distance on average. The boundary layer proximity reduced diffusion of the scalar and therefore these trends were not present within the downwind extent of the test section. We believe these same trends may occur at greater distances, but were not observed in these datasets.

The dynamic nature of turbulent plumes makes odour source localization difficult, but with a reliable proximity estimation of the odour source, navigation strategies can be devised to find the source of the odour. We observed consistent relationships between bout statistics and the odour source distance across the freestream datasets. These could be used to compensate for wind speed and reliably and rapidly estimate odour source distance in turbulent odour plumes.

4

IN-SILICO INSECT-LIKE NAVIGATION STRATEGIES IN AIRBORNE TURBULENT PLUMES

Samuel Sutton [a], Aaron True [b], John Crimaldi [b], and Michael Schmuker [a]

[a] Centre of Data Innovation Research, School of Physics, Engineering & Computer Science, Department of Computer Science, Biocomputation Research Group, University of Hertfordshire, UK

[b] Civil, Environmental, and Architectural Engineering, University of Colorado Boulder, CO, USA

4.1 KEYWORDS

Odour source localisation; bio-inspired navigation; surge-and-cast; *Drosophila*; anemotaxis; agent-based simulation; turbulent plumes; planar laser-induced fluorescence

4.2 PREFACE

This chapter is a preliminary manuscript in which we compare the performance of three odour-gated anemotactic strategies in airborne odorant plumes recorded using the PLIF technique. We explore a flying moth inspired cast-and-surge strategy and two walking *Drosophila*-like strategies, one with the ability to follow odour direction and the other without. We comparatively analyse the success and speed of each strategy and explore the impact of the odour release condition on the odour source navigation performance.

4.3 CREDIT CONTRIBUTION STATEMENT

Samuel Sutton: Conceptualization, Investigation, Formal analysis, Software, Visualization, Writing - Original Draft, Writing - Review & Editing **Aaron True**: Data Curation, Conceptualization **John Crimaldi**: Data Curation, Conceptualization **Michael Schmuker**: Conceptualization, Writing - Review & Editing, Supervision

4.4 ABSTRACT

Insects reliably navigate turbulent airborne odour plumes to locate mates, find food and evade predation. Recent work suggests that *Drosophila melanogaster* biases airflow based turning decisions with the direction of motion of odours, sampled with a temporal correlation in odour signals between their antennae (Kadakia et al., 2022). Reconstructions of wind tunnel generated odour plume slices recorded with the PLIF technique allow for comparative

analysis of odour-based navigational strategies under varying release conditions, such as bulk airflow speed and odour release height. Through agent based simulations, we examine the performance and compare trajectories of three navigation strategies that differ in their ability to sense local odour gradients and their behaviour in the absence of odour. We find that the availability of local odour gradient information is vital for accurate odour direction following in proximity to the odour source. For efficient and successful navigation in a bounded environment accurate navigation was not key, instead a robust strategy for locating the plume In the absence of odour was more important.

4.5 INTRODUCTION

Odour-guided navigation is an essential behaviour for many animals, encompassing foraging, locating mating partners, and escaping predators. Recently, interest in algorithms for odour source localization has also been growing in robotics and AI. Applications in which odour-guided navigation could be useful have been suggested e.g. in disaster management (Fan et al., 2019), environmental monitoring (Yuan et al., 2020), and agriculture (Valente et al., 2018).

Odour localisation in natural environments is difficult because airflow and therefore odour dispersal are dominated by turbulent processes, and gradient-ascent navigation strategies such as chemotaxis are unviable (Riffell, Abrell and Hildebrand, 2008). However, animals solve this problem reliably. The study of animal behaviour is therefore a promising route towards more efficient odour navigation algorithms. In their seminal work, C. T. David, Kennedy and Ludlow (1983) analysed how male gypsy moths locate mating partners over long distances, largely in the absence of visual cues, only on the basis of small quantities of pheromone released by the female. They described their behaviour as *odour-gated anemotaxis* with a *cast-and-surge* strategy: Move upwind when the target odour is present; move crosswind otherwise. The algorithm therefore switches between two behavioural programmes, i.e. exploration (moving crosswind) and exploitation (moving upwind), triggered by odour encounter events. Odour-gated anemotaxis is an attractive algorithm for robot implementation because of its simplicity. A similar strategy has been observed in the plume tracking behaviour of *Drosophila melanogaster* with the addition of a reliance on visual features (Kellogg, Frizel and Wright, 1962; van Breugel and Dickinson, 2014). Moths differ from flies in that they will not continue to fly upwind and instead cast when exposed to constant streams of odour (T. C. Baker, 1990; Kennedy, 1983; Kennedy and Marsh, 1974).

In its classical version, odour-gated anemotaxis functions with a single sensor. However, it has long been established that "stereo-olfaction" plays a crucial role for odour-guided navigation, in mammals, including humans (Porter, Craven et al., 2007; Rajan, Clement and Bhalla, 2006) as well as insects (Duistermars, Chow and Frye, 2009). A "stereo-version" of odour-gated anemotaxis has been described in walking *Drosophila melanogaster* (Kadakia et al., 2022), showing that they exploit the direction of local odour flow in relation to wind direction for navigation decisions.

Inspired by the two sensor virtual agents navigating simulated odour plumes (Kadakia et al., 2022), we simulated agents navigating in real odour plumes that were previously recorded (Connor, McHugh and J. P. Crimaldi, 2018). We explored whether virtual agents using the strategies outlined by Kadakia et al. (2022) could successfully navigate to the source of the recorded odour plume. We examined the impact of information gleaned from lagged correlation between the two sensors by the odour direction sensing (DS+) agents versus those not equipped with the ability to sense the odour direction (DS-). We compared

the odour source navigation performance of these strategies with our own implementation of the cast-and-surge strategy following the same set of navigation rules.

4.6 MATERIALS AND METHODS

4.6.1 *Plume Recordings*

Acetone plumes were recorded using planar laser-induced fluorescence (PLIF) in a wind tunnel (Connor, McHugh and J. P. Crimaldi, 2018). Two release configurations were used: a "freestream" configuration with gas released 14 cm above the floor of the wind tunnel, and a "near-bed" configuration with gas released 6 mm above the floor. The freestream configuration was tested at 10 cm/s and 20 cm/s (published in Connor, McHugh and J. P. Crimaldi (2018)) and at 5 cm/s (an unpublished configuration kindly provided to us by the original authors). The near-bed configuration was recorded only at 10 cm/s (Connor, McHugh and J. P. Crimaldi, 2018).

A 1mm laser sheet excited the acetone vapour in a horizontal 2D plane parallel to the floor of the test section causing the gas to fluoresce. The light sheet was then imaged using a high-quantum-efficiency camera. The data provides a high spatial resolution top-down view of the structure of the plume. The intensity of the recorded light can be considered as a proxy for the concentration of the gas. Each release configuration had a number of repeated trials, for freestream 5cm/s and 20cm/s there are 10 trials, for the freestream 10cm/s there are 9 trials and the near-bed there are 5 trials.

As previously described by Connor, McHugh and J. P. Crimaldi (2018), the raw images captured with the PLIF setup were converted into a ratiometric representation of gas concentration $\frac{C}{C_0}$ using the following equation adapted from J. P. Crimaldi (2008):

$$\frac{C}{C_0} = \frac{1}{a_c}\frac{I_N - b}{B - b}, \tag{4.1}$$

with I_N raw pixel intensities, B the distribution of light in a region of interest captured by the camera with a constant, maximum uniform acetone concentration, b the dark response obtained from 500 images in the absence of any acetone signal, and a_c a calibration coefficient to normalize the concentrations based on the source concentration C_0 at the tube exit. Connor, McHugh and J. P. Crimaldi (2018) established an rms noise of the PLIF system at $0.001C_0$ in the absence of acetone and reported a detectability limit equal to five times the rms noise floor ($0.005C_0$). To remove erroneous low-amplitude fluctuations below this detectability limit we zero out all data $< 0.005C_0$.

We reproduced instantaneous concentration plots showing the impact of the four flow cases on the spatial structure of the resultant odour plume, with consecutive frames revealing temporal effects. Figure 4.1 shows representative randomly selected non-consecutive frames from the first trial of each configuration. The plots demonstrate the significant structural differences of the turbulent plume under the four different combinations of experimental conditions.

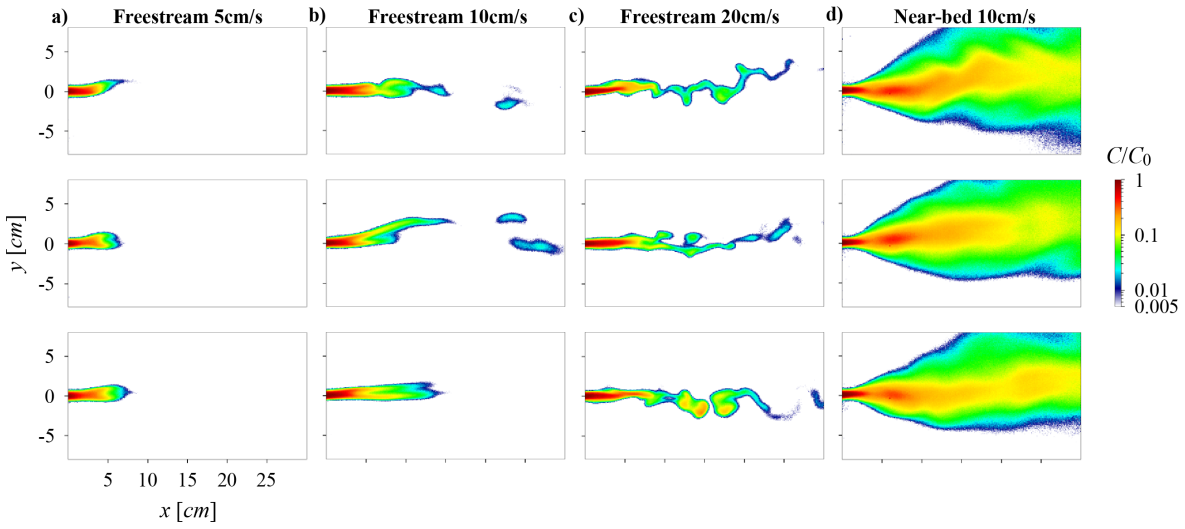

Figure 4.1: Instantaneous concentration plots of three representative frames (rows) from the first trial of the four flow cases (columns). **a-c)** Freestream release configuration at odour release wind velocities of $5cm/s$, $10cm/s$ and $20cm/s$, respectively. **d)** Near-bed release configuration at $10cm/s$. The log colour scale is between the noise floor ($C/C_0 = 5x10^{-3}$) and maximum observed value at the source ($C/C_0 = 1$).

When comparing the three freestream cases, it is clear that **a** shows a limited downwind extent of the odour plume at significant concentrations; comparatively, the main body of the plume doubles in downwind extent in **b** with infrequent filaments travelling the extent of the test section. **c** shows a doubling in downwind extent of the high concentration plume body, with a more narrow and broken plume than in **a** or **b**. One can also compare the plume imaged in the near-bed release configuration **d** to that of the freestream in **b**, both with a flow speed of $10cm/s$, and see significant lateral spreading of the plume and consistent high concentration throughout the downwind extent of the test section. It is clear from fig. 4.1 that the release configuration had a significant impact on the spatial structure of the generated odour plume that would impact how an organism would navigate such a plume.

4.6.2 *In-silico Agents*

We simulated virtual agents with two spatially separated sensors that navigated the PLIF odour plumes using the simple algorithm from Kadakia et al. (2022). In each frame ($66ms/15Hz$), agents turned left or right 90° or maintained an upwind heading depending on the navigation strategy and stepped forward $0.74mm$. The sensors were placed $0.74mm$ to the left or right of the agent centroid. Figure 4.2 **a** demonstrates the relative scale of the agent within an exemplary frame, **b** is a schematic of the agent demonstrating its initial upwind facing state with sensors (0.74mm) to the left (c_L) and right (c_R) of its centroid. The pixel magnification of the experimental data was $0.74mm/pixel$, a pixel corresponding to a physical area of $0.55\,mm^2$. The spatial separation of the sensors corresponds to the smallest possible separation of two sensors around a centroid within the experimental data. **c** shows

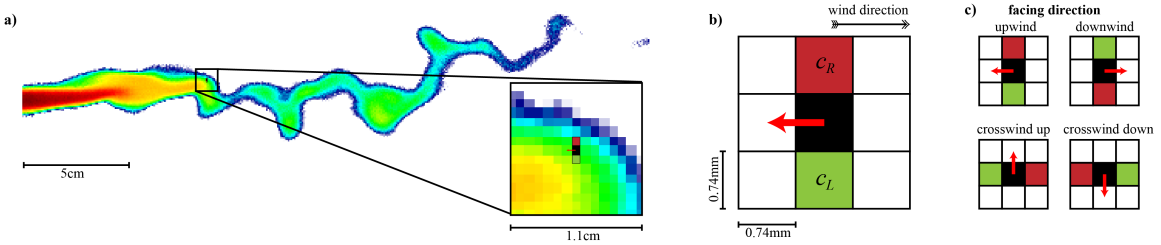

Figure 4.2: Agent Schematic Overview. **a)** Relative scale demonstration of agent in instantaneous plume frame. **b)** Agent with initial facing direction (red arrow) upwind, c_R and c_L are the agents sensors with each sensor one pixel ($0.74mm$) right and left of the centroid, respectively. **c)** Four possible facing directions of the agent.

the four possible facing directions of the agent, described here as upwind, downwind, crosswind up and crosswind down. Wind directions remained a fixed vector for all experiments and described the bulk air flow through the wind tunnel from the left to the right of the test section, with the upwind facing direction corresponding to decreasing x.

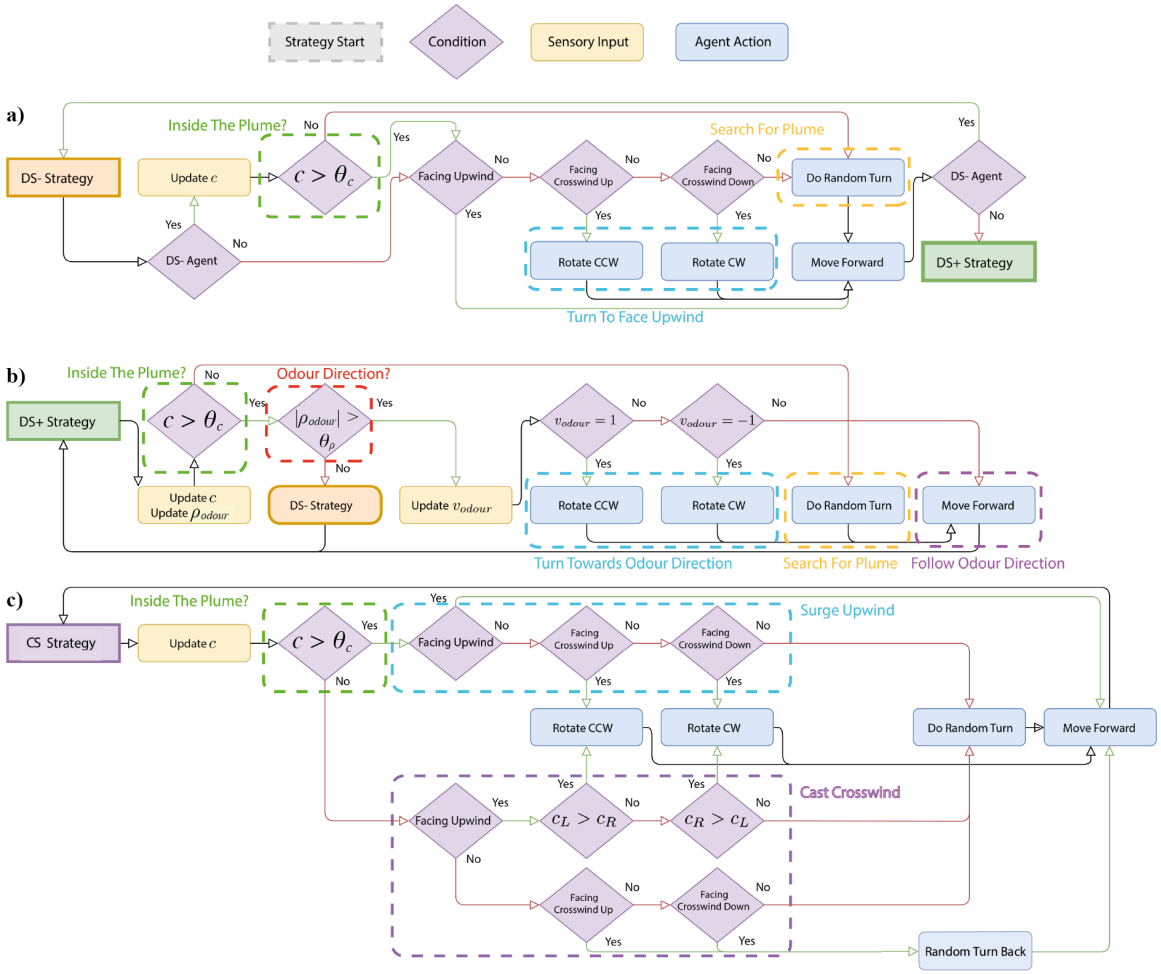

Figure 4.3: Agent Strategy Flow Charts. **a)** Non-direction sensing strategy (DS-). **b)** Direction sensing strategy (DS+). **c)** Cast-and-Surge strategy (CS).

The measured concentration of the odour signal was defined $c = \frac{(c_L + c_R)}{2}$, where the concentration in each sensor was c_L and c_R, respectively. The odour direction was inferred using a Hassenstein-Reichardt correlator-like (HRC) elementary motion detection model (Hassenstein and Reichardt, 1956). The lagged odour correlation between the two sensors was defined as $\rho_{odour}(t) = c_L(t)c_R(t + \Delta T) - c_L(t + \Delta T)c_R(t)$, where the delay time scale ΔT was chosen as 1 frame ($1/15s$). From ρ_{odour}, the direction of odour motion v_{odour} was defined as +1 if $|\rho_{odour}| > \theta_\rho$ and $sgn(\rho) > 0$; as -1 if $|\rho_{odour}| > \theta_\rho$ and $sgn(\rho_{odour}) < 0$; and as 0 otherwise, where θ_ρ was a selected lagged odour correlation threshold and $sgn(x) := -1\ if\ x < 0,\ 0\ if\ x = 0,\ 1\ if\ x > 0$. In general, odour signals with a left component over the virtual agent had $v_{odour} = 1$, while those with a right component had $v_{odour} = -1$. For DS+ flies, whenever the absolute ρ_{odour} was below the threshold $|\rho_{odour}(t)| < \theta_\rho$, but the odour was still detectable $c > \theta_c$, where θ_c was a selected threshold for the detection of the odour, the agent obeyed the DS- strategy (fig. 4.3).

Taking inspiration from the navigation strategies of gypsy moths (C. T. David, Kennedy and Ludlow, 1983) and expanding on the previously defined rule set of the DS- strategy (Kadakia et al., 2022), we derived a third strategy that followed the surging behaviour of the DS- agents in the presence of detectable odour. However, instead of random walking behaviour in the absence of odorant above the odour detection threshold ($c \leq \theta_c$) the agent would cast crosswind to locate the plume once again. We refer to this method as the cast-and-surge (CS) strategy. This strategy, much like the DS- strategy was dependent upon the facing direction of the agent. When facing upwind, the CS agent casts in the direction of the sensor with the greatest concentration. When facing crosswind (perpendicular to the wind direction), the agent continued forward without turning. If the agent was facing downwind, or was facing upwind and detected no difference between its sensor readings, the agent turned 90° randomly. Therefore, in the absence of detectable odour ($c \leq \theta_c$) the agent cast crosswind until the odour was detected once more, improving its chances of finding the odour plume once more. In the crosswind casting state, and when facing away from the plume centre line, the agents had a random turn back chance with an increasing probability as it moved towards the test section edge. This was achieved by normalising the y position of the agents within the test section to the range $[-1, 1]$, giving y_{norm}. Then for each time step in which the agent moved crosswind away from the centre line, a random value X was drawn from a continuous uniform distribution $X \sim U(a, b)$ with a probability density function (pdf) given by $f(x) = \frac{1}{b-a}$ for $a \leq x \leq b$ with $a = 0$ and $b = 1$, and therefore a pdf of $f(x) = 1$ or the likelihood of drawing any value being equal. Finally, the decision to turn back was determined by $X > y_{norm}^4$.

Simulations were carried out separately for agents that could sense (DS+), could not sense (DS-) odour motion, and those that cast crosswind instead of random walking (CS).

We conducted a systematic analysis in each of the PLIF odour release configuration datasets not only to explore the performance of the DS- and DS+ strategies in real odour

plumes, but also to compare the efficacy of casting to random walking in search of the odorant plume.

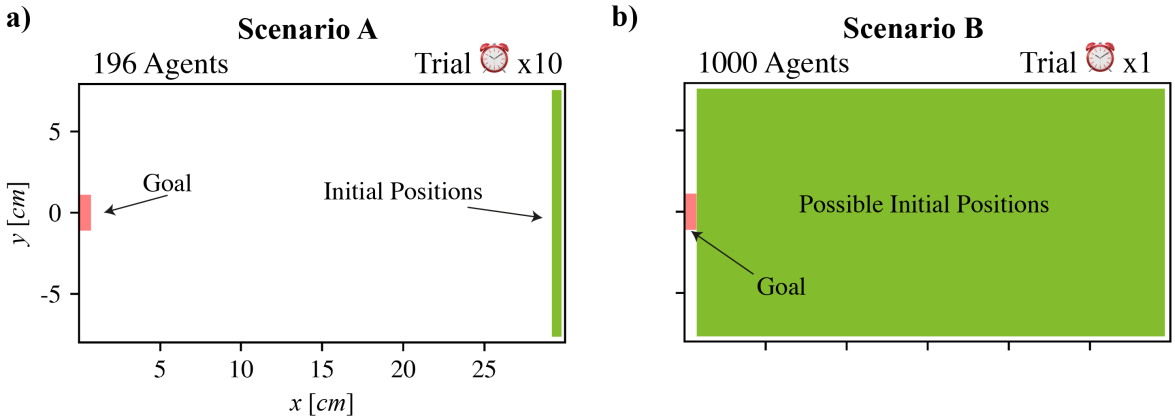

Figure 4.4: Initial Position Schematics. **a)** Scenario A, agents initially span lateral test section extent of the plume limiting the number of agents to 196 agents and time limit to navigate to goal is $10x$ the trial duration. **b)** Scenario B, 1000 agents with rand initial positions downwind of the goal area within lateral test section extent with time limit of $1x$ trial duration.

To determine the relative performance of the four bioinspired odour source localisation algorithms, we tested two scenarios. In Scenario A, fig. 4.4 left panel, we initialised 196 agents facing upwind at the downwind extent of the wind tunnel. Agents were stepped through ten consecutive repetitions of each dataset (i.e. the recorded trial was looped ten times), giving a total simulation time of approximately $2400s$ per agent (ten $\times$ $240s$ per trial). For Scenario B, fig. 4.4 right panel, we randomly initialised 1000 upwind facing agents at any location within the test section downwind of the goal. The simulation time was limited to a single repetition of the dataset ($240s$).

The aim of Scenario A was to determine the ability of the strategies to explore the test section and locate the odour plume effectively given a significant amount of time. Whilst in Scenario B, we significantly limited the time the agents were given to locate the odour source, and increased number of tested agents. By using the whole test section, we also increased the number of tested feasible starting positions and were able to further explore the odour plume and source localisation methods that the strategies used. When an agent reached the lateral boundary of the test section, it turned 180° to face back towards the centre of the test section. The only failure conditions for the agents were touching the upwind edge of the test section on either side of the goal area and not reaching the goal within the allotted time.

As shown in fig. 4.5, we initially explored 31 values between 0.001 and 1.0 of the odour detection threshold (θ_c) for the DS- and CS strategies and 31 values between 0.001 and 1.0 of both odour detection and odour correlation θ_ρ thresholds for the DS+ strategy. We highlight only the best-performing simulations here, but show full performance metrics for Scenario A in appendix B.1 and Scenario B in appendix B.2. The selected values of θ_c and/or θ_ρ for each

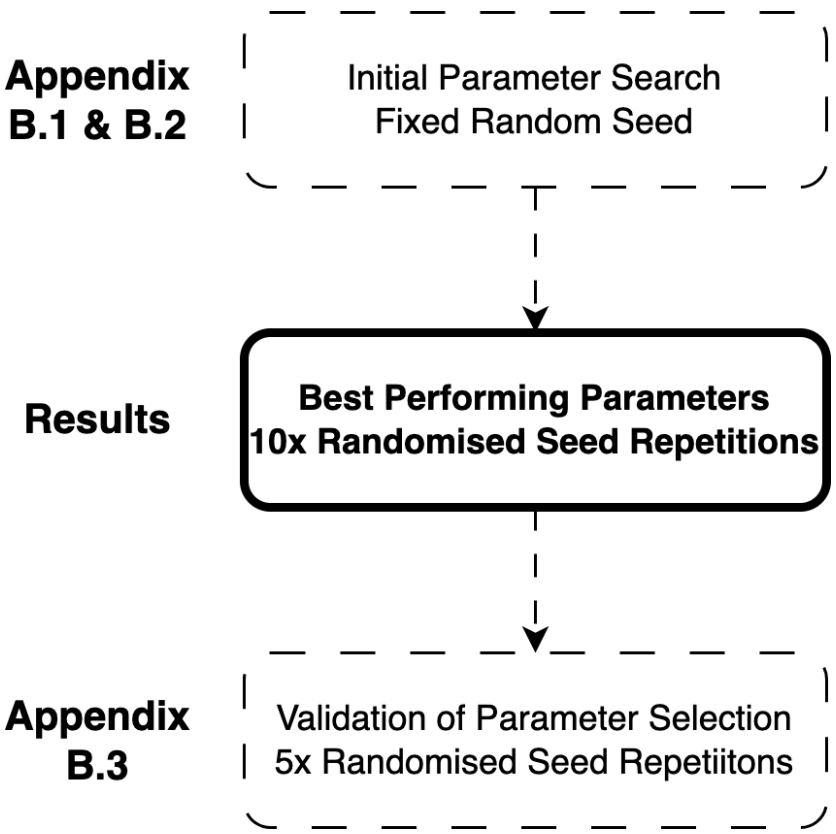

Figure 4.5: Simulation Pipeline Flow Chart showing an overview of how the best performing parameters where determined and validated. Dotted lines denote results shown in the appendix.

release configuration, wind speed, and navigation strategy for Scenario A are highlighted in table B.1 and Scenario B are highlighted in table B.2.

We carried out further simulations of the best performing parameters determined but randomised the seeds responsible for the initial agent positions, turning and turning back and show those results in section 4.7. Finally, we carried out further validation simulations that are discussed in appendix B.3.

4.7 RESULTS

In this section, we explore the performance of the three navigation strategies under different odour release configurations. We tested two Scenarios; Scenario A in which 196 agents had to navigate from the downwind extent of the test section with little time constraint, and Scenario B in which 1000 agents were unrestricted in their initial position but were given a strict time constraint to locate the odour source. For each Scenario and release configuration, we selected the best performing values of the odour detection threshold θ_c and the correlation threshold θ_ρ (only for DS+ agents) determined in appendices B.1 and B.2; the chosen values are tabulated in table B.1 (Scenario A) and table B.2 (Scenario B). We then performed a further 10 repetitions on each trial of the four release configurations of Scenario A and Scenario B. For each repetition we randomised the seeds that were responsible for the turning in random walking behaviour and for initial agent positions in Scenario B. Here, we examine the trajectories that result from each strategy in the four release configurations and then compare their performance.

4.7.1 *Scenario A: Agents Position initialised at Downwind Extent*

For Scenario A, we initialised the 196 agents at the downwind edge of the test section and gave the agents $2400s$ or $10x$ the trial duration to navigate to the goal area at the odour source. To compare the trajectories produced by agents using the three navigation strategies, we plot the trajectories of the repetition with the highest success percentage and the lowest mean success time. For Scenario A and for each of the three strategies (figs. 4.6 to 4.8), we show all 196 of the agent trajectories. We highlight the successful agent with the median success time and plot its normalised sensed odour concentration (c_L, c_R) and use statistics (c, $|\rho_{odour}|$ for DS+ only) for the duration of the agent's navigation.

For Scenario A and the DS- agents (fig. 4.6), we found that the agents spent most of the time random walking, only showing long-duration surges where the agent remained close to the centre line of the plume. The DS- strategy required very low odour concentration thresholds θ_c in the freestream datasets for successful odour source navigation due to limited probability of encounter and difficulty remaining within the plume in the absence of odour direction following. In contrast, DS- agents in the near-bed release configuration had greater success with a higher odour concentration threshold θ_c due to the wider plume and therefore the increased probability of odour encounter.

The freestream $5cm/s$ (fig. 4.6**a**) shows that the limited downwind extent of the plume required extensive random walking by agents, with the majority of agents not successfully locating plume within the time limit. The highlighted median agent found the plume intermittently between $10cm < x < 15cm$ and continuously $x < 10cm$, but spent more than $2000s$ trying to locate the plume by random walking. Note the white space $x < 10cm$ and the failure trajectories $x > 15cm$ & $|y| > 2cm$ caused by the absence of significant or consistent

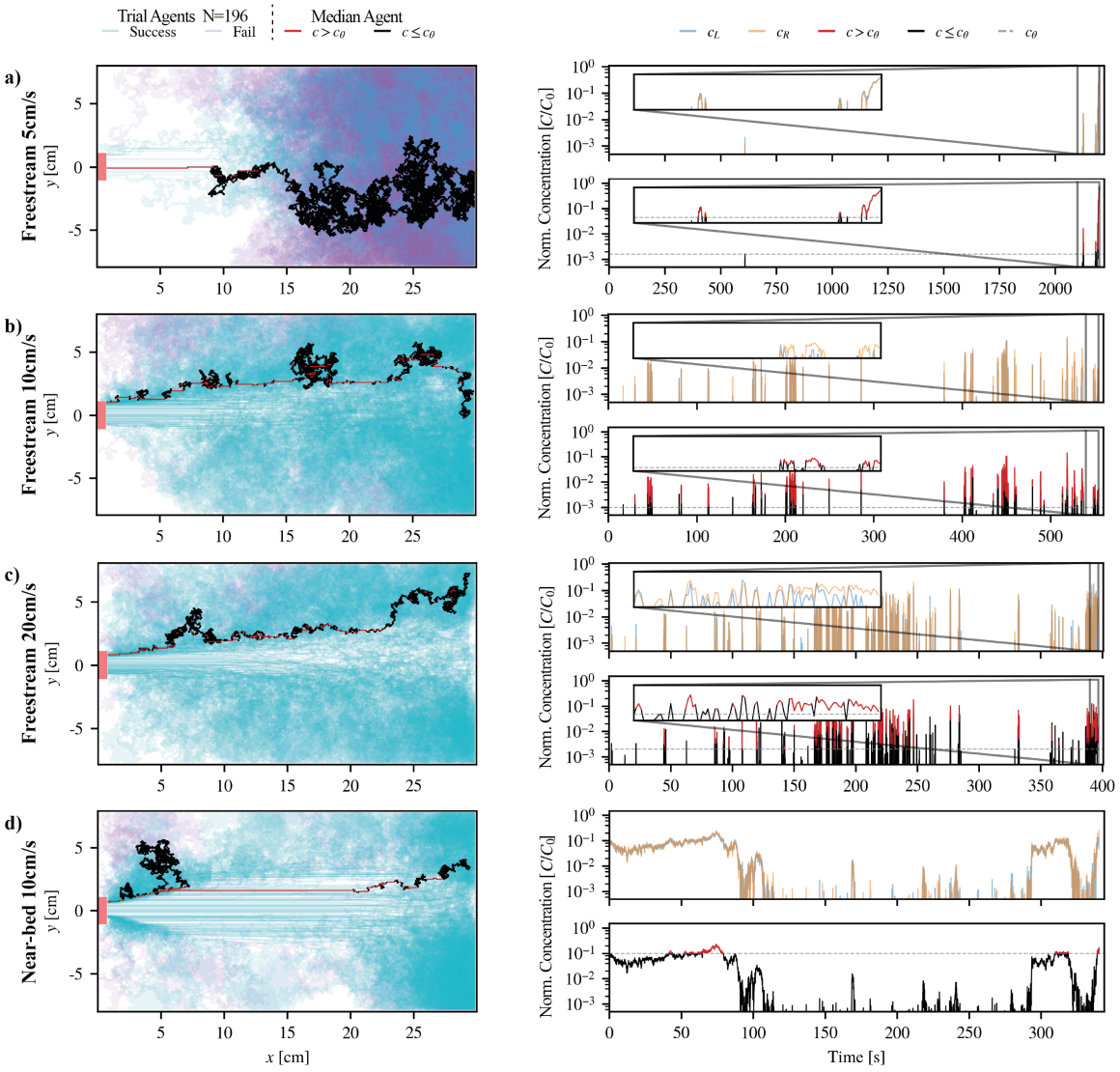

Figure 4.6: Scenario A: DS- Trajectories. Rows **a-d)** show the release configurations freestream $5cm/s$, $10cm/s$ and $20cm/s$ and near-bed $10cm/s$, respectively. For each row, the left panel shows all 196 agent trajectories from the best-performing trial and repetition coloured by whether they successfully navigated to the goal *light blue* or failed to do so *purple*. We highlight the median performing agent and plot where the agent did not encounter the odour *black* ($c \leq \theta_c$) and where it did in *red* ($c > \theta_c$). The red box in the plot illustrates the location of the goal; reaching it ceases the agent's navigation and signifies a success. The right upper panel for each row shows median agent left (c_L) and right (c_R) sensor values. In the right lower panel we plot the mean sensor readings (c) for the median agent, highlighting odour encounters ($c > \theta_c$) in red and the concentration threshold (θ_c) with a dashed grey line. Artefacts where the black line is above the θ_c are caused by instantaneous encounters where c crosses the threshold.

odour encounters that reached the agents at the downwind extent. The freestream $10cm/s$ (fig. 4.6**b**) saw odour encounters along the entire downwind extent of the test section. The highlighted median agent remained at the edge of the plume, intermittently surging upwind when it encountered the odorant and random walking for longer periods otherwise. The frequency of encounter of the highlighted agent was significantly increased compared to fig. 4.6**a**. The failure trajectories were far fewer and only occurred at the test section y edges, likely caused by agents that consistently random walked and did not locate the plume. The freestream $20cm/s$ (fig. 4.6**c**) saw a higher percentage of successful agents than lower wind speeds. The straight-line surging trajectories extended further downwind along the plume centre line due to the increased wind speed. Odour encounters occurred further crosswind at the downwind area of the test section, but the odour encounters were shorter in duration due to the increased turbulence. The highlighted agent spent much less time random walking compared to those in fig. 4.6**a** and **b** with significantly more odour encounters during a shorter successful navigation duration. The near-bed $10cm/s$ (fig. 4.6**d**) showed a higher number of agents initialised within the confines of the plume that caused earlier odour encounters compared to all of the freestream trials. With greater horizontal dispersion of the plume, the agents more rapidly located the plume at a high odour concentration and surged upwind. However, agents at edge of the plume lost the plume where it narrowed close to the odour source and had to random walk back to find the edge of the plume. Although the trajectory of the highlighted agent shows a large surge, the time series shows that it spent the majority of the time random walking after reaching the upwind edge of the plume.

The DS- agents that initially encountered the plume at the edges (where encounters were intermittent) continuously lost the plume and had to random walk to find the plume once more in order to successfully navigate to the odour source. The freestream datasets with lower wind speeds saw agents have longer continuous odour encounters when the plume was finally located, suggesting that encounter durations were inversely correlated with wind speed. Initially, finding the plume was the most time-consuming aspect of this strategy, with random walking not always resulting in the agent locating the plume. Agents on the positive y edge of the plume saw $cL > cR$ and those on the negative y edge of the plume saw $cR > cL$ on average, with agents not addressing this unbalance of the sensor signals where $c > \theta_c$. The DS+ strategy should address the unbalanced sensor signals through odour direction sensing and following.

For Scenario A, the DS+ agents (fig. 4.7) would consistently initially random walk to the edge of the plume, intermittently surging upwind with an edge following behaviour, and finally follow the odour direction to locate the plume centre line when in proximity to the odour source. The odour direction sensing behaviour produced a funnelling of the trajectories towards the plume centre line, where the sensed normalised odour concentration was high enough to produce a significant lagged odour correlation $|\rho_{odour}|$. Similarly to the trajectories produced by the DS- strategy, the DS+ strategy required a significant amount of

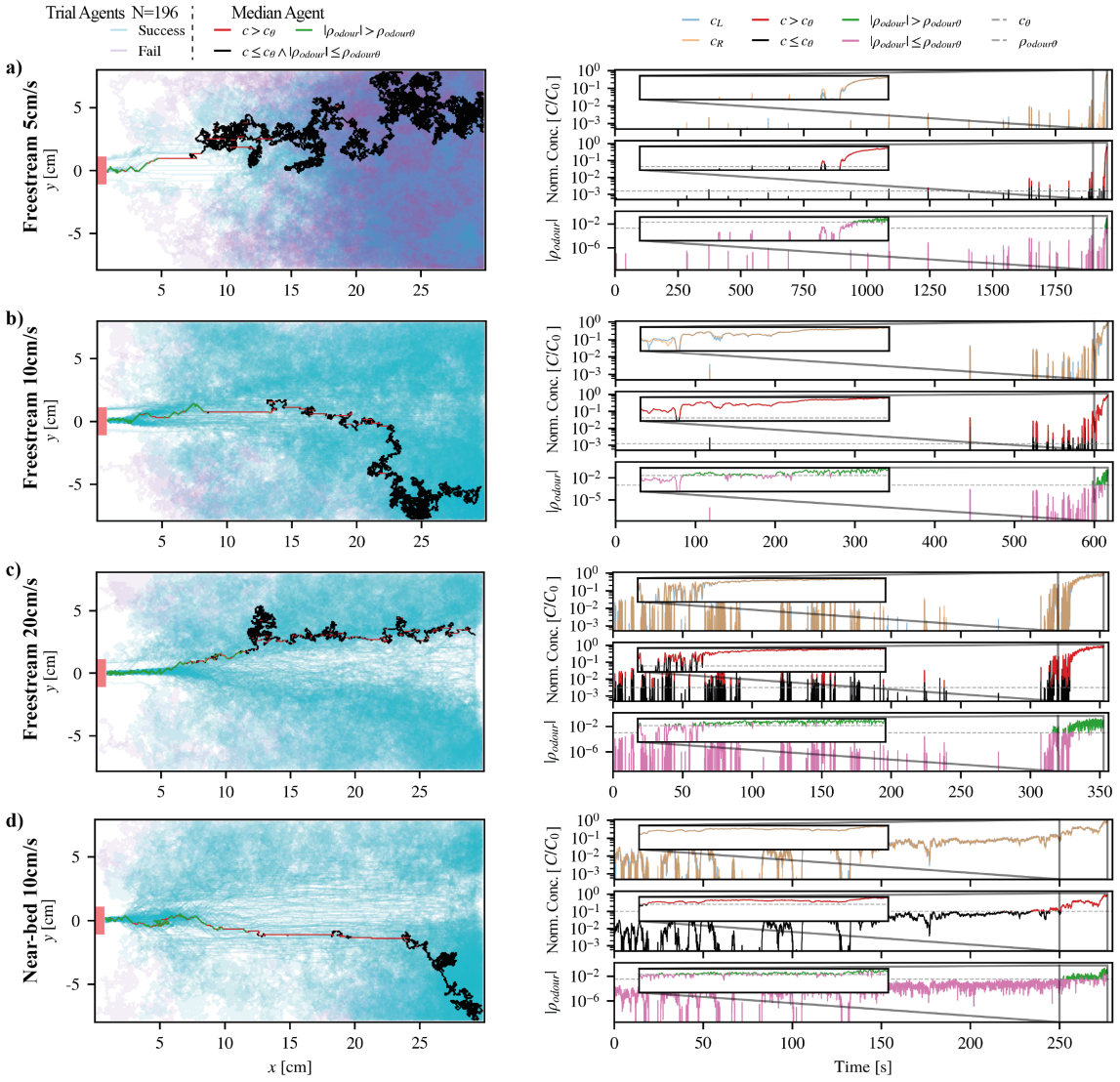

Figure 4.7: Scenario A: DS+ Trajectories. Rows **a-d)** show the release configurations freestream $5cm/s$, $10cm/s$ and $20cm/s$ and near-bed $10cm/s$, respectively. For each row, the left panel shows agent trajectories from the best-performing trial and repetition, colouring the trial agent trajectories of the agents that successfully navigate to the goal light blue and those that failed to do so purple. We highlight the median performing agent and plot where the agent did not encounter the odour and therefore had negligible odour correlation black ($c \leq \theta_c \wedge |\rho_{odour}| \leq \theta_\rho$), where the agent encountered odorant at a concentration greater than concentration threshold red ($c > \theta_c$). Where the median agent encountered lagged temporal correlation above the odour correlation threshold ($|\rho_{odour}| > \theta_\rho$) we highlight green. The red box in the plot illustrates the location of the goal, in which the agent ceases navigation and signifies a success. The right upper panel shows median agent left (c_L) and right (c_R) sensor values. In the right middle panel we plot the mean sensor readings (c) for the median agent, highlighting odour encounters ($c > \theta_c$) in red and the concentration threshold (θ_c) with a dashed grey line. In the right lower panel we plot the absolute lagged odour correlation ($|\rho_{odour}|$) and highlight in green where it exceeds the correlation threshold ($|\rho_{odour}| > \theta_\rho$) as well as the correlation threshold (θ_ρ) with a dashed grey line.

random walking to initially locate the plume and occasionally relocate it; however agents rarely lost the plume after odour direction following initiated.

The freestream $5cm/s$ (fig. 4.7**a**) showed the same extensive random walking with only intermittent odour encounters occurring further downwind as previously seen in (fig. 4.6**a**). Fail agent trajectories occurred throughout the test section, but all agent trajectories that passed within $x < 10cm$ & $|y| < 2cm$ successfully located the odour source. Within this area, we observed surging up to an $x = 5cm$, followed by odour direction following to the goal area. The highlighted agent shows random walking with no significant odour encounters for $\approx 1600s$, with only intermittent odour encounters. It finally reached the body of the plume in the last few seconds of the total navigation time. The freestream $10cm/s$ (fig. 4.7**b**) had an area of intermittent upwind surging between $10cm < x < 25cm$ & $|y| < 3cm$ similar to that of the DS- strategy (fig. 4.6**b**), and again success agents trajectories outnumber those of the failure agents only appearing at the test section edges. The difference seen here is clear odour direction following behaviour that consistently occurred $x < 10cm$. The highlighted agent only surged upwind closer to the centre line of the plume and more intermittently than in fig. 4.7**a**, but odour direction following initiated almost twice the downwind distance. The freestream $20cm/s$ (fig. 4.7**c**) showed an increase in the intermittency of odour encounters compared to fig. 4.7**b** but similarly to fig. 4.6**c**. The increased turbulence at $20cm/s$ produced more random walking between encounters and only very short straight-line surging trajectories. Funnelling due to odour direction following close to the source appears more dramatic and extends further downwind to $x = 13cm$, with the highlighted agent showing a much longer duration of odour following behaviour. The near-bed $10cm/s$ (fig. 4.7**d**) saw a similar amounts of surging behaviour as in fig. 4.7**b** with failure trajectories occurring only at the test section boundaries. As seen in the DS- strategy, the best performing odour detection threshold was significantly higher in the near-bed compared to the freestream because of the greater availability of odour encounters throughout the test section. The DS+ strategy solves the issue clearly seen in DS- (fig. 4.6**d**, in which agents lost the plume at its upwind bounds, here the agents instead followed the plume centre line to the odour source.

For all DS+ agents, the normalised sensed odour concentration c_L and c_R matched on average where its lagged odour correlation exceeded the correlation threshold $|\rho_{odour}| > \theta_\rho$. Hence we found agents consistently moving to the centre line of the plume while tracking upwind to odour source. However, this strategy still relies on random walking to initially locate and relocate the plume. The cast-and-surge strategy aimed to address the inefficiency of this random walking behaviour.

For the cast-and-surge agents in Scenario A (fig. 4.8), we found that for the three freestream release configurations, a similarly low concentration threshold θ_c performed best. For the near-bed release configuration a concentration threshold θ_c lower than that of the DS- and DS+ strategies (figs. 4.6 and 4.7) produces the most successful and fastest odour source navigation. This was likely a result of casting being a more reliable behaviour for relocating of the plume once lost than random walking. We saw that the agents lost the plume for

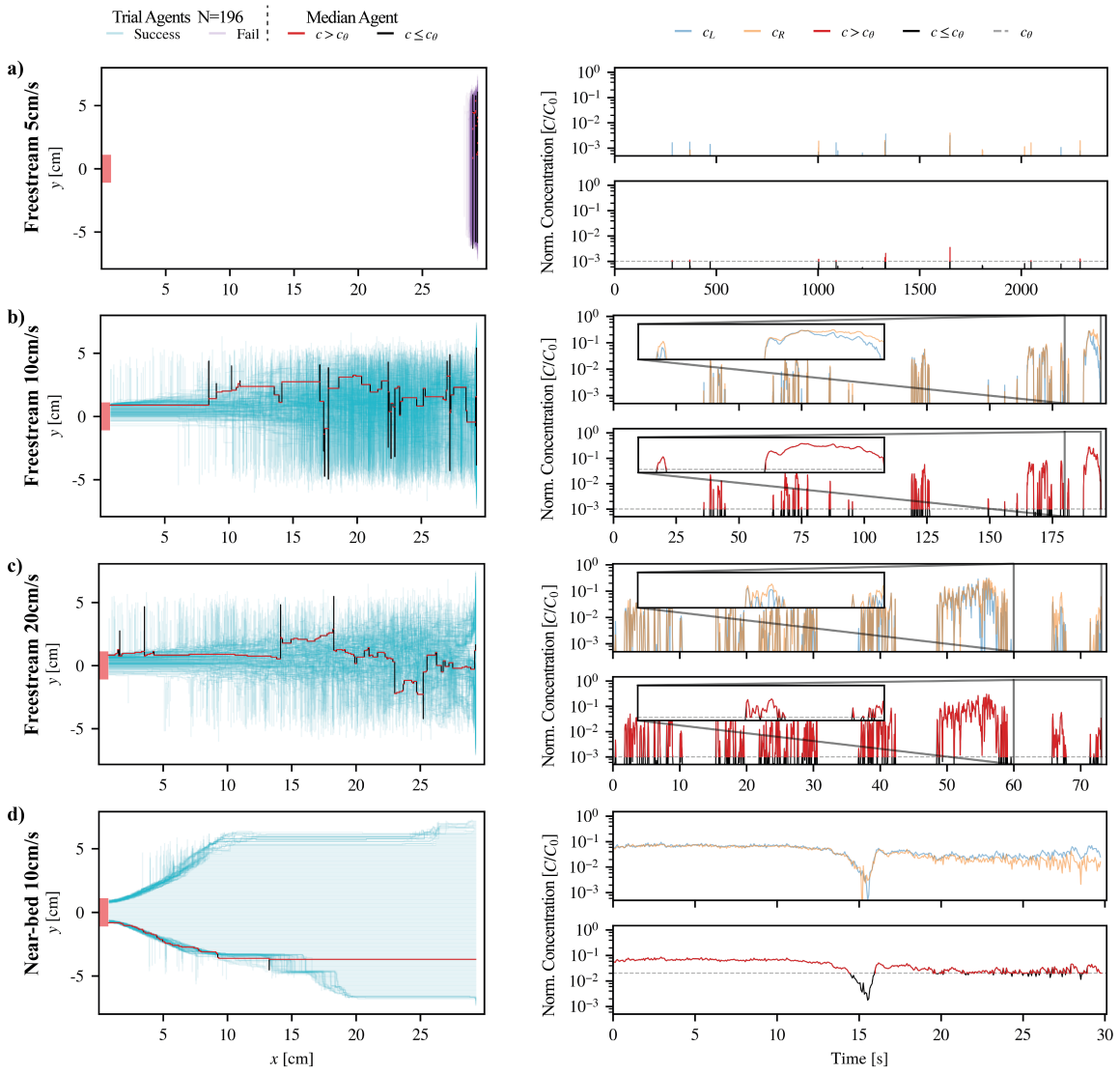

Figure 4.8: Scenario A: Cast Surge Trajectories. Rows **a-d)** show the release configurations freestream $5cm/s$, $10cm/s$ and $20cm/s$ and near-bed $10cm/s$, respectively. For each row, the left panel shows agent trajectories from the best-performing trial and repetition, colouring the trial agent trajectories of the agents that successfully navigate to the goal light blue and those that failed to do so purple. We highlight the median performing agent and plot where the agent did not encounter the odour black ($c \leq \theta_c$) and where it did so red ($c > \theta_c$). The red box in the plot illustrates the location of the goal, in which the agent ceases navigation and signifies a success. The right upper panel shows median agent left (c_L) and right (c_R) sensor values. The right lower panel we plot the mean sensor readings (c) for the median agent, highlighting odour encounters ($c > \theta_c$) in red and the concentration threshold (θ_c) with a dashed grey line. Artefacts where the black line was above θ_c were caused by instantaneous encounters where c crossed the threshold.

two main reasons; horizontal wavering of the plume caused casting at the plume edges, the agent surged past the upwind plume bounds. With the casting behaviour the agent was able to travel away from the plume centre line and towards the test section bounds and turn back once more to find to the plume.

The freestream $5cm/s$ (fig. 4.8**a**) was the only scenario/strategy combination that showed zero success. Agents remained in a casting state at downwind test section extent due to very intermittent and low-concentration odour encounters on one or both sensors. All agents failed due to the time limitation of $2400s$. The randomly selected median agents (due to the matching failure times and success of 0%) show only very intermittent periods in which it encountered the odour and generally only on a single sensor. In contrast, all other release configurations showed that the cast-and-surge agents achieved a success rate of 100%. The freestream $10cm/s$ (fig. 4.8**b**) shows casting trajectories close together that became spaced out as the agents moved upwind due to the increased probability of odour encounters closer to the source. The highlighted agent shows intermittent odour encounters that only reliably increased in duration near the odour source $x < 10cm$. Odour encounters were significantly more frequent and of greater odour concentration than those seen in fig. 4.8**a**. The freestream $20cm/s$ (fig. 4.8**c**) shows more equal spacing of casting trajectories throughout the test section (with an increased downwind extent of the odour plume at higher concentrations) although the surges appeared shorter compared to those seen in fig. 4.8**b** due to the increased turbulence caused by the higher wind speed. The near-bed $10cm/s$ (fig. 4.8**d**) showed early odour encounters for all agents with minimal initial casting where $y < |6|cm$. The agents lost the plume at the upwind edge where the plume narrowed but also at the negative y edge due to intermittent encounters in one or both sensors. These agents would cast out of the plume but always either relocated the plume edge or simply cast turn back towards the plume centre line before encountering the test section boundary and proceed back to the plume once again.

All highlighted agents demonstrated an imbalance in the left c_L and right c_R sensors. Without the ability to follow odour direction and simple upwind surging with odour encounters, this imbalance was not addressed. If agents did not randomly turn back and were penalised for touching the test section bounds, cast-and-surge would not be an adequate odour source localisation strategy and would likely show a significantly lower success percentage. This strategy is only successful because of the bounded nature of the input data and the scenarios tested here.

In Scenario A performance metric analysis fig. 4.9, we plot metrics calculated from all repetitions of each trial for each release configuration and for the three strategies. We show the percentage of agents who were either successful with an odour encounter, failed to locate the goal with an odour encounter, or failed without an odour encounter. We considered an encounter had occurred when an agent detected a mean concentration c on its left c_L and right c_R sensors above the concentration threshold θ_c, even if it was instantaneous or only occurred once. We plot the time of the first odour encounter for all successful and

unsuccessful agents and the goal time for only the successful agents. For comparison within the release configurations, we also plot the ratio of the initial encounter time to the goal time of the successful agents.

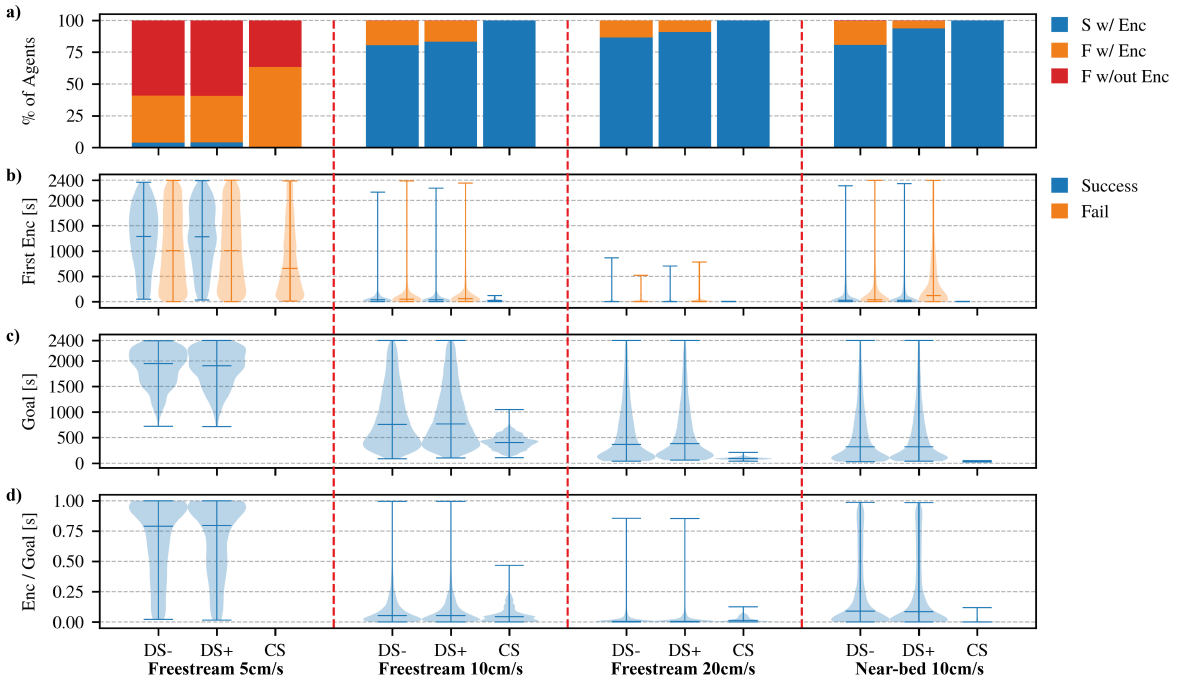

Figure 4.9: Scenario A: Performance Metric Analysis. **a)** agent performance metrics as a percentage of total agents of 10 repetitions of each trial and release configuration. Agents that successfully navigated to the goal and encountered the odorant above the odour detection threshold ($c > \theta_c$) are shown in blue. Those that failed to navigate to the goal within the time limit or missed the goal and touched the upwind test section boundary are shown in orange or red if they did or did not encounter the odorant at a concentration greater than the detection threshold, respectively. **b)** violin plot of the initial odour encounter times of each successful and failure agent shown in blue and orange, respectively. **c)** violin plot of the time each successful agent took to navigate to the goal. **d)** violin plot of first encounters individually divided by goal time of agent for all agents. Violin plot bars show minimum, median and maximum values for all agents in each repetition of each trial collated. Note absence of success violin plots for freestream $5cm/s$ release configuration in **b-d** due to 0% success of cast-and-surge strategy in this scenario.

From fig. 4.9**a**, we found that the freestream $5cm/s$ release configuration showed the lowest success rate for all three strategies, most notably the cast-and-surge strategy failed to have a single agent navigate to the odour source for any of the ten random seed repetitions of each trial within the time limit (0% success). In contrast, the cast-and-surge strategy achieved 100% success in each repetition of each trial for all other release configurations, with the fastest initial encounter and average success times of the three strategies. This suggests that the casting behaviour was more efficient than random walking where the odour was below the detection threshold, but only when the plume extended to the downwind extent of the test section. The limited downwind dispersal of the freestream $5cm/s$ plume caused it to be the only release configuration that saw agents fail to encounter the odorant within

the ten repetitions of the trial duration for Scenario A. We saw that for all strategies in the freestream release configurations, that with increasing wind speed the average success percentage increased, the mean and maximum first encounter times decreased, and the mean goal times decreased (as shown in fig. 4.9**a**). For reference, the DS- strategy achieved its highest freestream success rate of $\geq$ 87% in the 20cm/s configuration (consistent with the validation analysis in appendix B.3), with DS+ marginally exceeding this across all freestream configurations (see appendix B.1). This suggests that the initial encounter time and, by extension, encounter probability were a key factor in the performance of each strategy for Scenario A. The near-bed 10cm/s release configuration saw a marginal increase in the success percentage of the DS- agents but a significant increase in DS+ agents with an overall decrease in mean goal times compared to the freestream 10cm/s release configuration (see fig. 4.9**a,c**). This can likely be attributed to the upwind edge of the near-bed plume being difficult to navigate without odour following behaviour.

The violin plots of first encounter times (fig. 4.9**b**) show that successful agents encountered the odour earlier than unsuccessful agents across all strategies and release configurations. Encounter time distributions narrowed and shifted to shorter times with increasing wind speed, reflecting the greater downwind extent and higher concentration of the plume at higher wind speeds. The goal time distributions (fig. 4.9**c**) show that cast-and-surge agents navigated to the source faster and with less variance than both DS- and DS+ for all but the freestream 5cm/s configuration; the parameter search placed DS+ goal times in the range of 874.9s–1870.1s across configurations and parameter values (see appendix B.1). The ratio of first encounter time to goal time (fig. 4.9**d**) indicates what fraction of total navigation time was spent locating the plume versus navigating within it; cast-and-surge agents consistently showed a lower ratio, reflecting faster plume location through casting versus random walking.

The general success of the cast-and-surge strategy, compared to that of the DS- and DS+ strategies, is clearly demonstrated in fig. 4.9. The main difference being in the casting behaviour versus the random walking in the absence of sensed odour. The key limitation of this strategy is also laid bare in the freestream 5cm/s release configuration, in which the casting behaviour failed to handle very limited odour encounters. In the next section, we attempted to mitigate this limitation for a more generally fair but temporally harsh comparison of the performance of each strategy under the three release configurations.

4.7.2 *Scenario B: Agents Position Randomly initialised*

In Scenario A, we demonstrated that the success of the agents in the freestream 5cm/s and 10cm/s odour release configuration was limited by the downwind extent of the plume and therefore probability of odour encounter. Therefore, in Scenario B, we increased the number of agents from 196 to 1000 and randomly initialised the agent's positions anywhere within the test section downwind of the goal area. We also limited the time that the agents had

to navigate to the goal to the duration of the trial or 240s. For Scenario B and each of the three strategies (figs. 4.10 to 4.12), we plot all 1000 agent trajectories from the most successful repetition and trial of each release configuration. Again, we highlight the successful agent with the median success time and plot its sensed normalised odour concentration (c_L, c_R) and use statistics (c, $|\rho_{odour}|$ for DS+ only) for the duration of the agent's navigation.

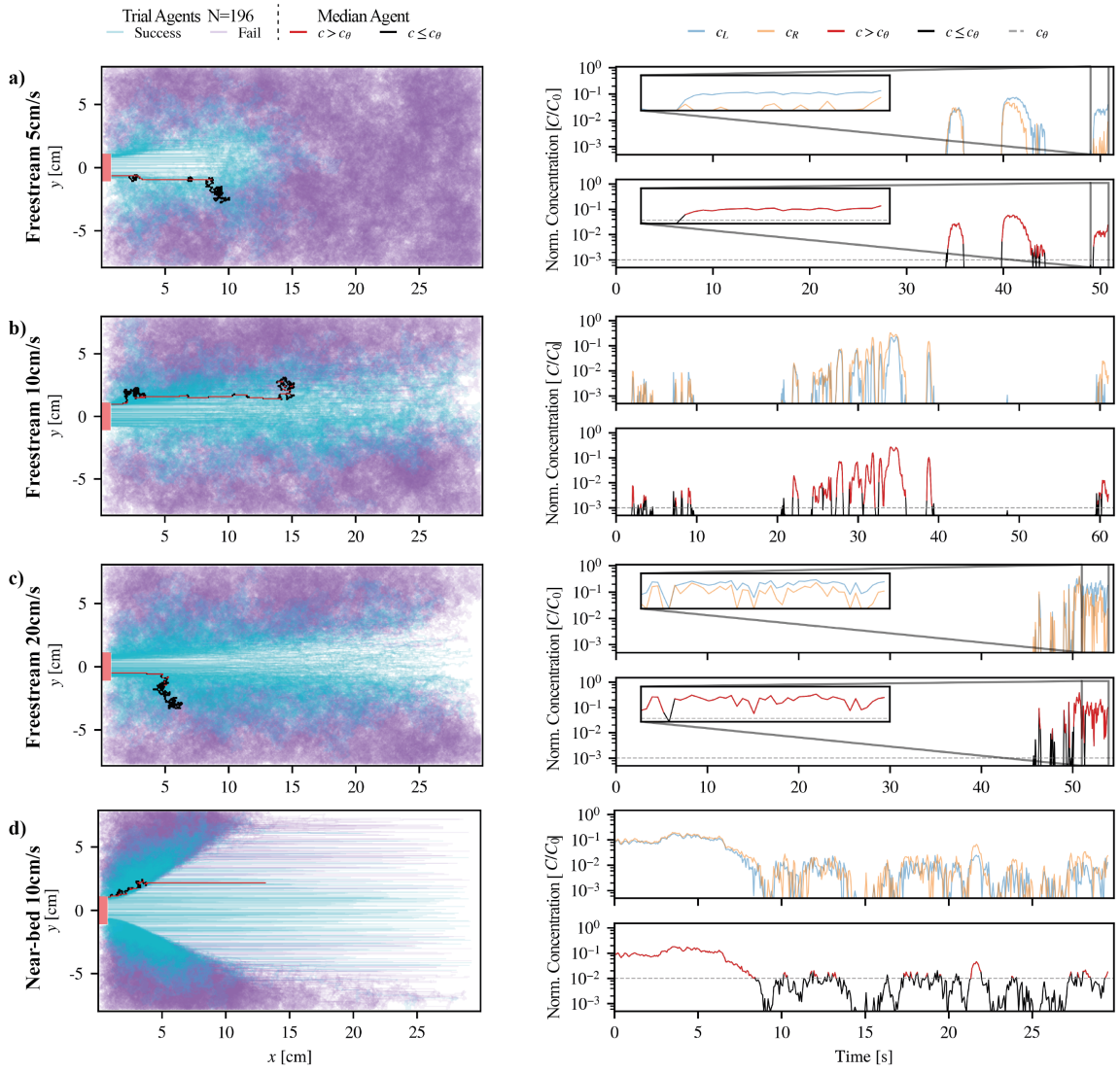

Figure 4.10: Scenario B: DS- Trajectories. Rows **a-d)** show the release configurations freestream $5cm/s$, $10cm/s$ and $20cm/s$ and near-bed $10cm/s$, respectively. For each row, the left panel shows agent trajectories from the best-performing trial and repetition, colouring the trial agent trajectories of the agents that successfully navigate to the goal light blue and those that failed to do so purple. We highlight the median performing agent and plot where the agent did not encounter the odour black ($c \leq \theta_c$) and where it did so red ($c > \theta_c$). The red box in the plot illustrates the location of the goal, in which the agent ceases navigation and signifies a success. The right upper panel shows median agent left (c_L) and right (c_R) sensor values. The right lower panel we plot the mean sensor readings (c) for the median agent, highlighting odour encounters ($c > \theta_c$) in red and the concentration threshold (θ_c) with a dashed grey line. Artefacts where the black line is above the θ_c are caused by instantaneous encounters where c crosses the threshold.

For Scenario B and the DS- agents (fig. 4.10), we found success limited by the inefficiency of random walking paired with the much harsher time limit compared to that of Scenario A. This is evident by the median agent trajectories for all release configurations being much shorter with less time random walking than those in fig. 4.6. The freestream release configurations saw greatest success with a low concentration threshold due to the likely limited odour encounter and limited lateral dispersion of the plumes. The near-bed release configuration required a slightly higher concentration threshold for the best performance due to the increased probability of odour encounter. The higher threshold may have improved the edge following behaviour at the upwind bound of the plume, as this likely limited the amount the surging behaviour overshot the edge. The random initial positions clearly impacted the performance of the DS- agents, where most successful agents appear to have started in immediate proximity to the plume.

The freestream $5cm/s$ (fig. 4.10**a**) shows upwind surging straight-line trajectories only where $x < 10cm$ & $|y| < 2cm$, elsewhere the trajectories show random walking behaviour. The highlighted agent shows edge following behaviour with intermittent low concentration odour encounters in which the odour concentration on the left sensor c_L shows a greater concentration than on the right sensor c_R where the agent was placed on the negative y edge of the plume. Successful agent trajectories occurred only where the agent's initial positions were $x < 20cm$ with the likelihood of success increasing closer to the source and to the plume centre line. This was due to an increased probability of odour encounters within the limited downwind extent of the $5cm/s$ plume. The freestream $10cm/s$ (fig. 4.10**b**) shows that the most successful agent trajectories occurred $|y| < 5cm$ with mainly failure trajectories $|y| \geq 5cm$, and with straight line surging trajectories most consistent $x < 12cm$. Further downwind the surges appeared intermittently dispersed with random walking behaviour. The highlighted agent frequently lost the plume because it followed the positive y edge, with the c_L sensor consistently showing a higher concentration than c_R. Its two longest periods of random walking occurred close to the source where the plume narrowed and at the furthest downwind part of the trajectory, potentially caused by lateral wavering of the plume. The freestream $20cm/s$ (fig. 4.10**c**) had a similar distribution of successful and failure trajectories to those seen in fig. 4.10**b** with less random walking $x > 15cm$ & $|y| < 5cm$ due to the greater downwind extent of plume. The highlighted agent saw shorter and less intermittent odour encounters with asymmetric sensor readings favouring c_R due to its negative y plume location. Initially, it began following the edge of the plume much closer to the source after more than $45s$ initial random walking to find the plume. Once it encounters the plume edge, it surges directly to the goal area. Intermittent surge trajectories were present within the bounds of the plume throughout the test section, giving agents initialised further downwind an easier time to initially locate the plume compared to those in fig. 4.10**a** and **b**. The near-bed $10cm/s$ (fig. 4.10**d**) shows the edges of the plume clearly from the surging trajectories where random walking trajectories occurred only outside of the plume bounds. The absence of odour direction following was evident from the increased

success of the agents that were initialised $|y| < 5cm$ and from the large amount of random walking outside of upwind edge of plume. The highlighted agent shows initial surging due to starting within the detectable plume bounds, but it lost the plume at its upwind edge and random walked to the source with intermittent edge following as the bounds narrowed. This limited success of agents initialised within the plume bounds with the initial surging behaviour (where $|y| \geq 5cm$) was likely due to the time limitation of Scenario B and the amount of time taken to intermittently follow the upwind plume bounds.

With strict time limitations and regardless of initial random positions, agents fig. 4.10 demonstrate the inefficiency of random walking in the absence of odour encounters. Failure trajectories are dominated by random walking, whilst successful ones show a combination of constant or intermittent surging. All highlighted agents show an imbalanced sensor reading with no trajectories crossing the plume as a result of a lack of odour direction following. This limited success to those agents that were initially either within or in close proximity to the plume.

For Scenario B and the DS+ agents (fig. 4.11), we again saw that the time limit of $240s$ bound the successful agents to those with an initial position in proximity to the extent of the plume. The odour direction following behaviour produced many trajectories that funnelled to the centre line of the plume. In particular, the random initial position produced more plume edge following close to the source than seen in fig. 4.7, these agents began navigation closer to the source but instead saw success from intermittent surging to the goal area.

The freestream $5cm/s$ (fig. 4.11**a**) successful agents only occurred $x < 17cm$ with surging trajectories $5cm < x < 10cm$ & $|y| < 2cm$ and odour direction sensing occurring $x < 5cm$ & $|y| < 1cm$. The time limitation and limited downwind extent of odour plume at significant concentration meant agents initialised $x > 17cm$ were unsuccessful. The highlighted agent followed the negative y plume bound with intermittent surging and random walking behaviours. It maintained asymmetric c_R dominated odour sensing dominated with long periods of random walking where odour concentration fell. The highlighted agent did not sense lagged odour correlation greater than θ_ρ and therefore never used the DS+ odour direction following behaviour. Instead it successfully navigated to the goal area using only DS- strategy surging and random walking behaviours. The freestream $10cm/s$ (fig. 4.11**b**) saw successful agents occur down the full downwind extent of the test section between $|y| < 5cm$. It shows intermittent surging and random walking trajectories $x > 10cm$ as seen in the DS- strategy fig. 4.10. However, odour direction following behaviour occurred intermittently between $4cm < x < 10cm$ and more consistently $x < 4cm$ & $|y| < 1cm$. The highlighted agent clearly demonstrated that c_L and c_R sensor reading became more balanced where odour direction following behaviour occurred. Periods of odour sensing appeared more intermittent than in the freestream $10cm/s$ fig. 4.11**a** with significant periods of random walking required to initially locate plume bounds. It intermittently surged when within plume bound $5cm < x < 10cm$ and finally zigzagged when odour direction sensing to locate odour source $x < 5cm$. The freestream $20cm/s$ (fig. 4.11**c**) saw successful agents

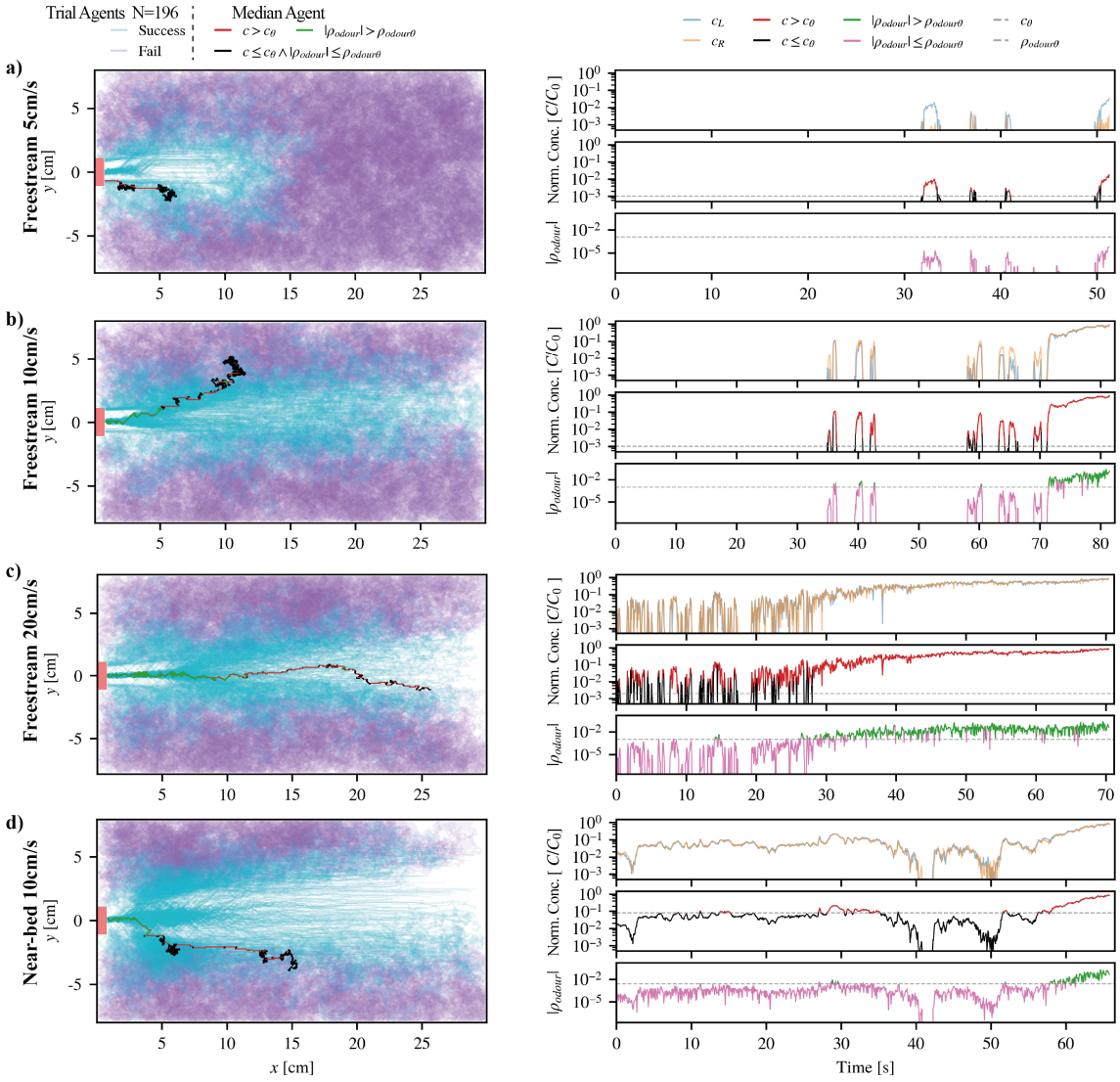

Figure 4.11: Scenario B: DS+ Trajectories. Rows **a-d)** show the release configurations freestream $5cm/s$, $10cm/s$ and $20cm/s$ and near-bed $10cm/s$, respectively. For each row, the left panel shows agent trajectories from the best-performing trial and repetition, colouring the trial agent trajectories of the agents that successfully navigate to the goal light blue and those that failed to do so purple. We highlight the median performing agent and plot where the agent did not encounter the odour and therefore had negligible odour correlation black ($c \leq \theta_c \wedge |\rho_{odour}| \leq \theta_\rho$), where the agent encountered odorant at a concentration greater than concentration threshold red ($c > \theta_c$). Where the median agent encountered lagged temporal correlation above the odour correlation threshold ($|\rho_{odour}| > \theta_\rho$) we highlight green. The red box in the plot illustrates the location of the goal, in which the agent ceases navigation and signifies a success. The right upper panel shows median agent left (c_L) and right (c_R) sensor values. The right middle panel we plot the mean sensor readings (c) for the median agent, highlighting odour encounters ($c > \theta_c$) in red and the concentration threshold (θ_c) with a dashed grey line. The right lower panel we plot the absolute lagged odour correlation ($|\rho_{odour}|$) and highlight where it exceeds the correlation threshold ($|\rho_{odour}| > \theta_\rho$) as well as the correlation threshold (θ_ρ) with a dashed grey line. The asterisk ($*$) signifies the time at which the agent reached the goal.

with more intermittent surging and random walking trajectories than in fig. 4.11**a** and **b** as a result of the increased turbulence at this wind speed. Very sparse odour direction following occurred $x > 13cm$ & $|y| < 5cm$, with equal surging and odour direction following between $8cm < x < 13cm$ and consistent odour direction following $x < 8cm$. There was less time spent random walking by successful agents at the downwind extent within the plume bounds due to increased odour encounter of greater odour concentration than in fig. 4.11**b**. The highlighted agent was initialised within the plume bounds and saw frequent but intermittent odour encounters for the first $30s$ surging until it reached $x \approx 12cm$. From here it saw high odour concentrations and was able to follow the odour direction, balancing its sensed odour $c_L \approx c_R$ and following the plume centre line to the goal. The near-bed $10cm/s$ (fig. 4.11**d**) saw wider crosswind extent of successful agents with odour direction sensing evident from more crosswind and consistent zigzag trajectories up to $x < 15cm$ and surging occurring further downwind. This saw the best performance from the highest odour concentration threshold θ_c of both Scenarios and highest odour correlation threshold θ_ρ of all DS+ simulations in Scenario B. These thresholds minimised the edge following at the upwind bounds of this plume and increased likelihood of odour direction following behaviour closer to the plume centre line and therefore saw the best mean successful agent percentage but not the lowest goal time. The highlighted agent followed the plume edge for the majority of its navigation time (up to $\approx 55s$), random walking for the majority of the time and surging intermittently. It began odour direction following where $x < 5cm$ and promptly moved to the centre line of the plume. Its sensed odour remained consistently high throughout the navigation time but with higher thresholds it relied heavily on random walking to locate the plume.

Odour direction following that occurred in proximity to the odour source meant that the DS+ agents fig. 4.11 were less likely to lose the plume at its upwind edges compared to the DS- agents shown in fig. 4.10. However, random walking in the absence of detected odour, with a higher detection threshold θ_c remained an inefficient method of initially locating and relocating the plume. Regardless of the random initial positions, the time limitation for Scenario B clearly demonstrated this in the failure trajectories that were dominated by the random walking behaviour.

For Scenario B and the cast-and-surge agents (fig. 4.12), the overall success was greater than in Scenario A fig. 4.8 due to the random initialisation of the agent positions. This enabled a higher probability of encountering the odour for those agents initially positioned closer to the source of the odour. The limitation of not progressing upwind when in the casting behaviour meant that the imposed time limitation was the main limiting factor for agent success in the freestream $5cm/s$ and $10cm/s$. The greatest success in the freestream $20cm/s$ and near-bed $10cm/s$ required higher odour detection thresholds θ_c than in the lower wind speed freestream datasets, most likely due to its limiting of the lateral spread of the sensed upwind plume bound. This was only effective because of the efficiency of the cast behaviour in relocating the plume once lost.

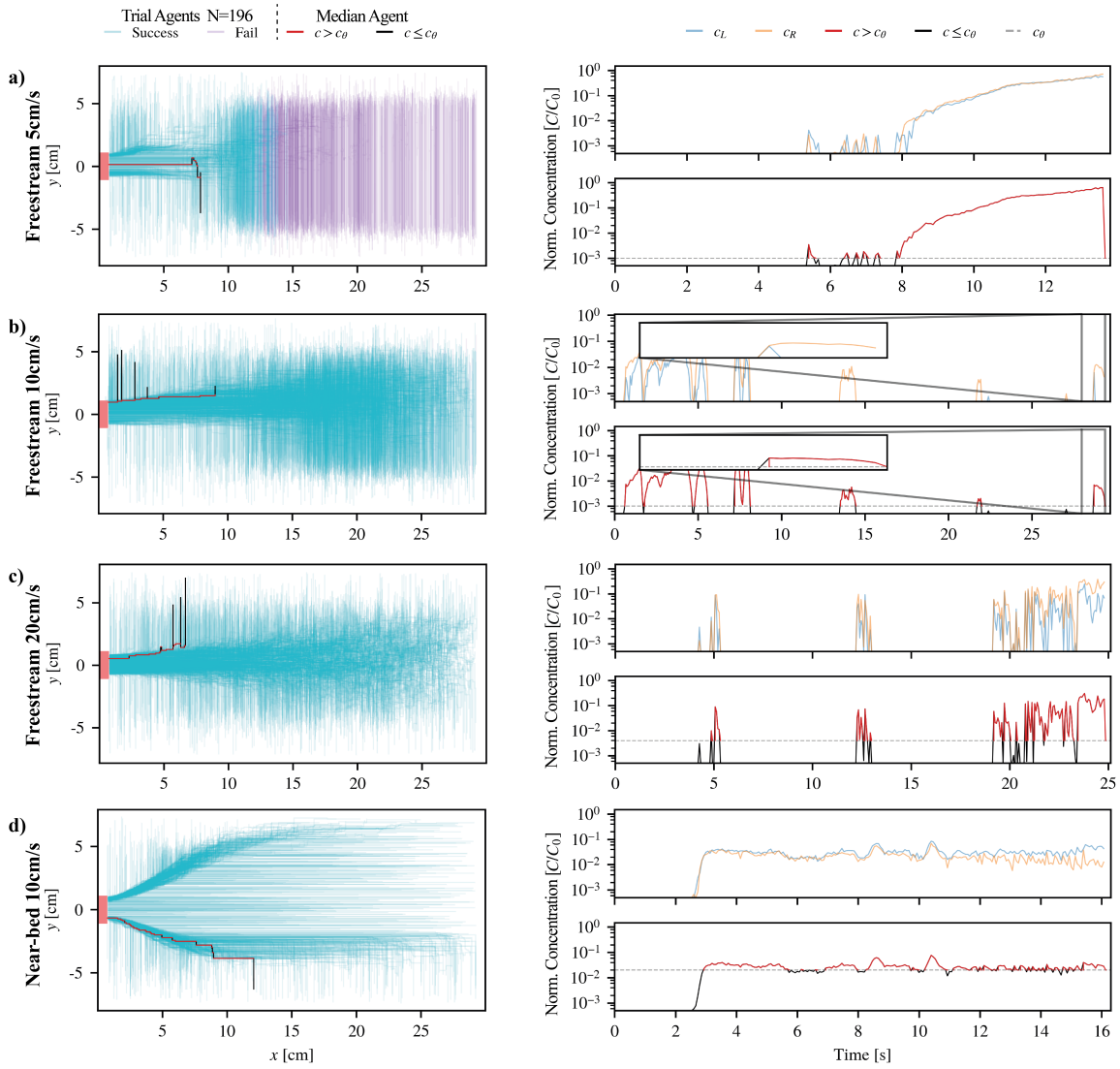

Figure 4.12: Scenario B: Cast Surge Trajectories. Rows **a-d)** show the release configurations freestream $5cm/s$, $10cm/s$ and $20cm/s$ and near-bed $10cm/s$, respectively. For each row, the left panel shows agent trajectories from the best-performing trial and repetition, colouring the trial agent trajectories of the agents that successfully navigate to the goal light blue and those that failed to do so purple. We highlight the median performing agent and plot where the agent did not encounter the odour black ($c \leq \theta_c$) and where it did so red ($c > \theta_c$). The red box in the plot illustrates the location of the goal; reaching it ceases navigation and signifies a success. The right upper panel shows median agent left (c_L) and right (c_R) sensor values. The right lower panel we plot the mean sensor readings (c) for the median agent, highlighting odour encounters ($c > \theta_c$) in red and the concentration threshold (θ_c) with a dashed grey line. Artefacts where the black line is above the θ_c are caused by instantaneous encounters where c crosses the threshold.

The freestream $5cm/s$ (fig. 4.12**a**) showed more success than in Scenario A (fig. 4.8**a** with successful agents exclusively randomly initialised $x < 13cm$. The highlighted agent remained on the negative edge of the plume, as evidenced by its unbalanced sensor reading with $c_L < c_R$ on average. It initially cast directly into the plume, intermittently encountered the plume for $2s$ and finally surged to the goal. The highlighted agent spent most of its navigation time casting, but was able to initially locate and relocate the plume more rapidly compared to the DS- agents fig. 4.10 with their random walking behaviour. The freestream $10cm/s$ (fig. 4.12**b**) saw a majority of successful agent trajectories with failure agents only initialised $x > 15cm$. There was a more extensive and consistent surging than in the freestream $5cm/s$ fig. 4.12**a** produced by a higher probability of odour encounters due to a greater downwind extent of the plume. After initially not detecting it and casting toward the negative y, the highlighted agent located the plume. Once it had detected the plume, it intermittently lost it with long casts and short surges. In general, it saw an unbalanced sensed odour concentration where $c_L < c_R$ because of its positive y plume edge positioning. The freestream $20cm/s$ (fig. 4.12**c**) shows that all agents successfully navigated to the odour source due to regular odour encounters even at the downwind boundary of the test section. Odour encounters may have been intermittent, but were frequent enough for all agents to surge upwind to the source with regular and mostly short distance casting. The highlighted agent saw its sensed concentration c_L and c_R more balanced overall due to travelling closer to the centre line when it surged upwind $x < 2cm$. It encountered regular periods of $c < \theta_c$ due to the increased turbulence at the $20cm/s$ wind speed. However, this helped the cast-and-surge agents locate the plume centre line more effectively than seen in the freestream $10cm/s$ fig. 4.12**b**, evidenced by the narrower area of solid blue close to the plume centre line. The near-bed $10cm/s$ (fig. 4.12**d**) showed that proximity to the floor laterally dispersed the plume and increased odour encounters throughout the test section, allowing 100% of the cast-and-surge agents to navigate to the source of the odour. The agents surged to the upwind edge of the plume and cast with intermittent surges to the source, causing an edge following trajectory. With the wide sensed plume, any casting agents quickly re-encountered the plume after turning back from travelling to the test section boundary and began surging upwind again. The highlighted agent shows a balanced concentration of the sensed odour c_L and c_R when initially surging inside the plume, but c_L dominated where it followed the negative y edge of the plume close to the source. A comparatively higher odour detection threshold θ_c than in Scenario A narrowed the lateral spread of the detectable plume and resulted in the best overall navigation time.

In Scenario B and the freestream $5cm/s$ and $10cm/s$ fig. 4.12**a** and **b** showed that the initial position of the agent significantly impacted whether the agents were successful in navigating to the source of the odour. For the freestream $20cm/s$ fig. 4.12**c** and near-bed $10cm/s$ fig. 4.12**d**, the initial position did not affect the success rate due to the increased probability of odour encounters throughout the test section. Compared to Scenario A fig. 4.8, the cast-and-surge saw less success than 100% in the freestream $10cm/s$ due to the time

limitation but also saw a nonzero success in the freestream $5cm/s$ because of the random initial agent positions. These imposed Scenario limitations provided a fairer comparison of navigation performance in relation to the DS- and DS+ strategies. We must remain cognisant that because of the random turn-back behaviour the cast-and-surge agents never touched the lateral test section boundaries. In unbounded navigation, this strategy would not be adequate for navigating to an intermittent or turbulent odour source without an internal memory of the time or distance since the plume was lost.

In the Scenario B performance metric analysis (fig. 4.13), we plot metrics calculated from all the repetitions of each trial for each release configuration and for the three strategies. We again show the percentage of agents that were either successful with an odour encounter, failed to locate the goal with an odour encounter or failed without an odour encounter. We considered that an encounter had occurred when an agent sensed a mean concentration c over its left c_L and right c_R sensors above the concentration threshold θ_c, even if it was instantaneous or only happened once. We plot the time of the first odour encounter for all successful and unsuccessful agents and the goal time for successful agents. For comparison of the strategies within each of the release configurations, we also plot the ratio of the initial encounter time to the goal time of the successful agents.

From fig. 4.13**a**, we found that the cast-and-surge strategy showed a higher success percentage and faster success times in every release configuration compared to the DS- and DS+ strategies. The most successful configuration was near-bed $10cm/s$ cast-and-surge, which achieved 99.8% success with odour encounter. The DS+ strategy marginally outperformed the DS- strategy success rate for all release configurations (see fig. 4.13**a**). The freestream $5cm/s$ and the near-bed $10cm/s$ saw the smallest and highest difference, respectively, in overall performance between strategies. This was likely due to the small plume size and low probability of odour encounter that limited the odour direction following in the DS+ agents in the former. In the latter case, the importance of accurate lateral tracking to the source was demonstrated by the DS+ odour direction sensing in the more dispersed plume. For each freestream wind speed, the DS- strategy had a lower success rate than the DS+ strategy, but a lower median goal time (fig. 4.13**c**). This apparent paradox — DS+ succeeds more often but takes longer when it does — can be attributed to the speed but decreased accuracy of straight-line upwind surging compared to the zigzag trajectory of odour direction following; direction following more reliably reaches the goal but at the cost of navigation time. Faster median odour encounter times caused the ratio of first odour encounter to goal time to be higher for DS- agents compared to DS+ in the freestream (fig. 4.13**d**), reflecting that DS- agents converted earlier encounters into source-finding more directly. For the near-bed configuration, the median first encounter times for DS- and DS+ agents were $0s$, skewing the encounter-to-goal-time ratio (fig. 4.13**d**) because many agents were initialised inside the plume; this metric should therefore be interpreted with caution for the near-bed configuration.

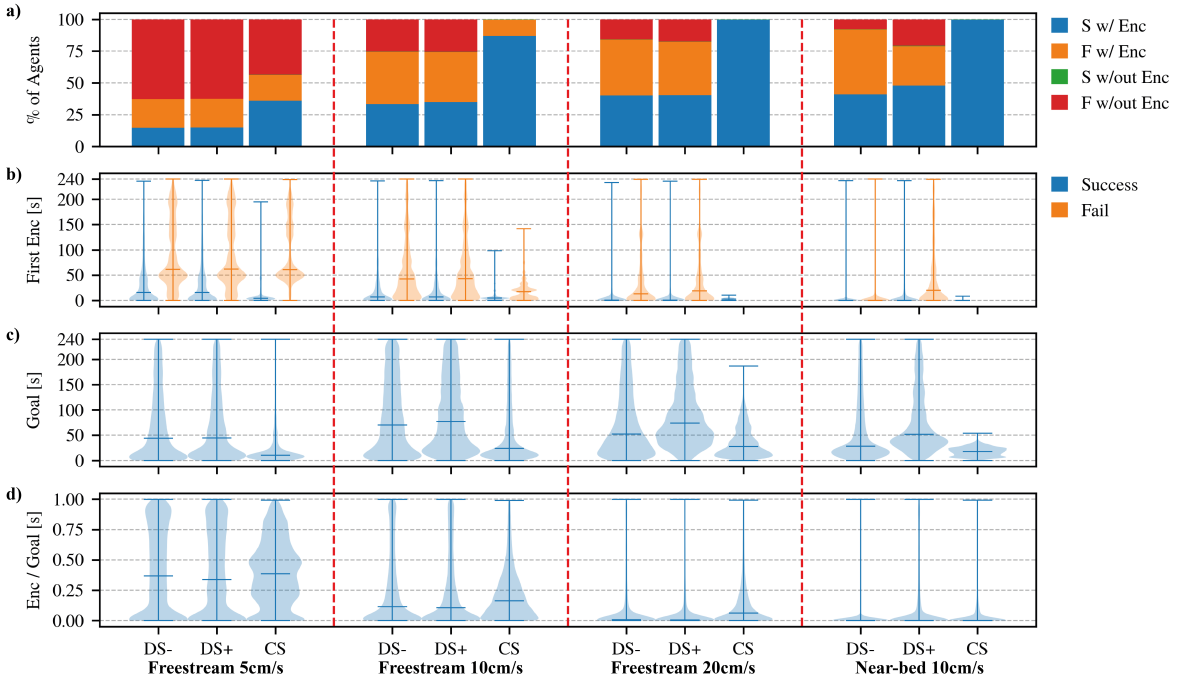

Figure 4.13: Scenario B: Performance Metric Analysis. **a)** agent performance metrics as a percentage of total agents of 10 repetitions of each trial and release configuration. Agents that successfully navigated to the goal and encountered the odorant above the odour detection threshold ($c > \theta_c$) are shown in blue, whilst the agents that did not are shown in green. Those that failed to navigate to the goal within the time limit or missed the goal and touched the upwind test section boundary are shown in orange or red if they did or did not encounter the odorant at a concentration greater than the detection threshold, respectively. **b)** violin plot of the initial odour encounter times in seconds of each successful and failure agent shown in blue and orange, respectively. **c)** violin plot of the time in seconds each successful agent took to navigate to the goal. **d)** violin plot of first encounters individually divided by goal time of agent for all agents. Violin plot bars show minimum, median and maximum values for all agents in each repetition of each trial collated.

The violin plots of first encounter times (fig. 4.13**b**) show narrower distributions for successful agents than for failed agents across all configurations, again confirming that earlier encounters were critical to success. Goal time distributions (fig. 4.13**c**) show that cast-and-surge agents navigated to the source fastest across all configurations, with the most compact distributions at high wind speeds where plume extent and encounter probability were greatest; DS+ goal times ranged from 63.9s to 95.0s across configurations and parameter values in the parameter search (see appendix B.2).

In general, we found that the number of agents failing without an odour encounter scaled inversely with increasing wind speed in the freestream. Where there were agents that failed to navigate to the source (all but the freestream 20cm/s and near-bed 10cm/s cast-and-surge strategy), the median first odour encounter of successful agents was consistently earlier than the failure agents. This suggests that earlier odour encounters were crucial to the success of all strategies. For the DS- and DS+ strategies being limited by the inefficiency of random walking, and for the cast-and-surge agents in the freestream it was general odour encounter availability with the downwind plume extent. All Scenario B strategies and release configurations saw $< 3\%$ of success without odour encounter, this did not occur for Scenario A and is a result of agents with initial positions in the immediate proximity to the goal. The most successful of all tested configurations was the cast-and-surge strategy in the near-bed 10cm/s release configuration that saw 99.8% success with odour encounter in the 10 random seed repetitions of each trial, and the remaining 0.2% saw success without encounter. This was likely due to the extensive and laterally spread plume combined with the reliability of the casting behaviour for efficiently locating and relocating the plume.

It is clear from these results that the cast-and-surge strategy was the most successful and efficient of the three strategies at bounded-odour source navigation. The DS+ and DS- strategies suffered from the inefficiency of random walking in the absence of odour encounters. From the trajectories we found that the DS+ traded the speed of surging upwind for the accuracy of locating the goal reliably when the direction-sensing behaviour occurred in proximity to the source. Scenario B saw the cast-and-surge strategy perform better in the freestream 5cm/s than in Scenario A due to the random agent positioning, but perform worse for the other freestream wind speeds due to the time limitation. A cast-and-surge strategy with odour direction following behaviour with source proximity may perform marginally better than overall, but would likely also see the slower navigation that the DS+ saw in comparison to the DS- strategy.

4.8 DISCUSSION

The application of simple agent navigation strategies inspired by walking *Drosophila* and flying moths in recorded odour plumes provided insight into the varying strategies utilised by insects to navigate the temporally complex and dynamic structure of real turbulent odour plumes. We tested two separate scenarios, Scenario A in which the time limit was $10x$ longer, but the agents were initialised at the downwind extent of the test section, and Scenario B in which the time was limited, but the agents were initialised throughout the test section. The first highlighted the ability of the agents to initially locate the odour plumes and pointed toward the feasibility of the strategies to efficiently locate odour sources in the real world. The second provided a fairer comparison of the strategies through the randomised initial position of the agents and time-limiting of the agents. It provided a clear distinction in the efficiency of the agents under different odour-release conditions.

We observed that overall agent performance improved with increasing wind speed for the freestream release configuration (figs. 4.9 and 4.13). The assumption that strategies inspired by walking *Drosophila* would perform best in boundary layer (near-bed) plumes and struggle to navigate freestream plumes was confirmed: all three strategies showed higher success rates and faster goal times in the near-bed $10cm/s$ configuration than in the freestream $10cm/s$ configuration. The near-bed plume's broader lateral extent and higher sustained concentration — a consequence of the boundary layer suppressing turbulent intermittency and driving shear-driven lateral dispersion (Connor, McHugh and J. P. Crimaldi, 2018; P. Moore and J. Crimaldi, 2004) — increased the probability of an initial odour encounter regardless of starting position, and with the increased probability of an odour encounter from the lateral spread of the near-bed $10cm/s$ plume compared to the freestream $10cm/s$, we found that all strategies performed better for Scenarios A and B. We found that the cast-and-surge strategy outperformed DS- and DS+ in three of the four release configurations in Scenario A (freestream $10cm/s$, $20cm/s$, and near-bed $10cm/s$) and for all release configurations in Scenario B, in both the successful agent percentage and the time it took for successful agents to locate the goal.

Notably, the cast-and-surge strategy completely failed (0% success) in the freestream $5cm/s$ Scenario A configuration, while DS- and DS+ achieved nonzero success in the same configuration. This failure arose because the limited downwind extent of the $5cm/s$ plume meant agents spent almost the entire $2400s$ time limit casting at the downwind extent of the test section without ever reaching a concentration sufficient to trigger surging. The random walk in the absence of odour, used by DS- and DS+, occasionally resulted in agents wandering into the sparse plume region, whereas casting committed agents to the test section boundary and no useful upwind displacement occurred. This result exposes an important boundary condition of the cast-and-surge strategy: it is dependent on consistent odour availability throughout the test section, and fails when the plume does not reach the agent's initialisation zone.

A notable finding in Scenario B was that DS+ achieved a lower median goal time than DS- in the freestream configurations (fig. 4.13**c**), despite DS+ having a higher overall success rate than DS-. This apparent paradox is explained by the nature of the two strategies' in-odour behaviour: DS- surges directly upwind in a straight line, which is fast when the plume is located but frequently overshoots the plume edges or loses the plume centre; DS+ zigzags as it follows the odour direction gradient, which is slower per unit distance but more reliably tracks the centre line to the goal. This trade-off mirrors the distinction drawn by Kennedy (1978) between longitudinal and transverse chemo-klinotaxis: DS- approximates a pure surge response, modulating upwind speed in response to odour presence, while DS+ more closely resembles transverse klinotaxis, continuously steering towards the side of greater odour concentration to remain within the plume. In effect, DS- trades accuracy for speed: the agents that do succeed find the source quickly, while many others fail. DS+ trades speed for reliability: fewer agents fail, but those that succeed take slightly longer. This distinction is also visible in the encounter-to-goal-time ratio (fig. 4.13**d**): DS- agents spent a higher proportion of successful navigation time inside the plume (shorter ratio), whereas DS+ agents invested more time in the direction-following zigzag close to the source.

The DS- and cast-and-surge strategies relied solely on the average concentration over the two sensors to determine an odour encounter. In the absence of odour, the cast-and-surge strategy compared the sensor values to determine the casting direction perpendicular to the sensed wind vector, and the DS- strategy randomly walked. A comparison of DS- against cast-and-surge agents was therefore in essence a comparison of navigation strategies in the absence of odour, random walking versus crosswind casting. Crosswind casting in the absence of odour is the canonical lost-plume response of moths (T. C. Baker, 1990; Kennedy and Marsh, 1974) and flying *Drosophila* (Budick and Dickinson, 2006), and has been interpreted as a strategy that maximises the probability of re-encountering a plume whose lateral position is uncertain; the consistent advantage of casting over random walking observed here supports the view that this behaviour offers a systematic search geometry that random locomotion cannot match. The DS+ used the DS- strategy but also relied on the lagged correlation between its two stereo sensors, when it was greater than a threshold it provided an odour direction to follow. As all strategies were a form of odour-gated anemometry, when odour was encountered, the agents used the wind vector to determine a direction to turn and follow. The nature of the PLIF plumes, as opposed to the simulated plumes, meant the absence of a local wind direction vector field. We therefore assumed that the average wind flow direction, i.e. advection, would be adequate as a constant wind vector. The impact of this assumption was that surging upwind and casting crosswind trajectories tended to be straight lines. Our cast-and-surge strategy trajectories used purely crosswind casts, whereas examples of real cast-and-surge trajectories include zigzagging with partial upwind progression (Kennedy, Ludlow and Sanders, 1980; Marsh, Kennedy and Ludlow, 1978, 1981). Kadakia et al. (2022) expanded on their grid-based stereo-sensor simulations by allowing their agents to turn 360.000° and biased their turn directions using

local wind vectors from their simulated plumes. This allowed their agents to recreate more realistic walking *Drosophila* trajectories. Removing the limitation of 90.000° turns in favour of unlimited turns with a bias towards the global wind vector could produce more realistic navigation trajectories, albeit at greater computational cost.

The strategies used by insects vary depending on whether they are walking (Álvarez-Salvado et al., 2018; Demir et al., 2020) or flying (Kellogg, Frizel and Wright, 1962; Kramer, 1976; Traynier, 1968), and on their proximity to the odour source (Jayaram et al., 2023). It should also be noted that real insect behaviour is more complex than a two-state cast-and-surge, random walk-surge or three-state direction-following machine. However, these simple state machines produced complex trajectories as a result of the dynamic turbulent plumes that they were navigating.

Here we limited ourselves to the use of simple state machines that are evidently capable of efficient and robust navigation of the PLIF datasets, i.e. the cast-and-surge strategy. It is also important to note that all three strategies are bounded by the test section dimensions, and the cast-and-surge strategy in particular depends on the random turn-back behaviour at the test section walls to avoid being trapped at the lateral boundaries. As noted in section 4.7.1, in unbounded navigation the cast-and-surge strategy would not be adequate for navigating to an intermittent or turbulent odour source without an internal memory of the time or distance since the plume was last encountered.

All strategies explored here had limited memory: at most, DS+ integrates the temporal odour gradient across two consecutive frames. The fact that DS+ outperforms DS- in success rate despite using only two-frame temporal integration — a minimal form of memory — suggests that even brief directional information provides meaningful navigational benefit. In contrast, infotaxis, proposed by Vergassola, Villermaux and Shraiman (2007) and discussed in section 2.7, updates a posterior probability distribution for the source location using Bayes' formula, based on a continuous memory of intermittent odour encounters. An interesting performance comparison could be undertaken with infotaxis, which is notably a more complex and computationally expensive strategy. Given that DS+ already outperforms DS- using only two-frame memory, this comparison could quantify how much additional benefit accrues from continuous memory, and whether the computational overhead of infotaxis is justified by the performance gain in these turbulent, inhomogeneous plume environments.

Exploring the performance of these simple strategies in recorded plume data exposed some of the nuances of efficient plume navigation that could enhance the performance of robotic odour source navigation in the real world. The use of simple two-sensor grid-based odour-gated anemometry strategies on recorded odour plume data allowed for rapid comparative analysis of thousands of simulated agents with multiple parameters and two scenarios. Although bounded by the test section, the different release configurations went some way towards demonstrating the impact of environmental conditions that organisms face when navigating turbulent plumes in their natural habitat.

4.9 CONCLUSION

Odour direction sensing with stereo sensors was shown to be an effective method for agents to navigate to an odour source and was shown to be more effective than simply surging upwind when odour concentration exceeded a threshold. Random walking was previously used to explore the test section in the absence of odour. We determined that casting was more effective than random walking with the caveat that the plume extent had to reach beyond the agent's downwind position.

Irrespective of the navigation strategy used, agents more quickly and reliably navigated to the source in the near-bed than in the freestream, in which agent's success increased with wind speed. One exception to this was in Scenario A, in which the freestream 20cm/s had marginally higher success and similar average success time for DS- agents. Overall, the cast-and-surge strategy was more successful and faster than both the DS+ and DS- strategies regardless of release configuration.

With the DS strategies being inspired by walking *Drosophila*, we expected this difference in success between the near-bed and freestream release configurations. The improvement of the cast-and-surge strategy, inspired by flying insects, success rate and speed was expected in the freestream but not in the near-bed configuration. We suspect that the key to success of each of the navigation strategies was more heavily impacted by the probability of encounter within the test section. The detection limit of the PLIF system and therefore the minimum tested odour detection threshold likely limited the success where encounter probability was low. We saw that the cast-and-surge strategy only improved the ability of the agent to initially locate and relocate the odour plume when it was lost.

5

CONCLUSIONS

5.1 GENERAL DISCUSSION

In chapter 3, we demonstrated that bout analysis can be applied to PLIF data (Connor, McHugh and J. P. Crimaldi, 2018) with little modification. We established adequate filter parameters after initially conducting a spectral analysis (appendix A.1.1). Odour encounters are not necessarily cyclical, especially in natural environments, and so a spectral analysis has limited utility. J. Burgués and S. Marco (2020) suggest that filter parameters must be jointly optimized with the bout amplitude threshold and the type of regression model to be used. They do so through a grid search procedure in combination with cross-validation for best performance in source-receptor distance prediction. Our own exploration of filter parameters in appendix A.1.3 indicates potential for follow-up studies. An extension of this work would be a joint optimization of filters, bout amplitude and regression method for improved distance prediction.

As an initial step, we determined the plume location on average by adapting an existing method of fitting lateral Gaussians to the time and trial averaged scalar (Connor, McHugh and J. P. Crimaldi, 2018). It is not uncommon to use Gaussian approximations of odour plumes as they represent the time averaged structure of odour plumes well. The early eddy diffusion models of Sutton (1947, 1949) and Frenkiel (1953) have been described as assembled by an infinite superposition of overlapping Gaussian puffs emanating from a fixed origin translated by mean wind (Gifford, 1959). In doing so, we lost the lateral meandering of the plume with time as described by Murlis, Elkinton and Carde (1992). This could be mitigated if the plume bounds were mapped for each frame of each trial and release configuration as instantaneous plume bounds. This would increase the complexity of the analysis, but could potentially lead to better capturing of the evolving structure of the plume and its fluctuations.

We split analysis into downwind, crosswind, full plume and wind speed compensated downwind exploration to better illustrate the odour source proximity impact on the four explored bout statistics. Schmuker, Bahr and Huerta (2016) used a linear model to quantify the relationship between odour source proximity and bout count along the plume centre line and a mapping of bout count variance with lateral plume distance. However, Schmuker, Bahr and Huerta (2016) used the MOX sensor dataset produced by Vergara et al. (2013) that had nine simultaneously recorded crosswind positions and had temporally sequential downwind positions that limit the analysis of spatial relationships within their recorded plume. The freestream PLIF datasets that we explored have a much higher spatial resolution that reveal

the non-linear sigmoidal relationship between bout counts and odour source proximity along the approximate plume centre line. We did not see the expected mapping of bout count variance in the crosswind profiles. In all of the freestream datasets, we did see consistent Gaussian profiles of bout counts that decreased in their maxima with downwind distance, bimodal distributions of bout duration and amplitude with peaks either side of the centre line that also decreased and flattened with downwind distance, and an inverted Gaussian distribution of IBI that increased with downwind distance. These statistical relationships could be used in conjunction with a navigation strategy for robust odour source navigation.

Muezzinoglu et al. (2009) proposed a scheme in which a bank of features with different parameters could be evaluated in parallel and in real time to improve the accuracy of concentration and analyte classification. One could apply such a filter bank to potentially improve source-proximity estimation accuracy for different wind speeds and flow conditions. A useful comparison of information extracted using bout analysis against other transient features such as whiffs and blanks (Celani, Villermaux and Vergassola, 2014; Mylne and Mason, 1991; Rigolli, Magnoli et al., 2022; Yee, Chan et al., 1995; Yee, Kosteniuk et al., 1993) or intermittency (Connor, McHugh and J. P. Crimaldi, 2018; J. P. Crimaldi, Wiley and Koseff, 2002; Gumaste et al., 2024) for odour source proximity would be informative. Whiff duration and up-crossing time have been used to estimate source distance, but are sensitive to absolute odour concentration (Celani, Villermaux and Vergassola, 2014; Rigolli, Magnoli et al., 2022); bouts are extracted from the derivative of the sensor response and are thereby largely concentration-independent (Schmuker, Bahr and Huerta, 2016), which may make them more robust to the variable absolute concentrations encountered across different release configurations and distances from the source. Bout counts have been previously used in gas source localization and mapping and explored with respect to bout amplitude threshold and bout frequency (J. Burgués, Hernández et al., 2019). The use of other bout statistics has yet to be explored in regard to navigation. A bout-based navigation strategy that can utilize the expected combined bout statistical mappings may benefit over just the use of bout counts.

In chapter 4, we applied three simple biologically inspired navigation strategies to the PLIF data (Connor, McHugh and J. P. Crimaldi, 2018). Two of these demonstrated the strategies of walking *Drosophila*, one equipped with the ability to use stereo sensors to determine a lagged correlation and follow odour direction, the other used purely odour gated anemotaxis and random walking in the absence of detected odour (Kadakia et al., 2022). The third was a flying insect inspired cast-and-surge strategy (T. C. Baker, 1990; Budick and Dickinson, 2006; N. J. Vickers and T. C. Baker, 1994; Willis and Arbas, 1991) that cast crosswind in the absence of odour but surged upwind when it was detected. The goal of this work was to compare the performance of these simple strategies within the four release configurations with the presumption that walking strategies would perform best in the near-bed and flying strategies would perform best in the freestream. However, we found that the cast-and-surge agents outperformed the walking agents in the majority of the conditions, only failing in the situation in which agents did not sense the odorant at the downwind edge of the test section.

The results highlighted that this was in fact a comparison of how the strategies performed in the absence of odour or random walking versus casting.

The simple strategies we explored required minimal memory (few samples to compare) from the encountered plume, unlike previous methods such as infotaxis (Vergassola, Villermaux and Shraiman, 2007), which continuously updates a posterior probability distribution for the source location based on accumulated odour detections, and has been shown to produce casting-like trajectories qualitatively similar to those of navigating moths and flies. Infotaxis was designed for sparse, dilute turbulent environments and requires a statistical model of the plume field to be specified in advance; in the highly inhomogeneous plume structures recorded here, where mean concentration, intermittency, and spatial extent vary substantially between release configurations, the assumptions underlying that model may not hold, potentially limiting performance gains relative to simpler reactive strategies. A hybrid strategy that combines reactive response to sudden odour change with a memory-based model of the plume structure accumulated during navigation could combine the robustness of the reactive approach with the efficiency benefits of spatial memory, and would be a natural extension of the work presented here.

A key factor that we did not explore was the impact of the distance between the agents' sensors. Our sensors were separated by one pixel or $0.74mm$ and the spacing between sensors significantly impacts the sensory information organisms receive (M. Weissburg, 2000). M. Weissburg (2000) quantified this through the spatial integration factor (SIF) — the ratio of sensor separation to the characteristic turbulence length scale of the local plume — finding that wider sensor spacing relative to the plume's turbulent microstructure improves the ability to extract directional concentration gradients. At $0.74mm$, our sensor separation is likely well below the relevant turbulence length scales of the plume, which may have constrained the directional information available to DS+ and contributed to its modest advantage over DS− in the freestream configurations. Active sensing has recently become a topic of great interest (as we explore in section 2.2) and our sensors are fixed either side of the agents' centroid. Implementing a sweeping motion into the sensors, as many marine organisms (J. P. Crimaldi, M. A. Koehl and Koseff, 2002; M. A. Koehl et al., 2001; M. Koehl, 2006; Schmitt and Ache, 1979) and insects do (Cholé et al., 2022; Claverie, Buvat and Casas, 2023; Huston et al., 2015; Lei et al., 2022; Mertes, Carcaud and Sandoz, 2021), could significantly alter how the odour is perceived by the agent. Extending the sensor memory beyond a single frame, increasing the sensed area, and sensing while moving would further enhance odour perception.

Due to a lack of local wind direction vectors, we used the direction of bulk motion of the fluid as the wind direction; this resulted in straight lines in the agents' crosswind cast and upwind surge trajectories. Local wind direction vectors would likely significantly impact agent navigation performance. Joint PLIF and PIV (Liberzon, Gurka and Hetsroni, 2004; Raffel et al., 2018) recordings could provide local wind direction vectors at a spatial and temporal resolution that would benefit agent simulations. Other possible extensions to this

work could include stopping and sensing behaviours and using local wind direction to bias the turn in a non-grid-based navigation as was done in the main body of Kadakia et al. (2022). A bout-based method could provide stereo events to act upon that could be used to provide the agent information about its position within the plume.

In the future we intend to apply the knowledge gained here to enable a robotic platform equipped with novel and portable electronic noses, capable of resolving fast gas transients (Drix and Schmuker, 2021) and sensitive enough to recognize geographical locations purely based on unique olfactory signatures (Drix, Dennler and Schmuker, 2022), to derive biologically inspired strategies for robust and efficient autonomous robotic odour source localization in turbulent plumes.

Finally, a review of the results presented in Connor, McHugh and J. P. Crimaldi (2018), along with the subsequent analysis of these datasets undertaken in this thesis, raised concerns regarding the downwind extent of the detected fluorescent acetone vapour in the three freestream odour release configurations. We hypothesised that the double-diffusion phenomenon — where the carrier gas (an air–helium mixture) and the acetone vapour exhibit markedly different diffusion coefficients — might have contributed to this limited detection range. To examine this hypothesis and respond to these concerns, a preliminary report has been added as an addendum (appendix C.1). In this report, an Antoine calculation was performed to estimate the expected acetone vapour concentration (kg/m^3) under the specified release conditions along the centre line of the test section. Our initial findings indicated that the experimentally measured acetone vapour extended further downwind and at higher concentrations than those predicted by the model. This discrepancy may reflect a source effect at the point of odour release; however, without a direct mapping of vapour dispersion under identical laboratory conditions, this explanation remains speculative.

6

BIBLIOGRAPHY

Ackels, T. et al. (27th May 2021). 'Fast Odour Dynamics Are Encoded in the Olfactory System and Guide Behaviour'. In: *Nature* 593.7860, pp. 558–563. ISSN: 0028-0836, 1476-4687. DOI: 10.1038/s41586-021-03514-2. URL: https://www.nature.com/articles/s41586-021-03514-2.

Álvarez-Salvado, E. et al. (21st Aug. 2018). 'Elementary Sensory-Motor Transformations Underlying Olfactory Navigation in Walking Fruit-Flies'. In: *eLife* 7, e37815. ISSN: 2050-084X. DOI: 10.7554/eLife.37815. URL: https://elifesciences.org/articles/37815.

Arroyo, M. P. and K. D. Hinsch (2008). 'Recent Developments of PIV towards 3D Measurements'. In: *Particle Image Velocimetry*. Vol. 112. Berlin, Heidelberg: Springer Berlin Heidelberg, pp. 127–154. ISBN: 978-3-540-73527-4 978-3-540-73528-1. DOI: 10.1007/978-3-540-73528-1_7. URL: http://link.springer.com/10.1007/978-3-540-73528-1_7.

Arzi, A. and N. Sobel (July 2010). 'Spatial Perception: Time Tells Where a Smell Comes From'. In: *Current Biology* 20.13, R563–R564. ISSN: 09609822. DOI: 10.1016/j.cub.2010.04.048. URL: https://linkinghub.elsevier.com/retrieve/pii/S0960982210005270.

Atema, J. (Aug. 1996). 'Eddy Chemotaxis and Odor Landscapes: Exploration of Nature With Animal Sensors'. In: *The Biological Bulletin* 191.1, pp. 129–138. ISSN: 0006-3185, 1939-8697. DOI: 10.2307/1543074. URL: https://www.journals.uchicago.edu/doi/10.2307/1543074.

Atema, J. (1988). 'Distribution of Chemical Stimuli'. In: *Sensory Biology of Aquatic Animals*. Ed. by J. Atema et al. New York, NY: Springer New York, pp. 29–56. ISBN: 978-1-4612-8317-1 978-1-4612-3714-3. DOI: 10.1007/978-1-4612-3714-3_2. URL: http://link.springer.com/10.1007/978-1-4612-3714-3_2.

Atema, J. and D. G. Engstrom (July 1971). 'Sex Pheromone in the Lobster, Homarus Americanus'. In: *Nature* 232.5308, pp. 261–263. ISSN: 0028-0836, 1476-4687. DOI: 10.1038/232261a0. URL: https://www.nature.com/articles/232261a0.

Atema, J., R. R. Fay et al., eds. (1988). *Sensory Biology of Aquatic Animals*. New York, NY: Springer New York. ISBN: 978-1-4612-8317-1 978-1-4612-3714-3. DOI: 10.1007/978-1-4612-3714-3. URL: http://link.springer.com/10.1007/978-1-4612-3714-3.

Baker, K. L. et al. (31st Oct. 2018). 'Algorithms for Olfactory Search across Species'. In: *Journal of Neuroscience* 38.44, pp. 9383–9389. ISSN: 0270-6474, 1529-2401. DOI: 10.1523/JNEUROSCI.1668-18.2018. pmid: 30381430. URL: https://www.jneurosci.org/content/38/44/9383.

Baker, T. C. and K. F. Haynes (Mar. 1989). 'Field and Laboratory Electroantennographic Measurements of Pheromone Plume Structure Correlated with Oriental Fruit Moth Behaviour'. In: *Physiological Entomology* 14.1, pp. 1–12. ISSN: 0307-6962, 1365-3032. DOI: 10.1111/j.1365-

3032.1989.tb00931.x. URL: https://resjournals.onlinelibrary.wiley.com/doi/10.1111/j.1365-3032.1989.tb00931.x.

Baker, T. C. (1990). 'Upwind Flight and Casting Flight: Complementary and Tonic Systems Used for Location of Sex Pheromone Sources by Male Moths.' In: *Tenth International Symposium on Olfaction and Taste*. Tenth International Symposium on Olfaction and Taste. Oslo, Norway, pp. 18–25.

Barynin, J. and M. Wilson (Mar. 1972). 'Outdoor Experiments on Smell'. In: *Atmospheric Environment (1967)* 6.3, pp. 197–207. ISSN: 00046981. DOI: 10.1016/S0004-6981(72)80148-3. URL: https://linkinghub.elsevier.com/retrieve/pii/S0004698172801483.

Batchelor, G. K. (Jan. 1959). 'Small-Scale Variation of Convected Quantities like Temperature in Turbulent Fluid Part 1. General Discussion and the Case of Small Conductivity'. In: *Journal of Fluid Mechanics* 5.01, p. 113. ISSN: 0022-1120, 1469-7645. DOI: 10.1017/S002211205900009X. URL: http://www.journals.cambridge.org/abstract_S002211205900009X.

Bathellier, B., O. Gschwend and A. Carleton (2010). 'Temporal Coding in Olfaction'. In: *The Neurobiology of Olfaction*. Ed. by A. Menini. Frontiers in Neuroscience. Boca Raton (FL): CRC Press/Taylor & Francis. ISBN: 978-1-4200-7197-9. pmid: 21882423. URL: http://www.ncbi.nlm.nih.gov/books/NBK55968/.

Bennett, M. (July 1968). 'The Role of the Anterior Limb of the Anterior Commissure in Olfaction'. In: *Physiology & Behavior* 3.4, pp. 507–515. ISSN: 00319384. DOI: 10.1016/0031-9384(68)90003-6. URL: https://linkinghub.elsevier.com/retrieve/pii/0031938468900036.

Benton, R. et al. (Jan. 2009). 'Variant Ionotropic Glutamate Receptors as Chemosensory Receptors in Drosophila'. In: *Cell* 136.1, pp. 149–162. ISSN: 00928674. DOI: 10.1016/j.cell.2008.12.001. URL: https://linkinghub.elsevier.com/retrieve/pii/S0092867408015614.

Bhandawat, V., G. Maimon et al. (15th Dec. 2010). 'Olfactory Modulation of Flight in *Drosophila* Is Sensitive, Selective and Rapid'. In: *Journal of Experimental Biology* 213.24, pp. 4313–4313. ISSN: 1477-9145, 0022-0949. DOI: 10.1242/jeb.053546. URL: https://journals.biologists.com/jeb/article/213/24/4313/10031/Olfactory-modulation-of-flight-in-Drosophila-is.

Bhandawat, V., J. Reisert and K.-W. Yau (24th June 2005). 'Elementary Response of Olfactory Receptor Neurons to Odorants'. In: *Science* 308.5730, pp. 1931–1934. ISSN: 0036-8075, 1095-9203. DOI: 10.1126/science.1109886. URL: https://www.science.org/doi/10.1126/science.1109886.

Boreham, B. W. (Aug. 1986). 'A New Fast Response Probe for Diffusion Studies in Atmospheric Air'. In: *Journal of Physics E: Scientific Instruments* 19.8, pp. 637–642. ISSN: 0022-3735. DOI: 10.1088/0022-3735/19/8/011. URL: https://iopscience.iop.org/article/10.1088/0022-3735/19/8/011.

Boreham, B. W. and J. K. Harvey (Nov. 1984a). 'Bipolar Charged Particles as Markers for Dispersion Simulation in Wind Tunnels'. In: *Journal of Physics E: Scientific Instruments*

17.11, pp. 994–998. ISSN: 0022-3735. DOI: 10.1088/0022-3735/17/11/020. URL: https://iopscience.iop.org/article/10.1088/0022-3735/17/11/020.

Boreham, B. W., C. D. Jones and R. F. Griffiths (Mar. 1985). 'Field Evaluation of a New Langmuir-type Probe for Atmospheric Dispersion Studies Using Ions as a Tracer'. In: *Journal of Physics E: Scientific Instruments* 18.3, pp. 218–223. ISSN: 0022-3735. DOI: 10.1088/0022-3735/18/3/012. URL: https://iopscience.iop.org/article/10.1088/0022-3735/18/3/012.

Boreham, B. W. and J. K. Harvey (1984b). 'Monitoring the Atmospheric Diffusion of Puffs and Plumes with Bipolar Space Charge at Small Scale in Wind Tunnels'. In: *Atmospheric Dispersion of Heavy Gases and Small Particles*. Ed. by G. Ooms and H. Tennekes. Berlin, Heidelberg: Springer Berlin Heidelberg, pp. 297–306. ISBN: 978-3-642-82291-9 978-3-642-82289-6. DOI: 10.1007/978-3-642-82289-6_23. URL: http://link.springer.com/10.1007/978-3-642-82289-6_23.

Boreham, B. (Jan. 1986). 'Preliminary Wind Tunnel Investigation of the Dispersion of Pollutant Particles in Model Building Wake Flows Using Bipolar Space Charge'. In: *Atmospheric Environment (1967)* 20.8, pp. 1523–1536. ISSN: 00046981. DOI: 10.1016/0004-6981(86)90241-6. URL: https://linkinghub.elsevier.com/retrieve/pii/0004698186902416.

Borst, A. and M. Heisenberg (1982). 'Osmotropotaxis in Drosophila Melanogaster'. In: *Journal of Comparative Physiology ? A* 147.4, pp. 479–484. ISSN: 0340-7594, 1432-1351. DOI: 10.1007/BF00612013. URL: http://link.springer.com/10.1007/BF00612013.

Bossert, W. H. and E. O. Wilson (Nov. 1963). 'The Analysis of Olfactory Communication among Animals'. In: *Journal of Theoretical Biology* 5.3, pp. 443–469. ISSN: 00225193. DOI: 10.1016/0022-5193(63)90089-4. URL: https://linkinghub.elsevier.com/retrieve/pii/0022519363900894.

Boyd, A. M. et al. (Feb. 2015). 'Broadcasting of Cortical Activity to the Olfactory Bulb'. In: *Cell Reports* 10.7, pp. 1032–1039. ISSN: 22111247. DOI: 10.1016/j.celrep.2015.01.047. URL: https://linkinghub.elsevier.com/retrieve/pii/S2211124715000728.

Brann, D. H. and S. R. Datta (8th July 2020). 'Finding the Brain in the Nose'. In: *Annual Review of Neuroscience* 43.1, pp. 277–295. ISSN: 0147-006X, 1545-4126. DOI: 10.1146/annurev-neuro-102119-103452. URL: https://www.annualreviews.org/doi/10.1146/annurev-neuro-102119-103452.

Brunjes, P. C., K. R. Illig and E. A. Meyer (Dec. 2005). 'A Field Guide to the Anterior Olfactory Nucleus (Cortex)'. In: *Brain Research Reviews* 50.2, pp. 305–335. ISSN: 01650173. DOI: 10.1016/j.brainresrev.2005.08.005. URL: https://linkinghub.elsevier.com/retrieve/pii/S0165017305001177.

Buck, L. and R. Axel (Apr. 1991). 'A Novel Multigene Family May Encode Odorant Receptors: A Molecular Basis for Odor Recognition'. In: *Cell* 65.1, pp. 175–187. ISSN: 00928674. DOI: 10.1016/0092-8674(91)90418-X. URL: https://linkinghub.elsevier.com/retrieve/pii/009286749190418X.

Budick, S. A. and M. H. Dickinson (1st Aug. 2006). 'Free-Flight Responses of *Drosophila Melanogaster* to Attractive Odors'. In: *Journal of Experimental Biology* 209.15, pp. 3001–3017. ISSN: 1477-9145, 0022-0949. DOI: 10.1242/jeb.02305. URL: https://journals.biologists.com/jeb/article/209/15/3001/16203/Free-flight-responses-of-Drosophila-melanogaster.

Burgues, J., L. F. Valdez and S. Marco (May 2019). 'High-Bandwidth e-Nose for Rapid Tracking of Turbulent Plumes'. In: *2019 IEEE International Symposium on Olfaction and Electronic Nose (ISOEN)*. 2019 IEEE International Symposium on Olfaction and Electronic Nose (ISOEN). Fukuoka, Japan: IEEE, pp. 1–3. ISBN: 978-1-5386-8327-9. DOI: 10.1109/ISOEN.2019.8823158. URL: https://ieeexplore.ieee.org/document/8823158/.

Burgués, J., V. Hernández et al. (24th Jan. 2019). 'Smelling Nano Aerial Vehicle for Gas Source Localization and Mapping'. In: *Sensors (Switzerland)* 19.3, p. 478. ISSN: 14248220. DOI: 10.3390/s19030478. pmid: 30682827. URL: https://www.mdpi.com/1424-8220/19/3/478.

– (Feb. 2020). 'Gas Distribution Mapping and Source Localization Using a 3D Grid of Metal Oxide Semiconductor Sensors'. In: *Sensors and Actuators B: Chemical* 304, p. 127309. ISSN: 09254005. DOI: 10.1016/j.snb.2019.127309. URL: https://linkinghub.elsevier.com/retrieve/pii/S0925400519315084.

Burgués, J. and S. Marco (2019). 'Wind-Independent Estimation of Gas Source Distance From Transient Features of Metal Oxide Sensor Signals'. In: *IEEE Access* 7, pp. 140460–140469. ISSN: 2169-3536. DOI: 10.1109/ACCESS.2019.2940936.

– (2020). 'Feature Extraction for Transient Chemical Sensor Signals in Response to Turbulent Plumes: Application to Chemical Source Distance Prediction'. In: *Sensors and Actuators, B: Chemical* 320 (April), p. 128235. ISSN: 09254005. DOI: 10.1016/j.snb.2020.128235. URL: https://doi.org/10.1016/j.snb.2020.128235.

Burton, S. D. (1st Oct. 2017). 'Inhibitory Circuits of the Mammalian Main Olfactory Bulb'. In: *Journal of Neurophysiology* 118.4, pp. 2034–2051. ISSN: 1522-1598. DOI: 10.1152/jn.00109.2017. pmid: 28724776.

Cardé, R. T. and M. A. Willis (July 2008). 'Navigational Strategies Used by Insects to Find Distant, Wind-Borne Sources of Odor'. In: *Journal of Chemical Ecology* 34.7, pp. 854–866. ISSN: 0098-0331, 1573-1561. DOI: 10.1007/s10886-008-9484-5. URL: http://link.springer.com/10.1007/s10886-008-9484-5.

Carmel, L. et al. (Aug. 2003). 'A Feature Extraction Method for Chemical Sensors in Electronic Noses'. In: *Sensors and Actuators B: Chemical* 93.1-3, pp. 67–76. ISSN: 09254005. DOI: 10.1016/S0925-4005(03)00247-8. URL: https://linkinghub.elsevier.com/retrieve/pii/S0925400503002478.

Celani, A., E. Villermaux and M. Vergassola (28th Oct. 2014). 'Odor Landscapes in Turbulent Environments'. In: *Physical Review X* 4.4, p. 041015. ISSN: 2160-3308. DOI: 10.1103/PhysRevX.4.041015. arXiv: 1411.3507. URL: https://link.aps.org/doi/10.1103/PhysRevX.4.041015.

Charlton, R. E. and R. T. Cardé (Jan. 1982). 'Rate and Diel Periodicity of Pheromone Emission from Female Gypsy Moths, (Lymantria Dispar) Determined with a Glass-Adsorption Collection System'. In: *Journal of Insect Physiology* 28.5, pp. 423–430. ISSN: 00221910. DOI: 10.1016/0022-1910(82)90069-5. URL: https://linkinghub.elsevier.com/retrieve/pii/0022191082900695.

Cholé, H. et al. (8th July 2022). 'Antenna Movements as a Function of Odorants' Biological Value in Honeybees (Apis Mellifera L.)' In: *Scientific Reports* 12.1, p. 11674. ISSN: 2045-2322. DOI: 10.1038/s41598-022-14354-z. URL: https://www.nature.com/articles/s41598-022-14354-z.

Christensen, T. A. and J. G. Hildebrand (1st Feb. 1997). 'Coincident Stimulation With Pheromone Components Improves Temporal Pattern Resolution in Central Olfactory Neurons'. In: *Journal of Neurophysiology* 77.2, pp. 775–781. ISSN: 0022-3077, 1522-1598. DOI: 10.1152/jn.1997.77.2.775. URL: https://www.physiology.org/doi/10.1152/jn.1997.77.2.775.

Claverie, N., P. Buvat and J. Casas (23rd Aug. 2023). 'Active Sensing in Bees Through Antennal Movements Is Independent of Odor Molecule'. In: *Integrative And Comparative Biology* 63.2, pp. 315–331. ISSN: 1540-7063, 1557-7023. DOI: 10.1093/icb/icad010. URL: https://academic.oup.com/icb/article/63/2/315/7084986.

Cleland, T. A. (2014). 'Construction of Odor Representations by Olfactory Bulb Microcircuits'. In: *Progress in Brain Research*. Vol. 208. Elsevier, pp. 177–203. ISBN: 978-0-444-63350-7. DOI: 10.1016/B978-0-444-63350-7.00007-3. URL: https://linkinghub.elsevier.com/retrieve/pii/B9780444633507000073.

Collins, C. L. and S. F. Potts (1932). 'Attractants for the Flying Gypsy Moths as an Aid to Locating New Infestations.' In: *U.S.D.A. Tech. Bull.* 336, p. 43.

Connelly, T. et al. (13th Jan. 2015). 'G Protein-Coupled Odorant Receptors Underlie Mechanosensitivity in Mammalian Olfactory Sensory Neurons'. In: *Proceedings of the National Academy of Sciences* 112.2, pp. 590–595. ISSN: 0027-8424, 1091-6490. DOI: 10.1073/pnas.1418515112. URL: https://pnas.org/doi/full/10.1073/pnas.1418515112.

Connor, E. G., M. K. McHugh and J. P. Crimaldi (Sept. 2018). 'Quantification of Airborne Odor Plumes Using Planar Laser-Induced Fluorescence'. In: *Experiments in Fluids* 59.9, p. 137. ISSN: 0723-4864, 1432-1114. DOI: 10.1007/s00348-018-2591-3. URL: http://link.springer.com/10.1007/s00348-018-2591-3.

Couto, A., M. Alenius and B. J. Dickson (Sept. 2005). 'Molecular, Anatomical, and Functional Organization of the Drosophila Olfactory System'. In: *Current Biology* 15.17, pp. 1535–1547. ISSN: 09609822. DOI: 10.1016/j.cub.2005.07.034. URL: https://linkinghub.elsevier.com/retrieve/pii/S096098220500789X.

Crenshaw, H. C. (Dec. 1996). 'A New Look at Locomotion in Microorganisms: Rotating and Translating'. In: *American Zoologist* 36.6, pp. 608–618. ISSN: 0003-1569. DOI: 10.1093/icb/36.6.608. URL: https://academic.oup.com/icb/article-lookup/doi/10.1093/icb/36.6.608.

Crimaldi, J. P. (June 2008). 'Planar Laser Induced Fluorescence in Aqueous Flows'. In: *Experiments in Fluids* 44.6, pp. 851–863. ISSN: 0723-4864, 1432-1114. DOI: 10.1007/s00348-008-0496-2. URL: http://link.springer.com/10.1007/s00348-008-0496-2.

Crimaldi, J. P. and H. S. Browning (2004). 'A Proposed Mechanism for Turbulent Enhancement of Broadcast Spawning Efficiency'. In: *Journal of Marine Systems*. DOI: 10.1016/j.jmarsys.2003.06.005.

Crimaldi, J. P., M. A. Koehl and J. R. Koseff (2002). 'Effects of the Resolution and Kinematics of Olfactory Appendages on the Interception of Chemical Signals in a Turbulent Odor Plume'. In: *Environmental Fluid Mechanics*. ISSN: 15677419. DOI: 10.1023/A:1016279617858.

Crimaldi, J. P. and J. R. Koseff (2001). 'High-Resolution Measurements of the Spatial and Temporal Scalar Structure of a Turbulent Plume'. In: *Experiments in Fluids*. ISSN: 07234864. DOI: 10.1007/s003480000263.

Crimaldi, J. P., M. B. Wiley and J. R. Koseff (2002). 'The Relationship between Mean and Instantaneous Structure in Turbulent Passive Scalar Plumes'. In: *Journal of Turbulence* 3 (June 2001), pp. 27–29. ISSN: 14685248. DOI: 10.1088/1468-5248/3/1/014.

Crimaldi, J. et al. (Feb. 2022). 'Active Sensing in a Dynamic Olfactory World'. In: *Journal of Computational Neuroscience* 50.1, pp. 1–6. ISSN: 0929-5313, 1573-6873. DOI: 10.1007/s10827-021-00798-1. URL: https://link.springer.com/10.1007/s10827-021-00798-1.

Cury, K. M. and N. Uchida (Nov. 2010). 'Robust Odor Coding via Inhalation-Coupled Transient Activity in the Mammalian Olfactory Bulb'. In: *Neuron* 68.3, pp. 570–585. ISSN: 08966273. DOI: 10.1016/j.neuron.2010.09.040. URL: https://linkinghub.elsevier.com/retrieve/pii/S0896627310007828.

Dahm, W. J. A. and P. E. Dimotakis (Sept. 1987). 'Measurements of Entrainment and Mixing in Turbulent Jets'. In: *AIAA Journal* 25.9, pp. 1216–1223. ISSN: 0001-1452, 1533-385X. DOI: 10.2514/3.9770. URL: https://arc.aiaa.org/doi/10.2514/3.9770.

Das Chakraborty, S. and S. Sachse (Jan. 2021). 'Olfactory Processing in the Lateral Horn of Drosophila'. In: *Cell and Tissue Research* 383.1, pp. 113–123. ISSN: 0302-766X, 1432-0878. DOI: 10.1007/s00441-020-03392-6. URL: https://link.springer.com/10.1007/s00441-020-03392-6.

Dasgupta, D. et al. (25th May 2022). 'Coupling of Mouse Olfactory Bulb Projection Neurons to Fluctuating Odor Pulses'. In: *The Journal of Neuroscience* 42.21, pp. 4278–4296. ISSN: 0270-6474, 1529-2401. DOI: 10.1523/JNEUROSCI.1422-21.2022. URL: https://www.jneurosci.org/lookup/doi/10.1523/JNEUROSCI.1422-21.2022.

David, C. T., J. S. Kennedy and A. R. Ludlow (June 1983). 'Finding of a Sex Pheromone Source by Gypsy Moths Released in the Field'. In: *Nature* 303.5920, pp. 804–806. ISSN: 0028-0836, 1476-4687. DOI: 10.1038/303804a0. URL: https://www.nature.com/articles/303804a0.

David, F. O. et al. (30th Oct. 2009). 'Specific Entrainment of Mitral Cells during Gamma Oscillation in the Rat Olfactory Bulb'. In: *PLoS Computational Biology* 5.10. Ed. by A. Morrison, e1000551. ISSN: 1553-7358. DOI: 10.1371/journal.pcbi.1000551. URL: https://dx.plos.org/10.1371/journal.pcbi.1000551.

De Bruyne, M., P. J. Clyne and J. R. Carlson (1st June 1999). 'Odor Coding in a Model Olfactory Organ: The *Drosophila* Maxillary Palp'. In: *The Journal of Neuroscience* 19.11, pp. 4520–4532. ISSN: 0270-6474, 1529-2401. DOI: 10.1523/JNEUROSCI.19-11-04520.1999. URL: https://www.jneurosci.org/lookup/doi/10.1523/JNEUROSCI.19-11-04520.1999.

De Bruyne, M., K. Foster and J. R. Carlson (May 2001). 'Odor Coding in the Drosophila Antenna'. In: *Neuron* 30.2, pp. 537–552. ISSN: 08966273. DOI: 10.1016/S0896-6273(01)00289-6. URL: https://linkinghub.elsevier.com/retrieve/pii/S0896627301002896.

De Meester, L. and C. Cousyn (1997). 'The Change in Phototactic Behaviour of a Daphnia Magna Clone in the Presence of Fish Kairomones: The Effect of Exposure Time'. In: *Cladocera: The Biology of Model Organisms*. Ed. by A. Brancelj, L. De Meester and P. Spaak. Dordrecht: Springer Netherlands, pp. 169–175. ISBN: 978-94-010-6084-4. DOI: 10.1007/978-94-011-4964-8_19. URL: http://link.springer.com/10.1007/978-94-011-4964-8_19.

Demir, M. et al. (3rd Nov. 2020). 'Walking Drosophila Navigate Complex Plumes Using Stochastic Decisions Biased by the Timing of Odor Encounters'. In: *eLife* 9, e57524. ISSN: 2050-084X. DOI: 10.7554/eLife.57524. URL: https://elifesciences.org/articles/57524.

Dennler, N., D. Drix, S. Rastogi et al. (28th Mar. 2022). 'Rapid Inference of Geographical Location with an Event-based Electronic Nose'. In: *Neuro-Inspired Computational Elements Conference*. NICE 2022: Neuro-Inspired Computational Elements Conference. Virtual Event USA: ACM, pp. 112–114. ISBN: 978-1-4503-9559-5. DOI: 10.1145/3517343.3517381. URL: https://dl.acm.org/doi/10.1145/3517343.3517381.

Dennler, N., D. Drix, T. P. A. Warner et al. (5th June 2024). *High-Speed Odour Sensing Using Miniaturised Electronic Nose*. arXiv: 2406.01904 [cs, eess]. URL: http://arxiv.org/abs/2406.01904. Pre-published.

Dennler, N., S. Rastogi et al. (June 2022). 'Drift in a Popular Metal Oxide Sensor Dataset Reveals Limitations for Gas Classification Benchmarks'. In: *Sensors and Actuators B: Chemical* 361, p. 131668. ISSN: 09254005. DOI: 10.1016/j.snb.2022.131668. URL: https://linkinghub.elsevier.com/retrieve/pii/S0925400522003100.

Díaz-Quesada, M. et al. (28th Feb. 2018). 'Inhalation Frequency Controls Reformatting of Mitral/Tufted Cell Odor Representations in the Olfactory Bulb'. In: *The Journal of Neuroscience* 38.9, pp. 2189–2206. ISSN: 0270-6474, 1529-2401. DOI: 10.1523/JNEUROSCI.0714-17.2018. URL: https://www.jneurosci.org/lookup/doi/10.1523/JNEUROSCI.0714-17.2018.

Drix, D., N. Dennler and M. Schmuker (29th May 2022). 'Rapid Recognition of Olfactory Scenes with a Portable MOx Sensor System Using Hotplate Modulation'. In: *2022 IEEE International Symposium on Olfaction and Electronic Nose (ISOEN)*. 2022 IEEE International Symposium on Olfaction and Electronic Nose (ISOEN). Aveiro, Portugal: IEEE, pp. 1–4. ISBN: 978-1-66545-860-3. DOI: 10.1109/ISOEN54820.2022.9789654. URL: https://ieeexplore.ieee.org/document/9789654/.

Drix, D. and M. Schmuker (2021). 'Resolving Fast Gas Transients with Metal Oxide Sensors'. In: *ACS Sensors* 6.3, pp. 688–692. ISSN: 23793694. DOI: 10.1021/acssensors.0c02006. pmid: 33524259.

Duistermars, B. J., D. M. Chow and M. A. Frye (Aug. 2009). 'Flies Require Bilateral Sensory Input to Track Odor Gradients in Flight'. In: *Current Biology* 19.15, pp. 1301–1307. ISSN: 09609822. DOI: 10.1016/j.cub.2009.06.022. URL: https://linkinghub.elsevier.com/retrieve/pii/S0960982209012950.

Dusenbery, D. B. (1992). *Sensory Ecology: How Organisms Acquire and Respond to Information*. New York: W.H. Freeman. 558 pp. ISBN: 978-0-7167-2333-2.

Elkinton, J. S. et al. (Dec. 1987). 'Pheromone Puff Trajectory and Upwind Flight of Male Gypsy Moths in a Forest'. In: *Physiological Entomology* 12.4, pp. 399–406. ISSN: 0307-6962, 1365-3032. DOI: 10.1111/j.1365-3032.1987.tb00766.x. URL: https://onlinelibrary.wiley.com/doi/10.1111/j.1365-3032.1987.tb00766.x.

Elmore, T. et al. (29th Oct. 2003). 'Targeted Mutation of a *Drosophila* Odor Receptor Defines Receptor Requirement in a Novel Class of Sensillum'. In: *The Journal of Neuroscience* 23.30, pp. 9906–9912. ISSN: 0270-6474, 1529-2401. DOI: 10.1523/JNEUROSCI.23-30-09906.2003. URL: https://www.jneurosci.org/lookup/doi/10.1523/JNEUROSCI.23-30-09906.2003.

Esquivelzeta Rabell, J. et al. (May 2017). 'Spontaneous Rapid Odor Source Localization Behavior Requires Interhemispheric Communication'. In: *Current Biology* 27.10, 1542–1548.e4. ISSN: 09609822. DOI: 10.1016/j.cub.2017.04.027. URL: https://linkinghub.elsevier.com/retrieve/pii/S0960982217304360.

Essa, K. S. M., S. M. Etman and M. S. El-Otaify (2020). 'Relation between the Actual and Estimated Maximum Ground Level Concentration of Air Pollutant and Its Downwind Locations'. In: *Open Journal of Air Pollution* 09.02, pp. 27–35. ISSN: 2169-2653, 2169-2661. DOI: 10.4236/ojap.2020.92003. URL: https://www.scirp.org/journal/doi.aspx?doi=10.4236/ojap.2020.92003.

Fackrell, J. E. (Oct. 1978). 'A System for Turbulent Concentration Measurements'. In: *Journal of Physics E: Scientific Instruments* 11.10, pp. 1015–1022. ISSN: 0022-3735. DOI: 10.1088/0022-3735/11/10/016. URL: https://iopscience.iop.org/article/10.1088/0022-3735/11/10/016.

Fan, H. et al. (7th Feb. 2019). 'Towards Gas Discrimination and Mapping in Emergency Response Scenarios Using a Mobile Robot with an Electronic Nose'. In: *Sensors* 19.3, p. 685. ISSN: 1424-8220. DOI: 10.3390/s19030685. URL: http://www.mdpi.com/1424-8220/19/3/685.

Findley, T. M. et al. (4th May 2021). 'Sniff-Synchronized, Gradient-Guided Olfactory Search by Freely Moving Mice'. In: *eLife* 10, e58523. ISSN: 2050-084X. DOI: 10.7554/eLife.58523. URL: https://elifesciences.org/articles/58523.

Finelli, C. M. et al. (Mar. 2000). 'Physical Constraints on Ecological Processes: A Field Test of Odor-Mediated Foraging'. In: *Ecology* 81.3, pp. 784–797. ISSN: 0012-9658. DOI: 10.1890/0012-

9658(2000)081[0784:PCOEPA]2.0.CO;2. URL: http://doi.wiley.com/10.1890/0012-9658(2000)081[0784:PCOEPA]2.0.CO;2.

Fishilevich, E. et al. (Dec. 2005). 'Chemotaxis Behavior Mediated by Single Larval Olfactory Neurons in Drosophila'. In: *Current Biology* 15.23, pp. 2086–2096. ISSN: 09609822. DOI: 10.1016/j.cub.2005.11.016. URL: https://linkinghub.elsevier.com/retrieve/pii/S0960982205013783.

Frenkiel, F. (1953). 'Turbulent Diffusion: Mean Concentration Distribution in a Flow Field of Homogeneous Turbulence'. In: *Advances in Applied Mechanics*. Vol. 3. Elsevier, pp. 61–107. ISBN: 978-0-12-002003-4. DOI: 10.1016/S0065-2156(08)70208-4. URL: https://linkinghub.elsevier.com/retrieve/pii/S0065215608702084.

Friedrich, R. W. and S. I. Korsching (May 1997). 'Combinatorial and Chemotopic Odorant Coding in the Zebrafish Olfactory Bulb Visualized by Optical Imaging'. In: *Neuron* 18.5, pp. 737–752. ISSN: 08966273. DOI: 10.1016/S0896-6273(00)80314-1. URL: https://linkinghub.elsevier.com/retrieve/pii/S0896627300803141.

Gardiner, J. M. et al. (2nd Apr. 2014). 'Multisensory Integration and Behavioral Plasticity in Sharks from Different Ecological Niches'. In: *PLoS ONE* 9.4. Ed. by J. M. Hemmi, e93036. ISSN: 1932-6203. DOI: 10.1371/journal.pone.0093036. URL: https://dx.plos.org/10.1371/journal.pone.0093036.

Gascue, F. et al. (June 2022). 'Antennal Movements Can Be Used as Behavioral Readout of Odor Valence in Honey Bees'. In: *IBRO Neuroscience Reports* 12, pp. 323–332. ISSN: 26672421. DOI: 10.1016/j.ibneur.2022.04.005. URL: https://linkinghub.elsevier.com/retrieve/pii/S2667242122000252.

Gaudry, Q., K. I. Nagel and R. I. Wilson (Apr. 2012). 'Smelling on the Fly: Sensory Cues and Strategies for Olfactory Navigation in Drosophila'. In: *Current Opinion in Neurobiology* 22.2, pp. 216–222. ISSN: 09594388. DOI: 10.1016/j.conb.2011.12.010. pmid: 22221864. URL: http://dx.doi.org/10.1016/j.conb.2011.12.010.

Geffen, M. N. et al. (Feb. 2009). 'Neural Encoding of Rapidly Fluctuating Odors'. In: *Neuron* 61.4, pp. 570–586. ISSN: 08966273. DOI: 10.1016/j.neuron.2009.01.021. URL: https://linkinghub.elsevier.com/retrieve/pii/S0896627309000889.

Gifford, F. (1959). 'Statistical Properties of A Fluctuating Plume Dispersion Model'. In: *Advances in Geophysics*. Vol. 6. Elsevier, pp. 117–137. ISBN: 978-0-12-018806-2. DOI: 10.1016/S0065-2687(08)60099-0. URL: https://linkinghub.elsevier.com/retrieve/pii/S0065268708600990.

Gire, D. H., J. D. Whitesell et al. (Aug. 2013). 'Information for Decision-Making and Stimulus Identification Is Multiplexed in Sensory Cortex'. In: *Nature Neuroscience* 16.8, pp. 991–993. ISSN: 1097-6256, 1546-1726. DOI: 10.1038/nn.3432. URL: https://www.nature.com/articles/nn.3432.

Gire, D. H., V. Kapoor et al. (May 2016). 'Mice Develop Efficient Strategies for Foraging and Navigation Using Complex Natural Stimuli'. In: *Current Biology* 26.10, pp. 1261–1273. ISSN:

09609822. DOI: 10.1016/j.cub.2016.03.040. URL: https://linkinghub.elsevier.com/retrieve/pii/S0960982216302500.

Gire, D. H., D. Restrepo et al. (May 2013). 'Temporal Processing in the Olfactory System: Can We See a Smell?' In: *Neuron* 78.3, pp. 416–432. ISSN: 08966273. DOI: 10.1016/j.neuron.2013.04.033. URL: https://linkinghub.elsevier.com/retrieve/pii/S0896627313003644.

Gleeson, R. A., M. A. Adams and A. B. Smith (Feb. 1987). 'Hormonal Modulation of Pheromone-Mediated Behavior in a Crustacean'. In: *The Biological Bulletin* 172.1, pp. 1–9. ISSN: 0006-3185, 1939-8697. DOI: 10.2307/1541602. URL: https://www.journals.uchicago.edu/doi/10.2307/1541602.

Gottfried, J. A. (Aug. 2005). 'A Truffle in the Mouth Is Worth Two in the Bush: Odor Localization in the Human Brain'. In: *Neuron* 47.4, pp. 473–476. ISSN: 08966273. DOI: 10.1016/j.neuron.2005.08.002. URL: https://linkinghub.elsevier.com/retrieve/pii/S0896627305006501.

Gschwend, O., J. Beroud and A. Carleton (17th Jan. 2012). 'Encoding Odorant Identity by Spiking Packets of Rate-Invariant Neurons in Awake Mice'. In: *PLoS ONE* 7.1. Ed. by M. Louis, e30155. ISSN: 1932-6203. DOI: 10.1371/journal.pone.0030155. URL: https://dx.plos.org/10.1371/journal.pone.0030155.

Gumaste, A. et al. (5th Mar. 2024). 'Behavioral Discrimination and Olfactory Bulb Encoding of Odor Plume Intermittency'. In: *eLife* 13, e85303. ISSN: 2050-084X. DOI: 10.7554/eLife.85303. URL: https://elifesciences.org/articles/85303.

Haddad, R. et al. (7th July 2010). 'Global Features of Neural Activity in the Olfactory System Form a Parallel Code That Predicts Olfactory Behavior and Perception'. In: *Journal of Neuroscience* 30.27, pp. 9017–9026. ISSN: 0270-6474, 1529-2401. DOI: 10.1523/JNEUROSCI.0398-10.2010. URL: https://www.jneurosci.org/lookup/doi/10.1523/JNEUROSCI.0398-10.2010.

Hadjitofi, A. and M. Wilson (Jan. 1979). 'Fast-Response Measurements of Air Pollution'. In: *Atmospheric Environment (1967)* 13.6, pp. 755–760. ISSN: 00046981. DOI: 10.1016/0004-6981(79)90265-8. URL: https://linkinghub.elsevier.com/retrieve/pii/0004698179902658.

Hallem, E. A., M. G. Ho and J. R. Carlson (June 2004). 'The Molecular Basis of Odor Coding in the Drosophila Antenna'. In: *Cell* 117.7, pp. 965–979. ISSN: 00928674. DOI: 10.1016/j.cell.2004.05.012. URL: https://linkinghub.elsevier.com/retrieve/pii/S0092867404004982.

Hassenstein, B. and W. Reichardt (1st Oct. 1956). 'Systemtheoretische Analyse der Zeit-, Reihenfolgen- und Vorzeichenauswertung bei der Bewegungsperzeption des Rüsselkäfers Chlorophanus'. In: *Zeitschrift für Naturforschung B* 11.9-10, pp. 513–524. ISSN: 1865-7117, 0932-0776. DOI: 10.1515/znb-1956-9-1004. URL: https://www.degruyter.com/document/doi/10.1515/znb-1956-9-1004/html.

Heinbockel, T., T. A. Christensen and J. G. Hildebrand (21st June 1999). 'Temporal Tuning of Odor Responses in Pheromone-Responsive Projection Neurons in the Brain of the

Sphinx mothManduca Sexta'. In: *The Journal of Comparative Neurology* 409.1, pp. 1–12. ISSN: 0021-9967, 1096-9861. DOI: 10.1002/(SICI)1096-9861(19990621)409:1<1::AID-CNE1>3.0.CO;2-7. URL: https://onlinelibrary.wiley.com/doi/10.1002/(SICI)1096-9861(19990621)409:1%3C1::AID-CNE1%3E3.0.CO;2-7.

Hengenius, J. B. et al. (May 2021). 'Olfactory Navigation in the Real World: Simple Local Search Strategies for Turbulent Environments'. In: *Journal of Theoretical Biology* 516, p. 110607. ISSN: 00225193. DOI: 10.1016/j.jtbi.2021.110607. URL: https://linkinghub.elsevier.com/retrieve/pii/S0022519321000291.

Hopfield, J. J. (Aug. 1991). 'Olfactory Computation and Object Perception.' In: *Proceedings of the National Academy of Sciences* 88.15, pp. 6462–6466. ISSN: 0027-8424, 1091-6490. DOI: 10.1073/pnas.88.15.6462. URL: https://pnas.org/doi/full/10.1073/pnas.88.15.6462.

Huerta, R. et al. (2016). 'Online Decorrelation of Humidity and Temperature in Chemical Sensors for Continuous Monitoring'. In: *Chemometrics and Intelligent Laboratory Systems* 157, pp. 169–176. ISSN: 18733239. DOI: 10.1016/j.chemolab.2016.07.004.

Huston, S. J. et al. (Oct. 2015). 'Neural Encoding of Odors during Active Sampling and in Turbulent Plumes'. In: *Neuron* 88.2, pp. 403–418. ISSN: 08966273. DOI: 10.1016/j.neuron.2015.09.007. URL: https://linkinghub.elsevier.com/retrieve/pii/S0896627315007643.

Illig, K. R. and L. B. Haberly (17th Mar. 2003). 'Odor-evoked Activity Is Spatially Distributed in Piriform Cortex'. In: *Journal of Comparative Neurology* 457.4, pp. 361–373. ISSN: 0021-9967, 1096-9861. DOI: 10.1002/cne.10557. URL: https://onlinelibrary.wiley.com/doi/10.1002/cne.10557.

Inagaki, S. et al. (June 2020). 'Widespread Inhibition, Antagonism, and Synergy in Mouse Olfactory Sensory Neurons In Vivo'. In: *Cell Reports* 31.13, p. 107814. ISSN: 22111247. DOI: 10.1016/j.celrep.2020.107814. URL: https://linkinghub.elsevier.com/retrieve/pii/S2211124720307956.

Iwata, R., H. Kiyonari and T. Imai (Dec. 2017). 'Mechanosensory-Based Phase Coding of Odor Identity in the Olfactory Bulb'. In: *Neuron* 96.5, 1139–1152.e7. ISSN: 08966273. DOI: 10.1016/j.neuron.2017.11.008. URL: https://linkinghub.elsevier.com/retrieve/pii/S089662731731036X.

Jayaram, V. et al. (11th May 2023). 'Temporal Novelty Detection and Multiple Timescale Integration Drive Drosophila Orientation Dynamics in Temporally Diverse Olfactory Environments'. In: *PLOS Computational Biology* 19.5. Ed. by B. Webb, e1010606. ISSN: 1553-7358. DOI: 10.1371/journal.pcbi.1010606. URL: https://dx.plos.org/10.1371/journal.pcbi.1010606.

Jinn, J., E. G. Connor and L. F. Jacobs (7th Nov. 2020). 'How Ambient Environment Influences Olfactory Orientation in Search and Rescue Dogs'. In: *Chemical Senses* 45.8, pp. 625–634. ISSN: 0379-864X, 1464-3553. DOI: 10.1093/chemse/bjaa060. URL: https://academic.oup.com/chemse/article/45/8/625/5907694.

Johnson, B. N., J. D. Mainland and N. Sobel (Aug. 2003). 'Rapid Olfactory Processing Implicates Subcortical Control of an Olfactomotor System'. In: *Journal of Neurophysiology*

90.2, pp. 1084–1094. ISSN: 0022-3077, 1522-1598. DOI: 10.1152/jn.00115.2003. URL: https://www.physiology.org/doi/10.1152/jn.00115.2003.

Jones, C. D. (Feb. 1977). 'Ion Concentration Variations at Short Distances Downwind of Continuous and Quasi-instantaneous Point Sources'. In: *Pesticide Science* 8.1, pp. 84–95. ISSN: 0031-613X, 1096-9063. DOI: 10.1002/ps.2780080113. URL: https://onlinelibrary.wiley.com/doi/10.1002/ps.2780080113.

– (Jan. 1983). 'On the Structure of Instantaneous Plumes in the Atmosphere'. In: *Journal of Hazardous Materials* 7.2, pp. 87–112. ISSN: 03043894. DOI: 10.1016/0304-3894(83)80001-6. URL: https://linkinghub.elsevier.com/retrieve/pii/0304389483800016.

Jones, C. D. and N. T. Guilliford (Apr. 1979). 'Developments in the Use of Ionised Air as a Wind Tunnel Tracer'. In: *Journal of Physics E: Scientific Instruments* 12.4, pp. 321–327. ISSN: 0022-3735. DOI: 10.1088/0022-3735/12/4/023. URL: https://iopscience.iop.org/article/10.1088/0022-3735/12/4/023.

Jones, C. D. and W. Hutchinson (May 1976). 'Plumes of Electric Space Charge in the Lower Atmosphere'. In: *Journal of Atmospheric and Terrestrial Physics* 38.5, pp. 485–494. ISSN: 00219169. DOI: 10.1016/0021-9169(76)90005-2. URL: https://linkinghub.elsevier.com/retrieve/pii/0021916976900052.

Justus, K. A. et al. (2002). 'Measurement of Odor-Plume Structure in a Wind Tunnel Using a Photoionization Detector and a Tracer Gas'. In: *Environmental Fluid Mechanics* 2.1-2, pp. 115–142. ISSN: 15677419. DOI: 10.1023/A:1016227601019.

Kadakia, N. et al. (9th Nov. 2022). 'Odour Motion Sensing Enhances Navigation of Complex Plumes'. In: *Nature*. ISSN: 0028-0836, 1476-4687. DOI: 10.1038/s41586-022-05423-4. URL: https://www.nature.com/articles/s41586-022-05423-4.

Kellogg, F. E., D. E. Frizel and R. H. Wright (Aug. 1962). 'The Olfactory Guidance of Flying Insects. IV. Drosophila'. In: *The Canadian Entomologist* 94.8, pp. 884–888. ISSN: 0008-347X, 1918-3240. DOI: 10.4039/Ent94884-8. URL: https://www.cambridge.org/core/product/identifier/S0008347X00075970/type/journal_article.

Kennedy, J. S. (June 1978). 'The Concepts of Olfactory 'Arrestment' and 'Attraction''. In: *Physiological Entomology* 3.2, pp. 91–98. ISSN: 0307-6962, 1365-3032. DOI: 10.1111/j.1365-3032.1978.tb00138.x. URL: https://resjournals.onlinelibrary.wiley.com/doi/10.1111/j.1365-3032.1978.tb00138.x.

– (June 1983). 'Zigzagging and Casting as a Programmed Response to Wind-borne Odour: A Review'. In: *Physiological Entomology* 8.2, pp. 109–120. ISSN: 0307-6962, 1365-3032. DOI: 10.1111/j.1365-3032.1983.tb00340.x. URL: https://resjournals.onlinelibrary.wiley.com/doi/10.1111/j.1365-3032.1983.tb00340.x.

Kennedy, J. S., A. R. Ludlow and C. J. Sanders (Dec. 1980). 'Guidance System Used in Moth Sex Attraction'. In: *Nature* 288.5790, pp. 475–477. ISSN: 0028-0836, 1476-4687. DOI: 10.1038/288475a0. URL: https://www.nature.com/articles/288475a0.

Kennedy, J. S. and D. Marsh (31st May 1974). 'Pheromone-Regulated Anemotaxis in Flying Moths'. In: *Science* 184.4140, pp. 999–1001. ISSN: 0036-8075, 1095-9203. DOI: 10.1126/

science.184.4140.999. URL: https://www.science.org/doi/10.1126/science.184.4140.999.

Kepecs, A., N. Uchida and Z. F. Mainen (1st Feb. 2006). 'The Sniff as a Unit of Olfactory Processing'. In: *Chemical Senses* 31.2, pp. 167–179. ISSN: 1464-3553, 0379-864X. DOI: 10.1093/chemse/bjj016. URL: http://academic.oup.com/chemse/article/31/2/167/285994/The-Sniff-as-a-Unit-of-Olfactory-Processing.

– (July 2007). 'Rapid and Precise Control of Sniffing During Olfactory Discrimination in Rats'. In: *Journal of Neurophysiology* 98.1, pp. 205–213. ISSN: 0022-3077, 1522-1598. DOI: 10.1152/jn.00071.2007. URL: https://www.physiology.org/doi/10.1152/jn.00071.2007.

Khan, A. G., M. Sarangi and U. S. Bhalla (28th Feb. 2012). 'Rats Track Odour Trails Accurately Using a Multi-Layered Strategy with near-Optimal Sampling'. In: *Nature Communications* 3.1, p. 703. ISSN: 2041-1723. DOI: 10.1038/ncomms1712. URL: https://www.nature.com/articles/ncomms1712.

Khorramifar, A. et al. (19th June 2023). 'Environmental Engineering Applications of Electronic Nose Systems Based on MOX Gas Sensors'. In: *Sensors* 23.12, p. 5716. ISSN: 1424-8220. DOI: 10.3390/s23125716. URL: https://www.mdpi.com/1424-8220/23/12/5716.

Kikas, T. et al. (1st Aug. 2001). 'Chemical Plume Tracking. 1. Chemical Information Encoding'. In: *Analytical Chemistry* 73.15, pp. 3662–3668. ISSN: 0003-2700, 1520-6882. DOI: 10.1021/ac0101813. URL: https://pubs.acs.org/doi/10.1021/ac0101813.

Koehl, M. A. et al. (2001). 'Lobster Sniffing: Antennute Design and Hydrodynamic Fittering of Information in an Odor Plume'. In: *Science (80-.).* 294.5548, pp. 1948–1951. ISSN: 00368075. DOI: 10.1126/science.1063724. pmid: 11729325.

Koehl, M. (1st Feb. 2006). 'The Fluid Mechanics of Arthropod Sniffing in Turbulent Odor Plumes'. In: *Chemical Senses* 31.2, pp. 93–105. ISSN: 1464-3553, 0379-864X. DOI: 10.1093/chemse/bjj009. URL: http://academic.oup.com/chemse/article/31/2/93/285974/The-Fluid-Mechanics-of-Arthropod-Sniffing-in.

Koochesfahani, M. M. and P. E. Dimotakis (Nov. 1985). 'Laser-Induced Fluorescence Measurements of Mixed Fluid Concentrationin a Liquid Plane Shear Layer'. In: *AIAA Journal* 23.11, pp. 1700–1707. ISSN: 0001-1452, 1533-385X. DOI: 10.2514/3.9154. URL: https://arc.aiaa.org/doi/10.2514/3.9154.

Kowadlo, G. and R. A. Russell (Aug. 2008). 'Robot Odor Localization: A Taxonomy and Survey'. In: *The International Journal of Robotics Research* 27.8, pp. 869–894. ISSN: 0278-3649, 1741-3176. DOI: 10.1177/0278364908095118. URL: http://journals.sagepub.com/doi/10.1177/0278364908095118.

Kramer, E. (Mar. 1976). 'The Orientation of Walking Honeybees in Odour Fields with Small Concentration Gradients'. In: *Physiological Entomology* 1.1, pp. 27–37. ISSN: 0307-6962, 1365-3032. DOI: 10.1111/j.1365-3032.1976.tb00883.x. URL: https://resjournals.onlinelibrary.wiley.com/doi/10.1111/j.1365-3032.1976.tb00883.x.

Kurian, S. M. et al. (Jan. 2021). 'Odor Coding in the Mammalian Olfactory Epithelium'. In: *Cell and Tissue Research* 383.1, pp. 445–456. ISSN: 0302-766X, 1432-0878. DOI: 10.1007/s00441-020-03327-1. URL: https://link.springer.com/10.1007/s00441-020-03327-1.

Laurent, G. (Nov. 2002). 'Olfactory Network Dynamics and the Coding of Multidimensional Signals'. In: *Nature Reviews Neuroscience* 3.11, pp. 884–895. ISSN: 1471-003X, 1471-0048. DOI: 10.1038/nrn964. URL: https://www.nature.com/articles/nrn964.

Lei, H. et al. (30th Mar. 2022). 'Novelty Detection in Early Olfactory Processing of the Honey Bee, Apis Mellifera'. In: *PLOS ONE* 17.3. Ed. by E. M. C. Skoulakis, e0265009. ISSN: 1932-6203. DOI: 10.1371/journal.pone.0265009. URL: https://dx.plos.org/10.1371/journal.pone.0265009.

Leitch, K. J. et al. (27th Apr. 2021). 'The Long-Distance Flight Behavior of *Drosophila* Supports an Agent-Based Model for Wind-Assisted Dispersal in Insects'. In: *Proceedings of the National Academy of Sciences* 118.17, e2013342118. ISSN: 0027-8424, 1091-6490. DOI: 10.1073/pnas.2013342118. URL: https://pnas.org/doi/full/10.1073/pnas.2013342118.

Lemon, W. C. and W. M. Getz (15th June 1997). 'Temporal Resolution of General Odor Pulses by Olfactory Sensory Neurons in American Cockroaches'. In: *Journal of Experimental Biology* 200.12, pp. 1809–1819. ISSN: 0022-0949, 1477-9145. DOI: 10.1242/jeb.200.12.1809. URL: https://journals.biologists.com/jeb/article/200/12/1809/7254/Temporal-Resolution-of-General-Odor-Pulses-by.

Li, A., D. H. Gire et al. (26th Nov. 2014). 'Precise Detection of Direct Glomerular Input Duration by the Olfactory Bulb'. In: *The Journal of Neuroscience* 34.48, pp. 16058–16064. ISSN: 0270-6474, 1529-2401. DOI: 10.1523/JNEUROSCI.3382-14.2014. URL: https://www.jneurosci.org/lookup/doi/10.1523/JNEUROSCI.3382-14.2014.

Li, A., X. Rao et al. (Jan. 2020). 'Complex Neural Representation of Odour Information in the Olfactory Bulb'. In: *Acta Physiologica* 228.1, e13333. ISSN: 1748-1708, 1748-1716. DOI: 10.1111/apha.13333. URL: https://onlinelibrary.wiley.com/doi/10.1111/apha.13333.

Li, C., H. Dong and K. Zhao (10th Aug. 2018). 'A Balance between Aerodynamic and Olfactory Performance during Flight in Drosophila'. In: *Nature Communications* 9.1, p. 3215. ISSN: 2041-1723. DOI: 10.1038/s41467-018-05708-1. URL: https://www.nature.com/articles/s41467-018-05708-1.

Li, J. and W. L. Shew (28th Sept. 2020). 'Tuning Network Dynamics from Criticality to an Asynchronous State'. In: *PLOS Computational Biology* 16.9. Ed. by A. Soltani, e1008268. ISSN: 1553-7358. DOI: 10.1371/journal.pcbi.1008268. URL: https://dx.plos.org/10.1371/journal.pcbi.1008268.

Liberzon, A., R. Gurka and G. Hetsroni (1st Feb. 2004). 'XPIV-Multi-plane Stereoscopic Particle Image Velocimetry'. In: *Experiments in Fluids* 36.2, pp. 355–362. ISSN: 0723-4864, 1432-1114. DOI: 10.1007/s00348-003-0731-9. URL: http://link.springer.com/10.1007/s00348-003-0731-9.

Lozano, A., B. Yip and R. K. Hanson (1992). 'Acetone: A Tracer for Concentration Measurements in Gaseous Flows by Planar Laser-Induced Fluorescence'. In: *Experiments in Fluids* 13.6, pp. 369–376. ISSN: 07234864. DOI: 10.1007/BF00223244.

Mafra-Neto, A. and R. T. Cardé (May 1994). 'Fine-Scale Structure of Pheromone Plumes Modulates Upwind Orientation of Flying Moths'. In: *Nature* 369.6476, pp. 142–144. ISSN: 0028-0836, 1476-4687. DOI: 10.1038/369142a0. URL: https://www.nature.com/articles/369142a0.

Malnic, B. et al. (Mar. 1999). 'Combinatorial Receptor Codes for Odors'. In: *Cell* 96.5, pp. 713–723. ISSN: 00928674. DOI: 10.1016/S0092-8674(00)80581-4. URL: https://linkinghub.elsevier.com/retrieve/pii/S0092867400805814.

Marin, A. C., A. T. Schaefer and T. Ackels (Jan. 2021). 'Spatial Information from the Odour Environment in Mammalian Olfaction'. In: *Cell and Tissue Research* 383.1, pp. 473–483. ISSN: 0302-766X, 1432-0878. DOI: 10.1007/s00441-020-03395-3. URL: http://link.springer.com/10.1007/s00441-020-03395-3.

Marsh, D., J. S. Kennedy and A. R. Ludlow (Sept. 1978). 'An Analysis of Anemotactic Zigzagging Flight in Male Moths Stimulated by Pheromone'. In: *Physiological Entomology* 3.3, pp. 221–240. ISSN: 0307-6962, 1365-3032. DOI: 10.1111/j.1365-3032.1978.tb00152.x. URL: https://resjournals.onlinelibrary.wiley.com/doi/10.1111/j.1365-3032.1978.tb00152.x.

– (June 1981). 'Analysis of Zigzagging Flight in Moths: A Correction'. In: *Physiological Entomology* 6.2, pp. 225–225. ISSN: 0307-6962, 1365-3032. DOI: 10.1111/j.1365-3032.1981.tb00645.x. URL: https://resjournals.onlinelibrary.wiley.com/doi/10.1111/j.1365-3032.1981.tb00645.x.

Martelli, C., J. R. Carlson and T. Emonet (10th Apr. 2013). 'Intensity Invariant Dynamics and Odor-Specific Latencies in Olfactory Receptor Neuron Response'. In: *The Journal of Neuroscience* 33.15, pp. 6285–6297. ISSN: 0270-6474, 1529-2401. DOI: 10.1523/JNEUROSCI.0426-12.2013. URL: https://www.jneurosci.org/lookup/doi/10.1523/JNEUROSCI.0426-12.2013.

Martinez, Burgués and Marco (18th Sept. 2019). 'Fast Measurements with MOX Sensors: A Least-Squares Approach to Blind Deconvolution'. In: *Sensors* 19.18, p. 4029. ISSN: 1424-8220. DOI: 10.3390/s19184029. URL: https://www.mdpi.com/1424-8220/19/18/4029.

Mathis, A. and R. F. Smith (Oct. 1993). 'Fathead Minnows, Pimephales Promelas, Learn to Recognize Northern Pike, Esox Lucius, as Predators on the Basis of Chemical Stimuli from Minnows in the Pike's Diet'. In: *Animal Behaviour* 46.4, pp. 645–656. ISSN: 00033472. DOI: 10.1006/anbe.1993.1241. URL: https://linkinghub.elsevier.com/retrieve/pii/S0003347283712418.

McLeese, D. W. (1st June 1973). 'Orientation of Lobsters (*Homarus Americanus*) to Odor'. In: *Journal of the Fisheries Research Board of Canada* 30.6, pp. 838–840. ISSN: 0015-296X. DOI: 10.1139/f73-140. URL: http://www.nrcresearchpress.com/doi/10.1139/f73-140.

Means, L. W., S. R. Alexander and M. F. O'Neal (Sept. 1992). 'Those Cheating Rats: Male and Female Rats Use Odor Trails in a Water-Escape "Working Memory" Task'. In: *Behavioral and Neural Biology* 58.2, pp. 144–151. ISSN: 01631047. DOI: 10.1016/0163-1047(92)90387-J. URL: https://linkinghub.elsevier.com/retrieve/pii/016310479290387J.

Meissner-Bernard, C. et al. (Feb. 2019). 'Encoding of Odor Fear Memories in the Mouse Olfactory Cortex'. In: *Current Biology* 29.3, 367–380.e4. ISSN: 09609822. DOI: 10.1016/j.cub.2018.12.003. URL: https://linkinghub.elsevier.com/retrieve/pii/S096098221831604X.

Meister, M. and T. Bonhoeffer (15th Feb. 2001). 'Tuning and Topography in an Odor Map on the Rat Olfactory Bulb'. In: *The Journal of Neuroscience* 21.4, pp. 1351–1360. ISSN: 0270-6474, 1529-2401. DOI: 10.1523/JNEUROSCI.21-04-01351.2001. URL: https://www.jneurosci.org/lookup/doi/10.1523/JNEUROSCI.21-04-01351.2001.

Mertes, M., J. Carcaud and J.-C. Sandoz (26th May 2021). 'Olfactory Coding in the Antennal Lobe of the Bumble Bee Bombus Terrestris'. In: *Scientific Reports* 11.1, p. 10947. ISSN: 2045-2322. DOI: 10.1038/s41598-021-90400-6. URL: https://www.nature.com/articles/s41598-021-90400-6.

Miller, J. R. and W. L. Roelofs (Mar. 1978). 'Sustained-Flight Tunnel for Measuring Insect Responses to Wind-Borne Sex Pheromones'. In: *Journal of Chemical Ecology* 4.2, pp. 187–198. ISSN: 0098-0331, 1573-1561. DOI: 10.1007/BF00988054. URL: http://link.springer.com/10.1007/BF00988054.

Miura, K., Z. F. Mainen and N. Uchida (June 2012). 'Odor Representations in Olfactory Cortex: Distributed Rate Coding and Decorrelated Population Activity'. In: *Neuron* 74.6, pp. 1087–1098. ISSN: 08966273. DOI: 10.1016/j.neuron.2012.04.021. URL: https://linkinghub.elsevier.com/retrieve/pii/S0896627312003893.

Modi, M. N., Y. Shuai and G. C. Turner (8th July 2020). 'The *Drosophila* Mushroom Body: From Architecture to Algorithm in a Learning Circuit'. In: *Annual Review of Neuroscience* 43.1, pp. 465–484. ISSN: 0147-006X, 1545-4126. DOI: 10.1146/annurev-neuro-080317-0621333. URL: https://www.annualreviews.org/doi/10.1146/annurev-neuro-080317-0621333.

Mombaerts, P. (1st Nov. 2006). 'Axonal Wiring in the Mouse Olfactory System'. In: *Annual Review of Cell and Developmental Biology* 22.1, pp. 713–737. ISSN: 1081-0706, 1530-8995. DOI: 10.1146/annurev.cellbio.21.012804.093915. URL: https://www.annualreviews.org/doi/10.1146/annurev.cellbio.21.012804.093915.

Monroy, J. G., J. González-Jiménez and J. L. Blanco (11th Oct. 2012). 'Overcoming the Slow Recovery of MOX Gas Sensors through a System Modeling Approach'. In: *Sensors* 12.10, pp. 13664–13680. ISSN: 1424-8220. DOI: 10.3390/s121013664. URL: https://www.mdpi.com/1424-8220/12/10/13664.

Moore, P. A. and J. Atema (Dec. 1991). 'Spatial Information in the Three-Dimensional Fine Structure of an Aquatic Odor Plume'. In: *The Biological Bulletin* 181.3, pp. 408–418. ISSN: 0006-3185, 1939-8697. DOI: 10.2307/1542361. URL: https://www.journals.uchicago.edu/doi/10.2307/1542361.

Moore, P. and J. Atema (June 1988). 'A Model of a Temporal Filter in Chemoreception to Extract Directional Information From a Turbulent Odor Plume'. In: *The Biological Bulletin* 174.3, pp. 355–363. ISSN: 0006-3185, 1939-8697. DOI: 10.2307/1541961. URL: https://www.journals.uchicago.edu/doi/10.2307/1541961.

Moore, P. and J. Crimaldi (2004). 'Odor Landscapes and Animal Behavior: Tracking Odor Plumes in Different Physical Worlds'. In: *Journal of Marine Systems* 49.1-4, pp. 55–64. ISSN: 09247963. DOI: 10.1016/j.jmarsys.2003.05.005.

Moore, P. A. and J. L. Grills (Nov. 1999). 'Chemical Orientation to Food by the Crayfish Orconectes Rusticus: Influence of Hydrodynamics'. In: *Animal Behaviour* 58.5, pp. 953–963. ISSN: 00033472. DOI: 10.1006/anbe.1999.1230. URL: https://linkinghub.elsevier.com/retrieve/pii/S0003347299912307.

Moore, P. A., M. J. Weissburg et al. (Feb. 1994). 'Spatial Distribution of Odors in Simulated Benthic Boundary Layer Flows'. In: *Journal of Chemical Ecology* 20.2, pp. 255–279. ISSN: 0098-0331, 1573-1561. DOI: 10.1007/BF02064435. URL: http://link.springer.com/10.1007/BF02064435.

Mori, K., H. Nagao and Y. Yoshihara (22nd Oct. 1999). 'The Olfactory Bulb: Coding and Processing of Odor Molecule Information'. In: *Science* 286.5440, pp. 711–715. ISSN: 0036-8075, 1095-9203. DOI: 10.1126/science.286.5440.711. URL: https://www.science.org/doi/10.1126/science.286.5440.711.

Mozell, M. M., P. F. Kent and S. J. Murphy (1991). 'The Effect of Flow Rate upon the Magnitude of the Olfactory Response Differs for Different Odorants'. In: *Chemical Senses* 16.6, pp. 631–649. ISSN: 0379-864X, 1464-3553. DOI: 10.1093/chemse/16.6.631. URL: https://academic.oup.com/chemse/article-lookup/doi/10.1093/chemse/16.6.631.

Muezzinoglu, M. K. et al. (2nd Apr. 2009). 'Acceleration of Chemo-Sensory Information Processing Using Transient Features'. In: *Sensors and Actuators B: Chemical* 137.2, pp. 507–512. ISSN: 09254005. DOI: 10.1016/j.snb.2008.10.065. URL: https://linkinghub.elsevier.com/retrieve/pii/S0925400508007119.

Murlis, J., J. S. Elkinton and R. T. Carde (1992). 'Odor Plumes and How Insects Use Them'. In: *Annual review of entomology. Vol. 37* 86, pp. 505–532. ISSN: 00664170. DOI: 10.1146/annurev.ento.37.1.505.

Murlis, J. and C. D. Jones (Mar. 1981). 'Fine-scale Structure of Odour Plumes in Relation to Insect Orientation to Distant Pheromone and Other Attractant Sources'. In: *Physiological Entomology* 6.1, pp. 71–86. ISSN: 0307-6962, 1365-3032. DOI: 10.1111/j.1365-3032.1981.tb00262.x. URL: https://resjournals.onlinelibrary.wiley.com/doi/10.1111/j.1365-3032.1981.tb00262.x.

Murlis, J., M. A. Willis and R. T. Carde (Sept. 2000). 'Spatial and Temporal Structures of Pheromone Plumes in Fields and Forests'. In: *Physiological Entomology* 25.3, pp. 211–222. ISSN: 0307-6962, 1365-3032. DOI: 10.1046/j.1365-3032.2000.00176.x. URL: http://doi.wiley.com/10.1046/j.1365-3032.2000.00176.x.

Mylne, K. R. and P. J. Mason (1991). 'Concentration Fluctuation Measurements in a Dispersing Plume at a Range of up to 1000 m'. In: *Quarterly Journal of the Royal Meteorological Society* 117.497, pp. 177–206. ISSN: 1477-870X. DOI: 10.1002/qj.49711749709. URL: https://onlinelibrary.wiley.com/doi/abs/10.1002/qj.49711749709.

Nagel, K. I. and R. I. Wilson (Feb. 2011). 'Biophysical Mechanisms Underlying Olfactory Receptor Neuron Dynamics'. In: *Nature Neuroscience* 14.2, pp. 208–216. ISSN: 1097-6256, 1546-1726. DOI: 10.1038/nn.2725. URL: https://www.nature.com/articles/nn.2725.

Najaran, M. H. T. (2021). 'How to Exploit Fitness Landscape Properties of Timetabling Problem: A New Operator for Quantum Evolutionary Algorithm'. In: *Expert Systems with Applications* 168 (June 2020), p. 114211. ISSN: 09574174. DOI: 10.1016/j.eswa.2020.114211. URL: https://doi.org/10.1016/j.eswa.2020.114211.

Narikiyo, K., H. Manabe and K. Mori (1st Jan. 2014). 'Sharp Wave-Associated Synchronized Inputs from the Piriform Cortex Activate Olfactory Tubercle Neurons during Slow-Wave Sleep'. In: *Journal of Neurophysiology* 111.1, pp. 72–81. ISSN: 0022-3077, 1522-1598. DOI: 10.1152/jn.00535.2013. URL: https://www.physiology.org/doi/10.1152/jn.00535.2013.

Nevitt, G. A., R. R. Veit and P. Kareiva (Aug. 1995). 'Dimethyl Sulphide as a Foraging Cue for Antarctic Procellariiform Seabirds'. In: *Nature* 376.6542, pp. 680–682. ISSN: 0028-0836, 1476-4687. DOI: 10.1038/376680ao. URL: https://www.nature.com/articles/376680a0.

Otazu, G. H. et al. (June 2015). 'Cortical Feedback Decorrelates Olfactory Bulb Output in Awake Mice'. In: *Neuron* 86.6, pp. 1461–1477. ISSN: 08966273. DOI: 10.1016/j.neuron.2015.05.023. URL: https://linkinghub.elsevier.com/retrieve/pii/S0896627315004304.

Pannunzi, M. and T. Nowotny (2019). 'Odor Stimuli: Not Just Chemical Identity'. In: *Frontiers in Physiology* 10 (November), pp. 1–20. ISSN: 1664042X. DOI: 10.3389/fphys.2019.01428.

Park, I. M. et al. (15th Jan. 2014). 'Intermittency Coding in the Primary Olfactory System: A Neural Substrate for Olfactory Scene Analysis'. In: *The Journal of Neuroscience* 34.3, pp. 941–952. ISSN: 0270-6474, 1529-2401. DOI: 10.1523/JNEUROSCI.2204-13.2014. URL: https://www.jneurosci.org/lookup/doi/10.1523/JNEUROSCI.2204-13.2014.

Pashami, S., A. Lilienthal and M. Trincavelli (27th Nov. 2012). 'Detecting Changes of a Distant Gas Source with an Array of MOX Gas Sensors'. In: *Sensors* 12.12, pp. 16404–16419. ISSN: 1424-8220. DOI: 10.3390/s121216404. URL: https://www.mdpi.com/1424-8220/12/12/16404.

Perez-Orive, J. et al. (19th July 2002). 'Oscillations and Sparsening of Odor Representations in the Mushroom Body'. In: *Science* 297.5580, pp. 359–365. ISSN: 0036-8075, 1095-9203. DOI: 10.1126/science.1070502. URL: https://www.science.org/doi/10.1126/science.1070502.

Perisse, E. et al. (Sept. 2013). 'Shocking Revelations and Saccharin Sweetness in the Study of Drosophila Olfactory Memory'. In: *Current Biology* 23.17, R752–R763. ISSN: 09609822. DOI: 10.1016/j.cub.2013.07.060. URL: https://linkinghub.elsevier.com/retrieve/pii/S0960982213009214.

Pfister, P. et al. (July 2020). 'Odorant Receptor Inhibition Is Fundamental to Odor Encoding'. In: *Current Biology* 30.13, 2574–2587.e6. ISSN: 09609822. DOI: 10.1016/j.cub.2020.04.086. URL: https://linkinghub.elsevier.com/retrieve/pii/S0960982220306345.

Poo, C. and J. S. Isaacson (June 2009). 'Odor Representations in Olfactory Cortex: "Sparse" Coding, Global Inhibition, and Oscillations'. In: *Neuron* 62.6, pp. 850–861. ISSN: 08966273. DOI: 10.1016/j.neuron.2009.05.022. URL: https://linkinghub.elsevier.com/retrieve/pii/S0896627309003973.

Porter, J., T. Anand et al. (Aug. 2005). 'Brain Mechanisms for Extracting Spatial Information from Smell'. In: *Neuron* 47.4, pp. 581–592. ISSN: 08966273. DOI: 10.1016/j.neuron.2005.06.028. URL: https://linkinghub.elsevier.com/retrieve/pii/S0896627305005349.

Porter, J., B. Craven et al. (1st Jan. 2007). 'Mechanisms of Scent-Tracking in Humans'. In: *Nature Neuroscience* 10.1, pp. 27–29. ISSN: 1097-6256, 1546-1726. DOI: 10.1038/nn1819. URL: https://www.nature.com/articles/nn1819.

Purves, D. (2017). *Neuroscience*. ISBN: 978-1-60535-380-7.

Quax, T. E., S.-V. Albers and F. Pfeiffer (14th Dec. 2018). 'Taxis in Archaea'. In: *Emerging Topics in Life Sciences* 2.4. Ed. by N. P. Robinson, pp. 535–546. ISSN: 2397-8554, 2397-8562. DOI: 10.1042/ETLS20180089. URL: https://portlandpress.com/emergtoplifesci/article/2/4/535/77322/Taxis-in-archaea.

Raffel, M. et al. (2018). *Particle Image Velocimetry: A Practical Guide*. Cham: Springer International Publishing. ISBN: 978-3-319-68851-0 978-3-319-68852-7. DOI: 10.1007/978-3-319-68852-7. URL: https://link.springer.com/10.1007/978-3-319-68852-7.

Rajan, R., J. P. Clement and U. S. Bhalla (3rd Feb. 2006). 'Rats Smell in Stereo'. In: *Science* 311.5761, pp. 666–670. ISSN: 0036-8075, 1095-9203. DOI: 10.1126/science.1122096. URL: https://www.science.org/doi/10.1126/science.1122096.

Rebello, M. R. et al. (16th Dec. 2014). 'Perception of Odors Linked to Precise Timing in the Olfactory System'. In: *PLoS Biology* 12.12. Ed. by L. Vosshall, e1002021. ISSN: 1545-7885. DOI: 10.1371/journal.pbio.1002021. URL: https://dx.plos.org/10.1371/journal.pbio.1002021.

Reddy, G., V. N. Murthy and M. Vergassola (10th Mar. 2022). 'Olfactory Sensing and Navigation in Turbulent Environments'. In: *Annual Review of Condensed Matter Physics* 13.1, pp. 191–213. ISSN: 1947-5454, 1947-5462. DOI: 10.1146/annurev-conmatphys-031720-032754. URL: https://www.annualreviews.org/doi/10.1146/annurev-conmatphys-031720-032754.

Reddy, G., J. D. Zak et al. (24th Apr. 2018). 'Antagonism in Olfactory Receptor Neurons and Its Implications for the Perception of Odor Mixtures'. In: *eLife* 7, e34958. ISSN: 2050-084X. DOI: 10.7554/eLife.34958. URL: https://elifesciences.org/articles/34958.

Reisert, J. (1st Aug. 2000). 'Adaptation-Induced Changes in Sensitivity in Frog Olfactory Receptor Cells'. In: *Chemical Senses* 25.4, pp. 483–486. ISSN: 14643553. DOI: 10.1093/chemse/25.4.483. URL: https://academic.oup.com/chemse/article-lookup/doi/10.1093/chemse/25.4.483.

Reisert, J. (1st Nov. 2010). 'Origin of Basal Activity in Mammalian Olfactory Receptor Neurons'. In: *Journal of General Physiology* 136.5, pp. 529–540. ISSN: 1540-7748, 0022-1295. DOI: 10.1085/jgp.201010528. URL: https://rupress.org/jgp/article/136/5/529/42868/Origin-of-basal-activity-in-mammalian-olfactory.

Reisert, J. and H. Zhao (1st Sept. 2011). 'Response Kinetics of Olfactory Receptor Neurons and the Implications in Olfactory Coding'. In: *Journal of General Physiology* 138.3, pp. 303–310. ISSN: 1540-7748, 0022-1295. DOI: 10.1085/jgp.201110645. URL: https://rupress.org/jgp/article/138/3/303/42992/Response-kinetics-of-olfactory-receptor-neurons.

Rennaker, R. L. et al. (14th Feb. 2007). 'Spatial and Temporal Distribution of Odorant-Evoked Activity in the Piriform Cortex'. In: *The Journal of Neuroscience* 27.7, pp. 1534–1542. ISSN: 0270-6474, 1529-2401. DOI: 10.1523/JNEUROSCI.4072-06.2007. URL: https://www.jneurosci.org/lookup/doi/10.1523/JNEUROSCI.4072-06.2007.

Riffell, J. A., L. Abrell and J. G. Hildebrand (July 2008). 'Physical Processes and Real-Time Chemical Measurement of the Insect Olfactory Environment'. In: *Journal of Chemical Ecology* 34.7, pp. 837–853. ISSN: 0098-0331, 1573-1561. DOI: 10.1007/s10886-008-9490-7. URL: http://link.springer.com/10.1007/s10886-008-9490-7.

Riffell, J. A., E. Shlizerman et al. (27th June 2014). 'Flower Discrimination by Pollinators in a Dynamic Chemical Environment'. In: *Science* 344.6191, pp. 1515–1518. ISSN: 0036-8075, 1095-9203. DOI: 10.1126/science.1251041. URL: https://www.science.org/doi/10.1126/science.1251041.

Rigolli, N., N. Magnoli et al. (12th Aug. 2022). 'Learning to Predict Target Location with Turbulent Odor Plumes'. In: *eLife* 11, e72196. ISSN: 2050-084X. DOI: 10.7554/eLife.72196. URL: https://elifesciences.org/articles/72196.

Rigolli, N., G. Reddy et al. (23rd Aug. 2022). 'Alternation Emerges as a Multi-Modal Strategy for Turbulent Odor Navigation'. In: *eLife* 11, e76989. ISSN: 2050-084X. DOI: 10.7554/eLife.76989. URL: https://elifesciences.org/articles/76989.

Rubin, B. D. and L. C. Katz (July 1999). 'Optical Imaging of Odorant Representations in the Mammalian Olfactory Bulb'. In: *Neuron* 23.3, pp. 499–511. ISSN: 08966273. DOI: 10.1016/S0896-6273(00)80803-X. URL: https://linkinghub.elsevier.com/retrieve/pii/S089662730080803X.

Saito, H. et al. (3rd Mar. 2009). 'Odor Coding by a Mammalian Receptor Repertoire'. In: *Science Signaling* 2.60. ISSN: 1945-0877, 1937-9145. DOI: 10.1126/scisignal.2000016. URL: https://www.science.org/doi/10.1126/scisignal.2000016.

Schaffer, E. S. et al. (2018). 'Odor Perception on the Two Sides of the Brain: Consistency Despite Randomness'. In: *Neuron* 98.4, 736–742.e3. ISSN: 10974199. DOI: 10.1016/j.neuron.2018.04.004. pmid: 29706585. URL: https://doi.org/10.1016/j.neuron.2018.04.004.

Schmitt, B. C. and B. W. Ache (13th July 1979). 'Olfaction: Responses of a Decapod Crustacean Are Enhanced by Flicking'. In: *Science* 205.4402, pp. 204–206. ISSN: 0036-8075, 1095-9203. DOI: 10.1126/science.205.4402.204. URL: https://www.science.org/doi/10.1126/science.205.4402.204.

Schmuker, M., V. Bahr and R. Huerta (Nov. 2016). 'Exploiting Plume Structure to Decode Gas Source Distance Using Metal-Oxide Gas Sensors'. In: *Sensors Actuators B Chem.* 235, pp. 636–646. ISSN: 09254005. DOI: 10.1016/j.snb.2016.05.098. URL: http://www.sciencedirect.com/science/article/pii/S0925400516307833%20https://linkinghub.elsevier.com/retrieve/pii/S0925400516307833.

Schoenfeld, T. A. and T. A. Cleland (Nov. 2005). 'The Anatomical Logic of Smell'. In: *Trends in Neurosciences* 28.11, pp. 620–627. ISSN: 01662236. DOI: 10.1016/j.tins.2005.09.005. URL: https://linkinghub.elsevier.com/retrieve/pii/S0166223605002523.

– (1st Feb. 2006). 'Anatomical Contributions to Odorant Sampling and Representation in Rodents: Zoning in on Sniffing Behavior'. In: *Chemical Senses* 31.2, pp. 131–144. ISSN: 1464-3553, 0379-864X. DOI: 10.1093/chemse/bjj015. URL: http://academic.oup.com/chemse/article/31/2/131/285992/Anatomical-Contributions-to-Odorant-Sampling-and.

Schuckel, J., P. H. Torkkeli and A. S. French (July 2009). 'Two Interacting Olfactory Transduction Mechanisms Have Linked Polarities and Dynamics in *Drosophila Melanogaster* Antennal Basiconic Sensilla Neurons'. In: *Journal of Neurophysiology* 102.1, pp. 214–223. ISSN: 0022-3077, 1522-1598. DOI: 10.1152/jn.00162.2009. URL: https://www.physiology.org/doi/10.1152/jn.00162.2009.

Scott, J. W. (1st Feb. 2006). 'Sniffing and Spatiotemporal Coding in Olfaction'. In: *Chemical Senses* 31.2, pp. 119–130. ISSN: 1464-3553, 0379-864X. DOI: 10.1093/chemse/bjj013. URL: http://academic.oup.com/chemse/article/31/2/119/285987/Sniffing-and-Spatiotemporal-Coding-in-Olfaction.

Scott, J. W. et al. (5th Feb. 2014). 'Tuning to Odor Solubility and Sorption Pattern in Olfactory Epithelial Responses'. In: *The Journal of Neuroscience* 34.6, pp. 2025–2036. ISSN: 0270-6474, 1529-2401. DOI: 10.1523/JNEUROSCI.3736-13.2014. URL: https://www.jneurosci.org/lookup/doi/10.1523/JNEUROSCI.3736-13.2014.

Shorey, H. H. (1976). *Animal Communication by Pheromones*. New York: Academic Press. 167 pp. ISBN: 978-0-12-640450-0.

Short, S. M. et al. (22nd Dec. 2016). 'Respiration Gates Sensory Input Responses in the Mitral Cell Layer of the Olfactory Bulb'. In: *PLOS ONE* 11.12. Ed. by J. Reisert, e0168356. ISSN: 1932-6203. DOI: 10.1371/journal.pone.0168356. URL: https://dx.plos.org/10.1371/journal.pone.0168356.

Shraiman, B. I. and E. D. Siggia (June 2000). 'Scalar Turbulence'. In: *Nature* 405.6787, pp. 639–646. ISSN: 0028-0836, 1476-4687. DOI: 10.1038/35015000. URL: https://www.nature.com/articles/35015000.

Shusterman, R. et al. (July 2011). 'Precise Olfactory Responses Tile the Sniff Cycle'. In: *Nature Neuroscience* 14.8, pp. 1039–1044. ISSN: 10976256. DOI: 10.1038/nn.2877. pmid: 21765422.

Silbering, A. F. and R. Benton (Mar. 2010). 'Ionotropic and Metabotropic Mechanisms in Chemoreception: 'Chance or Design'?' In: *EMBO reports* 11.3, pp. 173–179. ISSN: 1469-221X, 1469-3178. DOI: 10.1038/embor.2010.8. URL: https://www.embopress.org/doi/10.1038/embor.2010.8.

Singh, V. et al. (7th May 2019). 'Competitive Binding Predicts Nonlinear Responses of Olfactory Receptors to Complex Mixtures'. In: *Proceedings of the National Academy of Sciences* 116.19, pp. 9598–9603. ISSN: 0027-8424, 1091-6490. DOI: 10.1073/pnas.1813230116. URL: https://pnas.org/doi/full/10.1073/pnas.1813230116.

Smear, M. et al. (Nov. 2011). 'Perception of Sniff Phase in Mouse Olfaction'. In: *Nature* 479.7373, pp. 397–400. ISSN: 0028-0836, 1476-4687. DOI: 10.1038/nature10521. URL: https://www.nature.com/articles/nature10521.

Sobel, E. C. and D. W. Tank (1st Apr. 1993). 'Timing of Odor Stimulation Does Not Alter Patterning of Olfactory Bulb Unit Activity in Freely Breathing Rats'. In: *Journal of Neurophysiology* 69.4, pp. 1331–1337. ISSN: 0022-3077, 1522-1598. DOI: 10.1152/jn.1993.69.4.1331. URL: https://www.physiology.org/doi/10.1152/jn.1993.69.4.1331.

Spors, H. and A. Grinvald (Apr. 2002). 'Spatio-Temporal Dynamics of Odor Representations in the Mammalian Olfactory Bulb'. In: *Neuron* 34.2, pp. 301–315. ISSN: 08966273. DOI: 10.1016/S0896-6273(02)00644-X. URL: https://linkinghub.elsevier.com/retrieve/pii/S089662730200644X.

Spors, H., M. Wachowiak et al. (25th Jan. 2006). 'Temporal Dynamics and Latency Patterns of Receptor Neuron Input to the Olfactory Bulb'. In: *The Journal of Neuroscience* 26.4, pp. 1247–1259. ISSN: 0270-6474, 1529-2401. DOI: 10.1523/JNEUROSCI.3100-05.2006. URL: https://www.jneurosci.org/lookup/doi/10.1523/JNEUROSCI.3100-05.2006.

Stettler, D. D. and R. Axel (Sept. 2009). 'Representations of Odor in the Piriform Cortex'. In: *Neuron* 63.6, pp. 854–864. ISSN: 08966273. DOI: 10.1016/j.neuron.2009.09.005. URL: https://linkinghub.elsevier.com/retrieve/pii/S0896627309006849.

Stopfer, M. et al. (Nov. 1997). 'Impaired Odour Discrimination on Desynchronization of Odour-Encoding Neural Assemblies'. In: *Nature* 390.6655, pp. 70–74. ISSN: 0028-0836, 1476-4687. DOI: 10.1038/36335. URL: https://www.nature.com/articles/36335.

Su, C.-Y., K. Menuz and J. R. Carlson (Oct. 2009). 'Olfactory Perception: Receptors, Cells, and Circuits'. In: *Cell* 139.1, pp. 45–59. ISSN: 00928674. DOI: 10.1016/j.cell.2009.09.015. URL: https://linkinghub.elsevier.com/retrieve/pii/S0092867409011751.

Sutton, O. G. (July 1947). 'The Problem of Diffusion in the Lower Atmosphere'. In: *Quarterly Journal of the Royal Meteorological Society* 73.317-318, pp. 257–281. ISSN: 0035-9009, 1477-870X. DOI: 10.1002/qj.49707331704. URL: https://rmets.onlinelibrary.wiley.com/doi/10.1002/qj.49707331704.

– (Oct. 1949). 'The Application to Micrometeorology of the Theory of Turbulent Flow over Rough Surfaces'. In: *Quarterly Journal of the Royal Meteorological Society* 75.326, pp. 335–350. ISSN: 0035-9009, 1477-870X. DOI: 10.1002/qj.49707532602. URL: https://rmets.onlinelibrary.wiley.com/doi/10.1002/qj.49707532602.

Szurmant, H. and G. W. Ordal (June 2004). 'Diversity in Chemotaxis Mechanisms among the Bacteria and Archaea'. In: *Microbiology and Molecular Biology Reviews* 68.2, pp. 301–319. ISSN: 1092-2172, 1098-5557. DOI: 10.1128/MMBR.68.2.301-319.2004. URL: https://journals.asm.org/doi/10.1128/MMBR.68.2.301-319.2004.

Szyszka, P. et al. (2014). 'High-Speed Odor Transduction and Pulse Tracking by Insect Olfactory Receptor Neurons'. In: *Proceedings of the National Academy of Sciences of the United States of America*. ISSN: 10916490. DOI: 10.1073/pnas.1412051111. pmid: 25385618.

Tamburri, M. N. et al. (Dec. 1996). 'Chemical Induction of Larval Settlement Behavior in Flow'. In: *The Biological Bulletin* 191.3, pp. 367–373. ISSN: 0006-3185, 1939-8697. DOI: 10.2307/1543009. URL: https://www.journals.uchicago.edu/doi/10.2307/1543009.

Tennekes, H. and J. L. Lumley (1972). *A First Course in Turbulence*. 23. print. Cambridge, Mass.: MIT Press. 300 pp. ISBN: 978-0-262-20019-6.

Thar, R. and T. Fenchel (July 2001). 'True Chemotaxis in Oxygen Gradients of the Sulfur-Oxidizing Bacterium *Thiovulum Majus*'. In: *Applied and Environmental Microbiology* 67.7, pp. 3299–3303. ISSN: 0099-2240, 1098-5336. DOI: 10.1128/AEM.67.7.3299-3303.2001. URL: https://journals.asm.org/doi/10.1128/AEM.67.7.3299-3303.2001.

Thesen, A., J. B. Steen and K. B. Døving (1st July 1993). 'Behaviour of Dogs During Olfactory Tracking'. In: *Journal of Experimental Biology* 180.1, pp. 247–251. ISSN: 0022-0949, 1477-9145. DOI: 10.1242/jeb.180.1.247. URL: https://journals.biologists.com/jeb/article/180/1/247/6534/Behaviour-of-Dogs-During-Olfactory-Tracking.

Tian, X. and P. J. W. Roberts (1st Dec. 2003). 'A 3D LIF System for Turbulent Buoyant Jet Flows'. In: *Experiments in Fluids* 35.6, pp. 636–647. ISSN: 0723-4864, 1432-1114. DOI: 10.1007/s00348-003-0714-x. URL: http://link.springer.com/10.1007/s00348-003-0714-x.

Tomba, A. M., T. A. Keller and P. A. Moore (June 2001). 'Foraging in Complex Odor Landscapes: Chemical Orientation Strategies during Stimulation by Conflicting Chemical Cues'. In: *Journal of the North American Benthological Society* 20.2, pp. 211–222. ISSN: 0887-3593, 1937-237X. DOI: 10.2307/1468316. URL: https://www.journals.uchicago.edu/doi/10.2307/1468316.

Traynier, R. M. M. (Jan. 1968). 'Sex Attraction in the Mediterranean Flour Moth, Anagasta Kühniella: Location of the Female by the Male'. In: *The Canadian Entomologist* 100.1, pp. 5–10. ISSN: 0008-347X, 1918-3240. DOI: 10.4039/Ent1005-1. URL: https://www.cambridge.org/core/product/identifier/S0008347X00051208/type/journal_article.

Uchida, N., C. Poo and R. Haddad (8th July 2014). 'Coding and Transformations in the Olfactory System'. In: *Annual Review of Neuroscience* 37.1, pp. 363–385. ISSN: 0147-006X, 1545-4126. DOI: 10.1146/annurev-neuro-071013-013941. URL: https://www.annualreviews.org/doi/10.1146/annurev-neuro-071013-013941.

Uchida, N., Y. K. Takahashi et al. (Oct. 2000). 'Odor Maps in the Mammalian Olfactory Bulb: Domain Organization and Odorant Structural Features'. In: *Nature Neuroscience* 3.10, pp. 1035–1043. ISSN: 1097-6256, 1546-1726. DOI: 10.1038/79857. URL: https://www.nature.com/articles/nn1000_1035.

Vaaga, C. E. and G. L. Westbrook (15th Nov. 2016). 'Parallel Processing of Afferent Olfactory Sensory Information'. In: *The Journal of Physiology* 594.22, pp. 6715–6732. ISSN: 0022-3751,

1469-7793. DOI: 10.1113/JP272755. URL: https://physoc.onlinelibrary.wiley.com/doi/10.1113/JP272755.

Vaaga, C. E., J. T. Yorgason et al. (1st Mar. 2017). 'Presynaptic Gain Control by Endogenous Co-transmission of Dopamine and GABA in the Olfactory Bulb'. In: *Journal of Neurophysiology* 117.3, pp. 1163–1170. ISSN: 1522-1598. DOI: 10.1152/jn.00694.2016. pmid: 28031402.

Valente, J. et al. (Dec. 2018). 'Validation of a Small Flying E-Nose System for Air Pollutants Control: A Plume Detection Case Study from an Agricultural Machine'. In: *2018 IEEE International Conference on Robotics and Biomimetics (ROBIO)*. 2018 IEEE International Conference on Robotics and Biomimetics (ROBIO). Kuala Lumpur, Malaysia: IEEE, pp. 1993–1998. ISBN: 978-1-72810-377-8. DOI: 10.1109/ROBIO.2018.8664718. URL: https://ieeexplore.ieee.org/document/8664718/.

van Breugel, F. and M. H. Dickinson (Feb. 2014). 'Plume-Tracking Behavior of Flying Drosophila Emerges from a Set of Distinct Sensory-Motor Reflexes'. In: *Current Biology* 24.3, pp. 274–286. ISSN: 09609822. DOI: 10.1016/j.cub.2013.12.023. URL: https://linkinghub.elsevier.com/retrieve/pii/S0960982213015820.

Van Cruyningen, I., A. Lozano and R. K. Hanson (Oct. 1990). 'Quantitative Imaging of Concentration by Planar Laser-Induced Fluorescence'. In: *Experiments in Fluids* 10.1, pp. 41–49. ISSN: 0723-4864, 1432-1114. DOI: 10.1007/BF00187871. URL: http://link.springer.com/10.1007/BF00187871.

Van Der Goes Van Naters, W. and J. R. Carlson (Apr. 2007). 'Receptors and Neurons for Fly Odors in Drosophila'. In: *Current Biology* 17.7, pp. 606–612. ISSN: 09609822. DOI: 10.1016/j.cub.2007.02.043. URL: https://linkinghub.elsevier.com/retrieve/pii/S0960982207010202.

Van Vliet, E. et al. (July 2004). 'Time-Resolved, 3D, Laser-Induced Fluorescence Measurements of Fine-Structure Passive Scalar Mixing in a Tubular Reactor'. In: *Experiments in Fluids* 37.1, pp. 1–21. ISSN: 0723-4864, 1432-1114. DOI: 10.1007/s00348-004-0779-1. URL: http://link.springer.com/10.1007/s00348-004-0779-1.

Vergara, A. et al. (2013). 'On the Performance of Gas Sensor Arrays in Open Sampling Systems Using Inhibitory Support Vector Machines'. In: *Sensors and Actuators, B: Chemical* 185, pp. 462–477. ISSN: 09254005. DOI: 10.1016/j.snb.2013.05.027. URL: http://www.sciencedirect.com/science/article/pii/S092540051300590X.

Vergassola, M., E. Villermaux and B. I. Shraiman (2007). ''Infotaxis' as a Strategy for Searching without Gradients'. In: *Nature* 445.7126, pp. 406–409. ISSN: 14764687. DOI: 10.1038/nature05464. pmid: 17251974.

Verhagen, J. V., K. L. Baker et al. (1st Feb. 2023). 'Odor Encoding by Signals in the Olfactory Bulb'. In: *Journal of Neurophysiology* 129.2, pp. 431–444. ISSN: 0022-3077, 1522-1598. DOI: 10.1152/jn.00449.2022. URL: https://journals.physiology.org/doi/10.1152/jn.00449.2022.

Verhagen, J. V., D. W. Wesson et al. (Apr. 2007). 'Sniffing Controls an Adaptive Filter of Sensory Input to the Olfactory Bulb'. In: *Nature Neuroscience* 10.5, pp. 631–639. ISSN: 10976256. DOI: 10.1038/nn1892. pmid: 17450136.

Vickers, N. J. and T. C. Baker (21st June 1994). 'Reiterative Responses to Single Strands of Odor Promote Sustained Upwind Flight and Odor Source Location by Moths.' In: *Proceedings of the National Academy of Sciences* 91.13, pp. 5756–5760. ISSN: 0027-8424, 1091-6490. DOI: 10.1073/pnas.91.13.5756. URL: https://pnas.org/doi/full/10.1073/pnas.91.13.5756.

Vickers, N. J., T. A. Christensen et al. (Mar. 2001). 'Odour-Plume Dynamics Influence the Brain's Olfactory Code'. In: *Nature* 410.6827 (6827), pp. 466–470. ISSN: 1476-4687. DOI: 10.1038/35068559. URL: https://www.nature.com/articles/35068559.

Vickers, N. (Apr. 2000). 'Mechanisms of Animal Navigation in Odor Plumes'. In: *The Biological Bulletin* 198.2, pp. 203–212. ISSN: 0006-3185, 1939-8697. DOI: 10.2307/1542524. URL: https://www.journals.uchicago.edu/doi/10.2307/1542524.

Vosshall, L. B. et al. (Mar. 1999). 'A Spatial Map of Olfactory Receptor Expression in the Drosophila Antenna'. In: *Cell* 96.5, pp. 725–736. ISSN: 00928674. DOI: 10.1016/S0092-8674(00)80582-6. URL: https://linkinghub.elsevier.com/retrieve/pii/S0092867400805826.

Vuka, M. et al. (May 2017). 'Exploration and Localization of a Gas Source with MOX Gas Sensors on a Mobile Robot — A Gaussian Regression Bout Amplitude Approach'. In: *2017 ISOCS/IEEE International Symposium on Olfaction and Electronic Nose (ISOEN)*. 2017 ISOCS/IEEE International Symposium on Olfaction and Electronic Nose (ISOEN). Montreal, QC, Canada: IEEE, pp. 1–3. ISBN: 978-1-5090-2392-9. DOI: 10.1109/ISOEN.2017.7968898. URL: http://ieeexplore.ieee.org/document/7968898/.

Wachowiak, M. (Sept. 2011). 'All in a Sniff: Olfaction as a Model for Active Sensing'. In: *Neuron* 71.6, pp. 962–973. ISSN: 08966273. DOI: 10.1016/j.neuron.2011.08.030. pmid: 21943596. URL: http://dx.doi.org/10.1016/j.earlhumdev.2015.09.003%7B%5C%%7D5Cnhttp://dx.doi.org/10.1016/j.earlhumdev.2014.01.002%7B%5C%%7D5Cnhttp://dx.doi.org/10.1016/S0378-3782(12)70006-3%7B%5C%%7D5Cnhttp://www.sciencedirect.com/science/article/pii/S2341287914000763%7B%5C%%7D5Cnhttp://dx.doi.org/10.1016/.

Wachowiak, M. and L. B. Cohen (Nov. 2001). 'Representation of Odorants by Receptor Neuron Input to the Mouse Olfactory Bulb'. In: *Neuron* 32.4, pp. 723–735. ISSN: 08966273. DOI: 10.1016/S0896-6273(01)00506-2. URL: https://linkinghub.elsevier.com/retrieve/pii/S0896627301005062.

Wallace, D. G., B. Gorny and I. Q. Whishaw (Apr. 2002). 'Rats Can Track Odors, Other Rats, and Themselves: Implications for the Study of Spatial Behavior'. In: *Behavioural Brain Research* 131.1-2, pp. 185–192. ISSN: 01664328. DOI: 10.1016/S0166-4328(01)00384-9. URL: https://linkinghub.elsevier.com/retrieve/pii/S0166432801003849.

Warhaft, Z. (Jan. 2000). 'Passive Scalars in Turbulent Flows'. In: *Annual Review of Fluid Mechanics* 32.1, pp. 203–240. ISSN: 0066-4189, 1545-4479. DOI: 10.1146/annurev.fluid.32.1.203. URL: https://www.annualreviews.org/doi/10.1146/annurev.fluid.32.1.203.

Webster, D. R. and M. J. Weissburg (July 2001). 'Chemosensory Guidance Cues in a Turbulent Chemical Odor Plume'. In: *Limnology and Oceanography* 46.5, pp. 1034–1047. ISSN: 00243590. DOI: 10.4319/lo.2001.46.5.1034. URL: http://doi.wiley.com/10.4319/lo.2001.46.5.1034.

Weissburg, M. J. (1997). 'Chemo- and Mechanosensory Orientation by Crustaceans in Laminar and Turbulent Flows: From Odor Trails to Vortex Streets'. In: *Orientation and Communication in Arthropods*. Ed. by M. Lehrer. Basel: Birkhäuser Basel, pp. 215–246. ISBN: 978-3-0348-9811-9. DOI: 10.1007/978-3-0348-8878-3_8. URL: http://link.springer.com/10.1007/978-3-0348-8878-3_8.

Weissburg, M. (Apr. 2000). 'The Fluid Dynamical Context of Chemosensory Behavior'. In: *The Biological Bulletin* 198.2, pp. 188–202. ISSN: 0006-3185, 1939-8697. DOI: 10.2307/1542523. URL: https://www.journals.uchicago.edu/doi/10.2307/1542523.

Wesson, D. W. et al. (2008). 'Rapid Encoding and Perception of Novel Odors in the Rat'. In: *PLoS Biology*. ISSN: 15449173. DOI: 10.1371/journal.pbio.0060082. pmid: 18399719.

White, F. M. (1974). *Viscous Fluid Flow*. New York: McGraw-Hill. 725 pp. ISBN: 978-0-07-069710-2.

Willis, M. A. and EdmundA. Arbas (Oct. 1991). 'Odor-Modulated Upwind Flight of the Sphinx Moth, Manduca Sexta L.' In: *Journal of Comparative Physiology A* 169.4. ISSN: 0340-7594, 1432-1351. DOI: 10.1007/BF00197655. URL: http://link.springer.com/10.1007/BF00197655.

Wilson, C. D. et al. (14th Nov. 2017). 'A Primacy Code for Odor Identity'. In: *Nature Communications* 8.1, p. 1477. ISSN: 2041-1723. DOI: 10.1038/s41467-017-01432-4. URL: https://www.nature.com/articles/s41467-017-01432-4.

Wilson, D. A. and R. M. Sullivan (Nov. 2011). 'Cortical Processing of Odor Objects'. In: *Neuron* 72.4, pp. 506–519. ISSN: 08966273. DOI: 10.1016/j.neuron.2011.10.027. URL: https://linkinghub.elsevier.com/retrieve/pii/S0896627311009627.

Wilson, R. I. (8th July 2013). 'Early Olfactory Processing in *Drosophila* : Mechanisms and Principles'. In: *Annual Review of Neuroscience* 36.1, pp. 217–241. ISSN: 0147-006X, 1545-4126. DOI: 10.1146/annurev-neuro-062111-150533. URL: https://www.annualreviews.org/doi/10.1146/annurev-neuro-062111-150533.

Wilson, R. I. and Z. F. Mainen (21st July 2006). 'Early Events in Olfactory Processing'. In: *Annual Review of Neuroscience* 29.1, pp. 163–201. ISSN: 0147-006X, 1545-4126. DOI: 10.1146/annurev.neuro.29.051605.112950. URL: https://www.annualreviews.org/doi/10.1146/annurev.neuro.29.051605.112950.

Wright, R. H. (1964). *The Science of Smell*. George Allen & Unwun Ltd. 200 pp.

Wu, R. et al. (1st Nov. 2017). 'Activity Patterns Elicited by Airflow in the Olfactory Bulb and Their Possible Functions'. In: *The Journal of Neuroscience* 37.44, pp. 10700–10711. ISSN: 0270-

6474, 1529-2401. DOI: 10.1523/JNEUROSCI.2210-17.2017. URL: https://www.jneurosci.org/lookup/doi/10.1523/JNEUROSCI.2210-17.2017.

Wyatt, T. D. (2014). 'Introduction to Chemical Signaling in Vertebrates and Invertebrates'. In: *Neurobiology of Chemical Communication*. Ed. by C. Mucignat-Caretta. Frontiers in Neuroscience. Boca Raton (FL): CRC Press/Taylor & Francis. ISBN: 978-1-4665-5341-5. pmid: 24830039. URL: http://www.ncbi.nlm.nih.gov/books/NBK200995/.

Xu, L. et al. (10th Apr. 2020). 'Widespread Receptor-Driven Modulation in Peripheral Olfactory Coding'. In: *Science* 368.6487, eaaz5390. ISSN: 0036-8075, 1095-9203. DOI: 10.1126/science.aaz5390. URL: https://www.science.org/doi/10.1126/science.aaz5390.

Yao, C. A., R. Ignell and J. R. Carlson (14th Sept. 2005). 'Chemosensory Coding by Neurons in the Coeloconic Sensilla of the *Drosophila* Antenna'. In: *The Journal of Neuroscience* 25.37, pp. 8359–8367. ISSN: 0270-6474, 1529-2401. DOI: 10.1523/JNEUROSCI.2432-05.2005. URL: https://www.jneurosci.org/lookup/doi/10.1523/JNEUROSCI.2432-05.2005.

Yee, E., R. Chan et al. (1995). 'Measurements of Level-Crossing Statistics of Concentration Fluctuations in Plumes Dispersing in the Atmospheric Surface Layer'. In: *Boundary-Layer Meteorology* 73.1-2, pp. 53–90. ISSN: 0006-8314, 1573-1472. DOI: 10.1007/BF00708930. URL: http://link.springer.com/10.1007/BF00708930.

Yee, E., P. R. Kosteniuk et al. (July 1993). 'Statistical Characteristics of Concentration Fluctuations in Dispersing Plumes in the Atmospheric Surface Layer'. In: *Boundary-Layer Meteorology* 65.1-2, pp. 69–109. ISSN: 0006-8314, 1573-1472. DOI: 10.1007/BF00708819. URL: http://link.springer.com/10.1007/BF00708819.

Yen, J. and J. R. Strickler (Sum. 1996). 'Advertisement and Concealment in the Plankton: What Makes a Copepod Hydrodynamically Conspicuous?' In: *Invertebrate Biology* 115.3, p. 191. ISSN: 10778306. DOI: 10.2307/3226930. JSTOR: 3226930. URL: https://www.jstor.org/stable/3226930?origin=crossref.

Yoda, M., L. Hesselink and M. G. Mungal (25th Nov. 1994). 'Instantaneous Three-Dimensional Concentration Measurements in the Self-Similar Region of a Round High-Schmidt-number Jet'. In: *Journal of Fluid Mechanics* 279, pp. 313–350. ISSN: 0022-1120, 1469-7645. DOI: 10.1017/S0022112094003927. URL: https://www.cambridge.org/core/product/identifier/S0022112094003927/type/journal_article.

Yuan, H. et al. (2020). 'A Novel Vectorization Tracking Algorithm for Maritime Emission Monitoring Assisted with E-Nose Enabled Unmanned Aerial Vehicle'. In: *IEEE Sensors Journal*, pp. 1–1. ISSN: 1530-437X, 1558-1748, 2379-9153. DOI: 10.1109/JSEN.2020.3009529. URL: https://ieeexplore.ieee.org/document/9141305/.

Zak, J. D. et al. (3rd July 2020). 'Antagonistic Odor Interactions in Olfactory Sensory Neurons Are Widespread in Freely Breathing Mice'. In: *Nature Communications* 11.1, p. 3350. ISSN: 2041-1723. DOI: 10.1038/s41467-020-17124-5. URL: https://www.nature.com/articles/s41467-020-17124-5.

Zanen, P. O. et al. (Dec. 1994). 'Search Strategies of Fruit Flies in Steady and Shifting Winds in the Absence of Food Odours'. In: *Physiological Entomology* 19.4, pp. 335–341.

ISSN: 0307-6962, 1365-3032. DOI: 10.1111/j.1365-3032.1994.tb01060.x. URL: https://resjournals.onlinelibrary.wiley.com/doi/10.1111/j.1365-3032.1994.tb01060.x.

Zapiec, B. and P. Mombaerts (27th Oct. 2015). 'Multiplex Assessment of the Positions of Odorant Receptor-Specific Glomeruli in the Mouse Olfactory Bulb by Serial Two-Photon Tomography'. In: *Proceedings of the National Academy of Sciences* 112.43. ISSN: 0027-8424, 1091-6490. DOI: 10.1073/pnas.1512135112. URL: https://pnas.org/doi/full/10.1073/pnas.1512135112.

Zhan, C. and M. Luo (8th Dec. 2010). 'Diverse Patterns of Odor Representation by Neurons in the Anterior Piriform Cortex of Awake Mice'. In: *The Journal of Neuroscience* 30.49, pp. 16662–16672. ISSN: 0270-6474, 1529-2401. DOI: 10.1523/JNEUROSCI.4400-10.2010. URL: https://www.jneurosci.org/lookup/doi/10.1523/JNEUROSCI.4400-10.2010.

Zhang, X. and S. Firestein (Feb. 2002). 'The Olfactory Receptor Gene Superfamily of the Mouse'. In: *Nature Neuroscience* 5.2, pp. 124–133. ISSN: 1097-6256, 1546-1726. DOI: 10.1038/nn800. URL: https://www.nature.com/articles/nn800.

Zhou, Y. and R. I. Wilson (1st Oct. 2012). 'Transduction in *Drosophila* Olfactory Receptor Neurons Is Invariant to Air Speed'. In: *Journal of Neurophysiology* 108.7, pp. 2051–2059. ISSN: 0022-3077, 1522-1598. DOI: 10.1152/jn.01146.2011. URL: https://www.physiology.org/doi/10.1152/jn.01146.2011.

Zimmer, R. and C. Butman (Apr. 2000). 'Chemical Signaling Processes in the Marine Environment'. In: *The Biological Bulletin* 198.2, pp. 168–187. ISSN: 0006-3185, 1939-8697. DOI: 10.2307/1542522. URL: https://www.journals.uchicago.edu/doi/10.2307/1542522.

Zimmer-Faust, R. K. et al. (Apr. 1995). 'Odor Plumes and Animal Navigation in Turbulent Water Flow: A Field Study'. In: *The Biological Bulletin* 188.2, pp. 111–116. ISSN: 0006-3185, 1939-8697. DOI: 10.2307/1542075. URL: https://www.journals.uchicago.edu/doi/10.2307/1542075.

Zjacic, N. and M. Scholz (Feb. 2022). 'The Role of Food Odor in Invertebrate Foraging'. In: *Genes, Brain and Behavior* 21.2, e12793. ISSN: 1601-1848, 1601-183X. DOI: 10.1111/gbb.12793. URL: https://onlinelibrary.wiley.com/doi/10.1111/gbb.12793.

A

APPENDIX 1

A.1 PRELIMINARY DATA ANALYSIS

Here we include the initial data analysis we conducted in order to establish the filter parameters that were used in the main body of the paper.

A.1.1 *Spectral Analysis Along the Plume Centre Line*

Here we extract raw concentration data at select downwind distances along the centre line of the plume in order to establish reasonable filter parameters for the bout analysis carried out in the remainder of the chapter. We select six equally spaced distances from the odour source to the point at which trial average concentration falls below a threshold of $C/C_0 = 0.01$. This is to show the initial decrease in average odour concentration along the centre line of the plume and to clearly illustrate differences across the release configurations. The filter cascade originally applied in Schmuker, Bahr and Huerta (2016) was designed to remove the slow onset and offset of gas delivery and electrical noise present in the Vergara et al. (2013) MOX sensor recordings, and extract fast frequencies present within the dataset that could be used to predict gas source distance. With a change in sensory modality from MOX sensors to optical data, we saw fit to explore the filter parameters that can be used to extract this same critical information. We aim to pick one set of filter parameters that can be applied across the four release configurations for ease of comparison.

In fig. A.1 we show six selected downwind distances along the centre line of the plume in which we see transients travel in the form of fluctuations in the normalized odour concentration – this is data from the first trial of each of the datasets.

We can see clear differences in the strength of the odour fluctuations, not only downwind within a specific release configuration, but also across the different release configurations. There is an increase in the frequency of concentration fluctuations with increasing wind speed, with the $20cm/s$ wind speed dataset showing the highest frequency features. We also see that magnitude of the fluctuations decrease with downwind distance, with the rate of decrease inversely proportional to the wind speed. The $10cm/s$ near-bed dataset doesn't fall below the concentration threshold within the extent of the wind tunnel, with similar change in the magnitudes of the fluctuations over almost three times the distance shown in the $10cm/s$ freestream. It is clear from these comparisons that selecting a frequency range that can encode downwind distance from the odour source that works for each of these

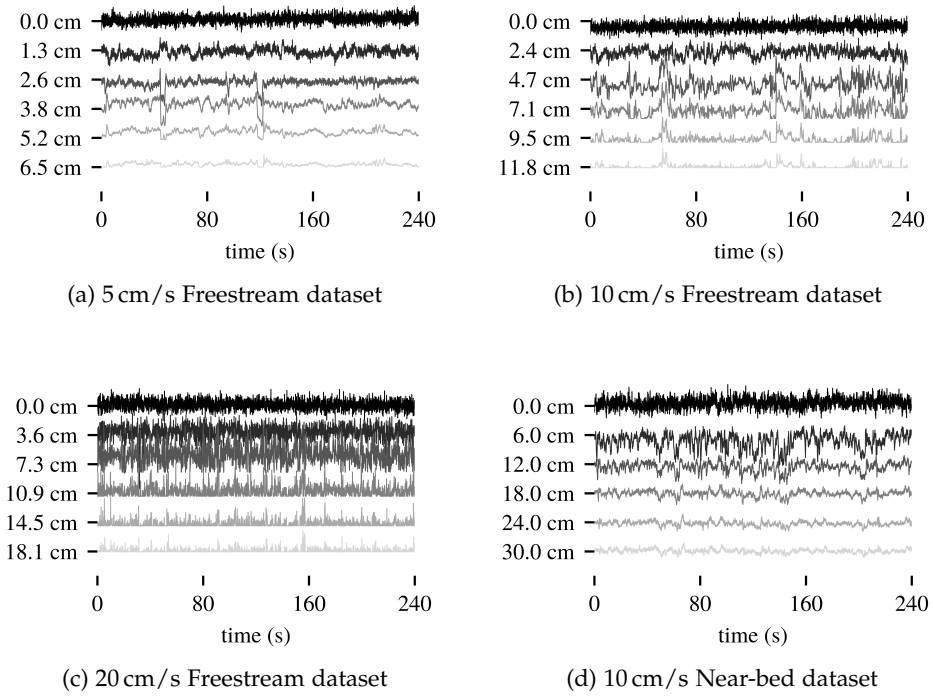

(a) 5 cm/s Freestream dataset

(b) 10 cm/s Freestream dataset

(c) 20 cm/s Freestream dataset

(d) 10 cm/s Near-bed dataset

Figure A.1: Impact of downwind distance on odour concentration.

release configurations will be challenging. In fig. A.2, we illustrate the impulse response of the second order low-pass and high-pass band-pass Butterworth filter.

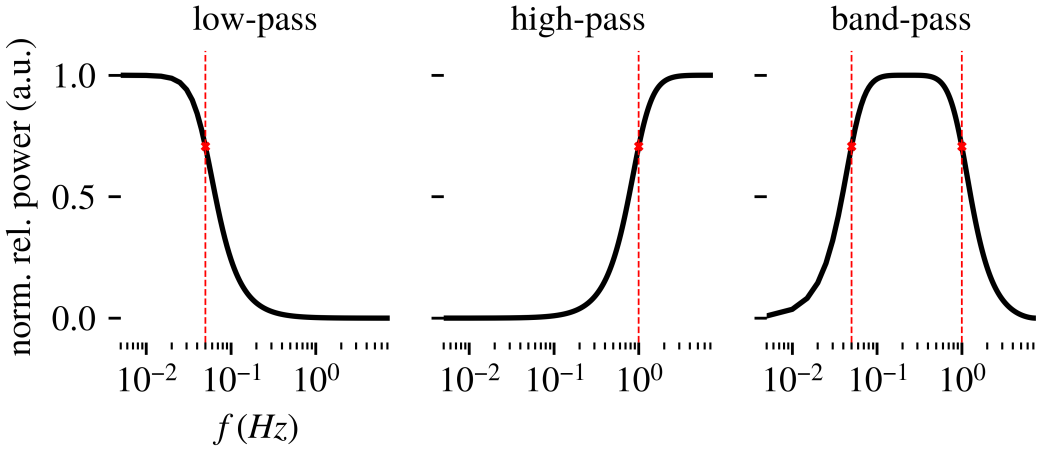

Figure A.2: Impulse response of low-pass, high-pass and band-pass Butterworth filters.

For the band-pass, we selected a lower cut-off frequency (f_{crit}^{low}) of $0.00\dot{6} * f_{nyquist}$ or $0.05Hz$ to remove the onset and offset of the gas delivery as well as some low frequency noise present in the signal. The higher cut-off frequency (f_{crit}^{high}) of $0.1\dot{3} * f_{nyquist}$ or $1.0Hz$ to remove high frequency noise potentially introduced by photon shot noise (being the primary contributor to the RMS noise (Connor, McHugh and J. P. Crimaldi, 2018)). With our Butterworth being a second order filter, the frequencies closer to the cut-off are not completely attenuated as

much as those farther away. In fig. A.3, we illustrate the impact of each of these filters. The low-pass extracts the lower frequencies, the high-pass shows the higher frequencies, and finally the band-pass demonstrates the signal after the removal of the illustrated lower and higher frequencies.

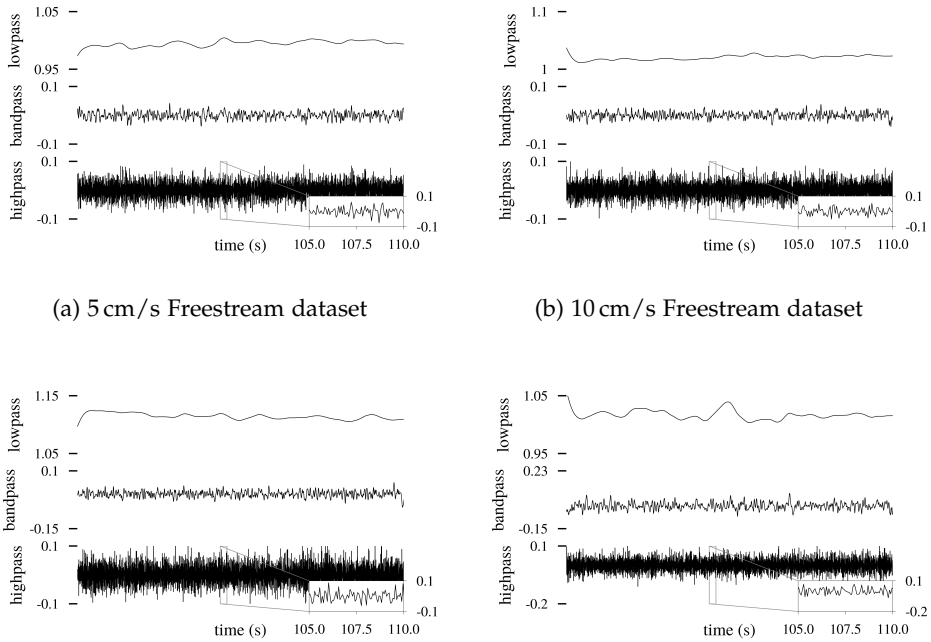

(a) 5 cm/s Freestream dataset

(b) 10 cm/s Freestream dataset

(c) 20 cm/s Freestream dataset

(d) 10 cm/s Near-bed dataset

Figure A.3: Signal at second sampled downwind distance split into low, middle, and high frequency components.

For each of the release configurations, we plot the low, middle, and high-frequency components of the second sampled downwind distance: $x = 1.3cm$ for the $5cm/s$ freestream; $x = 2.4cm/s$ for the $10cm/s$ freestream; $x = 3.6cm$ for the $20cm/s$ freestream; and $x = 6cm$ for the $10cm/s$ near-bed dataset. We selected the second downwind distance sample to reduce the impact of the high frequency noise in the initial downwind distance sample seen in fig. A.1, potentially caused by the source effect or an artefact of the image normalization, as the initial downwind distance sample occurs at the odour release location of $x = 0.0cm$. We see an initial increase in the odour concentration for the $5cm/s$ and $20cm/s$ freestream datasets, and an initial decrease in the odour concentration for both the $10cm/s$ freestream and $10cm/s$ near-bed datasets in the low frequency component at this distance. One unexpected result shown in this figure is the relative amplitude of the high-frequency component compared to that of the middle. Regardless of the release configuration, the high-frequency component shows much higher than expected amplitude fluctuations that could possibly be attributed to noise produced by the pre-processing of the data or by the experimental setup.

In fig. A.4, we show the results of spectral analysis conducted on the sampled distances along the centre line of the plume for each of the release configurations. The left panel shows the band-passed signals at the various sample distances from the first trial of each of the release configurations; the top right panel shows the average power spectra of the band-pass signals at each of the distances over each trial; and the bottom right panel shows the fraction of total power below $f_{crit}^{low\ vs\ high}$ against the sample distance. The power spectra show the average power for each of the frequencies between zero and the $f_{nyquist}$ present in the trial average of each of the downwind distance points. We plot the same estimator used by Schmuker, Bahr and Huerta (2016) P_{rel}, which is the fraction of power below a cut-off frequency f_{crit} for the mean over trials and each trial in each of the release configurations. We calculate the relative power of the frequencies below f_{crit} against the relative power of the frequencies between f_{crit} and $f_{nyquist}$ with the following equation:

$$P_{rel} = \frac{\sum_0^{f_{crit}} p_f}{\sum_{f_{crit}}^{f_{nyquist}} p_f}. \tag{A.1}$$

f_{crit} is calculated from the median maximum frequency of the six downwind spectra. Schmuker, Bahr and Huerta (2016) use the relationship between downwind distance and the ratio of power P_{rel} below the cut-off frequency as a rough predictor of source distance, and suggests this is because the number of plume filaments detected in a fixed time window linearly correlates to distance to source.

At the source in each release configuration, we see much lower amplitude fluctuations than we do downwind, and we only see transients originate in the second sampled downwind distance, but because of the sampling method that we chose, we see each of the transients travel the extent of the sampled distances. We see a key difference in the initial sample distance in the higher frequency bands $> 3Hz$ and $< 1Hz$, but all other sample distances show similar average spectra and trial-by-trial variance of ratios appear high, regardless of downwind distance. Beyond an initial increase in the first two samples of each of the release configurations, we see little trend in the remaining mean P_{rel} values. This, paired with the high trial-by-trial variance of the P_{rel} values, makes it impossible to fit a linear regression with a high accuracy. The difference from the spectral analysis conducted by Schmuker, Bahr and Huerta (2016) could be explained by the relatively smaller sample distances, though comparison cannot be directly made due to significant differences in the experimental setup and data capture. This analysis could point towards more subtle non-linear features present within the plume structure at this scale, however filtering does still appear to be necessary, as it removes noise introduced by the odour delivery onset (we do not see an offset because recording ends before the odour delivery ends) and also removes high frequency noise. For the sake of completeness, we include spectral analysis of the freestream datasets over the entire downwind extent fig. A.5.

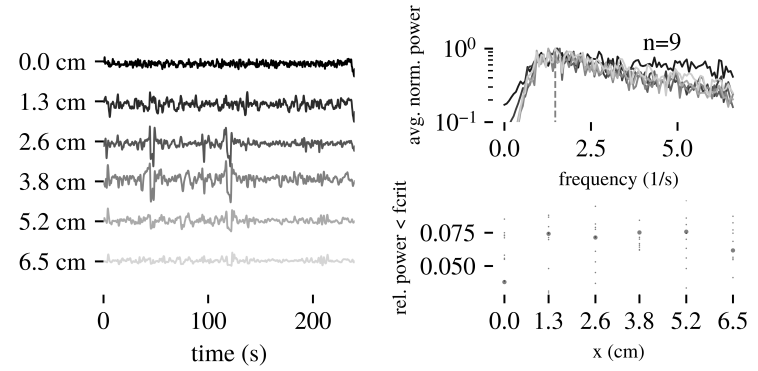

(a) 5 cm/s Freestream dataset

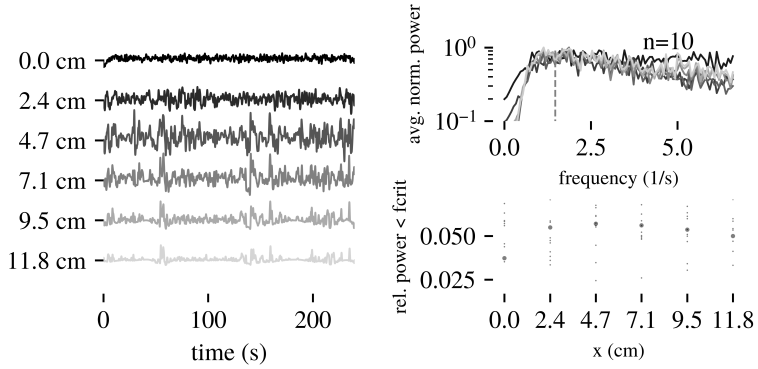

(b) 10 cm/s Freestream dataset

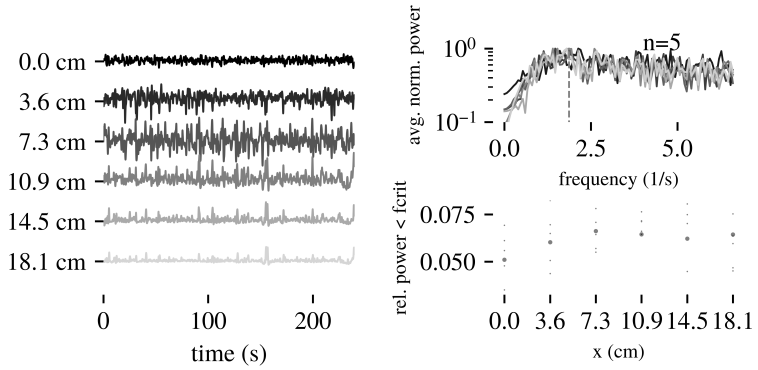

(c) 20 cm/s Freestream dataset

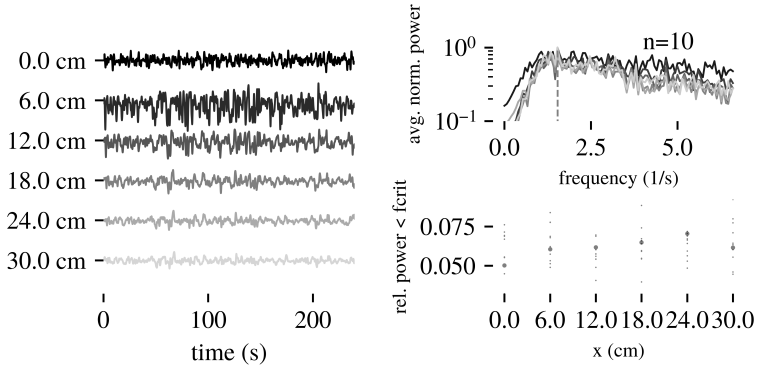

(d) 10 cm/s Near-bed dataset

Figure A.4: Spectral Analysis. We show n as the number of trials in each of the datasets. The dashed line shows the $f_{crit}^{low\ vs\ high}$, the critical frequency separating the low- and high-power bands used to quantify the frequency-distance relationship.

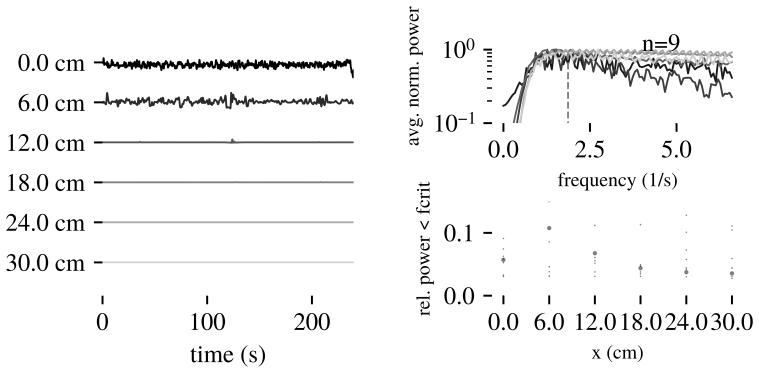

(a) 5 cm/s Freestream dataset

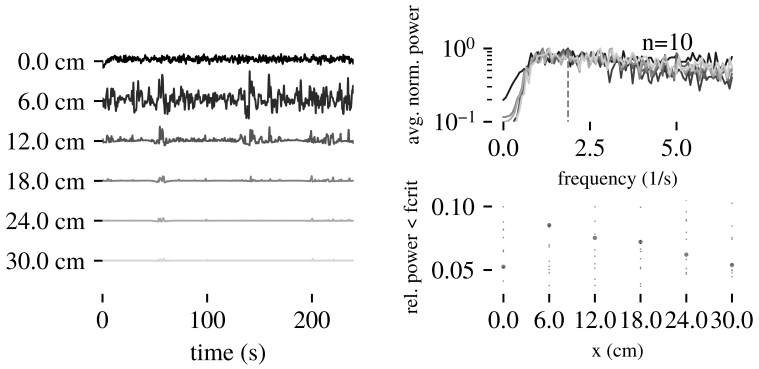

(b) 10 cm/s Freestream dataset

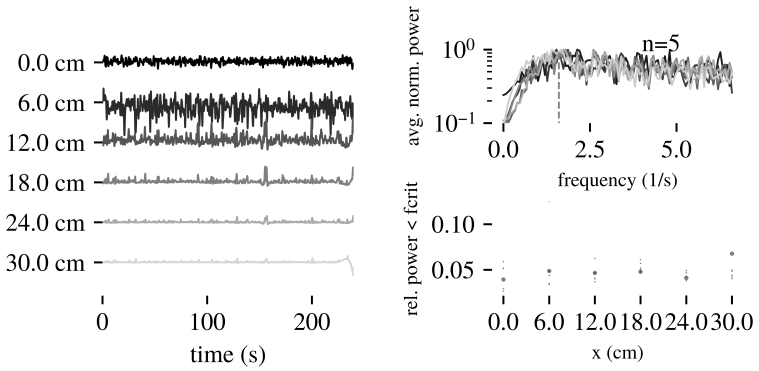

(c) 20 cm/s Freestream dataset

Figure A.5: Spectral analysis over the full downwind extent of the three freestream release configurations. Each panel shows the power spectral density at six equally spaced centre line locations from source to the downwind detectability limit. The dashed line marks $f_{crit}^{low\ vs\ high}$, the critical frequency separating the low- and high-power bands used to quantify the frequency-distance relationship.

Here we designed a band-pass Butterworth filter that extracts a range of frequencies across each of the release configurations. Although we did not see a linear relationship between the ratio of $f_{crit}^{low\ vs\ high}$ with downwind distance, we did show that there were changes in the frequency of the fluctuations with downwind distance in the middle frequency component extracted by this band-pass filter. The information represented by this change could still be used to predict downwind distance. To that end, we chose to proceed with a bout analysis and therefore selected Gaussian and EWMA parameters that would result in a band-pass filter cascade that targets the same range of frequencies, shown in fig. A.6.

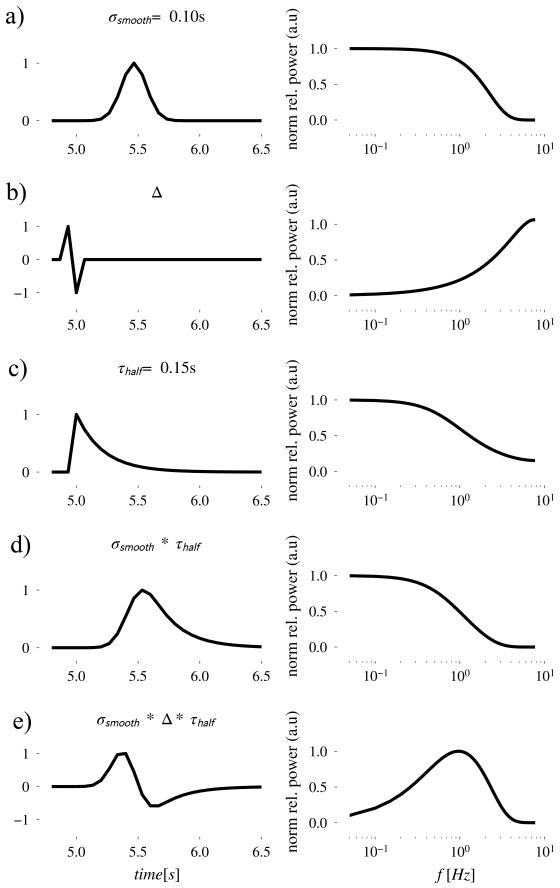

Figure A.6: Impulse response of Gaussian, Derivative, EWMA and the combined filters at 15Hz for our selected filter values

As explained in Schmuker, Bahr and Huerta (2016), the filter pipeline can be expressed as

$$S_{filt} = S * G * D * E, \tag{A.2}$$

where the signal S is convolved (denoted by $*$) by a Gaussian kernel G with width σ_{smooth}, a differentiating kernel D which is of the form $[1, -1]$ and finally an exponential kernel E with halflife τ_{half}. Figure A.6 shows the impulse response of each of these individual filter kernels (left panel for **a**, **b** and **c**) with an instantaneous pulse at 5s, as well as the normalized

power spectra of each of the responses (right panel), with the **d** panels showing the impulse response and power spectra of the convolution of each of these filters. The **e** panels show the result of our pipeline $S_{filt} = S * G * E$ without the derivative.

A.1.2 *Kernel Shapes*

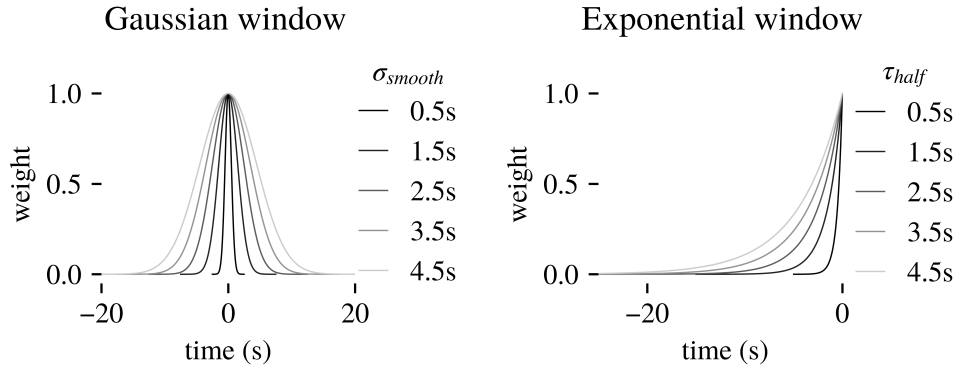

(a) Gaussian Kernel (b) Exponential Kernel

Figure A.7: Kernel Shapes for Bout Analysis Filter Cascade.

A.1.2.1 *Gaussian Curve Fitting to Lateral Scalar Profiles*

Figure A.8 demonstrates the Gaussian curve fitting pipeline for each release configuration. Here we show 5 sampled equally spaced y profiles of $\bar{C}/C_0$ and normalize the profiles to compare structure of the plumes across the x axis of the wind tunnel We show the normalized binned data equivalents to demonstrate the smoothing that occurs due to spatial binning and show the Gaussian curves fit to the binned data.

What was evident from fig. A.8 was the diversity of the lateral profiles caused by the release configuration. Figure A.8a did not show clear single peak distributions of concentration throughout the extent of the wind tunnel. The spatial binning mitigated some of the noise introduced by low odour concentration present in the majority of the wind tunnel where $x > 10cm$. The Gaussian curves showed a lateral shift of the plumes towards positive y with increasing x for all release configurations. This reinforced the necessity to track the plume position throughout the wind tunnel to approximate the centre line and edges of the plume. Figure A.8d shows that the near-bed configuration has more lateral extension of the plume initially and with increase x than any of the freestream plumes.

A.1.3 *Influence of Kernel Parameters on Bout Counts*

Throughout this chapter, we use fixed values for the Gaussian filter ($\sigma_{smooth} = 0.10s$) and for the EWMA ($\tau_{half} = 0.15s$) in the filter cascade that preludes the bout analysis. In fig. A.6, we

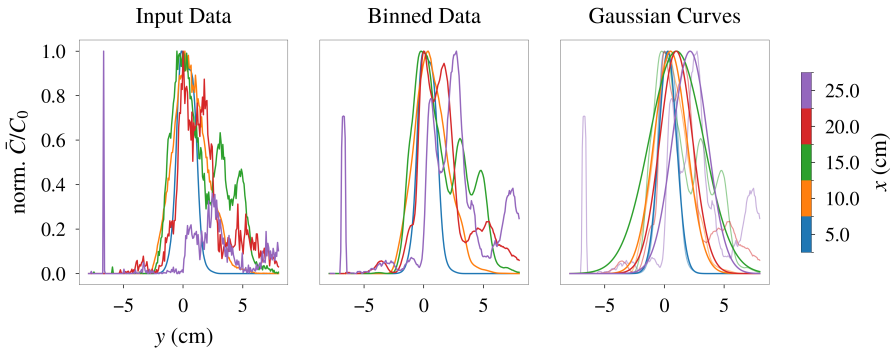

(a) 5 cm/s Freestream dataset

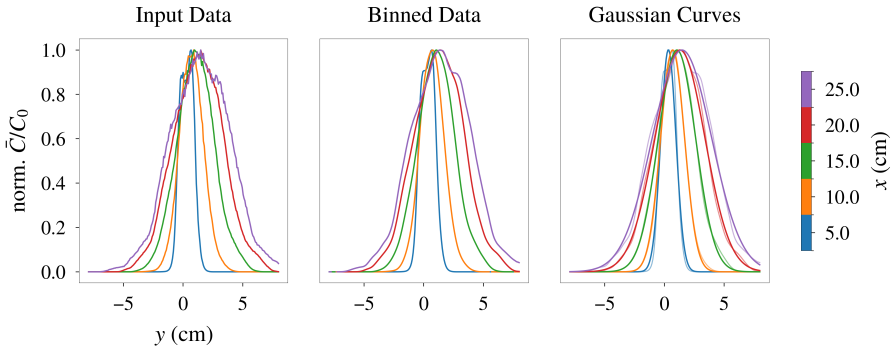

(b) 10 cm/s Freestream dataset

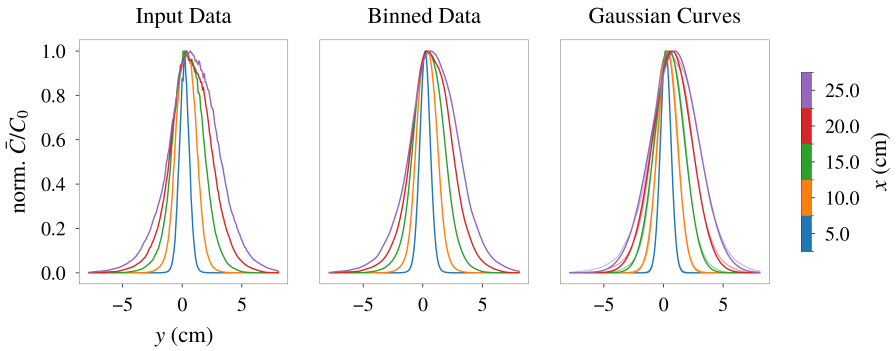

(c) 20 cm/s Freestream dataset

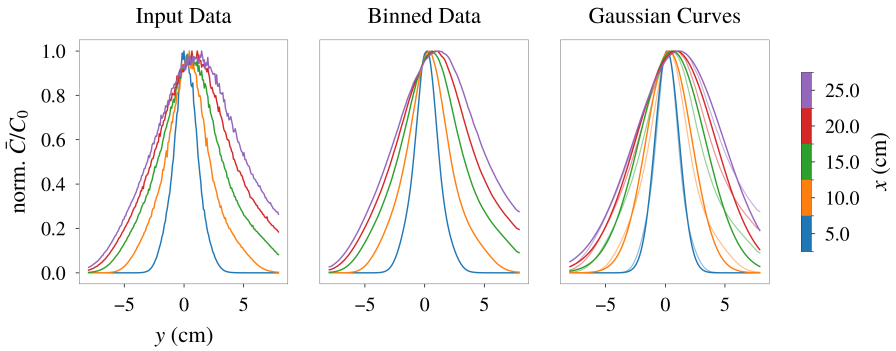

(d) 10 cm/s Near-bed dataset

Figure A.8: Gaussian curve fitting to lateral concentration profiles for each release configuration. Five equally spaced downwind positions are shown. Each panel shows the normalised time-averaged concentration profile $\bar{C}/C_0$ (solid), the spatially binned equivalent (dots), and the fitted Gaussian curve (dashed), which is used to estimate the plume centre line μ and lateral extent $\mu \pm 2\sigma$.

show the frequencies that these specific filters target both individually and when combined. The reason we use fixed filter parameters is for ease of comparison across different release configurations when exploring the bout statistical relationships. However, the filter values can be tailored to target specific wind speed or release configurations. One could even produce a filter bank to provide a more robust distance prediction.

To demonstrate the impact of the kernel parameters on the calculated bout counts, we show the bout count distance curves for a number of different combinations of the kernel parameters. For each x pixel on the plume centre line (μ), we plot bout count curves, fixing one of the kernel parameters and changing the other. For every combination of σ_{smooth} and τ_{half}, an amplitude threshold was generated, as previously discussed in section 3.6.4.

fig. A.9 shows that the overall range of mean and variance values of bout counts across trials consistently decreases when increasing either τ_{half} or σ_{smooth}, regardless of odour release configuration or wind speed. Increasing the σ_{smooth} Gaussian filter parameter extending the impact of the filter forwards in time this significantly decreases the targeted frequency band of the band-pass filter. The impact of increasing the τ_{half} parameter of the EWMA is an elongation of the exponential window that decreases the slope of the high frequency cut-off, but also decreases the targeted frequency band. This is demonstrated separately in fig. A.7. Increasing either parameter has the effect of removing more high frequency shorter duration bouts, but reintroduces longer low frequency bouts. The differential rate at which these parameters impact the band-pass kernel shape allow for fine-tuning of the impact on the bout count curves.

The τ_{half} parameter ranges shown have a much reduced impact on the overall decrease in bout counts in comparison to increasing σ_{smooth}. We see the filtering removal of bouts overall in $5cm/s$ and $10cm/s$ freestream datasets with a slight increase in the relative bout counts at the odour source. With a slight impact to the overall curve shape in the $10cm/s$ bout count curve, going from more flattened to rounding at the top and bottom of the sigmoid curve with increasing τ_{half}. We see a significant increasing in bout count variance with increasing τ_{half} in the $20cm/s$ freestream dataset, but this could be an artefact of the decreasing in overall bout counts. The overall curve appears to slightly flatten with the range decreasing by ≈ 100 bouts. The impact of τ_{half} on the $10cm/s$ near-bed dataset is less obvious with a overall decreasing the range of bout counts and a decrease in the variance of bout counts mostly after the secondary peak at $x \approx 5cm$ with increasing τ_{half}.

The σ_{smooth} parameter has a much clearer impact in the overall shape of the bout count curve for the range of tested values. A significant decrease in the bout counts $x < 5cm$ for the $5cm/s$ dataset is seen with an increase in noisy bouts at the downwind extent $x > 25cm$, showing that low values for this parameter remove noise in this area and at the odour source. The impact of σ_{smooth} is also less subtle than that of τ_{half} in the $10cm/s$ freestream dataset with a decrease in maxima from 600 to 100 bouts. $\sigma_{smooth} = 0.45s$ shows a much more exaggerated curving of the top and bottom areas of the sigmoidal curve with a significant reduction in the initial bout count peak at the source. The $20cm/s$ freestream dataset shows a

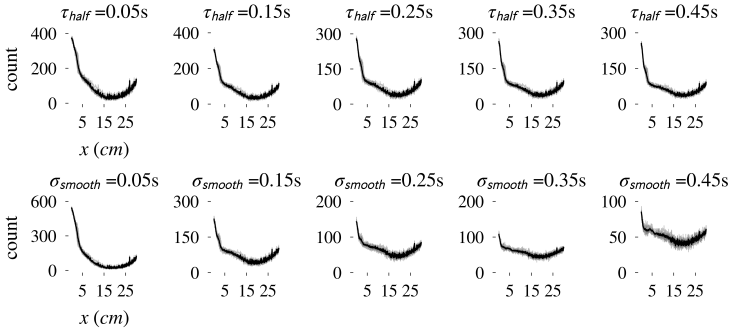

(a) 5 cm/s Freestream dataset

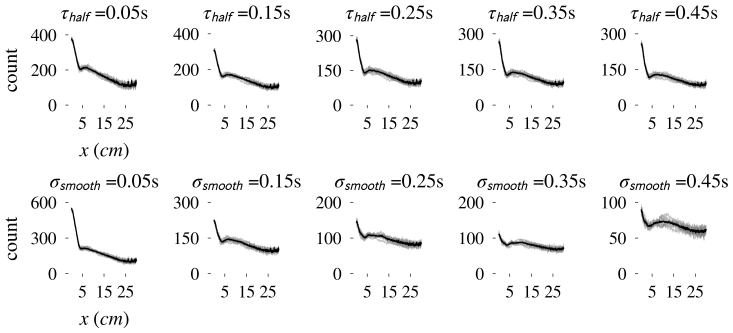

(b) 10 cm/s Freestream dataset

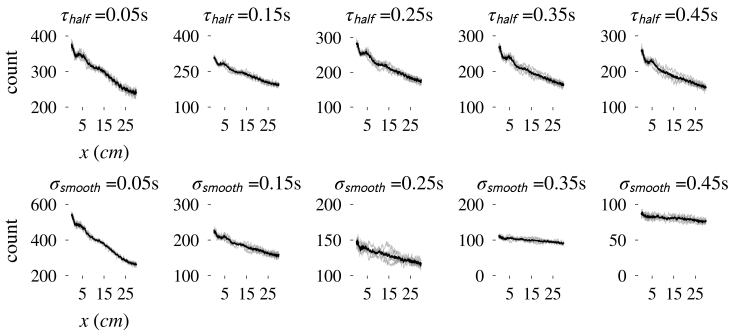

(c) 20 cm/s Freestream dataset

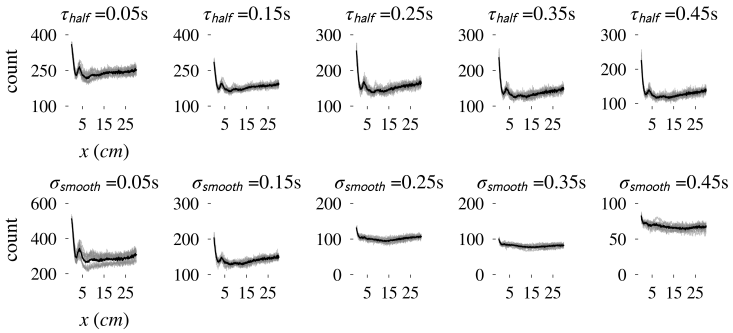

(d) 10 cm/s Near-bed dataset

Figure A.9: Effect of filter kernel parameters on bout count curves. Top panels show impact increasing τ_{half} from left to right with constant $\sigma_{smooth} = 0.1s$. Bottom panels show increasing σ_{smooth} with fixed $\tau_{half} = 0.15s$. Grey lines show individual trial values and the black line shows trial mean bout counts.

significant decrease in the gradient of bout counts with downwind distance when increasing the σ_{smooth} parameter. Finally the $10cm/s$ dataset shows an almost complete reduction in an initial maxima at the odour source and removal of a secondary peak at $x \approx 5cm$.

The overall shape of the bout count distance curves are generally maintained within the range of parameters shown, but the ranges of bout counts are impacted with even small changes to the filter parameters. The areas most affected by changes to the filter parameters are the extrema of the bout counts, where either high bout counts are produces by high frequency fluctuations or low bout counts occur at the downwind extent of the plume. This dataset provides enough spatial and temporal resolution to explore the non-linearities produced in the turbulent plumes. In applying a specific pair of filter parameters we have influenced the shape of the bout count curves and potentially differently in each of the release configurations - selecting the same specific range of frequencies that have different powers in the datasets caused by the different wind speeds and release heights. The complexity shown in the nature of these plumes makes odour source distance prediction more difficult i.e. sigmoid fitting in section 3.7.1.2. As suggested by Schmuker, Bahr and Huerta (2016), employing a bank of multiple filters with different filter settings in parallel may improve the accuracy of a distance estimate by targeting frequencies present in different areas of the plume.

A.2 IMPACT OF CROSSWIND DISTANCE ON NORMALIZED BOUT STATISTICS

Following the results shown in fig. 3.14, we chose to normalize the statistics to demonstrate the relationship of the bout statistic to the crosswind distance, removing the influence of downwind distance from the odour source. For each of the sampled distances, we normalize the statistics between the minimum and maximum values (min-max normalization) over the crosswind distance. This removes the magnitude of the statistic, but allows further exploration and better visualization of the impact of crosswind plume distance on the bout statistics.

With normalization applied, one can see in fig. A.10 the same bout statistical relationships with plume crosswind distance across all datasets, with anomalies appearing in all datasets at certain downwind distances. With increasing crosswind distance, we see non-linear decreasing average bout counts, bi-modal distributions of bout duration and amplitude, and an inverted 'bell'-shaped distribution of IBIs. Normalization has removed the relative magnitude of the statistic curves between downwind sampling distances, but has not removed the noise introduced by low bout counts at greater downwind distances.

In fig. A.10a, we see bout counts decrease with crosswind distance. With increasing downwind distance, the bout count curve narrows from $\pm 2\sigma$ to $\approx \pm 1\sigma$. Duration has a downwind distribution with two peaks $\mu \pm 1.5\sigma$ and a trough at the centre line. Amplitude has a similar bimodal distribution, with the peak in the positive σ direction having twice the normalized amplitude. IBI shows an inverted 'bell' shape with peaks at the plume

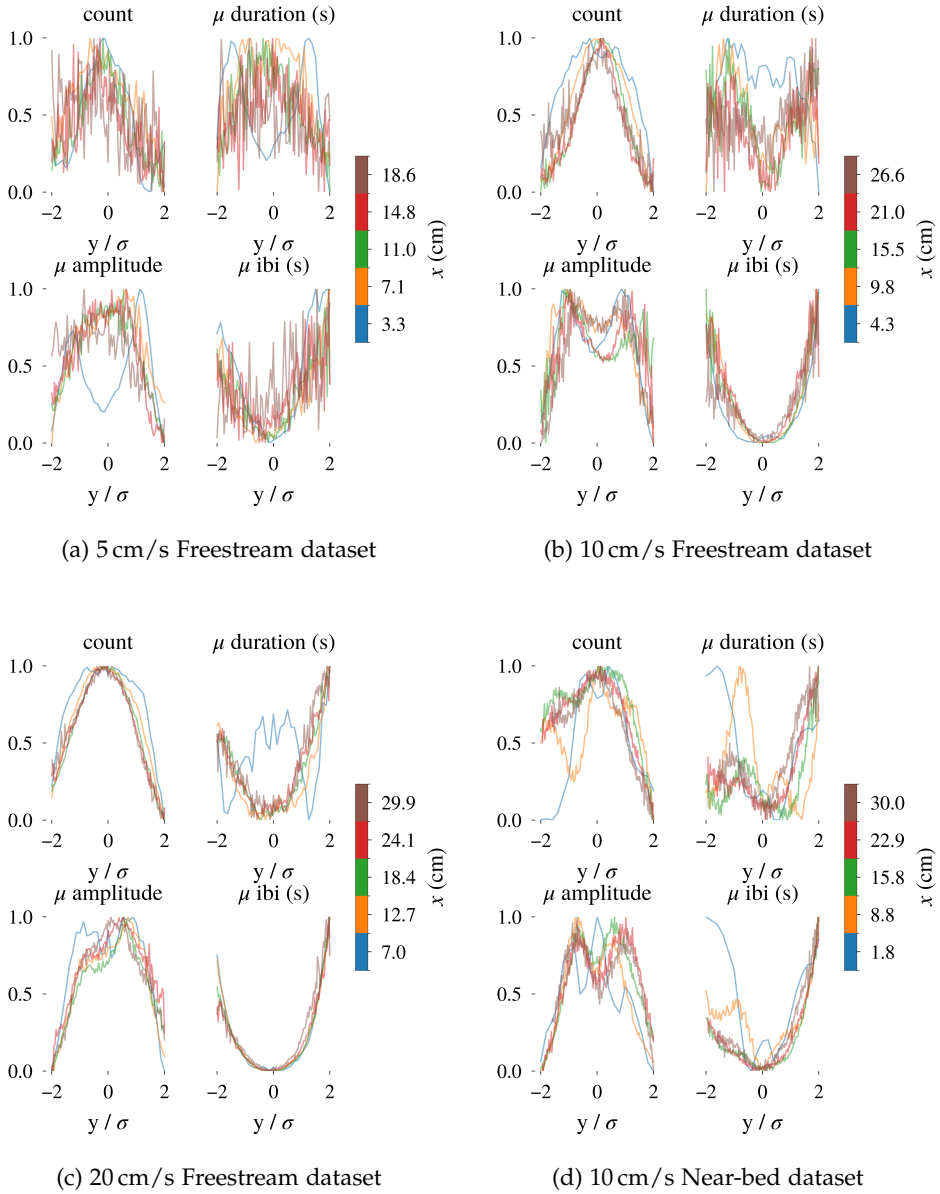

(a) 5 cm/s Freestream dataset

(b) 10 cm/s Freestream dataset

(c) 20 cm/s Freestream dataset

(d) 10 cm/s Near-bed dataset

Figure A.10: Min-max normalized statistics of bouts against crosswind distance. Top left panel shows bout count over the trial, top right shows the mean duration of the bouts, bottom left shows mean amplitude and bottom right shows inter-bout intervals.

edge and a trough at the centre line, narrowing with downwind distance. For all statistics, increasing downwind distance introduces more noise, with the curve closest to the plume source showing the smoothest crosswind distance relationship.

We see the same crosswind relationships as in the $5cm/s$ dataset in fig. A.10b. The data point closest to the plume source appears anomalous when compared to those further downwind, and does not follow the same trends, despite it being the smoothest of all the curves. It shows the widest bout count and IBI curves only significantly decreasing from $\geq \mu \pm 1.5\sigma$. All sample distances $\geq 10.7cm$ follow a much more consistent shape, with bout counts decreasing more linearly from $\mu \pm 0.5\sigma$ to the plume edge. Durations at these distances appear more noisy, with a bimodal distribution with minimum values at the plume edges and trough minima increasing with downwind distance. The bout amplitude appears to mirror the bimodal distribution of the duration, with a more clear decrease at the plume edges. Minimum values occur at the centre of the plume, potentially due to having a slightly wider curve, which means that, with increasing crosswind distance, bout amplitudes lag behind the bout durations. Finally, the IBIs appear to inversely mirror the bout counts with a skew towards positive σ.

The $20cm/s$ freestream dataset in fig. A.10c shows the most consistent statistical curves across downwind distances, with the most anomalous curve being the one closest to the odour source. The most differences between the bout count curves occur over the first three downwind sample points, where the bout count curve gradient decreases and the curve narrows with increasing downwind distance. Apart from this, the bout count curves appear to follow a consistent Gaussian distribution. With the duration crosswind distance curves, the anomalous first sample point appears the most clearly – showing an inverted bimodal distribution – whilst the sample points further downwind show an inverted normal distribution, each centred around the plume edge line. There's a skew towards positive σ with a normalized amplitude twice that of the negative σ plume edge. The $7cm$ amplitude crosswind distance curve shows a multi-modal distribution with three distinct peaks $\mu \pm 1\sigma$ and at the plume centre μ. However, the troughs of these distributions are not significant and are noisy. Sample points further downwind appear to only show one side of this multi-modal distribution and, in most cases, their maximum value occurs either at the positive σ plume edge or at positive $\mu + 1\sigma$. This could be a sign of poor approximation of the plume boundaries for this dataset. The IBIs also show a skew towards positive σ, with the plume edge at negative σ reaching only a normalized IBI of 0.5. However, the IBI curves remain consistent throughout each of the downwind sample points with an inverted 'bell'-shaped distribution over the sampled normalized crosswind extent.

For all statistics in fig. A.10d, we see the same positive σ skew due to a lateral shift in average concentration in the direction of negative σ. This is especially noticeable in the near-bed dataset, because we expect a Gaussian distribution of bout counts centred around the mid-point of the plume. However, we see a transition from the expected behaviour to a one-sided distribution as we move further downwind. For downwind distances, $\geq 15.8cm$

the negative σ plume edge only decreases down to ≈ 0.75, whilst the positive σ plume edge decreases to zero. This skew also impacts duration – with what should be a uniform bimodal distribution, we see a maxima at the positive σ plume edge and peaks in the negative σ direction reaching ≈ 0.4 for distances $\geq 15.8cm$. Amplitudes are least effected, with a transition from a multi-modal to bi-modal distribution occurring with increasing downwind distance, but with consistent peaks $\mu \pm 1\sigma$ and troughs reaching minima of ≈ 0.6 at the plume centre line. Again, IBIs appear to be cut off in the negative σ plume edge, otherwise we would expect this to be an inverted 'bell' shape. Previously, we assumed that IBIs mirrored the duration, but here they appear to most closely be an inverted version of the bout count curves. This statistic appears to be the most robust across downwind samples $\geq 15.8cm$.

Normalizing the crosswind distance curves allows us to analyse the statistical relationship between the bouts and crosswind distance without the impact of the magnitude of the statistic. We see more clearly that the same statistical relationships occur further downwind than we did in fig. 3.14: bout counts consistently decrease with crosswind distance; durations appear to increase and then decrease with crosswind distance due to proximity with the plume edge and therefore low bout count; amplitudes also appear to follow the same relationship (apart from in the $20cm/s$ dataset, which, as discussed, is either due to poor approximation of the plume bounds or lack of downwind sigmoid curve); and IBIs increase with crosswind distance consistently (in the $20cm/s$ dataset, IBIs appear to be more consistent than the bout count at determining crosswind distance, regardless of downwind distance). Across all datasets, the points closest to the flow transition point, although usually the most clear, do not appear to follow the trends of those sample points further downwind and therefore appear anomalous. There is a consistent lateral skew of the statistics that the plume bound approximation was unable to remove with most curves either having sections cut off or uneven plume edges. Regardless of this, the $20cm/s$ dataset shows the most consistent curves with the least noise of all the datasets. All datasets show some degree of noise either due to low bout count at greater downwind distances, or chosen sample locations, but this is a limitation of the dataset.

A.3 BOUT INTERMITTENCY

Throughout this chapter we analyse the bout count, duration and IBI as separate temporal bout statistics, however we see clear links between the occurrence of a bout and the time between bouts. To this end, we visualize the occurrence of bouts in terms of their intermittency. Bout intermittency is a measure of the percentage of time of the trial that a bout occurs. As bout intermittency is a temporal statistic, it is impacted by the bout count, duration and IBI, but is not impacted by the amplitude of the bouts. Bout intermittency differs from intermittency calculated in Connor, McHugh and J. P. Crimaldi (2018), in which

they calculate the percentage of time of the combined trials that the concentration is above a certain threshold.

We examine the values of the average and std of the bout intermittency over trials for each of the four release configurations. We calculate and plot bout intermittency for every pixel within $\mu \pm 2\sigma$ of the plume. The trial average bout intermittency highlights the areas in each of the plumes in which bouts occur most and least often. The std of the bout intermittency shows how much the bout intermittency varies from trial to trial. This should highlight the values of intermittency in which we have the highest error and allow us to compare between the release configurations.

In the $5cm/s$ freestream dataset, we see the largest range of intermittences over the plume area. The highest intermittency occurs close to the odour source, with values decreasing downwind and crosswind from the centre of the plume. Between $x > 5cm$ and $x < 10cm$, we see the greatest std between trials of bout intermittency of up to $\approx 10\%$. This high std area aligns with the area in which the average intermittency significantly decreases. The area of high bout intermittency shows a relatively low std, meaning that close to the source we consistently see bouts occurring regularly.

The $10cm/s$ freestream dataset shows a decreased range of mean intermittency but a greater extent of the higher values over a larger portion of the plume, with values decreasing both downwind from the source and crosswind from the centre of the plume. The std of bout intermittency across trials shows a much smaller range of values than seen in the $5cm/s$ dataset. The lowest values of intermittency occur at the source and at the edges of the plume, where the mean intermittency is at its highest or lowest values, respectively. We see the same curved area of high std as seen in the $5cm/s$ dataset, but with much lower std values stretched farther downwind by the higher wind speed.

Comparatively, the $20cm/s$ freestream dataset shows a smaller range of high percentages with less of a decrease in the mean intermittency downwind and crosswind. The std of intermittency is lower at the mid-point of the plume and increases towards the edges of the plume, where average intermittences are high and low, respectively. We see a band of lower values of std offset from the mid-line of the plume $y \approx 1cm$ that extends to the downwind plume extent from $x \approx 5cm$. We believe this band to be the same curve structure as seen in the $5cm/s$ and $10cm/s$ datasets, with a lower range of stds and stretched beyond the extent of the wind tunnel.

The $10cm/s$ near-bed dataset cannot be compared directly to the freestream datasets due to its proximity to the false floor. However, we see that it shows the lowest range of trial mean bout intermittency of all the datasets, with low values occurring only at the very edge of the plume. Again, std appears to be inversely correlated to the mean, with the highest area of variance occurring at the edge of the plume and the lowest std occurring along the mid-line. Overall, this dataset has the highest average bout intermittency and the lowest amount of variance across the plume extent, with no obvious trends such as those seen in the other datasets.

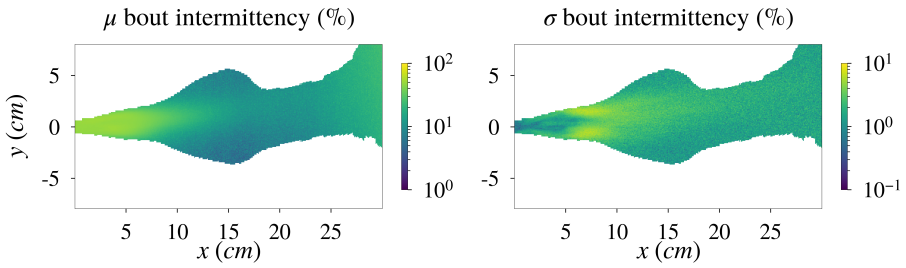

(a) 5 cm/s Freestream dataset

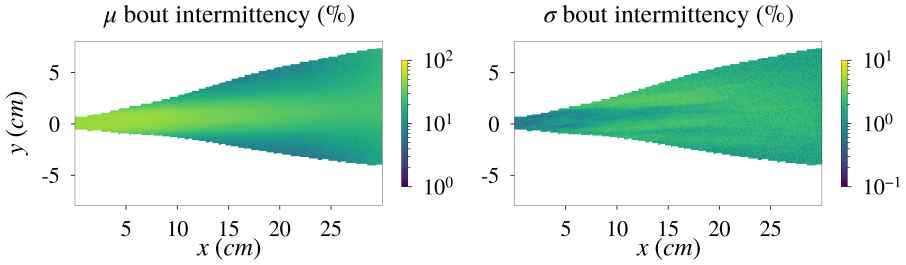

(b) 10 cm/s Freestream dataset

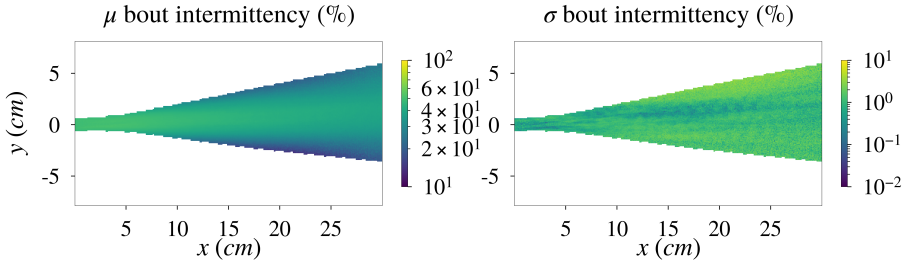

(c) 20 cm/s Freestream dataset

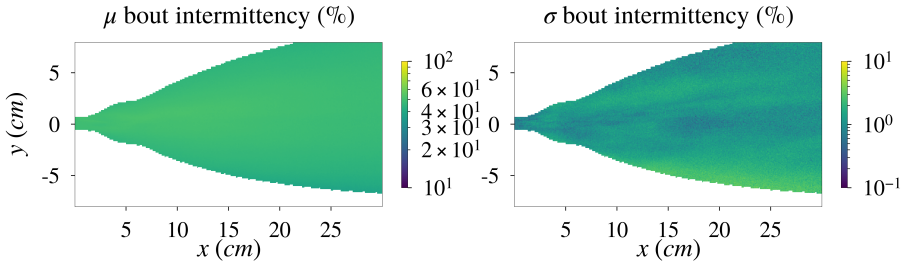

(d) 10 cm/s Near-bed dataset

Figure A.11: Spatial maps of bout intermittency — the fraction of trial time during which a bout is occurring — for each release configuration. Left panels show the trial-mean intermittency; right panels show the trial-to-trial standard deviation. Intermittency reflects the combined influence of bout count, duration, and IBI, but is independent of bout amplitude.

Bout intermittency combines the temporal bout statistics but appears to mainly follow the trends seen in the average bout count. The extent of high bout intermittency appears to increase with wind speed for the freestream datasets. The trial by trial variance appears to occur most often at the areas of the plume in which the high bout intermittences transition to lower values i.e. the edges of the plume or $5cm < x < 10cm$ in the $5cm/s$ dataset. In comparison, in the near-bed dataset, we see very low variances of bout intermittency overall and high std of bout intermittency only occurs at the plume edge due to greater advection of the odorant with proximity to the false floor.

A.4 IMPACT OF SAMPLE DURATION ON BOUT COUNT

The bout amplitude, duration and IBIs shown throughout this chapter are trial averages and are directly linked to the bout counts: the lower the bout count, the smaller the sample size of the other statistics. For each of the bout statistics calculated up until this subsection, we sample for the entire duration of each trial and report trial average values. Here we examine the impact of the sample duration on the average bout count over all trials for varying locations along the centre line of the plume μ. We plot the mean and std of the bout counts over all trials for each selected sample duration. We sampled according to fig. A.12 in which we split the total trial length into increasing equal divisions.

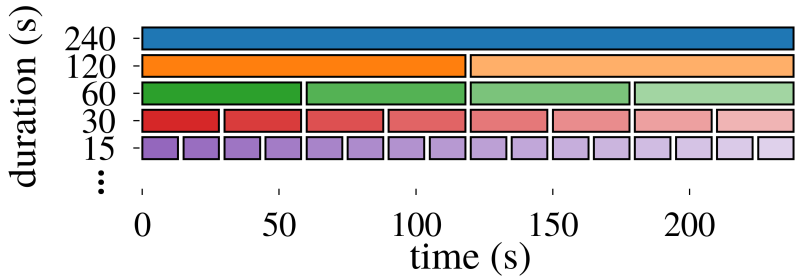

Figure A.12: Schematic illustrating the sampling duration procedure. The total trial length is divided into equal sub-windows of decreasing duration, and bout statistics are computed for each window independently. This allows the dependence of bout count and bout frequency estimates on sample duration to be characterised.

We plot the average bout count divided by the sample duration (or bout frequency) for nine sample durations between $240s$ (3600 frames) and $0.93s$ (14 frames) across all trials. The division of the bout count by the sample duration to produce bout frequency accounts for the sample duration in the calculated bout counts. For mean bout count we fit equation eq. (A.3) as we see a linear relationship between the sample duration and the average bout count in which the coefficient of the fit varies with change in downwind distance. We chose to fit equation eq. (A.4) to the mean bout frequency in order to account for the log spacing of the sample durations. Lastly, for std of bout counts and bout frequency, we fit equation

eq. (A.5) because we see a non-linear decreasing in std of bout counts with the non-linearly spaced sample durations.

$$f(T) = m \cdot T + b \tag{A.3}$$

$$f(T) = m \cdot \ln(T) + b \tag{A.4}$$

$$f(T) = e^{m \cdot \ln(T) + b} \tag{A.5}$$

For each release configuration we include coefficient (m), intercept (b), mean squared error (MSE) and R^2, shown in table table A.14. We select the same sample locations for each of the release configurations used when sampling along the centre line of the plume thus far. We therefore have to be cognisant of the changing sample locations before attempting to make direct comparisons between release configurations.

In fig. A.13 we see that sample duration has a positive linear correlation with mean bout count over trials, whilst the std logarithmically increases with sample duration. However, when we compensate for the sample duration in the statistic, the average bout count of sampling duration remains stable for all datasets. The intercept of bout frequency ($\mu \frac{count}{dur.}$) provides a good estimation for expected bout count per second. The lack of change in the gradient across sample durations and $x(cm)$ suggests that for all sample durations tested, there is not a significant impact on the average bout frequency. However, the std of the bout frequencies ($\sigma \frac{count}{dur.}$) is negatively correlated with the sample duration, decreasing exponentially with increasing sample duration. This suggests that the variance across datasets and sample durations increase with decreasing sample duration. This could be an artefact of our sampling method, with sample numbers doubling with decreasing sample duration, or it could be due to actual variance introduced by the decreasing sample duration.

All freestream datasets show a non-linearly decreasing intercept of the mean bout frequency with distance from source. The near-bed dataset shows an inverted relationship between the intercept of mean bout frequency and $x(cm)$. This is expected when we consider the bout count distance relationships shown in section 3.7.1.1. Here we only look at impact of downwind distance along the centre line of the plume. We therefore plot the coefficient and intercept of the functions eq. (A.4) and eq. (A.5) for mean and std bout frequency, respectively, for each pixel within the plume and each dataset.

In fig. A.13, we fit a regression to the mean and std of bout counts and frequencies against select sample durations for selected downwind distances (x). This is to establish the minimum sample duration required for an accurate bout frequency. Here (fig. A.14), we plot the coefficient and intercept from the regression of the mean using eq. (A.4) and the std

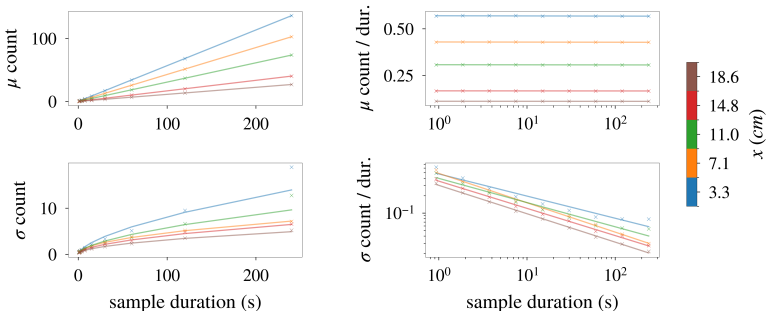

(a) 5 cm/s Freestream dataset

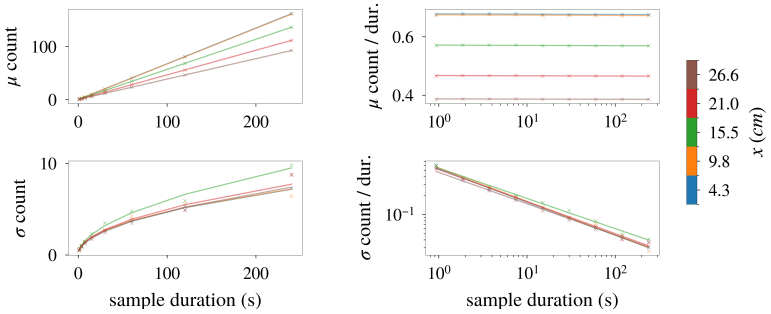

(b) 10 cm/s Freestream dataset

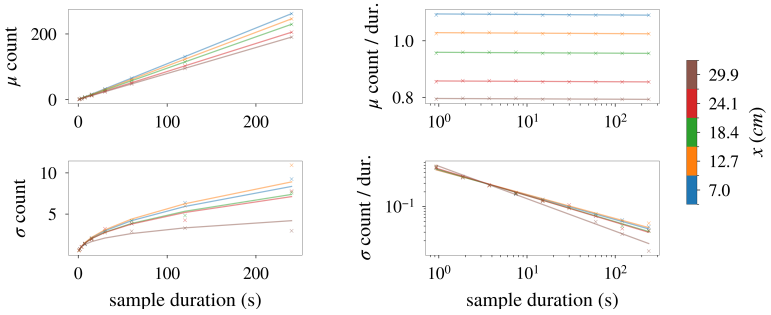

(c) 20 cm/s Freestream dataset

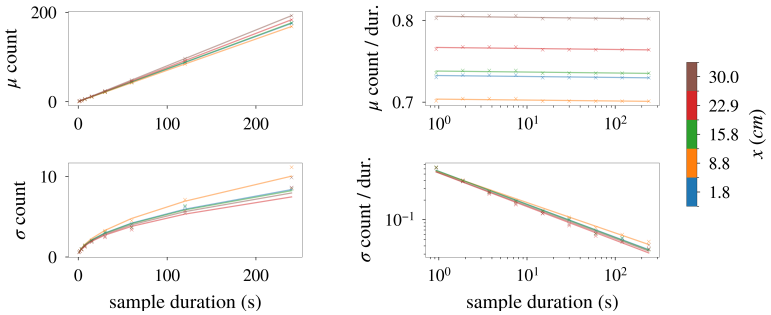

(d) 10 cm/s Near-bed dataset

Figure A.13: Impact of sampling duration on bout count and bout frequency along the plume centre line μ, for six equally spaced downwind distances. Each panel shows the mean (top) and standard deviation (bottom) of bout count and bout frequency across trials, as a function of sub-sample duration. The mean bout frequency (μ *count*/*dur*.) remains stable across durations, while the standard deviation decreases with increasing sample duration, indicating reduced estimation error at longer sample windows.

using eq. (A.5) of bout frequency against sample duration for every pixel location within the plume. The intercept is the bout frequency at sample duration of zero seconds. This is not possible, but where the coefficient is low it provides a close approximation of the expected bout frequency in that location. The coefficient is the gradient of the relationship between sample duration and bout frequency. A negative coefficient ($\frac{\mu}{dur.}$) suggests that mean bout frequency decreases with increasing sample duration. However, if we refer to the table A.14, we see that R^2 for $\mu\frac{count}{dur}$ are comparatively low. This is due to the very low total variation in the mean bout frequency with changing sample duration and reflected in the plotted coefficients occurring in the range of zero to $\approx 1e-5$.

For the std of bout frequency, the more negative the coefficient is, the higher the variance of the bout frequencies between sample durations and trials, or error caused by the smaller sample duration. The smallest possible value std can be is zero. However, all the plotted values of the intercept of the std are negative because the intercept is measured at a zero-second sample duration. One has to remember this is the y intercept of a log x and log y linear fit because it best approximates the trend of the std. We do still plot all the calculated values for the sake of completeness.

The reported coefficients of the bout frequency-sample duration $\frac{\mu}{dur.}$ regressions (top left panels) show values close to zero where we see little impact of sample duration on bout frequency, and more negative values close to the source for all datasets, where sample duration had a greater impact on bout frequency. These same areas have higher reported intercepts, suggesting where bout frequency is higher we see a greater impact of sample duration on the bout counts.

In the $5cm/s$ freestream dataset we see an area $x \approx 10cm$ with a less negative coefficient of the std of bout frequency. This area is the downwind edge of the plume, where the impact of sample duration on the variance in the bout counts across samples and trials appears to decrease – possibly as a result of fewer bouts occurring in this location.

All $\frac{\mu}{dur.}$ intercept values can be interpreted as being an expected bout frequency due to the very small coefficients. We see bout frequencies ranging from zero to $\approx 1.5Hz$ for all datasets, with all freestream datasets showing a decrease in bout frequency downwind and crosswind. The near-bed dataset shows little change in average bout frequency downwind, but some decrease crosswind in hotspots of higher coefficients.

Overall, average bout frequencies did not appear to be significantly impacted by the selected sample durations across the entire plume. Reducing the sample duration did impact the std of the bout frequencies, either where bout frequency was high or where sample duration was very low. To determine a low error average frequency, a longer sample duration helps but is not necessary in the range of tested sample durations.

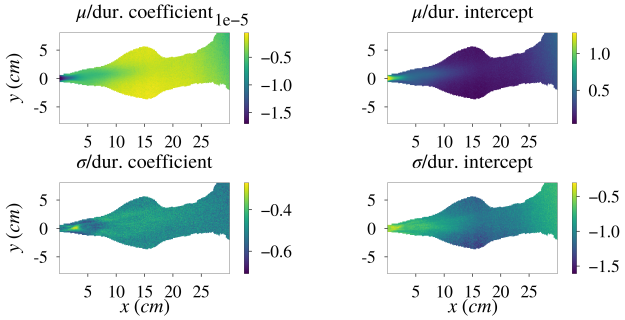

(a) 5 cm/s Freestream dataset

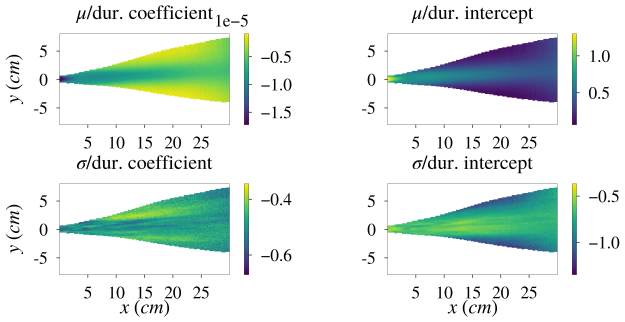

(b) 10 cm/s Freestream dataset

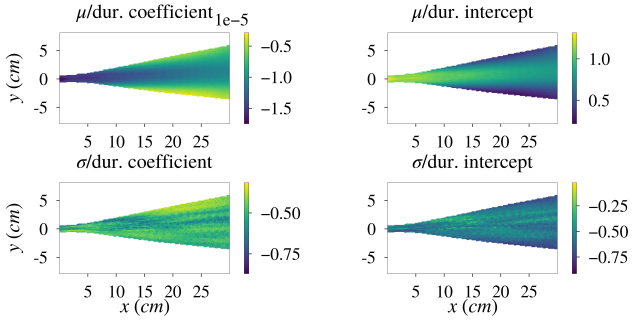

(c) 20 cm/s Freestream dataset

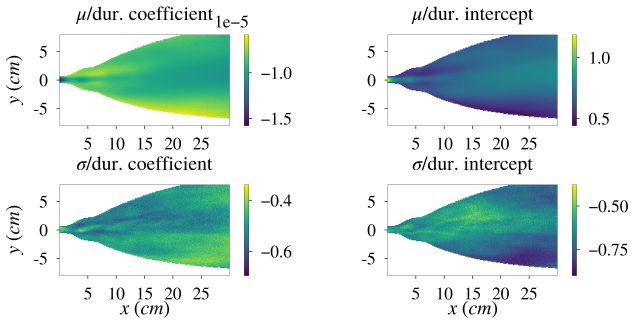

(d) 10 cm/s Near-bed dataset

Figure A.14: Spatial maps of regression coefficients from fitting bout frequency against sample duration across every pixel within the plume ($\mu \pm 2\sigma$). Top-left panels show the slope of mean bout frequency vs. duration ($\mu\ count/dur.$); top-right panels show the intercept. Bottom-left panels show the slope of the standard deviation ($\sigma\ count/dur.$); bottom-right show the intercept. Values close to zero in the slope maps indicate locations where bout frequency is stable across sample durations; more negative values indicate a stronger duration dependence.

A.5 DOWNWIND PCA TABLES

The following three tables accompany the downwind PCA results presented in section 3.7. Table A.1 shows the percentage of total variance explained by each principal component (PC1–PC4) for each release configuration; in all cases PC1 captures the majority of variance ($\geq$ 76%), confirming that a single axis dominates the structure of the downwind bout statistics. Table A.2 gives the pairwise Pearson correlations between the four bout features (count, duration, amplitude, and inter-bout interval); the strong negative correlation between count and inter-bout interval ($r \approx -0.91$ to -0.99) reflects the mathematical relationship between these quantities. Table A.3 lists the PC feature loadings (eigenvectors), showing how each bout statistic contributes to each principal component across release configurations.

Release Config.	Wind Speed (cm/s)	PC1 (%)	PC2 (%)	PC3 (%)	PC4 (%)
Freestream	5	80.21	10.77	7.87	1.15
	10	79.47	16.55	3.68	0.30
	20	80.20	16.74	2.96	0.10
Near-bed	10	81.99	13.07	4.80	0.14

Table A.1: Downwind Explained Variance

Release Config.	Wind Speed (cm/s)	Feature	count	duration	amplitude	ibi
Freestream	5	count	1.00	0.74	0.79	−0.91
		duration	0.74	1.00	0.69	−0.68
		amplitude	0.79	0.69	1.00	−0.59
		ibi	−0.91	−0.68	−0.59	1.00
	10	count	1.00	0.48	0.79	−0.98
		duration	0.48	1.00	0.77	−0.54
		amplitude	0.79	0.77	1.00	−0.77
		ibi	−0.98	−0.54	−0.77	1.00
	20	count	1.00	−0.72	0.83	−0.99
		duration	−0.72	1.00	−0.35	0.62
		amplitude	0.83	−0.35	1.00	−0.84
		ibi	−0.99	0.62	−0.84	1.00
Near-bed	10	count	1.00	−0.95	−0.66	−0.91
		duration	−0.95	1.00	0.71	0.76
		amplitude	−0.66	0.71	1.00	0.52
		ibi	−0.91	0.76	0.52	1.00

Table A.2: Downwind Feature Covariance Table

Release Config.	Wind Speed (cm/s)	Component	count	duration	amplitude	ibi
Freestream	5	PC1	−0.54	−0.48	−0.48	0.50
		PC2	0.21	−0.24	−0.68	−0.66
		PC3	0.28	−0.84	0.46	−0.08
		PC4	−0.77	−0.03	0.31	−0.56
	10	PC1	−0.52	−0.43	−0.52	0.52
		PC2	−0.46	0.76	0.23	0.40
		PC3	−0.06	−0.46	0.80	0.36
		PC4	0.72	0.14	−0.17	0.66
	20	PC1	−0.55	0.41	−0.48	0.54
		PC2	0.01	−0.82	−0.56	0.13
		PC3	0.29	0.38	−0.67	−0.57
		PC4	−0.78	−0.16	0.08	−0.60
Near-bed	10	PC1	−0.54	0.53	0.43	0.49
		PC2	−0.23	−0.03	−0.83	0.51
		PC3	0.17	−0.69	0.36	0.61
		PC4	−0.79	−0.50	0.02	−0.35

Table A.3: Downwind Feature Loading Table

A.6 CROSSWIND PCA TABLES

The following three tables accompany the crosswind PCA results. Table A.4 shows the explained variance per component for each release configuration; PC1 captures between 58% and 80% of variance, with the remaining components accounting for progressively less structure. Table A.5 gives the pairwise Pearson correlations between bout features in the crosswind dimension, and table A.6 lists the corresponding feature loadings for each component and release configuration.

Release Config.	Wind Speed (cm/s)	PC1 (%)	PC2 (%)	PC3 (%)	PC4 (%)
Freestream	5	74.41	16.30	6.12	3.18
	10	57.81	31.93	7.48	2.78
	20	79.61	16.17	3.07	1.15
Near-bed	10	68.88	27.04	3.59	0.50

Table A.4: Crosswind Explained Variance

Release Config.	Wind Speed (cm/s)	Feature	count	duration	amplitude	ibi
Freestream	5	count	1.00	0.70	0.64	−0.84
		duration	0.70	1.00	0.75	−0.57
		amplitude	0.64	0.75	1.00	−0.45
		ibi	−0.84	−0.57	−0.45	1.00
	10	count	1.00	0.10	0.62	−0.84
		duration	0.10	1.00	0.54	0.08
		amplitude	0.62	0.54	1.00	−0.38
		ibi	−0.84	0.08	−0.38	1.00
	20	count	1.00	−0.91	0.63	−0.92
		duration	−0.91	1.00	−0.53	0.87
		amplitude	0.63	−0.53	1.00	−0.43
		ibi	−0.92	0.87	−0.43	1.00
Near-bed	10	count	1.00	−0.89	−0.19	−0.92
		duration	−0.89	1.00	0.46	0.70
		amplitude	−0.19	0.46	1.00	−0.04
		ibi	−0.92	0.70	−0.04	1.00

Table A.5: Crosswind Feature Covariance Table

Release Config.	Wind Speed (cm/s)	Component	count	duration	amplitude	ibi
Freestream	5	PC1	−0.54	−0.51	−0.47	0.48
		PC2	0.31	−0.37	−0.60	−0.64
		PC3	0.19	−0.78	0.60	−0.02
		PC4	−0.76	0.01	0.24	−0.60
	10	PC1	−0.61	−0.24	−0.54	0.53
		PC2	0.24	−0.78	−0.37	−0.45
		PC3	−0.02	0.58	−0.68	−0.45
		PC4	−0.75	−0.07	0.33	−0.56
	20	PC1	−0.55	0.53	−0.39	0.52
		PC2	0.07	−0.21	−0.90	−0.38
		PC3	−0.17	−0.80	−0.08	0.58
		PC4	−0.81	−0.21	0.20	−0.50
Near-bed	10	PC1	−0.59	0.57	0.20	0.53
		PC2	−0.14	−0.19	−0.90	0.38
		PC3	0.01	−0.70	0.40	0.60
		PC4	−0.79	−0.40	0.01	−0.46

Table A.6: Crosswind Feature Loading Table

A.7 FULL PLUME PCA TABLES

The following three tables accompany the full-plume PCA results, in which bout statistics were pooled across both the downwind and crosswind sampling dimensions. Table A.7 shows the explained variance per component, table A.8 the pairwise feature correlations, and table A.9 the PC feature loadings, each reported separately for every release configuration.

Release Config.	Wind Speed (cm/s)	PC1 (%)	PC2 (%)	PC3 (%)	PC4 (%)
Freestream	5	74.52	16.99	5.84	2.65
	10	56.07	32.77	7.99	3.17
	20	79.13	16.36	3.20	1.31
Near-bed	10	69.35	26.94	3.23	0.49

Table A.7: Full Plume Explained Variance

Release Config.	Wind Speed (cm/s)	Feature	count	duration	amplitude	ibi
Freestream	5	count	1.00	0.75	0.65	−0.84
		duration	0.75	1.00	0.75	−0.53
		amplitude	0.65	0.75	1.00	−0.42
		ibi	−0.84	−0.53	−0.42	1.00
	10	count	1.00	−0.03	0.59	−0.83
		duration	−0.03	1.00	0.47	0.14
		amplitude	0.59	0.47	1.00	−0.39
		ibi	−0.83	0.14	−0.39	1.00
	20	count	1.00	−0.91	0.59	−0.92
		duration	−0.91	1.00	−0.52	0.87
		amplitude	0.59	−0.52	1.00	−0.42
		ibi	−0.92	0.87	−0.42	1.00
Near-bed	10	count	1.00	−0.89	−0.23	−0.92
		duration	−0.89	1.00	0.52	0.69
		amplitude	−0.23	0.52	1.00	−0.01
		ibi	−0.92	0.69	−0.01	1.00

Table A.8: Full Plume Feature Covariance Table

Release Config.	Wind Speed (cm/s)	Component	count	duration	amplitude	ibi
Freestream	5	PC1	−0.54	−0.51	−0.47	0.47
		PC2	0.27	−0.36	−0.59	−0.67
		PC3	0.00	−0.75	0.64	−0.17
		PC4	−0.79	0.23	0.12	−0.55
	10	PC1	−0.63	−0.12	−0.52	0.57
		PC2	0.19	−0.81	−0.43	−0.35
		PC3	0.00	0.56	−0.67	−0.49
		PC4	−0.76	−0.10	0.32	−0.56
	20	PC1	−0.55	0.53	−0.38	0.52
		PC2	0.10	−0.19	−0.91	−0.36
		PC3	−0.18	−0.80	−0.08	0.56
		PC4	−0.81	−0.20	0.16	−0.53
Near-bed	10	PC1	−0.59	0.57	0.24	0.52
		PC2	−0.17	−0.19	−0.87	0.42
		PC3	0.02	−0.70	0.43	0.58
		PC4	−0.79	−0.40	0.01	−0.47

Table A.9: Full Plume Feature Loading Table

A.8 WIND SPEED PCA TABLES

The following three tables accompany the wind-speed-compensated PCA, in which bout statistics were normalised by freestream wind speed prior to dimensionality reduction. Table A.10 shows the explained variance per component, table A.11 the pairwise feature correlations, and table A.12 the PC feature loadings for each release configuration.

PC1 (%)	PC2 (%)	PC3 (%)	PC4 (%)
62.96	22.94	12.24	1.86

Table A.10: Wind Speed Explained Variance

Feature	count	duration	amplitude	ibi
count	1.00	−0.67	0.60	−0.76
duration	−0.67	1.00	−0.11	0.30
amplitude	0.60	−0.11	1.00	−0.47
ibi	−0.76	0.30	−0.47	1.00

Table A.11: Wind speed Feature Covariance Table

Component	count	duration	amplitude	ibi
PC1	−0.61	0.41	−0.43	0.52
PC2	0.10	−0.76	−0.61	0.20
PC3	0.00	0.29	−0.61	−0.74
PC4	−0.78	−0.42	0.26	−0.38

Table A.12: Wind speed Feature Loading Table

A.9 SAMPLE DURATION REGRESSION TABLE

Tables A.13 and A.14 report linear regression fits of bout statistics against sample duration at each sampled downwind position, for all release configurations. Four statistics are reported at each position: the mean bout count (μ count), the standard deviation of bout count (σ count), the mean bout frequency (μ count/duration), and its standard deviation (σ count/duration). Mean bout count increases linearly with sample duration ($R^2 \approx 1.0$), as expected since longer recordings accumulate more events. The standard deviation of bout count also shows a strong positive relationship with sample duration ($R^2 \geq 0.97$), reflecting the dependence of count variability on recording length. By contrast, the mean bout frequency (count normalised by duration) shows near-zero R^2 (≈ 0.36) and negligible regression coefficients, confirming that it is essentially independent of sample duration and therefore a stable, duration-robust measure of plume encounter rate.

Release Config.	Wind Speed (cm/s)	Statistic	x (cm)	Coefficient	Intercept	MSE	R^2
Freestream	5	μ count	3.33	0.56802450	0.00536756	0.00003300	0.99999998
			7.10	0.42821733	0.00404645	0.00001875	0.99999998
			10.95	0.30692766	0.00290032	0.00000963	0.99999998
			14.80	0.16758343	0.00158358	0.00000287	0.99999998
			18.65	0.11203091	0.00105864	0.00000128	0.99999998
		σ count	3.33	0.61660822	-0.74381576	0.02765349	0.97784300
			7.10	0.49187144	-0.72224371	0.00346835	0.99555374
			10.95	0.58121539	-0.92080913	0.02083981	0.98114344
			14.80	0.52894461	-1.03091610	0.00254736	0.99717154
			18.65	0.50865001	-1.19836049	0.00133179	0.99839892
		μ count / dur.	3.33	-0.00039606	0.57000774	0.00000088	0.36495919
			7.10	-0.00029858	0.42971243	0.00000050	0.36495919
			10.95	-0.00021401	0.30799929	0.00000026	0.36495919
			14.80	-0.00011685	0.16816854	0.00000008	0.36495919
			18.65	-0.00007812	0.11242206	0.00000003	0.36495919
		σ count / dur.	3.33	-0.38339178	-0.74381576	0.02765349	0.94463457
			7.10	-0.50812856	-0.72224371	0.00346835	0.99583253
			10.95	-0.41878461	-0.92080913	0.02083981	0.96430264
			14.80	-0.47105539	-1.03091610	0.00254736	0.99643626
			18.65	-0.49134999	-1.19836049	0.00133179	0.99828439
	10	μ count	4.29	0.67621303	0.00638989	0.00004677	0.99999998
			9.84	0.67287988	0.00635839	0.00004631	0.99999998
			15.47	0.56955219	0.00538200	0.00003318	0.99999998
			21.02	0.46580786	0.00440166	0.00002219	0.99999998
			26.64	0.38622888	0.00364968	0.00001526	0.99999998
		σ count	4.29	0.47788501	-0.64664353	0.00257763	0.99649604
			9.84	0.47026463	-0.60213055	0.00450143	0.99369869
			15.47	0.52233471	-0.61038419	0.00408330	0.99535908
			21.02	0.49349927	-0.65942813	0.00361775	0.99539351
			26.64	0.50477953	-0.76355258	0.00581282	0.99294304
		μ count / dur.	4.29	-0.00047150	0.67857400	0.00000124	0.36495919
			9.84	-0.00046917	0.67522921	0.00000123	0.36495919
			15.47	-0.00039713	0.57154076	0.00000088	0.36495919
			21.02	-0.00032479	0.46743422	0.00000059	0.36495919
			26.64	-0.00026930	0.38757739	0.00000041	0.36495919
		σ count / dur.	4.29	-0.52211499	-0.64664353	0.00257763	0.99706288
			9.84	-0.52973537	-0.60213055	0.00450143	0.99502746
			15.47	-0.47766529	-0.61038419	0.00408330	0.99445553
			21.02	-0.50650073	-0.65942813	0.00361775	0.99562594
			26.64	-0.49522047	-0.76355258	0.00581282	0.99266999

Table A.13: Sample Duration Regression Table

Release Config.	Wind Speed (cm/s)	Statistic	x (cm)	Coefficient	Intercept	MSE	R^2
Freestream	10	μ count	6.96	1.09077369	0.01030729	0.00012169	0.99999998
			12.65	1.02494396	0.00968523	0.00010744	0.99999998
			18.43	0.95578107	0.00903168	0.00009343	0.99999998
			24.12	0.85495325	0.00807890	0.00007476	0.99999998
			29.90	0.79328996	0.00749621	0.00006436	0.99999998
		σ count	6.96	0.49655378	-0.59838899	0.00716574	0.99102727
			12.65	0.51019411	-0.60919386	0.01063072	0.98743648
			18.43	0.46788280	-0.56479791	0.00323386	0.99541897
			24.12	0.45575541	-0.53484947	0.00854057	0.98735247
			29.90	0.33571232	-0.40538375	0.03322777	0.91587711
		μ count / dur.	6.96	-0.00076056	1.09458209	0.00000323	0.36495919
			12.65	-0.00071466	1.02852252	0.00000285	0.36495919
			18.43	-0.00066643	0.95911815	0.00000248	0.36495919
			24.12	-0.00059613	0.85793829	0.00000198	0.36495919
			29.90	-0.00055313	0.79605970	0.00000171	0.36495919
		σ count / dur.	6.96	-0.50344622	-0.59838899	0.00716574	0.99126914
			12.65	-0.48980589	-0.60919386	0.01063072	0.98638333
			18.43	-0.53211720	-0.56479791	0.00323386	0.99645453
			24.12	-0.54424459	-0.53484947	0.00854057	0.99109723
			29.90	-0.66428768	-0.40538375	0.03322777	0.97707925
Near-bed	10	μ count	1.78	0.72996009	0.00689778	0.00005450	0.99999998
			8.81	0.70121166	0.00662612	0.00005029	0.99999998
			15.84	0.73537646	0.00694896	0.00005531	0.99999998
			22.87	0.76412489	0.00722062	0.00005972	0.99999998
			29.97	0.80203948	0.00757889	0.00006579	0.99999998
		σ count	1.78	0.49729532	-0.59957295	0.00226858	0.99715031
			8.81	0.53553815	-0.62801603	0.00578253	0.99375793
			15.84	0.49433870	-0.60059621	0.00464433	0.99411400
			22.87	0.48681955	-0.65768247	0.00905289	0.98823955
			29.97	0.49695872	-0.64995815	0.01083351	0.98651831
		μ count / dur.	1.78	-0.00050897	0.73250872	0.00000145	0.36495919
			8.81	-0.00048893	0.70365992	0.00000134	0.36495919
			15.84	-0.00051275	0.73794400	0.00000147	0.36495919
			22.87	-0.00053280	0.76679280	0.00000159	0.36495919
			29.97	-0.00055923	0.80483977	0.00000175	0.36495919
		σ count / dur.	1.78	-0.50270468	-0.59957295	0.00226858	0.99721114
			8.81	-0.46446185	-0.62801603	0.00578253	0.99171835
			15.84	-0.50566130	-0.60059621	0.00464433	0.99437317
			22.87	-0.51318045	-0.65768247	0.00905289	0.98940426
			29.97	-0.50304128	-0.64995815	0.01083351	0.98683811

Table A.14: Sample Duration Regression Table Continued

B

APPENDIX 2

B.1 SCENARIO A: AGENTS POSITION INITIALIZED AT DOWNWIND EXTENT

As in section 4.6, we outline the two scenarios designed to compare the performance of navigation strategies. Scenario A saw 196 agents navigate from the downwind edge of the test section with a generous time limit of $10x$ the dataset length or $2400s$. To determine the optimal parameters for each navigation strategy and for each release configuration for Scenario A, we initially explored the performance of the agents in terms of the percentage of successful agents and the time it took for the successful agents to reach the goal whilst maintaining a fixed random seed (responsible for random walking choices only). In this supplementary section we show the initial parameter search results used to select the parameter used in section 4.7.

We tested 31 values of odour detection threshold (θ_c) between 1.000×10^{-3} and 1.0 evenly spaced on a log scale. For the odour direction sensing (DS+) agents, we show the θ_c range for the correlation threshold (θ_ρ) with the best performance (highest agent success percentage and lowest success time). The full parameter search is plotted in fig. B.2 and select values are shown in table B.1. In fig. B.1, we plot the average percentage of agents that successfully navigated to the goal (with minimums and maximums as transparent) and the average time of the successful agents over a range of θ_c for the three navigation strategies and for each trial of each release configuration.

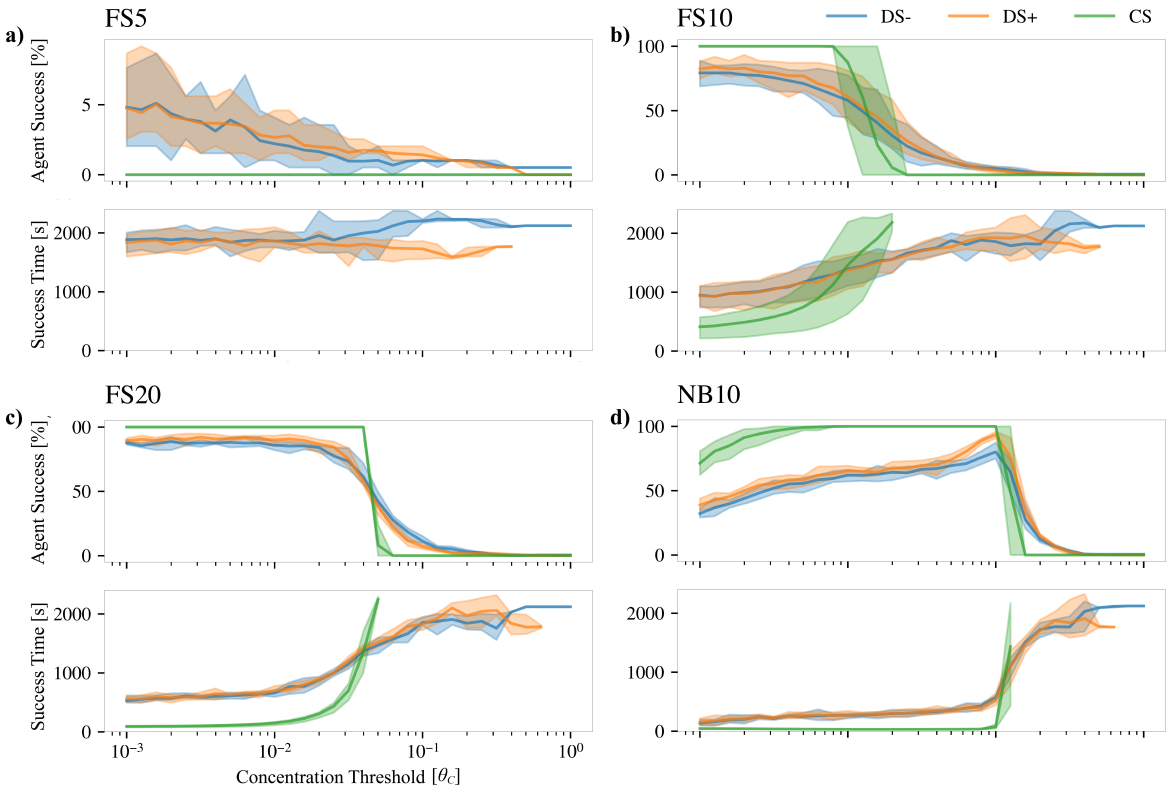

Figure B.1: Scenario A: Navigation Strategy Performance Analysis. **a-d** are the four release configurations with each showing the average performance in all trials of the release configuration. The top panel of each shows the agent success percentage and the bottom panel show the success times, both for each of the 31 concentration threshold values (θ_c). The non odour direction sensing strategy (DS-) is plotted as blue line, the direction sensing (DS+) in orange and cast-and-surge (CS) in green. The mean values are plotted as a line with the minimum and maximum values are plotted as transparent. Points in which the success percentage reached 0% are not plotted in the success time plots.

We saw that for every odour release configuration, the performance of the agents decreased non-linearly with increasing odour concentration threshold θ_c. The DS+ marginally outperformed the DS- strategy in all release configurations. The performance of the cast-and-surge agents was significantly impacted by the release configuration, with zero percent success in fig. B.1 **a** throughout the tested θ_c range. Conversely, the cast-and-surge strategy achieved 100% success below a release configuration-specific θ_c threshold for the $10cm/s$ and $20cm/s$ freestream odour release configurations and showed only an improvement in success time with decreasing θ_c. In fig. B.1 **b** and **c**, DS+ and DS- success% the curves follow an inverse sigmoid curve with cast-and-surge following the same trend with an increased slope, lower midpoint and increased peak performance. On average, we saw that with decreasing performance, the time taken by the successful agents to reach the goal increased. However, the DS+ curve in fig. B.1 **a** showed an area in which agents success time was lower than at the peak success percentage, we consider this an artefact produced from sampling of fewer successful agents. The average percentage and the point below which the agent performance

peaked increased with greater wind speed across the freestream datasets, with the minimum times for the successful agents to reach the goal decreasing with greater wind speed and with increasing percentage of successful agents. The near-bed release configuration saw a different success percentage and time trend for the three tested strategies. Agent performance for DS+ and DS- strategies increased non-linearly and peaked before falling with decreasing θ_c, while the cast-and-surge agent success% also peaked after increasing from a lower θ_c value with a steeper gradient remained at 100% for a greater θ_c range and only decreased at much lower values of θ_c. The minimum average success time for successful agents did not coincide with the maximum percentage of successful DS- and DS+ agents. This suggests that in the near-bed datasets the agents that most efficiently navigated to the goal were not the most reliable agents to do so. From these initial results we surmise that agents utilizing the three navigation strategies in the freestream benefited most from being sensitive to the presence of odour and those in the near-bed plume required specifically tuned odour sensitivity to most reliably navigate to the source. Although the most sensitive agents still most efficiently navigated to the odour source.

Figure B.2 shows the results of the DS+ agent parameter search in which we explored both the 31 values of odour concentration threshold θ_c and 31 values of the odour correlation threshold both between 1.000×10^{-3} and 1.000 evenly spaced on a log scale for a total of 961 combinations for each trial. We show the mean percentage of the 196 agents that successfully navigated to the goal and the mean time of all successful agents across each trial and release configuration.

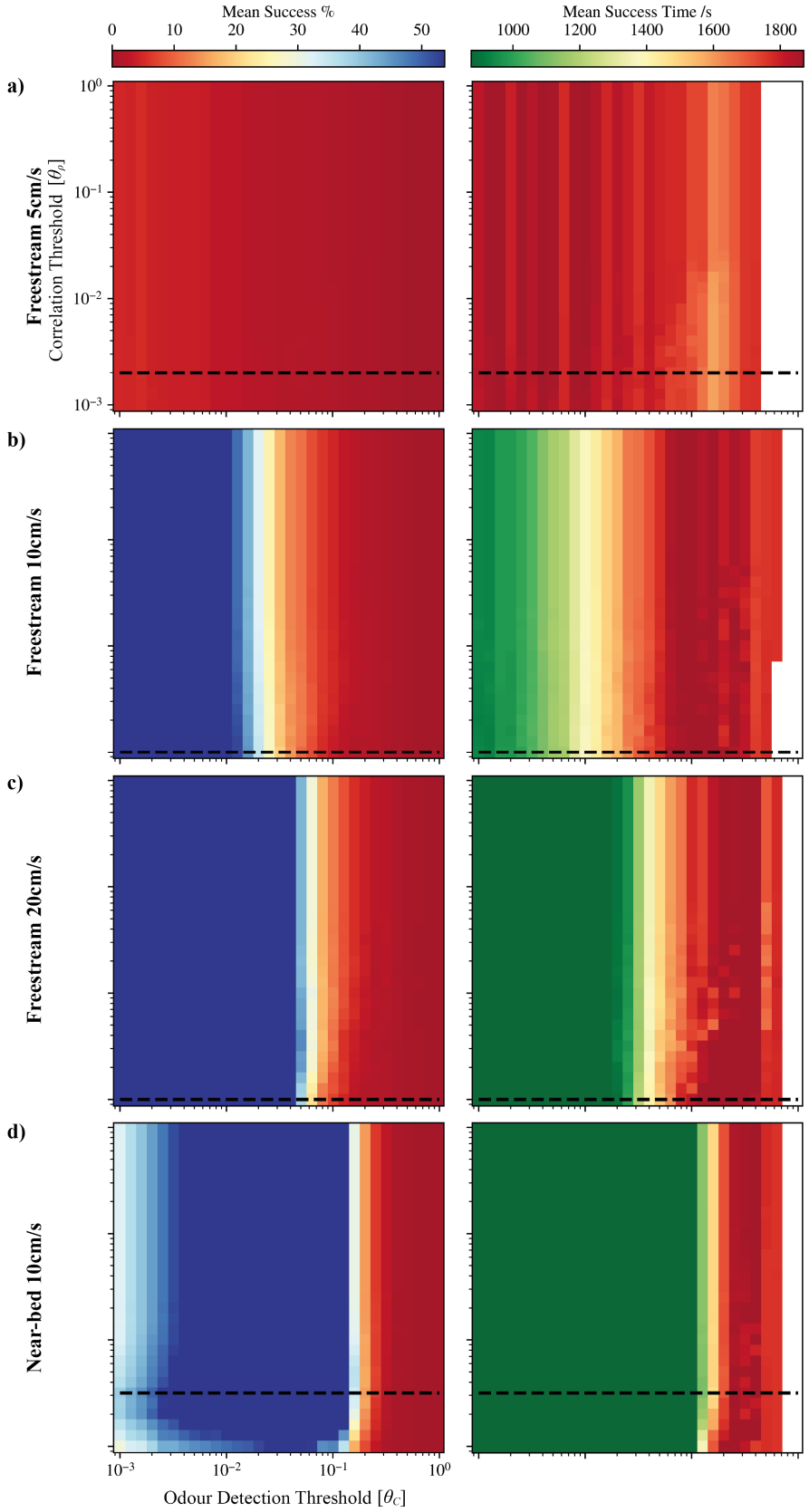

Figure B.2: Scenario A: DS+ Parameter Search. Each row is the release configuration dataset the navigation simulations where performed upon. The left side shows the mean success % of agents for each of pair of DS+ parameters with the colour map ranging between 0% and 53.7%. The right side shows mean success time with colour map between 874.9s and 1870.1s. Areas in which no agents successfully navigated to the goal remained white in the mean success time plots. The black dotted line shows an intersection with the selected best performing parameter pair plotted in fig. B.1.

In section 4.7.1, we use the selected best performing agent parameters for further analysis of Scenario A agent performance. To select these parameters we primarily sorted by the highest mean agent success percentage θ_c and secondly by the lowest average success time. We outline these parameters in following table B.1.

Release Conf.	Wind Speed (cm/s)	Strategy	θ_c	θ_ρ
Freestream	5	DS-	1.585×10^{-3}	–
		DS+	1.585×10^{-3}	1.995×10^{-3}
		CS	1.000×10^{-3}	–
	10	DS-	1.000×10^{-3}	–
		DS+	1.259×10^{-3}	1.000×10^{-3}
		CS	1.000×10^{-3}	–
	20	DS-	1.995×10^{-3}	–
		DS+	3.162×10^{-3}	1.000×10^{-3}
		CS	1.000×10^{-3}	–
Near-bed	10	DS-	1.000×10^{-1}	–
		DS+	1.000×10^{-1}	3.162×10^{-3}
		CS	1.585×10^{-2}	–

Table B.1: Scenario A: Best performing agent parameters

B.2 SCENARIO B: AGENTS POSITION RANDOMLY INITIALIZED

For the initial parameter search, we fixed the random seeds responsible for the initial location of the agents and the random walking, and we tested a range of θ_c (and θ_ρ for DS+ agents) to find the best performing parameter configuration for each strategy and in each odour release configuration. over a range of θ_c.

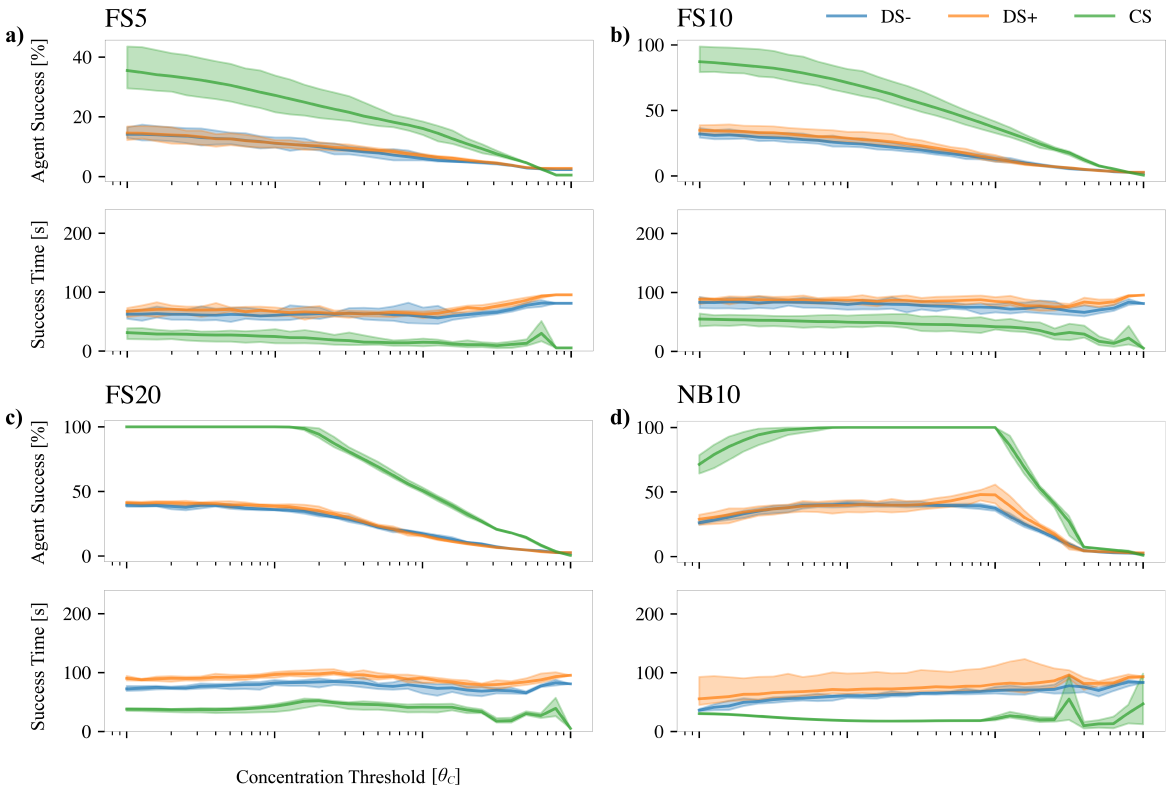

Figure B.3: Scenario B: Navigation Strategy Performance Analysis. **a-d** are the four release configurations with each showing the average performance in all trials of the release configuration. The top panel of each shows the agent success percentage and the bottom panel show the success times, both for each of the 31 concentration threshold values (θ_c). The non odour direction sensing strategy (DS-) is plotted as blue line, the direction sensing (DS+) in orange and cast-and-surge (CS) in green. The mean values are plotted as a line with the minimum and maximum values are plotted as transparent. Areas in which the success percentage reached 0% are not plotted in the success time plots.

Figure B.3 shows that with the time limitation we saw a significant decrease in the overall percentage of successful agents, but with the randomized initial positions we also saw that the cast-and-surge agents show a significant increase in success in the freestream $5cm/s$ dataset. For all freestream datasets, the overall performance of all agent strategies showed an inverse correlation with θ_c within the tested range. The cast-and-surge strategy outperforms all other strategies with higher percentage of successful agents and lower time to goal on average. The near-bed dataset again showed the best performance between within the range $0.008 > \theta_c > 0.02$ with a significant and sudden decrease in performance for $\theta_c > 0.02$ and a slow decrease in performance $\theta_c < 0.008$.

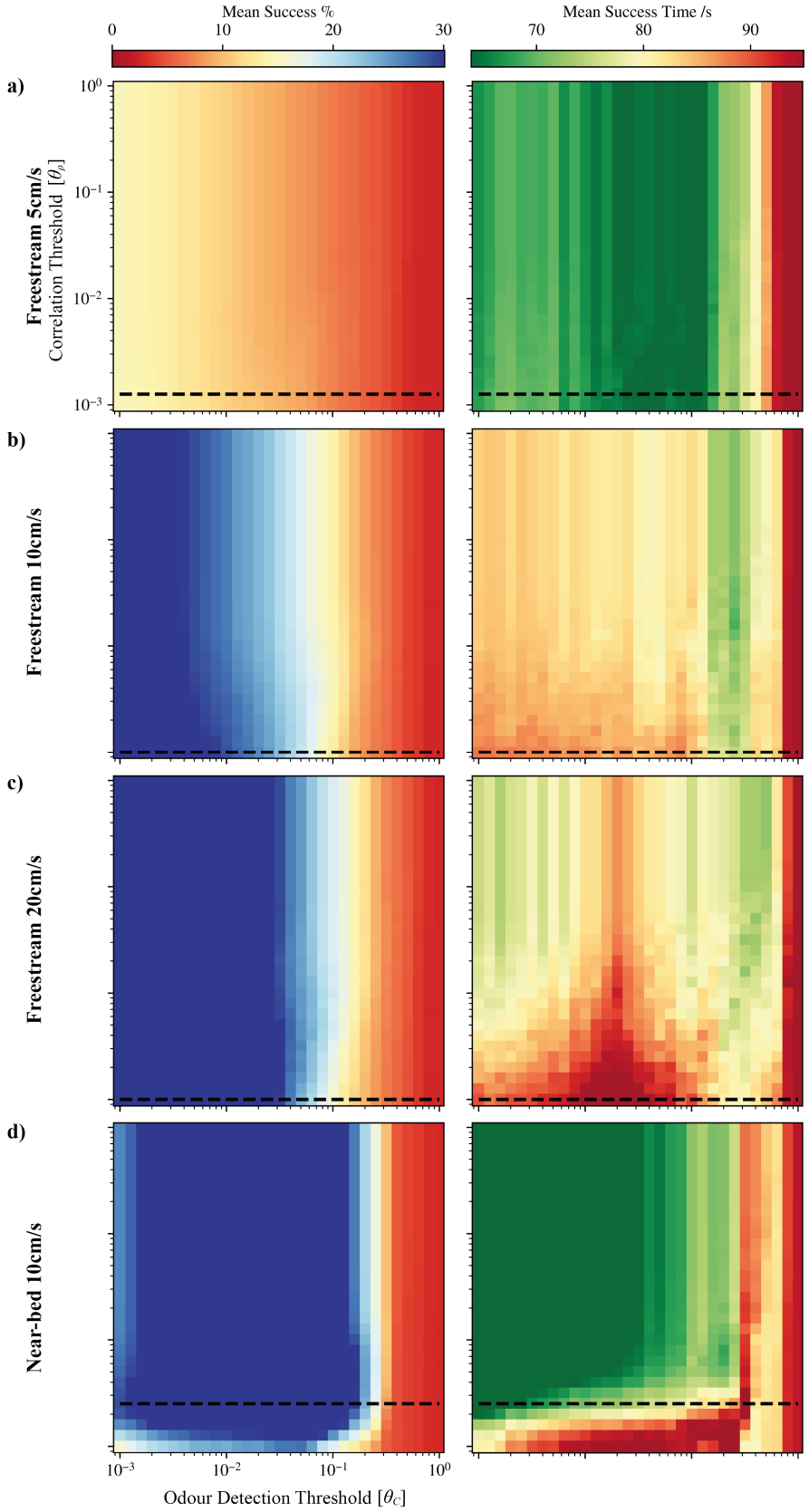

Figure B.4: Scenario B: DS+ Parameter Search. Each row is the release configuration dataset the navigation simulations where performed upon. The left side shows the mean success % of agents for each of pair of DS+ parameters with the colour map ranging between 0% and 30.1%. The right side shows mean success time with colour map between 63.9s and 95.0s. Areas in which no agents successfully navigated to the goal remained white in the mean success time plots. The black dotted line shows an intersection with the selected best performing parameter pair plotted in fig. B.3.

Figure B.4 shows that the tested range of correlation threshold had much less of an impact on agent performance than the odour detection threshold. The DS+ agents in the freestream datasets generally performed best with very low correlation thresholds where most impact was seen in the success time. They marginally benefited from a slightly higher threshold in the $5cm/s$ wind speed and the near-bed release configurations.

The best performing parameters of each strategy for each release configuration are outlined in table B.2.

Release Conf.	Wind Speed (cm/s)	Strategy	θ_c	θ_ρ
Freestream	5	DS-	1.000×10^{-3}	–
		DS+	1.000×10^{-3}	1.259×10^{-3}
		CS	1.000×10^{-3}	–
	10	DS-	1.000×10^{-3}	–
		DS+	1.000×10^{-3}	1.000×10^{-3}
		CS	1.000×10^{-3}	–
	20	DS-	1.000×10^{-3}	–
		DS+	1.995×10^{-3}	1.000×10^{-3}
		CS	1.585×10^{-3}	–
Near-bed	10	DS-	1.000×10^{-2}	–
		DS+	7.943×10^{-2}	2.512×10^{-3}
		CS	7.943×10^{-2}	–

Table B.2: Scenario B: Best performing agent parameters

B.3 VALIDATION OF PARAMETER SELECTION

We selected the agent performance metrics of percentage of successful agents and the average success time with the intention of simplifying the overall analysis of the strategies under varying odour release configurations. Although having using such metrics as a method of initially selecting parameters for the extended random comparison used to generate the plots for the results section, for each strategy under each of the release configuration, it is possible that we have introduced a bias. In this section, we aim to address this potential issue by way of validation.

Here we explore the results of a grid search of release configuration and concentration threshold for the DS- and CS strategies and both concentration and correlations threshold for the DS+ strategy. For both concentration threshold and correlation threshold we select five log-spaced values including and between 1.0 and 0.001. For each Scenario and release configuration dataset, we conduct five repeats of each trial and randomize seed responsible

for turning, as well as turning back (CS strategy) and initial position (Scenario B) where applicable. This limited number of search values for the threshold was necessary with the multiplicative increase in simulations required compared to appendix B.2) and (section 4.7.1 due to the introduction of random seed repeats of each trial and dataset.

As in the initial parameter search (appendix B.1 and appendix B.2), and in results (section 4.7.1 and section 4.7.2), Scenario A agents had 196 agents, had $10x$ the trial time of $240s$ and were initially positioned at the downwind extent of the test section. Scenario B has 1000 agents and had $240s$ to locate the goal with initial positions randomly placed within the test section.

For each scenario, release configuration and threshold, we plot the overall average success percentage and goal times for successful agents. By conducting this further grid search, we aimed to remove any doubt that selecting only the best performing parameters for randomised comparison introduced bias that skewed the latter results. In doing so, we also hope to gain a better understanding of the parameter space of the performance of agents when randomising the seed of the random aspects of the simulations.

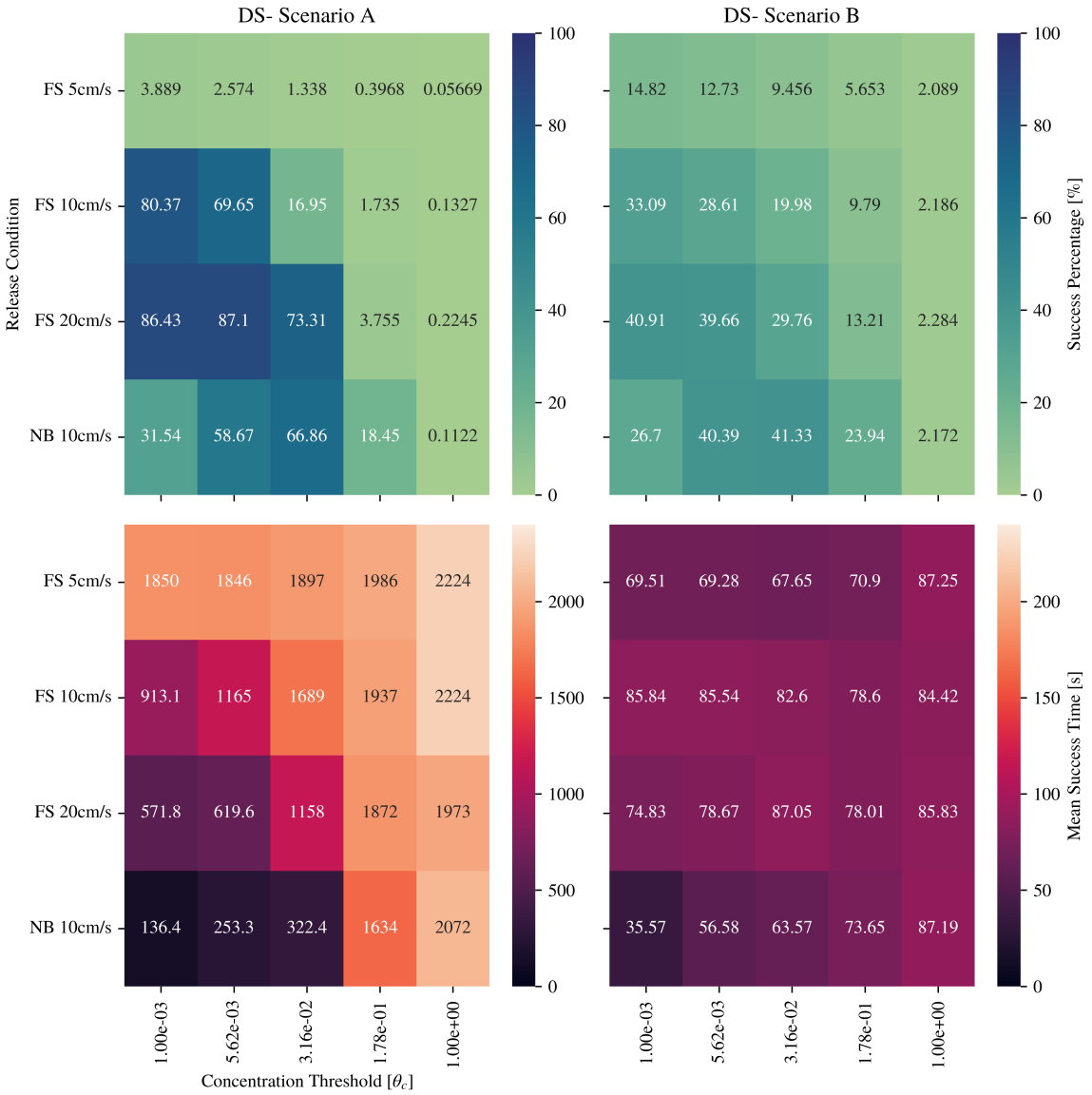

Figure B.5: Validation Parameter Search for DS- showing success percentage (top panels) and mean success times (bottom panels) for Scenario A (left panels) and Scenario B (right panels). Each panel is divided into the four release conditions (y-axis) and the five explored concentration thresholds θ_C (x-axis).

In fig. B.5, we plot the validation grid search results for the DS- strategy. From this we can see that Scenario A saw higher percentages of successful agents than Scenario B, with the greater success generally occurring where concentration threshold was low. The $10cm/s$ freestream performed best with the lowest value, $20cm/s$ with the second lowest and the near-bed release configuration performed best with the middle value but generally better on the lower side. This pattern of success percentage is completely mirrored by Scenario B but with significantly lower maximum values. Overall, the highest value of concentration threshold performed the worst in terms of success percentage and mean success times. The Scenario A $5cm/s$ freestream dataset saw the lowest success percentages overall, due

to the limited downwind extent of the detectable plume, as seen throughout. For $5cm/s$, Scenario B generally out performed the best of Scenario A results undoubtedly because of the randomized initial positions.

In Scenario A $20cm/s$ freestream saw the greatest success percentage, with a concentration threshold of 5.620×10^{-3} or 87.1% the second best percentage of 86.43% showed a significantly lower mean success time of $571.8s$ compared to $619.6s$. Overall, we see a decrease in mean success time with decreased concentration threshold, this suggests that even in instances of decreased success percentage, a lower concentration threshold led to more efficient navigation with the trade off of being less robust.

For Scenario B, overall we saw the same trend in success times, with significantly shorter success times due to the time limitation. For both Scenarios, the near-bed release configuration saw the lowest mean success times. This can be attributed to the overall ease of odour encounter with the more laterally spread detectable plume.

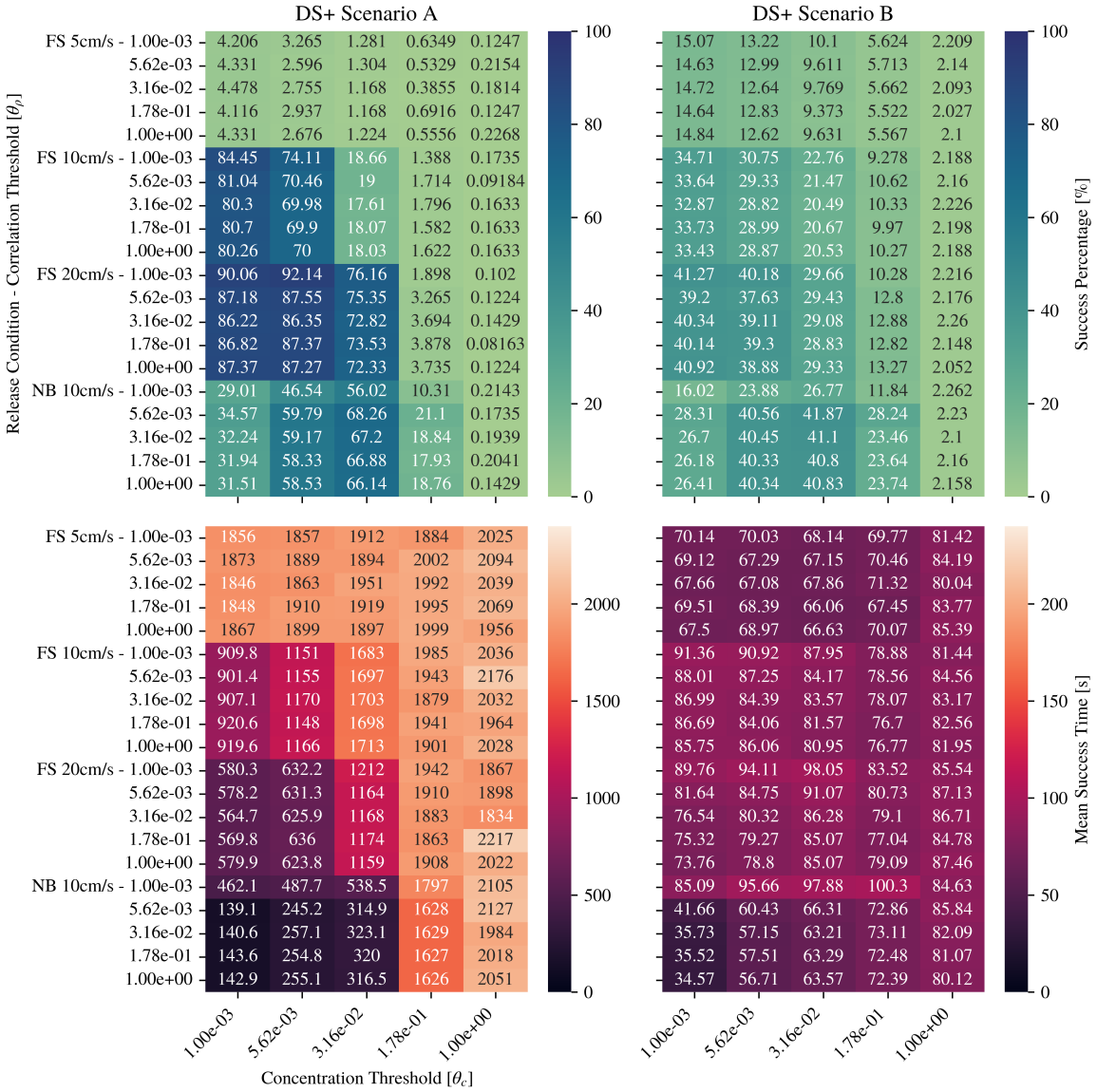

Figure B.6: Validation Parameter Search for DS+ showing success percentage (top panels) and mean success times (bottom panels) for Scenario A (left panels) and Scenario B (right panels). Each panel is divided into the four release conditions, subdivided by the five explored correlation thresholds θ_ρ (y-axis) and the five explored concentration thresholds θ_C (x-axis).

Figure B.6 shows the grid search results for the DS+ strategy in which we explored both the concentration and the correlation threshold for each release configuration and scenario. As in fig. B.5 for the freestream datasets, the lowest θ_C achieved the highest success percentage for $5cm/s$ and $10cm/s$, the lowest for Scenario B and the second lowest for Scenario A. For the near-bed release configuration 3.160×10^{-2} performed best for both scenarios. Generally, for both freestream and near-bed, we saw that the success time was positively correlated with the θ_C and with the correlation threshold θ_ρ but had a much less significant impact.

Overall, fig. B.6 shows that DS+ achieved marginally higher success percentages than DS- in fig. B.5 with marginally slower success times caused by the plume centre line tracking behaviour explored in fig. 4.7 and fig. 4.11.

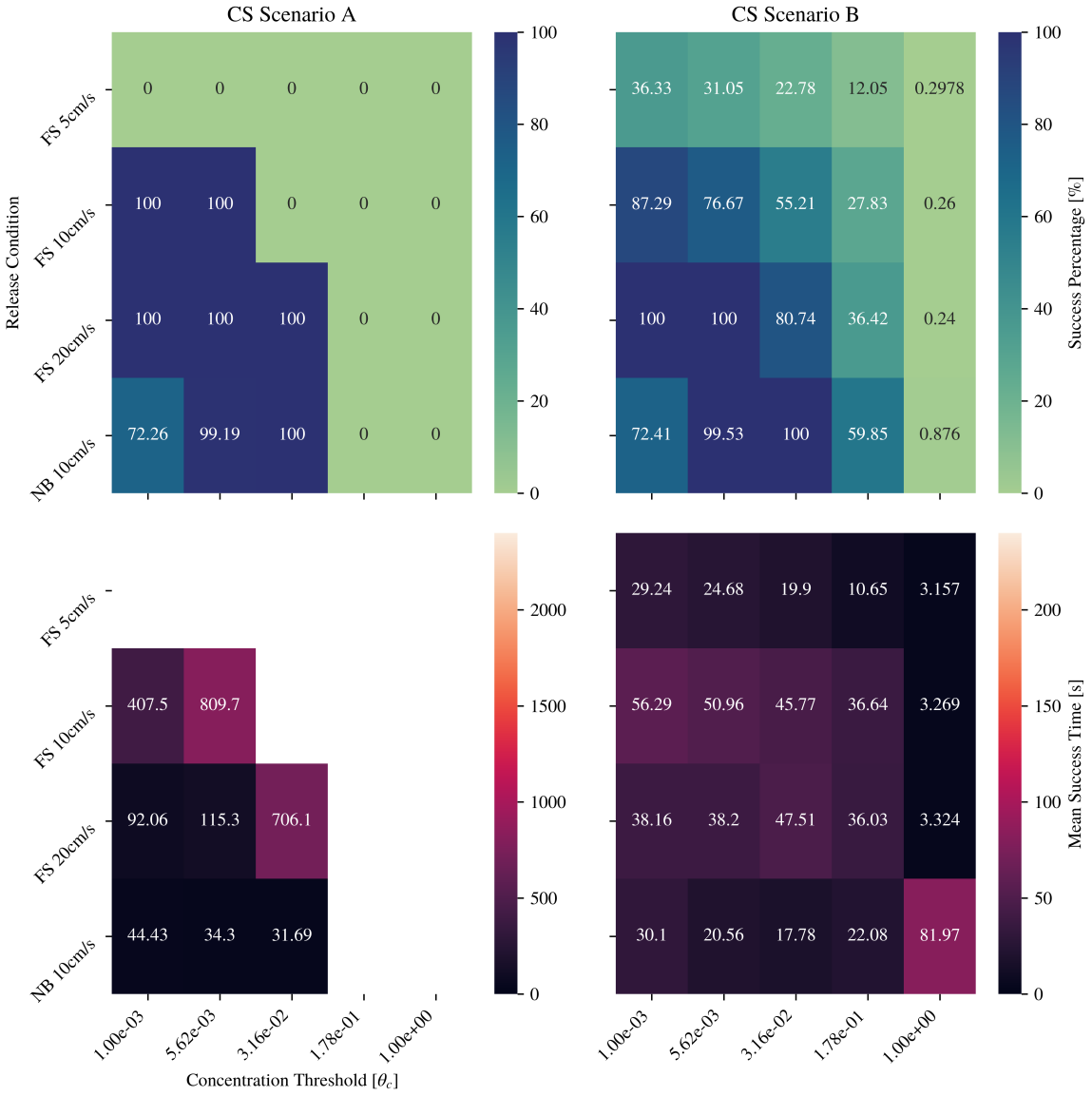

Figure B.7: Validation Parameter Search for CS showing success percentage (top panels) and mean success times (bottom panels) for Scenario A (left panels) and Scenario B (right panels). Each panel is divided into the four release conditions (y-axis) and the five explored concentration thresholds θ_C (x-axis).

For the CS strategy, fig. B.7 shows in the freestream datasets and for both scenarios, the success percentage was negatively correlated with θ_C and θ_C was positively correlated with mean success time. In the near-bed the best performing θ_C was with 3.160×10^{-2} with lower values performing better than higher values. As in fig. 4.8 and appendix B.1, in Scenario A the CS strategy saw 0% success in the $5cm/s$% freestream dataset, due to the limited

downwind extent of the plume and the downwind initialisation of the agent. The CS strategy saw significantly 6 configurations of Scenario A with perfect 100% success percentage and 3 in Scenario B. This strongly suggests that when the cast surge agents detect the plume they show robust navigation to the source within a reasonable time limit. As previously suggest this can be attributed the efficiency of the casting behaviour in response to not detecting the plume and is bolstered by the random turn back behaviour.

The validation simulations support the claims made in the section 4.7 and show that the best performing parameters selected from $6x$ high parameter resolution search shown in appendix B.1 and appendix B.2 do not appear to be biased and only marginally outperform the results demonstrated here.

C

APPENDIX 3

C.1 ADDENDUM: DO THE PLIF ACETONE VAPOUR PLUMES (CONNOR, MCHUGH AND J. P. CRIMALDI, 2018) DISSIPATE TOO QUICKLY IN THE TEST SECTION? - A LAB REPORT

C.1.1 *Gaussian Model*

We investigate why the PLIF plumes from Connor, McHugh and J. P. Crimaldi (2018) appear to dissipate too quickly as they travel through the test section, using a Gaussian plume model. Gaussian plume models are typically used for approximating a passive scalar quantity such as the temperature or concentration of a fluid passing through another fluid. Various factors impact scalar plumes. The Gaussian plume model we will apply is defined as:

$$C = \frac{\dot{M}}{4\pi D} Ei\left(\frac{x - {x_0}^2}{4\pi D}\right) \tag{C.1}$$

The two factors that affect the scalar quantity that we are modelling, odour concentration (C), are the source mass emission rate ($\dot{M}$) and the odour diffusivity (D). In this model, the values downwind of the odour source are approximated using an exponential integral Ei.

For non-zero values of x, this is defined as:

$$\mathrm{Ei}(x) = -\int_{-x}^{\infty} \frac{e^{-t}}{t}\, dt = \int_{-\infty}^{x} \frac{e^{t}}{t}\, dt. \tag{C.2}$$

C.1.2 *Odour Source*

The mass emission rate of the acetone at the odour source $\dot{M}$ is calculated by:

$$\dot{M} = \rho_{mixture} \cdot Q \tag{C.3}$$

where $\rho_{mixture}$ is the density of the odour helium-acetone mixture and Q describes the mass flux at the odour release tube orifice. It is defined by:

$$Q = u \cdot A \tag{C.4}$$

where u is the source release velocity and the area of the release tube orifice A.

We calculate A based on the tube diameter $d = 0.953 \times 10^{-2}\,\mathrm{m}$ and the following:

$$\begin{aligned} A &= \frac{\pi}{4} \cdot d^2 \\ &= 7.133 \times 10^{-5}\,\mathrm{m}^2 \end{aligned} \tag{C.5}$$

Connor, McHugh and J. P. Crimaldi (2018) state that a mixture of 41% helium and 59% air was used as a carrier gas for the acetone vapour for the PLIF experiments.

C.1.3 *Mixture Density*

In order to establish the density of the odour mixture $\rho_{mixture}$ for our model, we assume an ambient temperature of 20.000 °C, or 293.150 K and we use values of density for air, helium and acetone are taken from https://www.engineeringtoolbox.com/.

The density values are as follows:

$$\begin{aligned} \rho_{air} &= 0.986\,\mathrm{kg/m^3}, \\ \rho_{helium} &= 0.136\,\mathrm{kg/m^3}, \\ \rho_{acetone} &= 1.978\,\mathrm{kg/m^3} \end{aligned} \tag{C.6}$$

We use the Antoine Equation, named after the French chemist Louis-Camille Antoine who proposed the equation, to determine the apparent acetone vapour pressure. It is used to compute the vapour pressure of pure substances based on the temperature and coefficients of the substance. The general form of the Antoine Equation is:

$$\ln(P_{sat}) = A - B/(T + C) \tag{C.7}$$

Where P is the vapour pressure of the substance, T is the temperature, and coefficients A, B, and C are constants specific to the substance, in this instance acetone.

The acetone coefficients shown in table C.1.

A	B	C
16.650	2940.460	−35.930

Table C.1: Acetone Coefficients for Antoine Equation taken from https://www.chesolver.com/antoine.

The resulting calculation we used to determine the saturation vapour pressure of acetone was as follows:

$$\begin{aligned} P_{sat} &= \exp\left(A - B/(T + C)\right) \\ &= \exp\left(16.65 - 2940.46/\left(293.150\,\mathrm{K} - 35.93\right)\right) \\ &= 184.621\,\mathrm{Hg \cdot mm} = 0.246\,\mathrm{bar} \end{aligned} \tag{C.8}$$

The mole fraction $X_{acetone}$ of acetone was then established by $X_{acetone} = P_{sat}/P_{lab}$ where $P_{lab} = 0.830\,\text{bar}$. From this we determine the percent helium for neutral buoyancy using:

$$\%_{helium} = \left(\frac{(\rho_{air} - X_{acetone} \cdot \rho_{acetone})}{\frac{((1.0 - X_{acetone} \cdot (\rho_{helium} - \rho_{air})) - \rho_{air}}{(\rho_{helium} - \rho_{air})}} \right) \cdot 100. \tag{C.9}$$

From this we calculated $\%_{helium} = 49.190\,\%$.

Finally, we determined the density of the mixture using:

$$\rho_{mixture} = (1.0 - X_{acetone}) \cdot (\%_{helium} \cdot \rho_{helium} + (1.0 - \%_{helium}) \cdot \rho_{air}) + X_{acetone} \cdot \rho_{acetone}. \tag{C.10}$$

From this we got $\rho_{mixture} = 0.986\,\text{kg/m}^3$.

C.1.4 *Mass Emission Rate and Flux*

With all of these values established, we were able to model the mass flux (Q) and therefore the mass emission rate ($\dot{M}$) of acetone at the source for three wind speeds or advection velocities. We outline them in the table C.2.

u [m/s]	Q [m^3/s]	Q [ml/m]	$\dot{M}$ [kg/s]
0.050	3.567×10^{-6}	213.992	3.517×10^{-6}
0.100	7.133×10^{-6}	427.983	7.034×10^{-6}
0.200	1.427×10^{-5}	855.967	1.407×10^{-5}

Table C.2: Mass flux Q in m/s m^3/s and the mass emission rate $\dot{M}$ in ml/m of acetone at the source for three wind speeds.

Using these values, along with the diffusivity of acetone:

$D_{acetone} = 0.178 \times 10^{-5}\,\text{m}^2/\text{s}$, we have everything required to model the freestream passive release of acetone transported in a helium air mixture at the three wind speeds.

C.1.5 *Results*

Figure C.1 shows the modelled plumes plotted within the downwind distance extent of the PLIF dataset and with the average measured concentration overlaying the modelled values. The measured concentration values were previously normalised between the odour source fluorescence pixel intensity and the camera dark response. Here, we scaled the already normalised measured concentration to be within the range of values produced by the model.

$$x' = (x \cdot (max(X) - min(X))) + min(X) \tag{C.11}$$

Where x was the measured concentration, x' was the scaled measured concentration, $max(X)$ was the maximum value of the modelled concentration and $min(X)$ was the minimum value of the modelled concentration.

There is no widely established direct mapping of acetone fluorescence to its concentration. Although the mapping is generally considered linear, the relationship between the fluorescence intensity and the concentration of acetone can exhibit nonlinear behaviour, particularly at higher concentrations due to phenomena such as quenching or saturation Lozano, Yip and Hanson (1992).

The nature of this data makes it difficult to establish whether the modelled concentration is a good fit to the measured fluorescence data because of this. We can only compare the shape of the measured and modelled plumes. The model takes into account advection and diffusion and a source concentration that is positively and linearly correlated with the wind speed. The concentration exponentially decreased with downwind distance and the initial source concentration meant that the higher wind speeds reach a greater distance at higher concentrations.

The greatest difference between the concentration–distance curves appears to be due to a source effect: the modelled curves decrease more gradually with downwind distance after the initial release than the measured data. The initial linear flow of the plume, before a turbulent regime is established, could be responsible for this more gradual decrease in concentration with source distance.

C.1.6 *Discussion*

Here we modelled only the freestream release configurations. It is possible to model the near-bed release configuration with Gaussian plume models and it is generally modelled as the sum of the above ground plume and reflection from the floor (Essa, Etman and El-Otaify, 2020), but this does not account for the viscous sub layer. Gaussian plumes are limited in their utility for modelling the average odour concentration of a turbulent plume, however serve as a reasonable estimation of expected concentration with source distance.

Here we have shown, if anything, that the downwind extent of the measured PLIF plume is greater than expected. However, if the model is not correct due to a lack of a mapping between fluorescence and concentration, the problem of double diffusion could be a cause of the limited downwind distance measured by the PLIF system. The diffusivity coefficient of helium $D_{helium} = 0.697 \times 10^{-4}\,\mathrm{m}^2/\mathrm{s}$ is a factor of ≈ 6.6 times greater than that of acetone at the temperature measured in the lab. It is possible that the acetone dropped out of the air-helium carrier gas and therefore out of the laser sheet responsible for causing the acetone to fluoresce and be measured. Until a direct mapping of concentration and fluorescence is established, it is difficult to rule this out as a possibility.

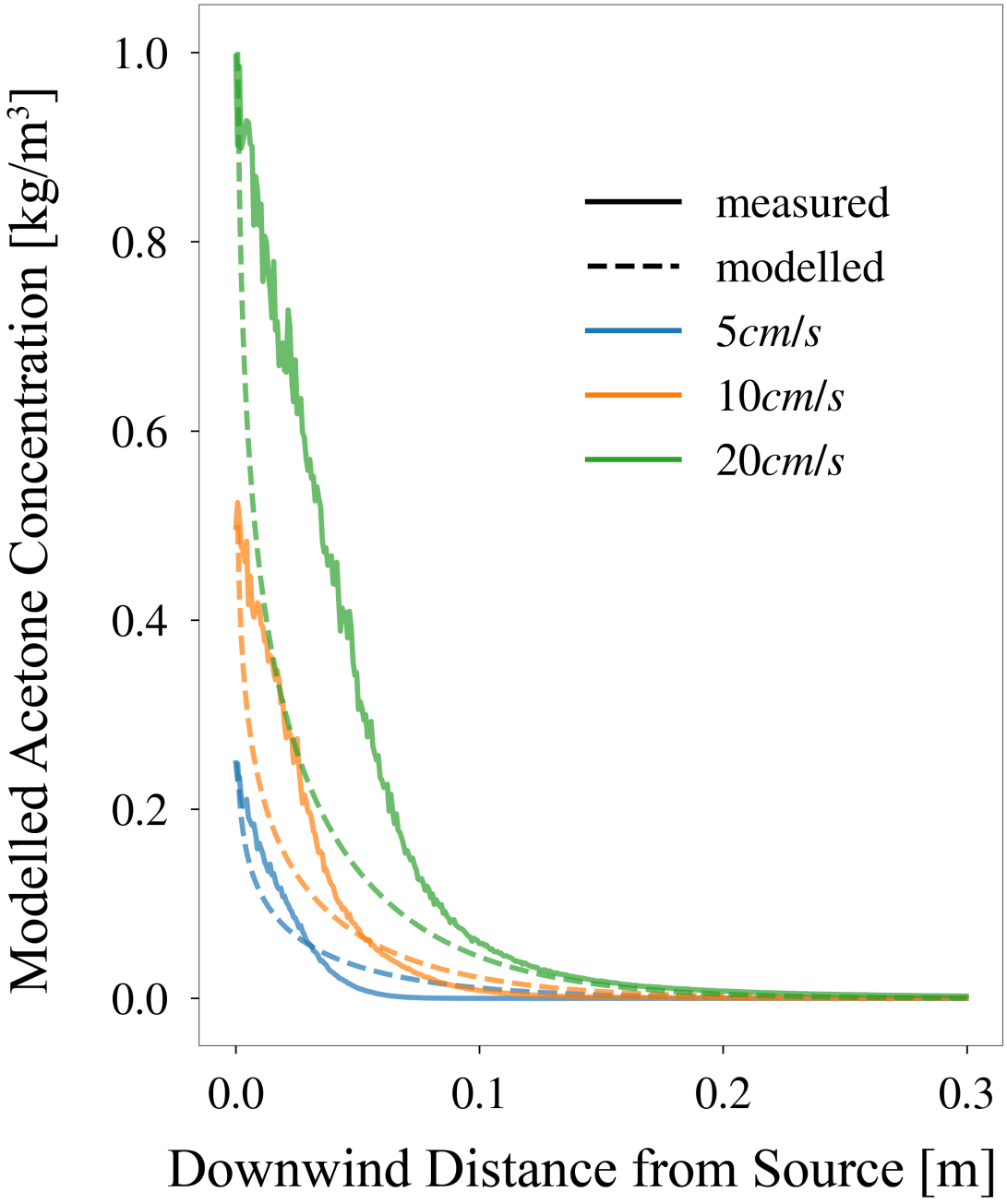

Figure C.1: Modelled diffusion of acetone (dashed) with measured average PLIF normalized concentration $\bar{C}/C_0$ over all datasets and sampled at $y = 0$ and min-max normalized by wind speed.